Encapsulation Polymer Degradation and Its Impact on the Deterioration of Solar Modules

Von dem Promotionszentrum Ingenieurwissenschaften und Informationstechnologien
an der Hochschule Anhalt
angenommene

DISSERTATION

zur Erlangung des akademischen Grades

DOCTOR RERUM NATURALIUM
(Dr. rer. nat.)

Vorgelegt von

M.Sc. Robert Heidrich

Die Anname der Dissertation wurde empfohlen von:

1. Prof. Dr. Valentin Cepus, Hochschule Merseburg
2. Prof. Dr. Franziska Scheffler, Otto-von-Guericke-Universität Magdeburg

Die Verleihung des akademischen Grades erfolgt mit Bestehen
der Verteidigung am 26.06.2025 mit dem **Gesamturteil summa cum laude**.

“Eine genaue Messung ist wertvoller als tausend Expertenmeinungen.”
“One accurate measurement is worth a thousand expert opinions.”

Grace Hopper, Computerpionierin

Kurzfassung

Diese Arbeit beschäftigt sich mit grundlegenden Degradationsmechanismen von Solarmodulen. Ein besonderer Fokus liegt hierbei auf den verwendeten polymeren Verkapselungsmaterialien und den darin enthaltenen Additiven. Durch selbstentwickelte Messverfahren basierend auf Pyrolyse-Gaschromatographie-Massenspektrometrie (PY-GCMS) und ultraviolet–visible (UV/VIS)-Spektralphotometrie wird die Quantifizierung dieser Additive durchgeführt, was eine Vielzahl weiterer Analyseansätze ermöglicht. Einerseits werden so innerhalb dieser Arbeit grundlegende Effekte wie die Additivdiffusion studiert. Andererseits wird das Degradationsverhalten der Polymere in Abhängigkeit der stabilisierenden Additive untersucht.

Im Verlauf der Arbeit werden Solarmodule unterschiedlichen Stressbedingungen wie UV-Strahlung, hoher Luftfeuchte und hohen Temperaturen im Rahmen von beschleunigten Alterungstests unterzogen. Dabei werden die Stressoren einzeln, aber auch kombiniert verwendet, um die daraus resultierenden Degradationseffekte der Solarmodule zu analysieren. Die Analysen beinhalten dabei sowohl makroskopische Charakterisierungsmethoden wie I-V Kennlinien und Elektrolumineszenz (EL)-Messungen als auch verschiedenste Methoden der Polymeranalytik wie Fourier-Transformations-Infrarot Spektrometrie (FTIR), Evolved-Gas-Analysis (EGA)-FTIR, Dynamische Differenzkalorimetrie (DSC) und UV/VIS-Spektralphotometrie. Die Wechselwirkungen der Additive wurden mittels PY-GCMS, paramagnetischen Elektronenresonanz-Spektroskopie (EPR) und Orbitrap Massenspektrometrie bestimmt.

Durch die Kombination dieser Messverfahren war es möglich die Degradationskette von Solarmodulen vom Verbrauch stabilisierender Additive, über die Degradation der Verkapselungspolymere bis hin zur Degradation der Solarzelle selbst und deren elektrischer Verbinder nachzuvollziehen. Dabei konnte insbesondere darauf eingegangen werden, welche Degradationsreaktionen in Folge des in verschiedenen Punkten im Modul vorherrschenden Mikroklimas zu erwarten sind. In diesem Zusammenhang konnten Modelle abgeleitet werden, welche die Degradation von UV Stabilisatoren und UV Absorbern in Abhängigkeit der Umgebungsparameter vorhersagen. Durch die Vielzahl der durchgeführten beschleunigten Alterungsserien konnte außerdem der UV Alterungsstandard IEC 62788-7-2 validiert werden. Es stellte sich heraus, dass die im Standard aufgeführten UV-A Fluoreszenzlampen im Gegensatz zu Xenonlampen mit Tageslichtfiltern nicht zu Alterungseffekten führen, die im Feld beobachtet wurden. Folglich sind erstere als ungeeignet einzustufen, um Polymermaterialien für Solarmodule zu qualifizieren.

Aus den Ergebnissen der Arbeit lassen sich einerseits diverse grundlegende Effekte wie die Additivwechselwirkungen und deren Diffusion in Mehrschichtsystemen ableiten, andererseits können klare Schlussfolgerungen für die Industrie gezogen werden, um die Lebensdauer von Solarmodulen zukünftig zu erhöhen. Letzteres ist von besonderem Interesse für die Einführung neuartiger Zell Technologien wie TOPCon (Tunnel Oxide Passivated Contact) oder HJT (Hetero Junction) und den damit einhergehenden, neuartigen Verkapselungsmaterialien POE (Polyolefin Elastomer) und TPO (Thermoplastisches Polyolefin).

Abstract

This thesis deals with the basic degradation mechanisms of solar modules, focusing on the polymer encapsulation materials used and the additives they contain. Using self-developed measurement methods based on pyrolysis gas chromatography mass spectrometry (PY-GCMS) and ultraviolet-visible (UV/VIS) spectrophotometry, the quantification of these additives is carried out, enabling a variety of further analysis approaches. On the one hand, fundamental effects such as additive diffusion are studied within this work. On the other hand, the degradation behavior of the polymers is investigated as a function of the stabilizing additives.

In this work, solar modules are subjected to different stress conditions such as UV irradiation, high humidity, and high temperatures as part of accelerated aging tests. The stressors are used individually and in combination to analyze the resulting degradation effects of the solar modules. The analyses include macroscopic characterization methods such as I-V and electroluminescence (EL) measurements as well as various methods of polymer analysis such as Fourier transform infrared spectrometry (FTIR), evolved gas analysis (EGA)-FTIR, differential scanning calorimetry (DSC) and UV/VIS spectrophotometry. The interactions of the additives were determined using PY-GCMS, electron paramagnetic resonance spectroscopy (EPR), and Orbitrap mass spectrometry.

By combining these measurement methods, it was possible to trace the degradation chain of solar modules from the consumption of stabilizing additives through the degradation of the encapsulation polymers to the degradation of the solar cell itself and its electrical connectors. In particular, the degradation reactions to be expected due to the prevailing microclimate at different positions within the modules could be investigated. In this context, models that predict the degradation of UV stabilizers and UV absorbers could be derived depending on the environmental parameters. The UV aging standard IEC 62788-7-2 was also validated thanks to the large number of accelerated aging series carried out. It was found that the UV-A fluorescent lamps listed in the standard, in contrast to xenon lamps with daylight filters, do not lead to the aging effects observed in the field. Consequently, the former are to be classified as unsuitable for qualifying polymer materials for solar modules.

On the one hand, various fundamental effects, such as additive interactions in multilayer systems and their diffusion behavior, can be derived from the results of the work. On the other hand, clear conclusions can be drawn for the industry to increase the service life of solar modules in the future. The latter is of particular interest for the introduction of new cell technologies such as TOPCon (tunnel oxide passivated contact) or HJT (hetero junction) and the associated new encapsulation materials POE (polyolefin elastomer) and TPO (thermoplastic polyolefin).

Contents

Abbreviations and nomenclature

As this work is a cumulative dissertation, it was not possible to use consistent nomenclature and abbreviations throughout. All abbreviations and terms are explained when they first appear in the main text or the respective publication. However, abbreviations are written out again if appropriate at specific points in the text to improve the reading flow.

1. Introduction

1.1. Motivation

In the near future, climate change will not only cause immense damage to living creatures and the environment, but most people will also suffer a significant loss of prosperity [1, 2]. This will be accompanied by an ever-increasing demand for energy, which will also be enhanced by climate change itself due to global warming [3]. Reducing CO_2 emissions is essential to have a lasting, positive impact on the climate [4]. Photovoltaics (PV) as a renewable energy source, in particular, has not only experienced a massive upswing in recent years [5–7], it is also considered to be comparatively reliable and less at risk from climate change [8]. However, due to their outdoor use, solar modules are exposed to various environmental influences, which can lead to a variety of degradation effects and significantly affect their service life [9–12]. Solar modules are designed to function in the field for at least 25 years. However, this is only economical if the annual degradation rate does not exceed 0.73 % [13]. In reality, however, values far above 1 % are possible and malfunctions must be expected at any time [14, 15]. It is therefore essential to understand and predict the degradation behavior of solar modules to make the supply of PV energy as reliable as possible.

The long-term behavior of the solar modules is determined in particular by the polymeric encapsulation materials used, as these shield the solar cell from harmful environmental influences [9, 16]. In addition, the polymer layers influence effects such as potential induced degradation (PID) [17, 18]. Thus, it is not surprising that many of the module failures observed are due to the degradation of the encapsulation materials [19]. However, there are only a few studies that directly correlate the degradation of the encapsulation material with the degradation of the overall module [20, 21]. So far, many models for predicting degradation have been empirical, without reference to underlying physical and chemical processes of the encapsulation material [15, 22–28].

Figure 1 shows the schematic structure of a silicon-based solar module with ethylene-vinyl acetate copolymer (EVA) encapsulant and the acting stressors. Typically, solar modules are exposed to UV irradiation, moisture ingress, thermomechanical stresses, and other environmental influences during their use [9–12]. To enable polymer crosslinking, which determines the mechanical behavior, and to ensure that the encapsulation material has the necessary properties to protect the cell from all these environmental influences, additives are added to the base polymer [29–31]. Consequently, stabilizing additives in particular significantly determine the degradation behavior of the encapsulant [30, 32–39], which in turn determines the degradation behavior of the overall module [9, 16]. However, since most of the work in this area only relates to the interaction of additives in single polymer layers [35, 39–43], the results cannot simply be transferred to a multilayer system such as a solar module. Furthermore, there is currently no suitable method for quickly and easily determining the quantities of additives in PV encapsulants. This is problematic because additives tend to diffuse within a single polymer layer as soon as there is a concentration gradient, and the influence of these migration effects cannot be adequately assessed without the possibility of additive quantification [44–46].

To fully understand the long-term behavior of solar modules, the interaction potential of the smallest components, such as polymer additives, must be considered. In addition, there are various possibilities of interaction between the different layers, such as between the polymer layers, the polymers and the glass or the polymers and the cell. Solar modules are physically complex multilayer systems and the current approach is too simplistic to make reliable predictions regarding their degradation behavior.

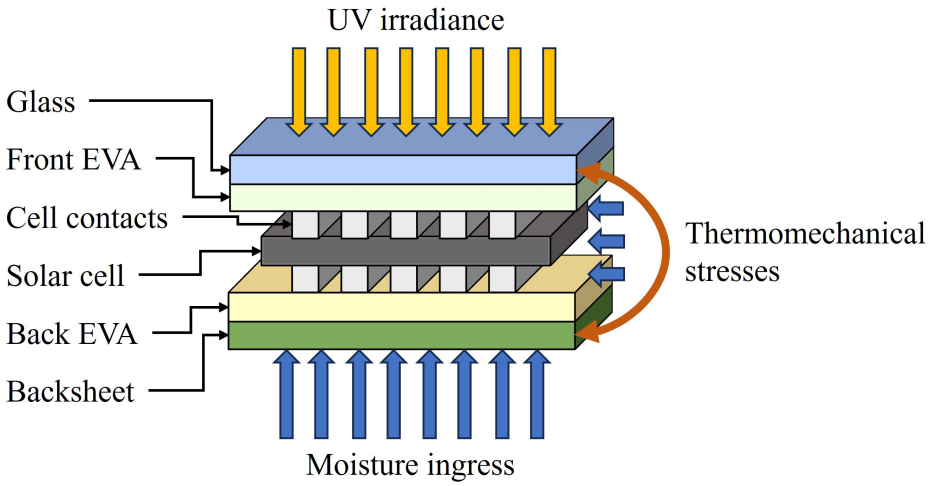

Figure 1: Schematic structure of a solar module with ethylene-vinyl acetate copolymer (EVA) encapsulant and the impacting stressors.

1.2. Research question and objectives

The degradation of solar modules depends, on the one hand, on the existing environmental influences and, on the other hand, on the combination of selected materials. The degradation behavior can only be fully understood if both points are considered. Currently, PERC-based modules with EVA encapsulant have the largest market share [47], so this work focuses on this material combination. The aim is to fully understand the degradation chain of the solar module composition. The influence of the various stressors on the stabilizing additives and, subsequently, on the encapsulation material shall be investigated. The degradation of the latter shall then be linked to the degradation of the solar cell and the electrical connectors. Accelerated aging tests based on IEC 61215 and IEC 62788-7-2 are used to achieve results in relatively short time intervals [48, 49]. However, it is unclear at this stage to what extent these tests can reflect real aging effects, so their validity must also be investigated. To fulfill the main objective, smaller sub-objectives can be defined:

i Analysis of the degradation behavior of solar modules and their separate components under individual stress conditions.

ii Degradation analysis of solar modules and their separate components under combined stress conditions to estimate synergy effects of several stressors.

iii Development of a method for additive quantification and investigations of additive degradation and interactions.

iv Validation of the new UV aging standard for polymer materials in the PV sector IEC 62788-7-2 with reference to real aging effects in the field.

1.3. Scientific approach and methodology

To fulfill the objectives of the work, a large number of measuring devices, experimental parameters, and self-prepared samples were used. Measurement data was generally exported in raw format and processed using Python and its libraries. The respective methodology is described in detail in the individual publications and separate sections suitable for publication. Therefore, this chapter only intends to provide a brief overview of the procedures used to fulfill the objective.

Sample preparation and accelerated aging

To investigate degradation effects in encapsulants and the overall module, various samples were produced in-house. Starting with the analysis of individual polymer additives, various encapsulants were later produced using a polymer kneader and a hydraulic press. The possibility of defining the additivation opened up the possibility of additive quantification on the one hand. On the other hand, the effects of individual additives and their interactions on the degradation behavior of the films could be studied. In the next step, glass/encapsulant/glass laminates and coupon samples (glass/encapsulant/busbar/encapsulant/backsheet) were produced, and the degradation behavior of the polymers was investigated. The production of these samples was made possible by using a laminator. To enable correlation with commercial solar modules, mini modules with a conventional structure (glass/encapsulant/PERC-based solar cell/encapsulant/backsheet) were also produced, artificially aged and examined for their degradation behavior.

The accelerated aging of the samples took place in different climate chambers with varying parameters. Both, the influence of individual stressors such as UV radiation or high humidity in conjunction with high temperatures and their combination were investigated. The variation of different UV lamp spectra and their intensities allowed conclusions to be drawn about the dependence of the degradation behavior of solar modules and encapsulants on the photon distribution. Since the combination of stressors has not yet been standardized, basic research on the influence on module degradation could be carried out in this area.

Additive quantification

The quantification of additives in PV encapsulants was mainly carried out using pyrolysis-gas chromatography-mass spectrometry (PY-GCMS). This device is already used in the qualitative analysis of additives, but a method for quantification was only developed and published within this thesis. The self-produced film samples with different additive concentrations were used to derive calibration functions to determine the additive density

in unknown film samples. Using ultraviolet-visible (UV/VIS) spectrophotometry, a non-destructive method for quantifying UV absorbers in polymer films was also developed. Based on these results, a patent application was filed for an inline-capable measuring device for non-destructive quality control of polymer films.

Encapsulant and additive degradation analysis

The properties and degradation of the encapsulants studied were characterized using various polymer analysis methods. In addition to standard measurement methods such as Fourier-transform infrared spectroscopy (FTIR), differential scanning calorimetry (DSC), and UV/VIS spectrophotometry, methods such as thermogravimetric analysis (TGA) were also used, but the results were not included in this work. In addition, comparatively novel measurement methods, such as the coupling of the FTIR spectrometer with evolved gas analysis (EGA-FTIR) and Orbitrap mass spectrometry, which corresponds to a Fourier transform mass spectrometry (FTMS), were used. The latter was carried out in cooperation with TotalEnergies OneTech in Solaize, France.

Additives were mainly investigated by using the PY-GCMS method. However, the behavior of the UV absorbers could also be studied using UV/VIS measurements. Furthermore, electron paramagnetic resonance measurements (EPR) were used to investigate the functional cycle (Denisov cycle) of UV stabilizers (hindered amine light stabilizer HALS) and were also carried out in cooperation with TotalEnergies OneTech in Solaize, France.

Evaluation of solar module degradation

The degradation of solar modules was studied as holistically as possible. On the one hand, the modules were non-destructively characterized at regular intervals using I-V curves and electroluminescence (EL) measurements during aging. On the other hand, modules were removed after these time intervals, and the polymer layers were extracted. The polymer and additive characterization methods described above were carried out on these layers (or on cut-off parts of the entire modules - see EPR). In this way, the degradation chain could be traced from start to finish, and it was possible to correlate the consumption of the stabilizing additives with the encapsulant degradation, which in turn could be linked to the macroscopically measurable degradation of the solar modules (performance losses, etc.)

1.4. Structure of this cumulative thesis

At the beginning of this work, a comprehensive understanding of the scientific background is provided. It not only goes into detail about additives, their possible interaction, various encapsulation polymers, and their degradation mechanisms. A solar cell's basic physical concepts are also highlighted to explain the diode characteristic curve or phenomena such as electroluminescence. Subsequently, the degradation mechanisms of PERC solar cells will be discussed in more detail to substantiate the later results. The

last fundamentals chapter deals with various forms of accelerated aging and presents some of the tests used in this work.

The results section of this thesis contains six publications [50–55], which are dealt with in separate chapters, underpinned by supplementary analyses and linked by short text passages. In the beginning, the degradation behavior of solar modules under individual stressors is examined to investigate their effects on module degradation and the mechanisms of stabilizing polymer additives. Subsequently, methods for quantifying different polymer additives are presented, and commercial films are examined for their additive content. The two previous findings are used to validate the test conditions of the UV aging standard IEC 62788-7-2. By determining optimal UV test parameters, the diffusion behavior of UV additives, their influence on polymer degradation, and their interaction potential are subsequently investigated. Finally, aging parameters are combined in a new series of experiments, and all previous findings are pooled to understand the degradation chain of solar modules as a whole.

The discussion chapter discusses the effects of different stress conditions on additives and polymers. The interaction between the two material groups is also considered. Subsequently, the degradation chain of PERC-based solar modules is examined in detail. The findings are then extrapolated to various new module materials to assess future forms of degradation. Furthermore, common degradation models are presented and it is argued how the results of this work could improve modeling and predictive power. Before the thesis concludes, essential points are summarized that the industry could consider to enhance the longevity of solar modules.

2. Scientific background

2.1. Polymer components and their modes of degradation

The following chapter deals with the encapsulation polymers commonly used in the photovoltaic industry, the additives they contain, and the potential degradation mechanisms that may occur. The behavior of ethylene-vinyl acetate copolymer (EVA), polyolefin elastomer (POE), and thermoplastic olefin (TPO) is examined in detail. The type of backsheet used in the further course of this work is also presented. Furthermore, the functionality of the individual additives, potential interactions, and general physical effects are described. The encapsulant, in particular, must meet clearly defined requirements. These were already discussed by Czanderna and Pern in 1996 and are still relevant [30, 31]:

i mechanical support of the solar cell circuit during the manufacturing process, transportation, storage, installation, and operation in all environmental conditions [30, 31]

ii compensation of the different thermal expansion coefficients of the materials used to avoid stress and cell breakage [56]

iii maximum optical coupling between the solar cell and the incident radiation should be enabled and maintained during the operating time [30, 31]

iv physical isolation of the solar cell and the components of the electrical circuit from harmful environmental factors [30, 31]

v reliable electrical insulation of the components of the solar cell circuit over the service life of the modules [30, 31]

The chapter assumes a basic knowledge of organic chemistry and polymer science. Interested readers are recommended to read the works of Rubinstein and Colby (polymer physics) [57], Ehrenstein and Pongratz (degradation of polymers) [58], Zweifel (stabilization of polymers) [59], and Yang, French and Bruckman (durability of polymers in photovoltaic modules) to gain a basic understanding [60].

2.1.1. Polymer additives

Depending on the base polymer used, a variety of additives can be added to improve its properties. In addition to additives that enable the polymer chains to crosslink in the first place, UV absorbers, stabilizing additives, and adhesion promoters are also used. Table 1 lists the additives contained in a commercial POE encapsulant that was investigated during the period of this work. The quantities correspond to data from various publications and from the quantification procedure developed within this work [29, 51, 61, 62]. Surprisingly, the general composition of the additives contained has not changed for almost 40 years [29]. Only the use of crosslinking accelerators is a relatively

new topic, and the literature in the field of photovoltaics is very sparse. However, as this additive only provides bonds during the lamination process and does not actively contribute to the crosslinking enthalpy, it can be assumed that the proportion must be lower than that of the crosslinking peroxide. The following sections will go into detail about how the various additives work.

Trade name	Function	Typical amount [wt.%]
Luperox TBEC	crosslinking peroxide	0.6 - 1.5
Silane A 174	adhesion promoter	$\approx$ 1.2
NSC 174502	primary antioxidant	$\approx$ 0.25
ADK STAB LA 82	UV stabilizer	0.1 - 0.2
TAIC	crosslinking accelerator	0.05 - 0.15
Cyasorb UV 531	UV absorber	$\approx$ 0.3
Tinuvin 770	UV stabilizer	0.1 - 0.2
Naugard 524	secondary antioxidant	$\approx$ 0.25
D 16-834	secondary antioxidant	$\approx$ 0.25

Table 1: A list of additives contained in a commercial POE encapsulant that was analyzed in the course of this work. The typical amounts of additives listed are based on [29, 51, 61, 62] and the quantification carried out in later chapters.

Crosslinking peroxides and crosslinking accelerators

The EVAs and POEs currently used are generally crosslinking polymers [51, 52, 61–63]. This is necessary to ensure the required mechanical stability over a wide temperature range [63, 64]. As the encapsulants shield the cell and optical coupling must also be maintained, a certain degree of crosslinking is essential [63–66]. To achieve this, a system consisting of two additives with different functionalities is usually used. These are a crosslinking peroxide and a crosslinking accelerator [51, 52, 61, 62]. Both additives and their principle of work with an example EVA crosslinking mechanism are displayed in Figure 2.

The crosslinking process of encapsulants for solar modules typically takes place during lamination in the manufacturing process. For this purpose, crosslinking peroxides **a)** (e.g., Luperox TBEC) are added to the polymer matrix [67–70]. The O-O bond (blue ellipsis in Figure 2) is thermally destroyed during the lamination process and two radicals are formed [69, 70]. In the next step, the resulting radicals react via hydrogen abstraction either with the added crosslinking accelerator **b)** (TAIC) creating TAIC radicals **d)** or with the polymer chains creating macro radicals **c)**[69–72]. The newly formed radicals recombine and establish covalent bonds between different polymer chains or polymer chains and crosslinking accelerator molecules forming a 3D polymer network **e)** [67–70, 72]. In general, the crosslinking reaction of polyethylene-based polymers proceeds similarly. For EVA, however, the crosslinking reaction can take place between the vinyl acetate groups of the individual chains, between the vinyl acetate and polyethylene group, or between two polyethylene groups, whereby bridges can be formed between the

functional groups by TAIC molecules [63, 72, 73]. In the case of crosslinking by UV radiation, it must be mentioned that TAIC molecules themselves can also contribute to hydrogen abstraction, so the crosslinking reaction takes place differently [74, 75]. However, as this case is not relevant to solar modules, it will not be discussed further.

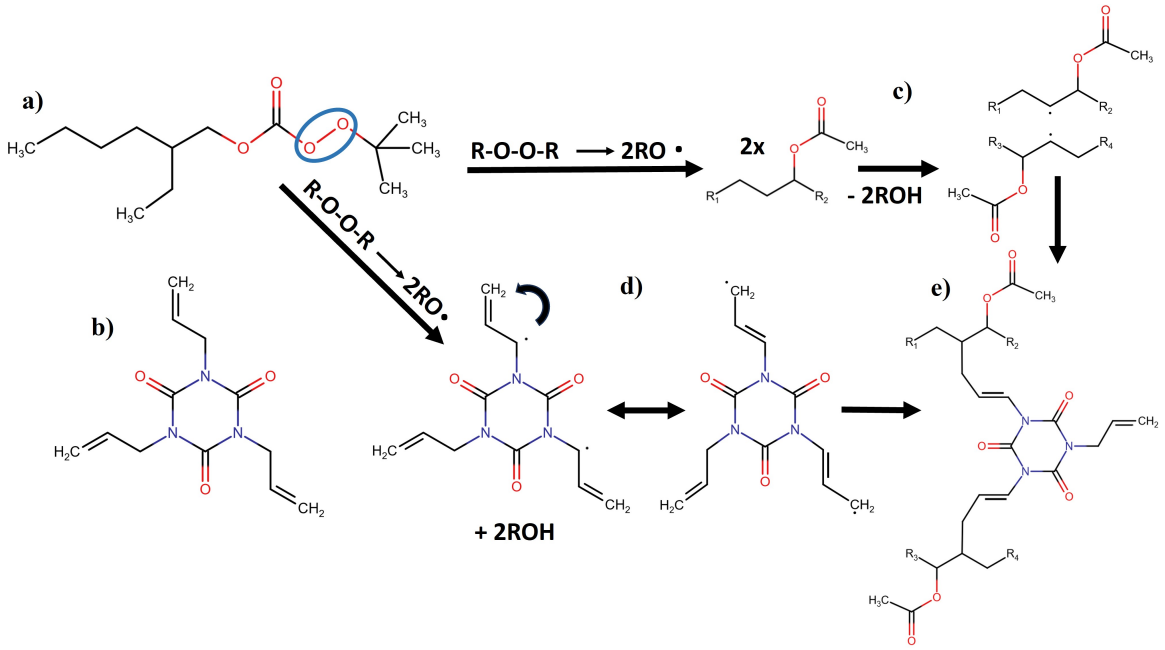

Figure 2: a) crosslinking peroxide (Luperox TBEC), b) crosslinking accelerator (TAIC), c) radicalized EVA chains, d) radicalized crosslinking accelerator, and e) crosslinking of two EVA chains using a crosslinking accelerator molecule for bridging.

Adhesion promoters

Sufficient adhesion of the various polymer layers to each other, to the solar cell, and to the glass is essential to prevent subsequent reactions due to delamination [76–78]. Depending on the mounting position and in particular due to the new glass-glass modules, the adhesion between encapsulant and glass as well as encapsulant and solar cell becomes all the more important [78]. Adhesion promoters are usually added to the polymer matrix to improve adhesion between the encapsulant and the glass [51, 52, 61, 62]. These adhesion promoters are typically based on silane molecules and form covalent bonds between the polymer network and the glass surface [78–81]. The functional principle is shown in Figure 3.

Silane-based adhesion promoters are added to the polymer matrix. During the lamination process of the solar modules, the reactions shown in Figure 3 take place with the glass surface. In the beginning, a hydrolysis reaction **a)** of the methyl group takes place, and methanol is formed [78, 79]. The moisture required for this process comes from the atmosphere of the laminator. In the next step, the resulting silanol groups condense and form oligomers **b)** [78, 79]. Hydrogen bonds are formed between the glass surface and

the oligomers **c)**. In the last step **d)**, covalent bonds are formed between the adhesion promoter and the glass surface during dehydration [78–80]. It must be mentioned that the listed reactions are shown sequentially but can take place simultaneously after the hydrolysis step [79].

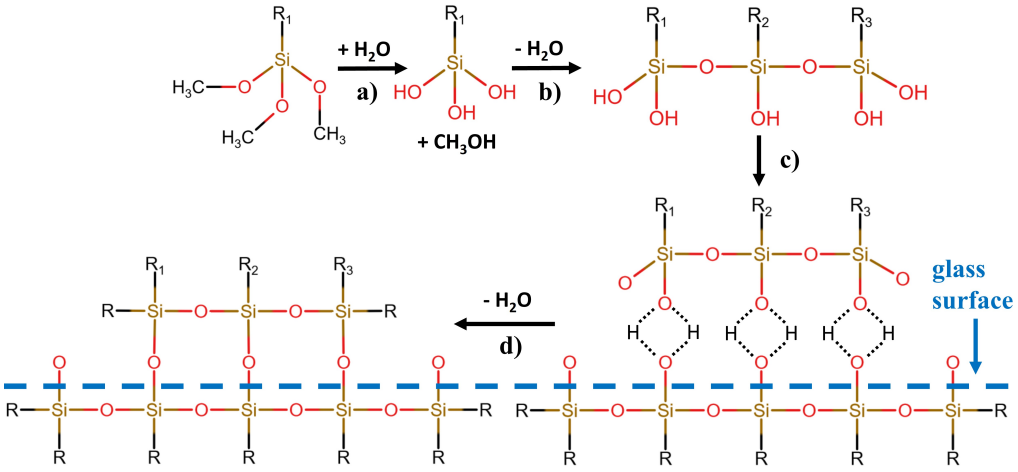

Figure 3: a) hydrolysis of the functional silane group, b) condensation to oligomers, c) hydrogen bonding to the glass surface, d) dehydration and formation of covalent bonds [78–81]

The R_1, R_2, and R_3 groups on the opposite side of the adhesion promotor typically contain terminal methyl and methylidine groups [80, 81]. The radicals formed after thermally induced crosslinking peroxide decomposition, as listed in the previous section, also react with these groups under hydrogen abstraction. As a result, covalent bonds are formed between the coupling agent and the polymer network in the subsequent step. In general, a monolayer of polysiloxanes is desired. Depending on the concentration of the adhesion promoter, however, several layers can also be formed [79].

UV absorbers

UV absorbers are used to absorb high-energy photons that could otherwise destroy the polymer components of the solar modules [30, 32, 33]. In contrast to antioxidants and UV stabilizers, however, they should not react directly with radicals or polymer fragments.

There are a large number of different UV absorbers for photovoltaic encapsulants. In general, however, a distinction can be made between two classes. On the one hand, benzotriazole-based UV absorbers and on the other hand, hydroxybenzophenone-based UV absorbers [36, 40, 41]. Within each category, there are various modifications with different structural and molecular formulas [36, 40]. However, the functional group is usually the same. What all UV absorbers have in common is that the principle of action is reversible as long as the photon energy is not so high that molecular bonds are destroyed [36, 42]. The mode of action of both UV absorber classes is shown in Figure 4. Benzotriazole-based UV absorbers absorb the UV radiation and release the absorbed

energy in the form of heat through proton transfer [36, 82]. Hydroxybenzophenone-based UV absorbers work by means of keto-enol tautomerism [36, 42, 83]. The keto form absorbs UVB and UVC radiation [83]. The absorbed energy is also released in the form of heat using proton transfer.

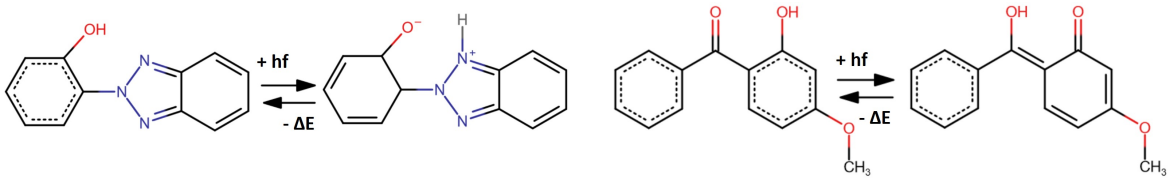

Figure 4: UV absorption and energy dissipation mechanism of benzotriazole-based UV absorbers (left) and hydroxybenzophenone-based UV absorbers (right). Adapted from [36].

Although the mode of action is supposed to be reversible, excessive UV radiation can also cause degradation of the UV absorber. This can result in fragments such as phenol cleavage products, radicals, or chromophores [32, 34, 41, 42]. There are several studies on the degradation behavior of UV absorbers depending on the irradiation intensity [40–42]. It was found that the degradation kinetics depend on the absorption properties of the polymer matrix [40, 41]. Furthermore, it is possible that UV absorbers react with other additives (especially crosslinking peroxides) [34]. They can themselves be radicalized by this process and react to form chromophores, which leads to browning of the encapsulant and thus to a loss of performance of the solar module [34, 64].

UV stabilizers

To protect the encapsulation polymers from reactions with radicals and the resulting degradation, radical scavengers in the form of hindered amine light stabilizers (HALS) are usually added to the polymer matrix[51, 52, 61, 62, 84]. In contrast to the UV absorber, these additives do not absorb UV radiation but bind radicals that are created by the degradation processes of the encapsulant and prevent them from further damaging reactions [34, 36–39]. By combining UV absorbers and UV stabilizers, synergy effects can be achieved that protect the encapsulant all the better against degradation [34, 35].

Since HALS molecules undergo reactions according to their principle of work, at least the number of base molecules is not preserved [37–39, 52, 53]. The complex interaction behavior of the HALS molecules is called the Denisov cycle (after Evguenii T. Denisov) [37, 39]. A simplified form of the cycle is shown in Figure 5 while the HALS molecule is represented by its functional amine group 2,2,6,6-tetramethylpiperidine [39]. During reaction **a)**, the HALS molecule is oxidized to the nitroxide radical 2,2,6,6-tetramethylpiperidin-1-loxyl (TEMPO) [39]. Due to the steric hindrance of the two methyl groups, the radical cannot react with polymer chains but reacts very quickly with carbon-centered radicals [59, 85]. It is assumed that this reaction is caused by interaction with a hydroperoxide (in the case of photovoltaic encapsulants, for example, by oxygenation and photooxidation), which forms a hydroxylamine or an alkoxylamine

and is subsequently oxidized by a peroxyl radical [39, 86]. Alternatively, direct photooxidation via acylperoxyl radicals generated by Norrish type II degradation and their aldehyde products has been proposed [39, 43].

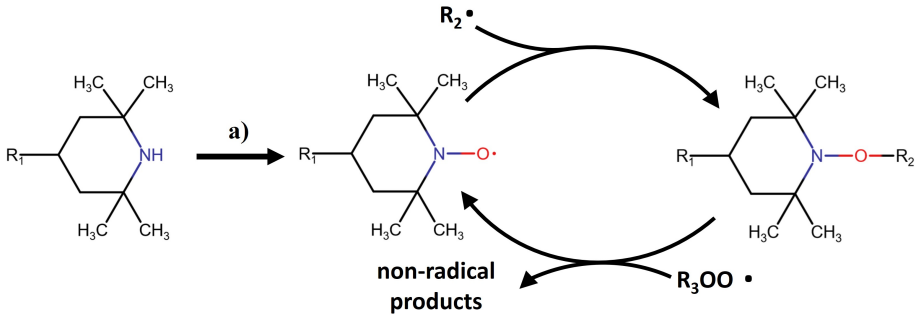

Figure 5: Simplified form of the Denisov cycle (adapted from [39]).

Starting from TEMPO, the actual cycle of the functional group begins. During the last decades, over 30 potential reactions have been postulated. However, recently these reactions have been reduced to a smaller number of energetically more probable processes [39]. Depending on whether the nitroxide reacts with an ROO•, RO• or R• group, different reaction chains take place, which temporarily stop at local energetic minima [39]. Most reactions take place through interaction with polymeric radicals (R•). These react with the intermediate formation of alkoxyamines and hydroxylamines to form nitroxides again [39]. The reactions with the other two groups also ultimately lead to nitroxide formation and a potential restart of the cycle [39]. Through slower reactions with peroxyl radicals ROO• and intermediate formation of a trioxide species N-O-O-O-R, further reactions can even restore the original amine group [39].

Antioxidants

In addition to the UV stabilizers mentioned above, antioxidants are also an effective way of preventing polymer degradation. Like the other additives, the antioxidants can be added during the production of the encapsulant, or they can be added as a process stabilizer during the production of the raw material granules [51, 84]. In general, a distinction is made between two types of antioxidants. Primary antioxidants act as radical scavengers, and secondary antioxidants convert hydroperoxides into forms that are potentially less harmful to the polymer [59, 87, 88]. Primary antioxidants (see Figure 6) are usually phenol-based and secondary antioxidants (see Figure 7) are mostly organic phosphites [59, 87, 88].

Figure 6 shows the simplified function of a primary antioxidant using the example of butylated hydroxytoluene (BHT). However, this can differ depending on the degree of steric hindrance for other antioxidants [59]. In the example shown, process **a)** begins with the formation of hydroperoxides after hydrogen abstraction from BHT and thus the stabilization of the initial radical with the formation of a phenoxyl radical which

is comparatively stable due to the functional groups at the 2- and 6- positions [59]. In the next step **b)**, a reversible redistribution of the electronic structure occurs, resulting in a ketone group [59]. In this form, the antioxidant is able to bind another radical through reaction **c)** and convert it into a peroxide [59]. Depending on the degree of steric hindrance, a variety of other reactions can occur, which lead to irreversible C-C bonds (coupling with the polymer matrix) [59]. If oxygen-centered and carbon-centered radicals react, this leads to reversible C-O bonds [59].

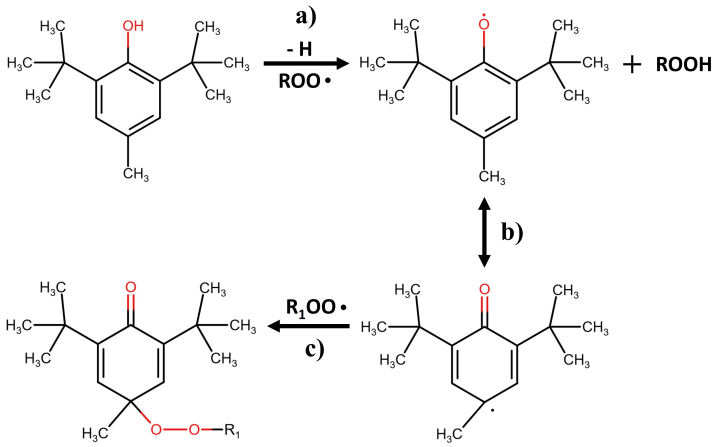

Figure 6: Simplified functional principle of the phenol-based primary antioxidant butylated hydroxytoluene (BHT) (adapted from [59]).

The mechanism of action of a phosphite-based antioxidant is visualized in Figure 7. The residual groups R_1 to R_3 are usually relatively large structures (see e.g., Irgafos 168) in order to achieve steric hindrance. Otherwise, this type of antioxidant tends to hydrolyze [59, 89]. Hydroperoxides react exactly stoichiometrically to form the respective alcohol, oxidizing the phosphite to the respective phosphate [59].

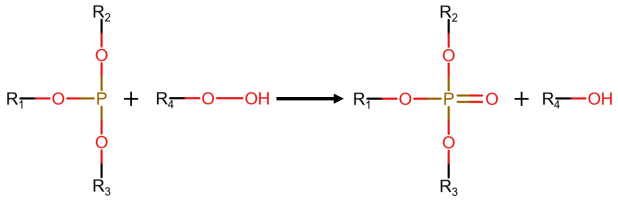

Figure 7: Functional principle of a phosphite-based secondary antioxidant (adapted from [59]).

2.1.2. Expected interactions

This chapter deals with the expected interactions of the various additives. This does not refer to the functionalities presented but to undesirable effects that can occur when the additives are combined. In addition, the general effect of diffusion is discussed, as

this occurs for all mobile species (without covalent bonding to macromolecules such as polymer chains) such as additives, water, oxygen, etc. [44]. In particular, the diffusion of stabilizing additives is an important topic and has already been discussed in the literature, as these additives determine the long-term behavior of the polymer [46, 90–93].

Diffusion effects

With sufficient energy input (usually a certain temperature), diffusion is an effect that can be statistically substantiated [94–97]. In the case of concentration differences and free particles, the undirected particle movements automatically result in a net particle transport if a sufficient time interval is considered [94, 96, 97]. Consequently, the general assumption for diffusion theory is that the transfer rate (flux) F through a unit area is proportional to the concentration gradient [94, 95], i.e.

$$F = -D\frac{\partial C}{\partial x} \tag{1}$$

with the concentration C, the space coordinate normal to the section x and the diffusion constant D [94]. At this point, it should be mentioned that the diffusion constant can also be concentration-dependent, e.g., in the case of polymers [94]. The following derivation of the diffusion equation from Equation 1 is based on the work of John Crank [94].

Let A, B, C, D, A', B', C', D' be the vertices of a cuboid volume element with side lengths $2\mathrm{d}x$, $2\mathrm{d}y$, $2\mathrm{d}z$. Let $P(x, y, z)$ also be the center of the volume element at which the concentration of the substance under consideration is C. Then, according to Figure 8, the diffusion rate of a substance passing through perpendicularly the area $ABCD$ into the plane $x - \mathrm{d}x$ is given by

$$4\mathrm{d}y\mathrm{d}z\left(F_x - \frac{\partial F_x}{\partial x}\mathrm{d}x\right), \tag{2}$$

with the flux in x direction F_x through the unit area through P. In the same sense, the outflow rate of the diffused substance can be determined by means of

$$4\mathrm{d}y\mathrm{d}z\left(F_x + \frac{\partial F_x}{\partial x}\mathrm{d}x\right). \tag{3}$$

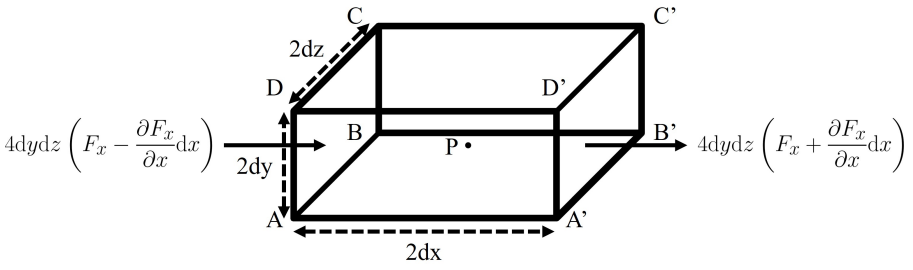

Figure 8: Element of volume with a flux in x-direction (adapted from [94]).

If the net flow rate is now calculated by subtracting the contributions of Equation 2 and Equation 3, the contribution to rate changes is

$$-8\mathrm{d}x\mathrm{d}y\mathrm{d}z\frac{\partial F}{\partial x}. \tag{4}$$

The calculation of the other cuboid areas is carried out in the same way to obtain similar results as Equation 4, and it also applies that the rate of change of the concentration is given by

$$8\mathrm{d}x\mathrm{d}y\mathrm{d}z\frac{\partial C}{\partial t}. \tag{5}$$

From Equation 4, the results of the other lateral surfaces and Equation 5 follows

$$\frac{\partial C}{\partial t}+\frac{\partial F_x}{\partial x}+\frac{\partial F_y}{\partial y}+\frac{\partial F_z}{\partial z}=0. \tag{6}$$

If the diffusion constant D is independent of the concentration, inserting Equation 1 into Equation 6 yields the diffusion equation

$$\frac{\partial C}{\partial t}=D\left(\frac{\partial^2 C}{\partial x^2}+\frac{\partial^2 C}{\partial y^2}+\frac{\partial^2 C}{\partial z^2}\right). \tag{7}$$

Equation 7 will be further investigated in a later chapter and solved numerically to simulate the movement of mobile species in encapsulation polymers.

Consumption of stabilizing additives

As the function of the additives contained in the polymer films is partly contradictory, certain interactions cannot be avoided. This applies in particular to crosslinking peroxides and stabilizing additives. The former generate radicals for the crosslinking reaction [69, 70], while the latter are added to bind radicals [34, 36–39, 59, 87, 88]. In particular, the combination of UV absorbers, UV stabilizers, and crosslinking peroxides in EVA encapsulants within solar modules has been investigated in the past [29, 34].

Klemchuk et al. found that significant amounts of UV absorber and UV stabilizer (HALS) were consumed within 12 weeks of artificial aging when 1.5 wt % crosslinking peroxide content was added to the encapsulant. Since primary antioxidants have a similar mode of action to HALS, it can be assumed that these additives can also be consumed by reactions with crosslinking peroxides [59, 87, 88]. It is therefore important that the addition of crosslinking peroxides and stabilizing additives is coordinated with each other and with the lamination process. On the one hand, as many peroxides as possible must be used up during lamination in order to avoid subsequent reactions. On the other hand, depending on the application, a larger quantity of stabilizing additives must be added to compensate for the consumption of peroxides during the crosslinking reaction. The remaining crosslinking peroxides due to incorrect lamination lead to discoloration of the encapsulant. This has already been observed in the literature and is discussed in more detail in the next chapter [34, 64].

UV Absorber consumption and chromophore formation

As previously mentioned, the UV absorber can degrade through irradiation with high photon energy [40–42]. Pickett et al. and Bubev et al. have extensively studied the UV radiation-induced degradation behavior of various UV absorbers [40–42]. First order kinetics was observed for low absorbing polymer matrix, while for highly absorbing polymer matrix, the degradation behavior resembles zero order kinetics [40]. The latter behavior is probably due to the fact that with an absorbent matrix, only the upper layers contribute to photo degradation, and the lower layers are shielded. This means that the UV absorber consumption is almost independent of the absolute absorption of the system [40].

In addition to degradation due to excessive UV radiation, the UV absorber can react with radicals. Klemchuk et al. have elaborated hypothetical reactions that explain the formation of chromophore precursors by the reaction of UV absorber molecules with radicals [34]. These reactions are shown in Figure 9 while R_1 represents the rest group OC_8H_{17}. It is assumed that radicals interact with the functional OH group of the UV absorber molecules via hydrogen abstraction [34]. The UV absorber molecules thus become radicals themselves, interact with other UV absorber molecules, and thus form chromophores [34]. In this case, the benefit of the UV absorber is reversed, and it absorbs part of the solar spectrum that should actually reach the solar cell [34, 64, 98]. This reaction potential shows once again that stabilization by means of radical scavengers is of great importance and that the crosslinking peroxide content should be consumed during lamination in order to avoid subsequent reactions.

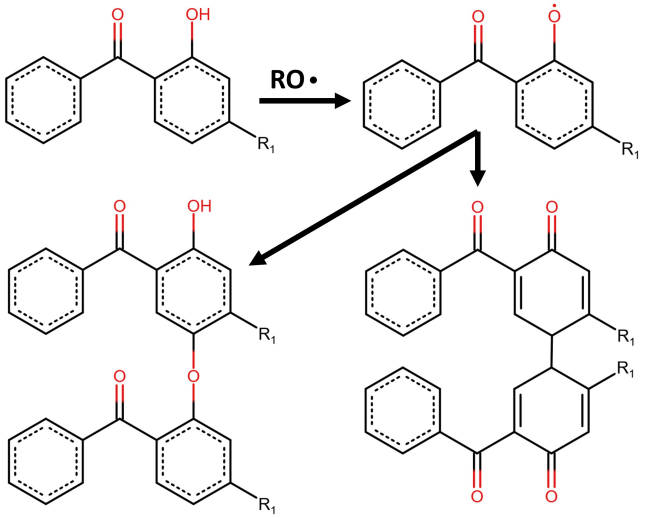

Figure 9: Possible chromophore precursor formations by the reaction of UV absorber molecules and radicals (adapted from [34]).

2.1.3. Ethylene-vinyl acetate copolymer

Ethylene-vinyl acetate copolymer (EVA) is currently the most widely used encapsulant in the photovoltaic sector [31, 99, 100]. Although the market is slowly moving towards

polyolefin elastomer (POE)-based encapsulants and thermoplastic polyolefins (TPO) are emerging [52, 56, 84], EVA-based modules will continue to be used in the field for many years to come [47]. Work is also continuing on composite films made of EVA and POE in order to combine the positive properties of both materials [100, 101]. The behavior of EVA will therefore continue to influence the properties of solar modules for a long time span.

Figure 10 shows the structural formula of EVA, which consists of polyethylene (PE) (n repeat units) and vinyl acetate segments (VA) (m repeat units). The arrangement of the segments is random [102], with the proportion of vinyl acetate groups determining the elasticity, crystallinity, and transparency [31, 103]. Typically, EVA with a vinyl acetate content of 28 % to 33 % is used in the PV sector [31, 56, 104]. In particular, ratios above 33 % can be problematic because the thermal or UV-induced degradation can be autocatalytic if two VA segments are directly adjacent [105, 106]. As the VA content increases, the elastic properties and transparency of the EVA increase, as the acetate side chains interfere with the crystallization of the PE segments [103]. This is desirable because thermo mechanical stresses can be equalized and cell breakage is avoided. As described in the previous chapter, EVA is crosslinked by reactions with peroxide radicals and a 3-dimensional polymer network is formed during lamination [56]. This leads to an elastic behavior above the glass transition temperature of −33 °C [107]. Although EVA has many good properties, the degradation of the encapsulant is problematic because, among other things, corrosive acetic acid is produced [31, 56]. The various degradation reactions are discussed in detail below.

Depending on the respective stressor, EVA can degrade in different ways. Figure 10 shows the most important types of degradation known for EVA [30, 31, 108–113]. Most reactions take place at the VA segments. This is due to the fact that the pure PE segments do not absorb UV light. Chromophoric defects are required for the absorption of these wavelengths, which are created by C=C double bonds, hydroperoxides or carbonyl groups (VA segments) [31, 113].

a) describes the hydrolysis process of EVA by reaction with water. Acetic acid is formed and vinyl alcohol groups are generated on the backbone of the polymer chains [110–112]. This is problematic as the reaction of EVA with acetic acid is autocatalytic, and therefore, intact parts of the polymer chains degrade more quickly [114–117].

Reactions **b)** to **d)** describe Norrish Type I, Norrish Type II, and Norrish Type III photo degradation. For Norrish type I reactions **b)**, the carbonyl group splits off below the single bonded oxygen of the VA segment [31, 108, 109]. The resulting reaction products (radicals) can react further and produce substances such as acetaldehyde, CO, CO_2 or CH_4 [31, 108, 109]. These gases can be trapped between the interfaces and lead to delamination [118]. **c)** describes the Norrish type II reaction in which the VA segments are cleaved off and C=C double bonds are formed in the polymer main chain [31, 108, 109]. In addition, corrosive acetic acid is formed, which leads to the problems already mentioned [31, 108, 109]. If the EVA is subject to Norrish type III reactions **d)**, the bond is cleaved below the singly bound oxygen of the vinyl acetate group [31, 108, 109]. The oxygen on the main chain forms a double bond and as a result, a ketone is formed from the fragments of the VA groups and an aldehyde from the main chain [31,

108, 109].

Reaction **e)** is also caused by high temperatures or UV radiation and describes the backbiting process of the VA segments. The vinyl acetate group reacts with a neighboring CH2 group and forms a cyclic lactone structure with the generation of methane.

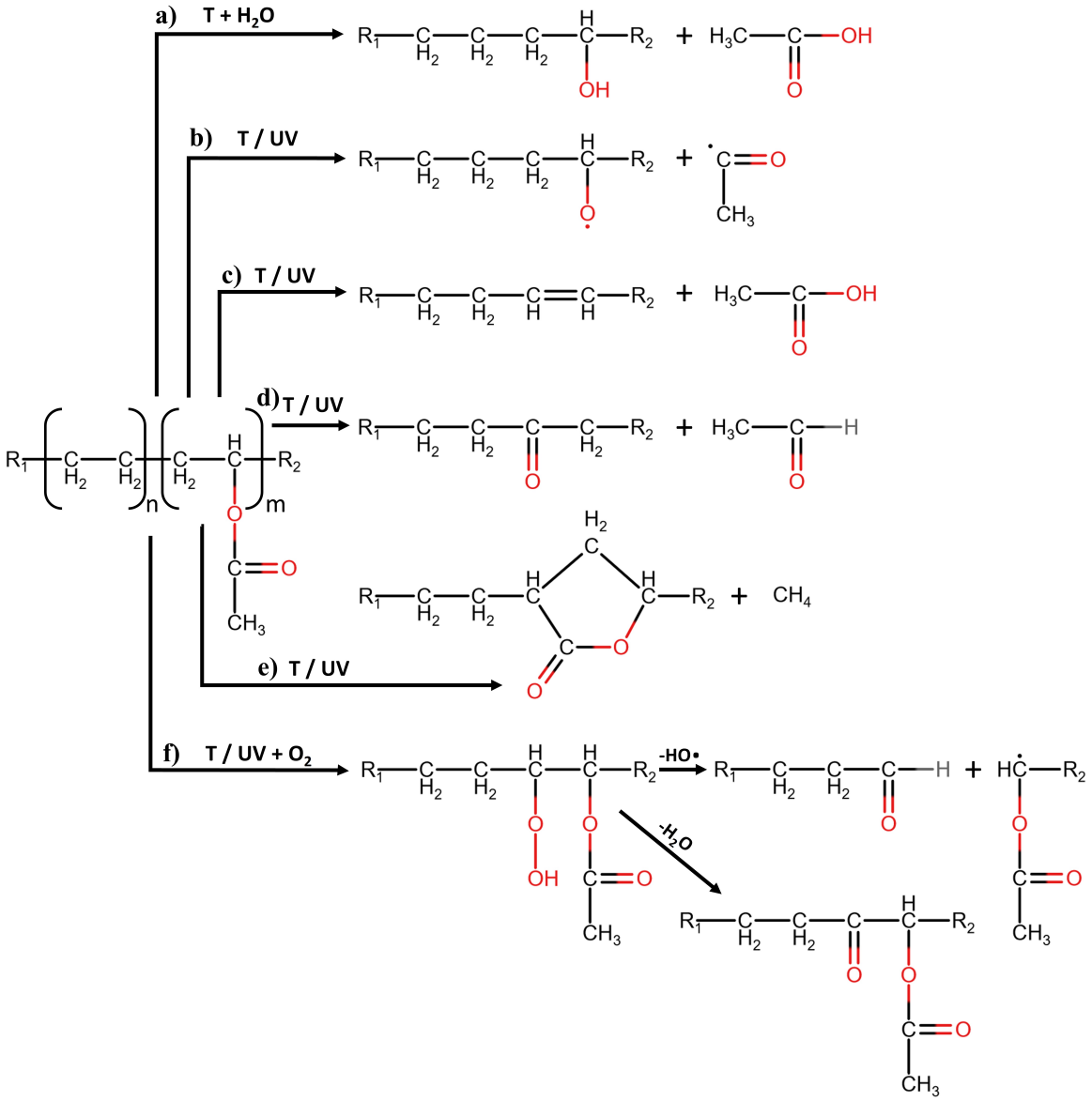

Figure 10: EVA with n polyethylene segments and m vinyl acetate segments. The R_1 and R_2 groups represent the continuation of the polymer chain. The degradation reactions are based on the works of [30, 31, 108–113].

Reaction **f)** is the only interaction that does not take place via the VA segments and therefore also occurs in other polymers that have a PE base structure [113]. As mentioned at the beginning, however, it is necessary that chromophoric defects are

present so that UV radiation can be absorbed [31, 113]. In the case of EVA, this is possible via the VA segments [31]. In the first step, the CH_2 groups react with oxygen under the influence of temperature or UV radiation and form hydroperoxides [31, 108, 109, 113]. There are a number of possible subsequent reactions, which are discussed in more detail in the next chapter dealing with POE encapsulants [113]. In the case of EVA, it is assumed that two main reactions occur. Either the hydroperoxide decomposes (e.g., due to the influence of UV radiation), the polymer chain is cleaved and a radical ketone group is formed [31, 108, 109, 113]. Alternatively, water is cleaved off, and a C=O bond is formed at the CH_2 group, which originally reacted with the oxygen [31, 108, 109].

It should be mentioned that certain reactions can occur simultaneously (e.g. the breakdown of hydroperoxides with the Norrish reactions or lactone formation). The degradation behavior of EVA is complex and determined by the respective microclimate and the stressors present.

2.1.4. Polyolefin elastomer and thermoplastic polyolefin

As mentioned above, novel encapsulants based on polyolefin elastomer (POE) and thermoplastic polyolefin (TPO) are also increasingly being used [56, 84, 100]. Unfortunately, the nomenclature in the PV sector is incorrect with regard to this topic, as photovoltaic POE and TPO encapsulants are usually based on polyethylene copolymers [56]. In general, however, the term polyolefin describes a polymer produced from alkenes (olefins) by chain polymerization and also TPOs can consist of different polymers [119, 120].

Like EVA, POEs are also crosslinked by crosslinking peroxides during the lamination process [56]. In contrast to POEs, TPOs utilize reversible physical crosslinks by ionic bonds, hydrogen bonds or by the formation of crystallites [56]. Typically, TPOs have melting temperatures of around 100 °C and as there is no need to wait for a crosslinking reaction, the lamination process can take place relatively quickly [56]. Furthermore, both new encapsulant types do not contain vinyl acetate groups, so the problematic formation of acetic acid cannot occur [56].

There are several studies that compare the properties and long-term stability of POEs and TPOs with EVA [56, 84, 111, 121–124]. However, the results of these studies are often different, so that there can be no clear recommendation to prefer a certain encapsulant type. One reason for this is the unclear definition of the new encapsulants, as the PE backbone can have various possible side groups that degrade differently. On the other hand, the degradation behavior of the base polymer is strongly influenced by the additives contained.

For these reasons, the commercial POE and TPO encapsulants used later in this work are only briefly discussed below, as the majority of this work deals with EVA. As the POE investigated in this work is an almost pure PE, the properties of this material class are discussed. The investigated TPO is probably an ethylene ethyl acrylate copolymer.

Properties and photo degradation of POE (polyethylene)

Polyethylene is a versatile material that can fulfill a wide range of requirements [125,

126]. Its properties are largely defined by its density and the branching of the polymer chains, while the basic structure is displayed in Figure 11 [125, 127]. In general, a distinction is made between low density polyethylene (LDPE), high density polyethylene (HDPE), and crosslinked polyethylene (PEX) [125]. Depending on the conditions during the polymerization process, the desired type of PE can be produced [126]. PE is relatively inexpensive and can be easily installed in PV modules [128]. Unfortunately, depending on its density, it is comparatively opaque, which leads to reduced efficiency of the modules and the mechanical properties are often not optimal [128]. This led to the production of a copolymer with vinyl acetate to reduce the crystallinity of PE [128]. However, as described in the previous section, there is a shift from EVA to other PE-based encapsulants, particularly due to the degradation of the VA group (including the formation of acetic acid) [56, 84, 100]. The expected degradation mechanisms for encapsulants that are mainly based on PE are therefore briefly discussed below.

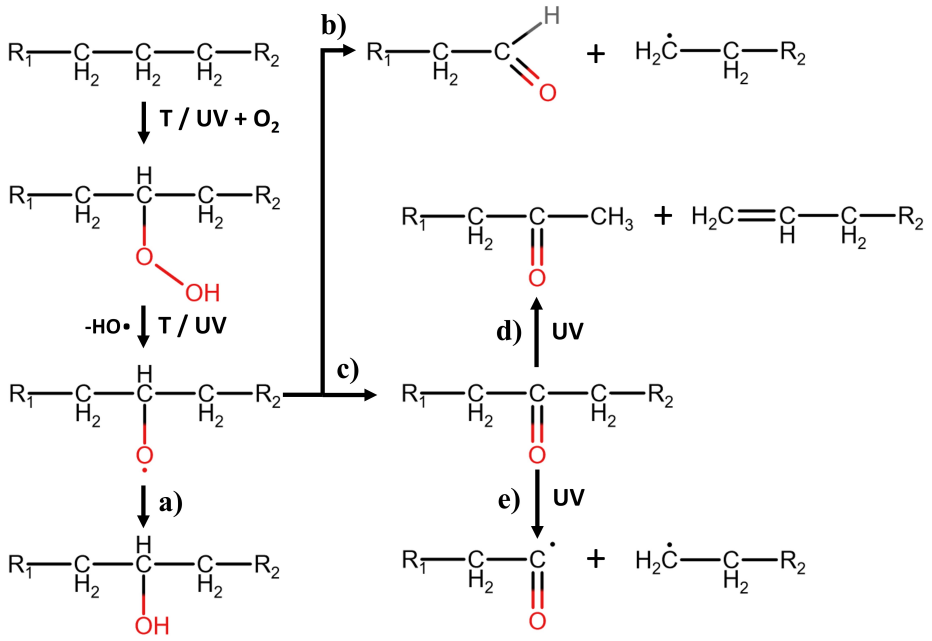

Figure 11: Structure and simplified degradation mechanisms of polyethylene. The R_1 and R_2 groups represent the continuation of the polymer chain. Adapted from [113].

It was already mentioned in the section on the degradation of EVA that pure PE should not absorb UV radiation [31, 113]. However, UV radiation can be absorbed by chromophoric defects (e.g., side groups, C=C bonds, etc.) and the first reaction shown in Figure 11 can occur in combination with oxygen, which results in the formation of hydroperoxides [113]. If energy is added again in the form of heat or high-energy photons, the O-O bond of the hydroperoxide is destroyed, and a radical position is formed on the polymer chain [113]. From this point, there are 3 different reaction pathways, all of which are related to the oxygen atom [113].

a) is the simplest reaction, which saturates oxygen atoms by hydrogen abstraction and forms a hydroxyl [113]. In the case of reaction **b)**, the main chain is cleaved by β-scission, resulting in an aldehyde and an unsaturated chain fragment [113]. These groups can react further and form carboxylic acids, esters, or lactones [113]. Reaction **c)** describes a cage reaction between the resulting radicals (unsaturated polymer chain and HO•) [113]. By splitting off water, ketone groups are formed in the main chain [113]. Based on reaction **c)**, there are now two further possible reaction pathways, both of which are based on Norrish-type photo degradation [113].

On the one hand, Norrish type II reactions, as shown in **d)**, can produce vinyl groups and ketones at the end of the chain by cleavage of the main chain [113]. The latter can undergo further Norrish type II reactions to form vinyl groups and acetone [113]. On the other hand, the main chain can also be cleaved by Norrish type I reactions, as shown in **e)** [113]. The aldehyde and ketone radicals can react further and thus also lead to the formation of carboxylic acids, esters, and lactones [113].

Properties and photo degradation of TPO (ethylene ethyl acrylate copolymer)

Thermoplastic polyolefins (TPOs) are a subclass of thermoplastic elastomers (TPEs) [129]. In general, they combine the properties of semi-crystalline thermoplastics and soft elastomers [130]. TPEs can be produced with different structures and morphologies [129]. Through block copolymers, which contain elastic and inelastic blocks, through blends of rubber and thermoplastics, or through dynamically vulcanized rubber or thermoplastic blends [129]. TPEs (and TPOs) are elastic in the range of their working temperature but are easy to process at higher temperatures (e.g., during the lamination process) [131]. The ethylene ethyl acrylate copolymer (EEA) used in the course of this work is one of these TPO representatives. The basic structure of EEA with n polyethylene segments and m ethyl acrylate segments is visualized in Figure 12. These materials have long been used for cables, medical hoses, seals, and many other things. They are characterized by toughness, flexibility, and elasticity, which also makes them suitable materials for PV encapsulants [132].

As shown in Figure 12, the degradation of EEA is similarly complex to that of EVA. All the degradation pathways discussed in the previous section for PE can also occur in the polyethylene segments of EEA [133]. In the course of these degradation pathways, chain scissions occur at different points [133]. A detailed summary of the PE segment degradation can be found in [133]. In the following, the focus will be on the degradation of the ethylene acetate group.

Reaction **a)** describes the cleavage of the OC_2H_5 group. A C=C double bond in the main chain and ethanol is formed with the release of CO. It is assumed that the resulting C=C bond breaks down in the further course of the reaction [133]. In reaction **b)** the complete $CO_2C_3H_5$ group is cleaved off, and an unsaturated bond is formed in the polymer chain [134]. This can either lead to crosslinking reactions with other chains [134], or a C=C bond is formed. **c)** is a precursor reaction for further degradation chains [133]. By rearranging the ethyl acrylate group and splitting off ethylene, a stable intermediate is formed [133]. Through exposure to photons or thermal energy, this can

lead to a polyethylene segment as shown in **d)** with the release of CO2 and rearrangement of the hydrogen atom [133]. However, it is also possible for reaction **e)** to occur from this point, leading to chain cleavage next to the COOH group [133]. The radical position is shifted by intramolecular transfer, and the chain splits again, forming a C=C bond. From this point, either an HO• radical can split off from the fragments, or acetic acid is formed [133].

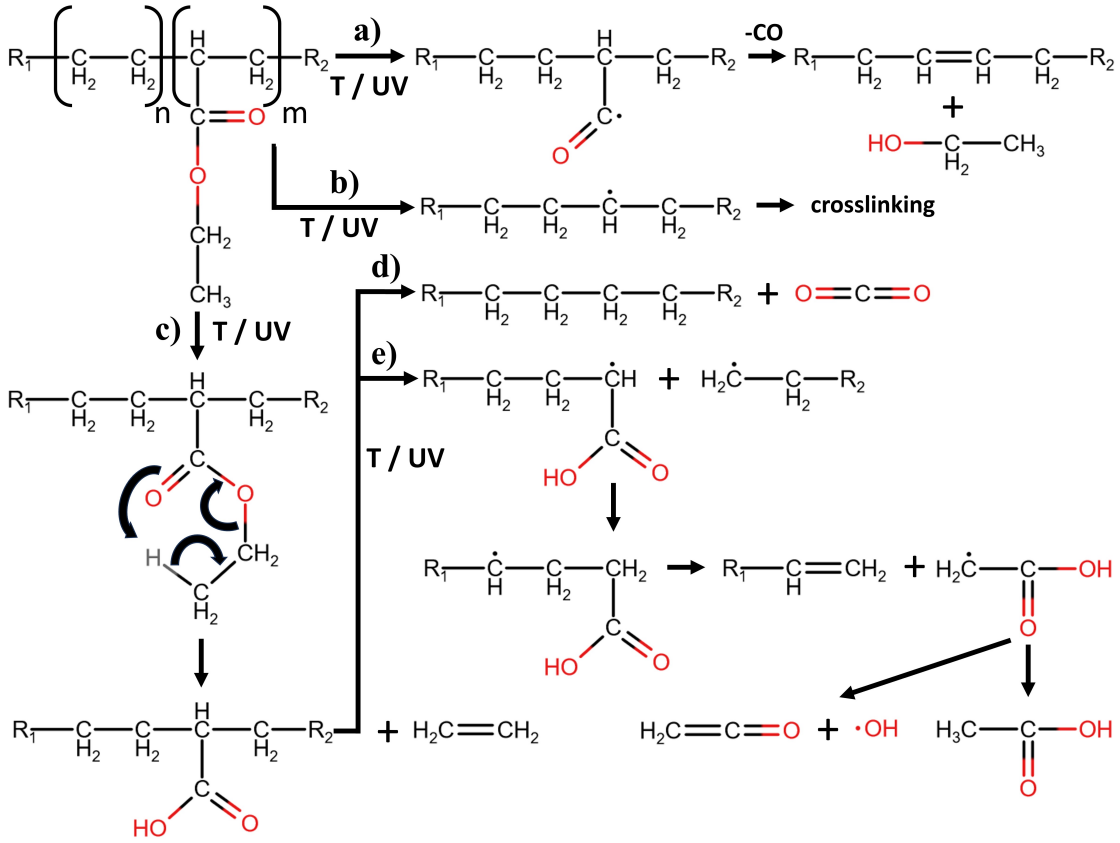

Figure 12: Structure and simplified degradation mechanisms of ethylene ethyl acrylate copolymer with n polyethylene segments and m ethyl acrylate segments. The R_1 and R_2 groups represent the continuation of the polymer chain. Adapted from [133, 134].

2.1.5. Backsheets

In addition to the encapsulant, the sealing material on the back of the solar module is another important protective layer against environmental influences [135–137]. Although modules are now also produced that use glass as the front and back closure, layers of polymer-based materials (backsheets) have been used for the back for many years [9, 20, 135–139]. With the increased use of bifacial solar cells, the role of transparent polymer backsheets is becoming more and more important alongside glass/glass structures [136, 139]. Since only backsheets based on polyethylene terephthalate (PET) are used in this

work, the following section focuses on the general properties of polymer backsheets and the degradation behavior of PET.

The backsheet has to fulfill a variety of tasks during its service life of approximately 25 years [135, 140]. They act as a barrier against environmental influences and as electrical insulation layers [135, 136]. In addition, they must give the module mechanical stability and prevent the ingress of moisture in order to minimize the corrosion of electrical contacts [136, 140]. Just like the encapsulant, the polymer backsheets are also equipped with various additives such as antioxidants, hydrolysis stabilizers, flame retardants, crosslinking additives, UV absorbers, and UV stabilizers in order to achieve the best possible long-term properties [141–143]. Transparent backsheets must also ensure good optical coupling to the cell in order to achieve the best possible performance [144]. There is a wide range of different polymer backsheet materials [136, 140, 145]. Many are multilayer systems that are either coextruded or coated [136, 137, 142, 145]. The PET backsheet used in this work is a monolayer film with coatings. Consequently, the properties and degradation of PET are briefly discussed below, while the basic structure and degradation mechanisms are visualized in Figure 13.

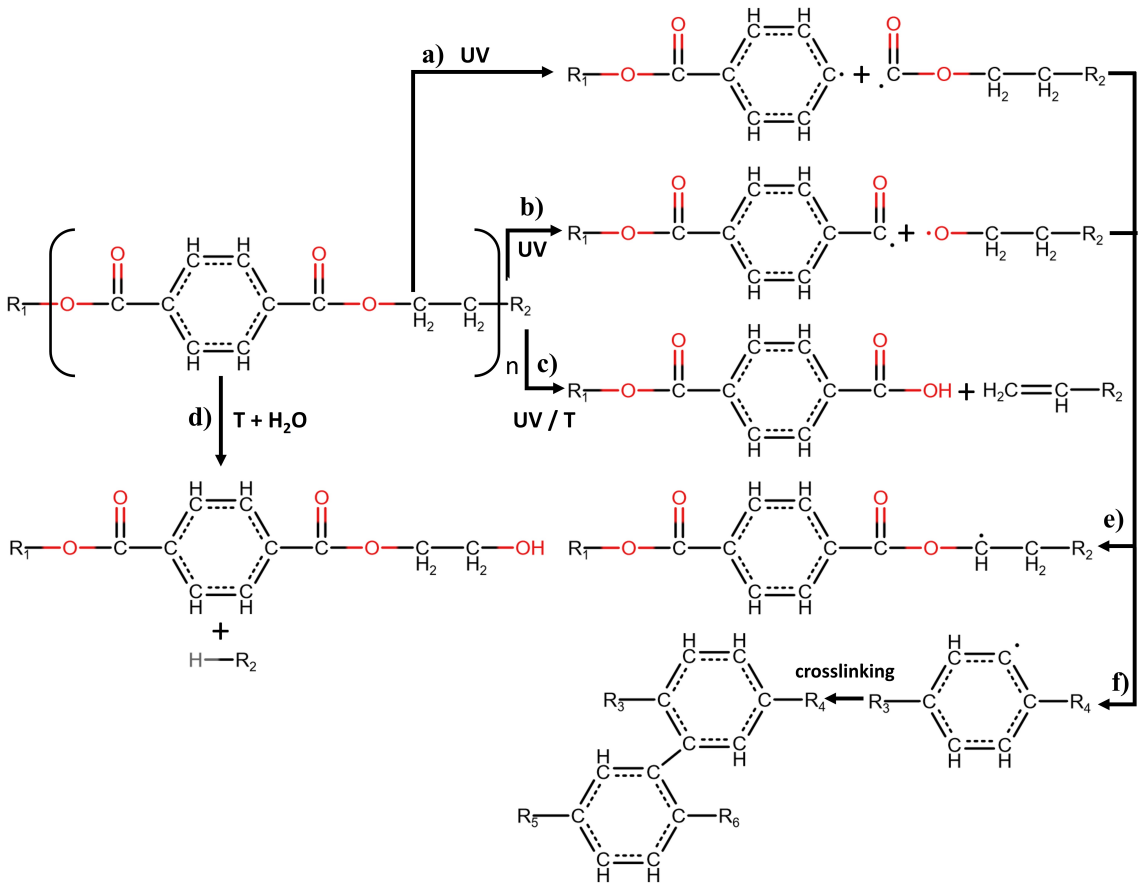

Figure 13: Structure and simplified degradation mechanisms of polyethylene terephthalate with n repeat units. The R_1, R_2, R_3, R_4, R_5 and R_6 groups represent the continuation of the polymer chain. Adapted from [146, 147].

PET is the third most common encapsulation material used in the packaging industry [148], so it is not surprising that it is also a potential choice for the backside encapsulation of photovoltaic modules [140, 145, 149]. PET is a thermoplastic, comparatively robust polymer that is impact-resistant and yet flexible during processing [148]. The polymer itself is colorless and can be transparent (if it is amorphous PET) [148]. It has good barrier properties against moisture and gases [146, 148]. Furthermore, it is relatively inert with regard to chemical interactions [148]. PET can be blended or copolymerized with other polymers [148].

Like the other polymer materials in this work, PET can also degrade in different ways. Reactions **a)** and **b)** describe Norrish type I photo oxidation [146]. The radicals of the reaction products can subsequently damage other parts of the polymer chain by hydrogen abstraction [146], which leads, for example, to reaction **e)** [146]. However, hydrogen abstraction can also occur at the ring structure, as shown in **f)**, resulting in crosslinking reactions between the aromatic rings [146]. In combination with oxygen, hydroperoxides can also be formed, whereby the photo unstable O-O bond can be easily cleaved, so that HO• radicals are formed [146]. **c)** describes the Norrish Type II photo degradation [146]. The polymer chain is split after the oxygen atom, and a vinyl group is formed on the other chain fragment [146]. This reaction can not only be UV-induced but also thermally stimulated [150]. **d)** shows the hydrolysis of PET [147]. It is based on the transformation of the ester group to the corresponding carboxylic acid and alcohol, whereby the polymer chain is cleaved [147, 151].

2.2. A brief introduction into solar cell physics

The following chapter provides a brief overview of the functionality and degradation of PERC-based silicon solar cells. This cell type was used in all experiments within this thesis. Due to the complexity of this subject area, it is not possible to go into all the fundamentals in detail and a basic understanding of solid state and semiconductor physics, as well as solar cell physics, is assumed by the reader. Interested readers are recommended to consult the works of Gross and Marx (solid state physics) [152], Smoliner (semiconductor physics) [153], Würfel and Würfel (physics of the solar cell) [154] and Brendel (physics of the silicon solar cell) [155].

2.2.1. Fundamental principles

Charge carrier densities within a semiconductor

Consider the band structure of an indirect semiconductor in the area of the band gap E_g as displayed in Figure 14. The energy E of electron states is dependent on their momentum $\mathbf{k}$ while the transition of energy states is either enabled trough photons γ or phonons Γ [152–154]. These energy transitions generally take place between the valence band maximum E_V and the conduction band minimum E_C. Thus, for the transition in the displayed indirect semiconductor, the interaction of a phonon and photon is required [152, 154]. In the area of E_C and E_V, the density of states for electrons and holes can

be approximated by a parabola which yields the density of states for electrons $D_C(E)$ and the density of states for holes $D_V(E)$

$$D_C(E) = \frac{V}{2\pi^2}\left(\frac{2m_e}{\hbar^2}\right)^{3/2}\sqrt{E - E_C} \tag{8}$$

$$D_V(E) = \frac{V}{2\pi^2}\left(\frac{2m_h}{\hbar^2}\right)^{3/2}\sqrt{E_V - E} \tag{9}$$

with the volume V in $\mathbf{k}$ space, the effective masses of electrons and holes m_e and m_h and the reduced Planck constant $\hbar$ [152].

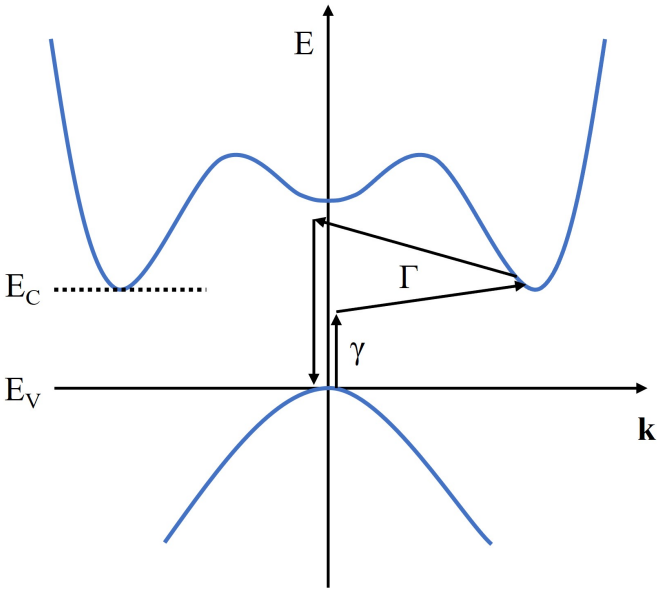

Figure 14: Energy E of electron states in dependence of their momentum $\mathbf{k}$ for an indirect semiconductor. E_C and E_V correspond to the energies of the conduction band minimum and valence band maximum. Electron transitions are possible by photons γ (same momentum) and phonons Γ (change in momentum and energy). Adapted from [154].

To determine the charge carrier density, it is necessary to take into account whether the respective energy states are occupied by charge carriers. Consequently, the respective charge carrier density must be multiplied by the occupation probability, whereby the electronic states within semiconductors are subject to the Fermi-Dirac statistics f_e for electrons and f_h for holes

$$f_e(E,T) = \frac{1}{e^{(E-\mu)/k_BT} + 1} \approx e^{-(E-\mu)/k_BT} \tag{10}$$

$$f_h(E,T) = \frac{1}{e^{(\mu-E)/k_BT} + 1} \approx e^{-(\mu-E)/k_BT} \tag{11}$$

with the chemical potential μ, the Boltzmann constant k_B and the temperature T [152]. The displayed approximation by a Boltzmann distribution is valid if there is a sufficiently large energetic distance between the band edges and the chemical potential (e.g., weakly doped or intrinsic semiconductors) [152]. Using the Equation 8, Equation 9, Equation 10 and Equation 11, the charge carrier densities of electrons n and holes h can be determined by integrating all states and their occupation probability for the corresponding energy interval which yields [152]

$$n = \frac{1}{V}\int_{E_C}^{\infty} D_C(E) f_e(E,T)\mathrm{d}E = 2\left(\frac{m_e k_B T}{2\pi\hbar^2}\right)^{3/2} e^{-(E_C-\mu)/k_B T} \tag{12}$$

$$p = \frac{1}{V}\int_{-\infty}^{E_V} D_V(E)[1-f_h(E,T)]\mathrm{d}E = 2\left(\frac{m_h k_B T}{2\pi\hbar^2}\right)^{3/2} e^{-(\mu-E_V)/k_B T}. \tag{13}$$

The chemical potential can be approximated by the Fermi energy E_F using Sommerfeld expansion as long as the temperature of the semiconductor is significantly lower than the Fermi temperature [156]. It follows that

$$\mu = E_F\left(1-\frac{1}{3}\left(\frac{\pi k_B T}{2E_F}\right)^2\right) \tag{14}$$

and the following chapters are discussed on the basis of the Fermi energy E_F.

By using Equation 12, Equation 13 and Equation 14, the law of mass action can be calculated with

$$np = n_i^2 = 4\left(\frac{k_B T}{2\pi\hbar^2}\right)^3 (m_e m_h)^{3/2} e^{-E_G/k_B T} \tag{15}$$

which directly leads to the charge carrier density of an intrinsic semiconductor n_i by extracting the root of Equation 15 [152].

Doping

Intrinsic semiconductors are unsuitable for most applications due to low charge carrier densities at room temperature [152]. By introducing impurities into the atomic lattice in the form of foreign atoms, the charge carrier densities can be increased [152]. This process is called doping. In the case of the PERC solar cells used in this work, the p-silicon substrate is doped with boron and the n-silicon emitter with phosphorus [157, 158]. The result of doping is shown in Figure 15. New energy levels are created by the introduction of additional electrons or the creation of defects [152]. If more electrons are available than in the intrinsic case, a donor level E_D is created. If fewer electrons are available, an acceptor level E_A is created.

The respective donor levels can be estimated with the help of the Bohr atomic model because the excess atom that is not required for bonding in the atomic lattice corresponds

to a hydrogen problem [152]. The Coulomb potential of the single positively charged trunk atom remains and thus follows

$$E_{\tilde{n}}^{H} = \frac{me^4}{2(4\pi\epsilon_0\hbar)^2}\frac{1}{\tilde{n}^2} \tag{16}$$

with the principal quantum number $\tilde{n}$, the electron mass m, the elementary charge e and the electrial field constant ϵ_0 [152]. Now, the electron mass is replaced with the effective band mass of the conduction band m_e, and the shielding of the Coulomb potential by surrounding silicon atoms is taken into account by introducing the dielectric constant ϵ yielding the energy of the donator level E_n^D [152, 154]

$$E_{\tilde{n}}^{D} = \frac{m_e e^4}{2(4\pi\epsilon\epsilon_0\hbar)^2}\frac{1}{\tilde{n}^2} = \frac{m_e}{m\epsilon^2}E_{\tilde{n}}^{H}. \tag{17}$$

For silicon, this results in E_1 of approximately 30 meV, which is in the range of the thermal energy at room temperature ($\approx$ 25 meV) [152].

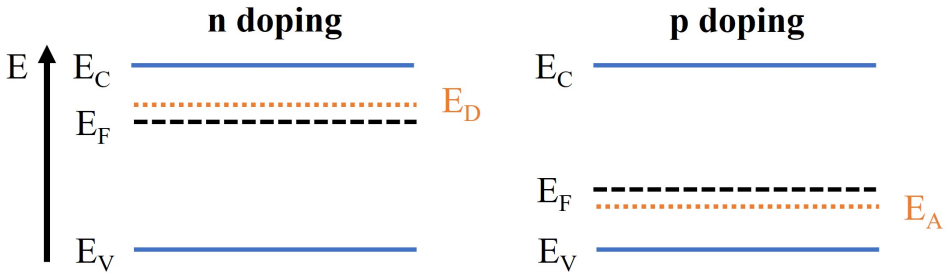

Figure 15: Energy diagram of a semiconductor at the valence band maximum E_V and conduction band minimum E_C, which has been doped either with atoms with additional electrons (n doping) or fewer electrons (p doping). The Fermi level E_F is dependent on the temperature [152]. Doping results in either donor energy levels E_D or acceptor energy levels E_A. Adapted from [152].

In the opposite case for acceptors, an electron occupying the free energy level (hole) has no Coulomb bond to the impurity atom [154]. Consequently, this electron is not as strongly bound as an electron in the valence band. Transitions from the valence band to the E_A level therefore require only small energies [154].

The acceptor and donor levels directly influence the position of the Fermi level E_F as a function of temperature [152]. In the typical temperature application range of a semiconductor, all impurities should be ionized, and E_F is located just below E_D or just above E_A [152]. A comprehensive discussion of this temperature dependence is carried out in the work of Gross and Marx [152].

The p-n junction

There will be no detailed derivation of the charge carrier distributions at this point. Depending on the application, this can be found in detail in the works of Smoliner [153], Gross and Marx [152] and Würfel and Würfel [154]. Instead, the general concept will be briefly discussed in order to motivate the construction of a PERC solar cell and the use of passivation layers.

The p and n conducting semiconductors listed in the previous chapter are combined in this chapter to form a p-n junction. The general principle is shown in Figure 16. On the left, the p-n junction is in equilibrium. On the right, an imbalance has been created by photon input or an external voltage. As before, it is important to note that the transitions in the p and n regions are only the section of the band structure shown in Figure 14, which describes the valence band maximum and the conduction band minimum. As shown in the figure, a bending of the energy bands occurs in the area of the transition between the two semiconductors [152–154]. This is due to the fact that the band bending is caused by the change in the macroscopic electrical potential $\phi(z)$, which is a result of the different electrochemical potentials (Fermi levels) of the two charge carrier types [154, 159]. In this case, the charge carrier densities of the individual areas can be determined using the Poisson equation

$$-\Delta\phi(z) = \frac{\rho(z)}{\epsilon\epsilon_0}. \tag{18}$$

The Poisson equation requires the twofold continuous differentiability of the potential, which results in the observed band bending. Equilibrium is reached when charge carriers migrate from one semiconductor to the other until the Fermi level of both semiconductors reaches the same value [159].

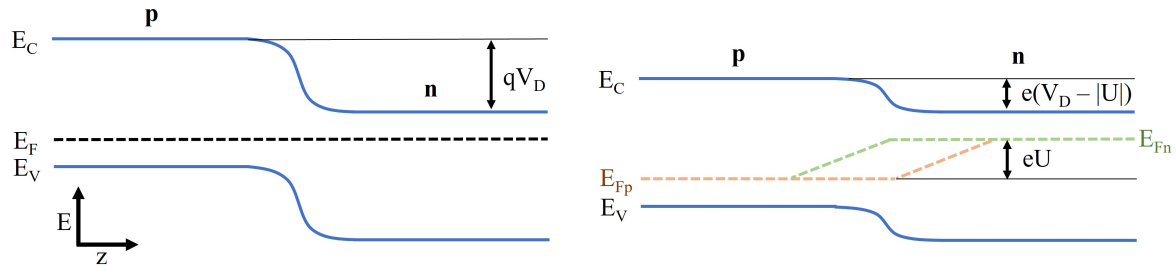

Figure 16: p-n junction in equilibrium (left) and disequilibrium (right). Adapted from [153].

A space charge region is created at the junction between the two semiconductors [152–154]. This can be understood by the fact that there is an excess of electrons in the n semiconductor and an excess of holes in the p semiconductor [152]. Consequently, the charge carriers diffuse into the other region and partially recombine there (recombination current) [152]. In the case of the n semiconductor, the migration of the electrons causes a

positive space charge region, as the stationary, positive atomic cores remain there [152]. In the case of the p semiconductor, the migration of the holes results in a negative space charge region, as the stationary acceptors remain [152]. The stationary acceptor and donor atoms on both sides of the p-n junction generate an electric field across the space charge region, and the potential difference between the p and n semiconductors is called the diffusion voltage V_D [152]. The charge carriers generated within the space charge region (e.g. thermally generated) are accelerated into the respective semiconductor by the electric field (generation current) [152]. In the case of thermal equilibrium, the generation and recombination currents are equal so that the Fermi level is also constant over the entire p-n junction [152].

In order to understand how a solar cell works, the p-n junction must be considered in disequilibrium. To explain the relationships, for the sake of simplicity, it is assumed that there are two direct semiconductors and only band-to-band recombination takes place. The p-n junction is now brought into disequilibrium by the incidence of photons or an external voltage. This imbalance can be explained by the fact that charge carriers are constantly being generated, which are dissipated into the respective p or n regions by the electric field [152]. As there are considerably more charge carriers available in this case than in darkness, there is a problem with the definition of the Fermi energy [153, 154]. There are now considerably more electrons available in the conduction band, so the Fermi energy should shift in the direction of the conduction band [154]. However, there are also considerably more holes available in the valence band, so the Fermi energy should shift in the direction of the valence band [154]. The solution to this problem is to define two different Fermi levels E_{F_n} for the electrons and E_{F_p} for the holes [154, 160]. These levels describe the states in the valence and conduction band and for shallow acceptor and donor levels [154]. The splitting into two Fermi levels can also be explained by the fact that band-to-band transitions are less likely than interactions with the atomic lattice. The electrons and holes are in thermal equilibrium with the atomic lattice but not in macroscopic equilibrium, as they would be through recombination [153, 154]. Considering Figure 14, this can be understood by the fact that electrons and holes must not only be at almost the same position in real space in order to recombine, but they must also be at the same position in **k** space, otherwise (or for silicon in any case), phonons are necessary.

The law of mass action does not apply to doped semiconductors, as there is an imbalance between the charge carrier types [154]. However, it does apply to the charge carriers generated by photons in the space charge region, as the same number of electrons as holes are generated in each case [154]. The same applies to the radiative (band to band) recombination of these charge carriers, as electrons and holes are required in each case [154]. Considering a recombination rate

$$R = Bnp \tag{19}$$

this must depend on the generated hole and electron density and a proportionality factor B. Using Equation 15, it follows that

$$R = Bn_i^2 e^{-\left(E_{F_p} - E_{F_n}\right)/k_B T}. \tag{20}$$

Equation 20 shows that the recombination rate for this simplified case is mainly dependent on the splitting of the quasi Fermi levels. If it is assumed that the generation rate G of the charge carriers is constant since the voltage applied at the p-n junction or the photon current is constant, G can be described by the recombination rate in the equilibrium case R_0 [154]. It follows that

$$R_0 = G = Bnp. \tag{21}$$

and thus in the case of disequilibrium

$$\Lambda = R - G = Bn_i^2 \left(e^{-\left(E_{F_p} - E_{F_n}\right)/k_B T} - 1 \right). \tag{22}$$

Equation 22 shows the difference between recombination rate and generation rate Λ that can be expected until the equilibrium state is restored and the splitting of the quasi Fermi levels is terminated. On the other hand, it shows what recombination current can be expected if the splitting of the quasi Fermi levels is maintained by an external voltage or a photon flux.

In Figure 16 it was implicitly assumed that the energy difference of the splitting of the quasi Fermi levels corresponds to a voltage U multiplied by the elementary charge e. This results directly from the solution of Equation 18 in the different semiconductor regions if the Schottky approximation is used (rectangular change of the space charge region) [152]. The potential barrier that the electrons or holes have to overcome corresponds to a Boltzmann factor $\exp(-q(V_D - U)/k_B T)$ [152]. The recombination current of the electrons is therefore proportional to the change in this potential barrier, and it follows that

$$J_n^{rec}(U) \propto e^{-e(V_D - U)/k_B T} \tag{23}$$

As before, it can now be argued that the generation current is independent of U and that recombination and generation currents are equal in the case of equilibrium ($U = 0$) [152]. Thus, it can be concluded that $J_n^{rec}(U = 0) = J_n^{gen}(U = 0) = J_n^{gen}(U)$ [152]. As in Equation 22, the total current J_n has the following dependence

$$J_n = J_n^{rec} - J_n^{gen} \propto J_n^{gen} \left(e^{(eU/k_B T)} - 1 \right) \tag{24}$$

which is in accordance with the dependencies of Equation 22 and describes the general diode curve [152]. The concept can be derived in a similar way for holes.

2.2.2. Electroluminescence

Radiative recombination within a p-n junction was introduced in the previous chapter and forms the basis for electroluminescence [154]. Electroluminescence describes the process when charge carriers induced by a voltage recombine radiantly [154, 161]. For indirect semiconductors such as silicon, in addition to the interaction of electron and

hole at the band gap, the absorption or emission of a phonon is necessary to adjust the electron momentum in **k** space (see Figure 14) [162]. The indirect band gap of silicon is

$$E_{G_S} = 1170 \text{ meV} - \frac{0.702T^3}{T + 1108} \text{ meV} \tag{25}$$

and temperature dependent as the probability of interaction of electrons with the crystal lattice changes with increasing temperature on the one hand, and the crystal lattice expands on the other [163]. According to the previous arguments, photons produced by recombination of electrons and holes within the p-n junction therefore have an energy in the range of the band gap energy. In experiments, the photon energy was measured between 900 meV and 1200 meV, depending on the semiconductor temperature [162]. On the one hand, this can be explained by the interaction of several phonons; on the other hand, the charge carriers can also be bound as excitons and subsequently recombine [162].

As will be shown in a following chapter, typical solar cells consist of a relatively wide bulk semiconductor, which takes up almost the entire cell, and two very thin, highly doped p and n layers [154]. If electrons are now injected into the p bulk through the very thin, highly doped n layer, it can be shown that the electron distribution can be described by the following relationship

$$n(V) = \frac{n_i^2}{N_A} e^{eV/k_B T} \tag{26}$$

with the acceptor ion density in the p bulk N_A [154].

Modern electroluminescence measurements are carried out with a charge-coupled device (CCD) camera [164–166]. The measurement can be used to determine the diffusion length of charge carriers [164–166]. By observing the polarization of the electroluminescence, which is based on internal charge anisotropy, crystal defects can be analyzed [167, 168]. In addition, the electroluminescence is dependent on the series resistance of the solar cell, so this quantity can be calculated from the measurement [169–171]. On the one hand, the degradation of solar cells due to changes in series resistance can be tracked [172], and on the other hand, cell defects such as cracks can be analyzed quickly [173, 174]. In the further course of this work, the degradation analysis of the solar modules after artificial, accelerated aging plays an important role, so the electroluminescence measurements also prove to be a valuable tool.

2.2.3. Functionality of a solar cell and resulting electrical parameters

The relationships derived in the chapter on the p-n junction must be explained further in order to understand how a solar cell works. When using the diffusion current approximation [152], it can be shown that the generation current presented in Equation 24 (for holes and electrons) corresponds to the saturation current J_S of the diode, resulting in a current of [152, 154]

$$J = J_S \left(e^{(eU/k_B T)} - 1 \right). \tag{27}$$

The resulting $J(V)$ characteristic of a diode is shown in Figure 17. The blue curve corresponds to a diode in the dark, the orange curve corresponds to a solar cell through additional generation of charge carriers by photon input. As shown in the equivalent circuit diagram, the additional generation current is described as a current source. This current source generates a short circuit current J_{SC}. The diode curve is shifted by the short circuit current J_{SC} under illumination so that for the characteristic curve of the solar cell one will find [152, 154]

$$J = J_S \left(e^{(eU/k_BT)} - 1\right) - J_{SC}. \tag{28}$$

As already described (and in more detail in the next chapter), a real solar cell consists of a comparatively thick bulk material (usually p conductive) and two thin p or n conductive layers on and under the bulk material [152, 166]. If the absorption in the thin n or p layer directly on the surface is neglected and only the charge carriers that are generated within a diffusion length (all others cannot be collected) are considered [154], than the short circuit current is directly proportional to the incoming photon flux with the spectral distribution of the sun $J_{Ph}(\hbar\omega)$ and it follows

$$J_{SC} = eJ_{Ph} = e\int_{\hbar\omega=E_G}^{\infty} \frac{\mathrm{d}J_{Ph}(\hbar\omega)}{\mathrm{d}\hbar\omega}\mathrm{d}\hbar\omega \tag{29}$$

while only the photons with higher energy than the band gap contribute to the photo current [152]. Equation 29 assumes that all photons are absorbed in the material. This is only correct as an approximation, as the probability of photon absorption depends on the density of states in the semiconductor and decreases exponentially with the penetration depth [154]. However, this relationship is of no significance for the further consideration within this work, so the work of Würfel and Würfel is recommended to the interested reader [154].

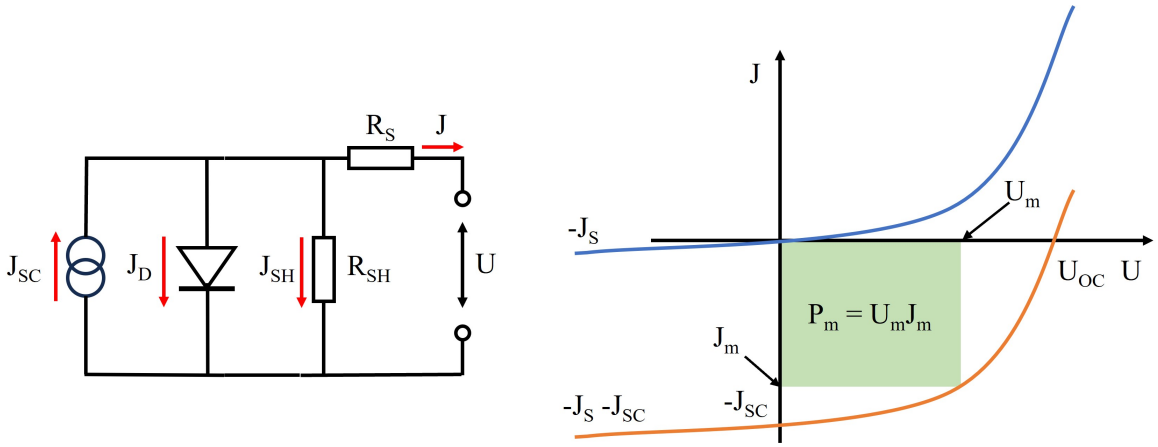

Figure 17: Equivalent circuit diagram of a solar cell (left) and J-U characteristics of a p-n junction in the dark (blue curve) and under illumination (orange curve) (right). Adapted from [152].

The shape of the diode curve under illumination results in significant points with which key parameters of a solar cell can be defined. In addition to J_{SC}, the open circuit voltage U_{OC} also plays an important role. From Equation 28 one can find

$$U_{OC} = \frac{k_B T}{e} \ln\left(\frac{J_{SC}}{J_S} + 1\right) \approx \frac{k_B T}{e} \ln\left(\frac{J_{SC}}{J_S}\right). \tag{30}$$

The maximum possible power P_m that can be used by a solar cell results from the rectangle with the largest possible area between the coordinate origin and the diode curve [152, 154]. The current and voltage at these points are denoted as J_m and U_m, respectively. From a geometrical point of view, it follows that the diode curve should be as rectangular as possible. The fill factor FF is thus defined as [154]

$$FF = \frac{J_m U_m}{J_{SC} U_{OC}}. \tag{31}$$

As described above, only photons whose energy is greater than E_G can contribute to the current [152, 154]. Photons with greater energy than E_G excite charge carriers, but the energy difference to E_G is thermalized in the lattice [152, 154]. Reflection effects also occur [152]. The efficiency of a solar cell η is thus defined by the ratio of the maximum possible power of the solar cell P_m and the irradiated power of the solar spectrum P_{in} [152]

$$\eta = \frac{P_m}{P_{in}} \tag{32}$$

In addition to these parameters, real solar cells have resistances, as shown in the equivalent circuit diagram [154]. The parallel (shunt) resistance R_{SH} describes shunts that can be present on the surface of the solar cell, at grain boundaries, or also at pinholes of the p n junction [154]. Ideally, R_{SH} should be infinitely large [154]. The series resistance R_S describes all voltage drops within the solar cell and the electrical connectors [154]. Ideally, R_S should be zero [154].

In fact, the energy levels and band bending of real solar cells must be very well matched to each other to enable an efficient cell [154]. This is due to the fact that the changes in energy levels that lead to the movement of the charge carriers are not selective and act in both directions (see Figure 16) [154]. In addition, the contacting at the boundaries of the p n junction must be considered. The voltage drops at these points must be as small as possible, otherwise the series resistance will be very high [154]. These requirements have led to a large number of different solar cell types, whereby the PERC cell relevant to this work will be examined in more detail below [47, 157, 175, 176].

2.2.4. The passivated emitter and rear cell (PERC) silicon solar cell

The behavior of a real solar cell is more complex than described in the previous chapter. In addition to the radiative recombination discussed, other effects such as Auger recombination, recombination at impurities, and surface and interface recombination occur

[154]. Furthermore, losses due to reflection must also be taken into account [157, 166, 177]. These challenges have led to the development of the PERC cell to increase the efficiency of conventional silicon cells [157, 177, 178]. Figure 18 shows the structure of a PERC cell used in this work.

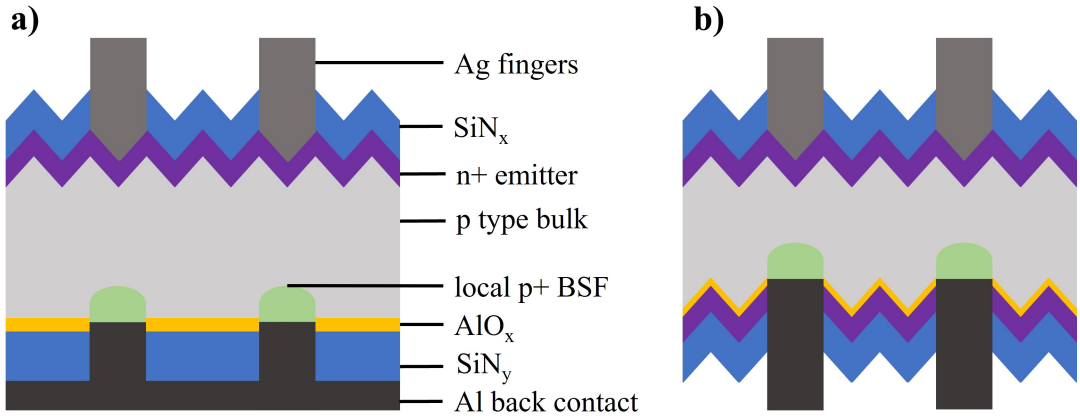

Figure 18: **a)** structure of a monofacial PERC solar cell and **b)** of a bifacial PERC solar cell. Adapted from [47, 157, 177].

The bulk material consists of boron-doped p-silicon, which is wet chemically etched into a random pyramid structure [177], with the entire wafer having a thickness of 200 µm to 300 µm [178]. Phosphor diffusion on the wafer surface generates a highly doped n+ emitter. In the case of monofacial cells, this emitter layer is removed again from the back of the wafer by wet chemical polishing [177]. The Ag fingers are deposited on the front of the emitter by screen printing [157]. The SiN_x layer is deposited on the emitter by plasma enhanced chemical vapor deposition (PECVD) [177–179]. On the one hand, this layer serves as an anti reflective layer, which increases the number of photons reaching the emitter [177–179]. On the other hand, the silicon nitride layer, which is typically produced from the reaction of SiH_4 and NH_3 gas, contains hydrogen atoms [179]. These hydrogen atoms create locally stable charge states (positive, neutral, or negative) [179]. Negative charge states can neutralize phosphorus atoms, and positive charge states can neutralize boron atoms [179]. The neutral charge state can be used as an intermediate band transition [179]. In addition, these neutral hydrogen atoms have a long diffusion length, as they do not interact with other charge carriers or are influenced by an electric field [179]. In this way, the surface recombination rate at the emitter can be reduced, allowing more charge carriers to leave the cell and increasing efficiency [178]. The high concentration of hydrogen atoms in these SiN_x layers is partly released by the firing process during production and can also passivate the defect states in the bulk of multi crystalline silicon solar cells [178]. However, the anti reflective properties of these layers are not ideal in the wavelength range of 300 nm to 600 nm, because the extinction coefficient increases [180]. Research is currently being carried out on SiO_zN_x layers, as these have similar passivation properties but a lower extinction coefficient [180].

A different approach must be used for passivation on the back of the cell, as a silicon nitride layer would represent an inversion layer at this point [178]. Consequently, a layer with a strong negative charge is required for passivation, which is made possible by aluminum oxide [157, 177, 178]. The AlO_x layer is also applied using PECVD in combination with a SiN_y capping layer [157, 177, 178]. Due to the strong negative charge, holes can accumulate on this layer, and the number of electrons is reduced [157]. The SiN_y layer acts as a dielectric so that the electrical contact with the semiconductor is only created by the thin contact columns [157]. The holes for the aluminum contacts on the back are formed using laser ablation [177]. The Al back contact is applied by screen printing with a subsequent firing process at 750 °C to 850 °C [177]. During this firing process, a local Si-Al layer is generated [177]. The silicon at the interface is doped by aluminum atoms and a local p+ layer is formed [157, 177]. The resulting p+ p junction generates a local electric field [181–184]. This field can greatly reduce the recombination velocity at the back contact, which leads to an increase in the open circuit voltage and the short circuit current [181–183].

2.2.5. Degradation of PERC solar cells

During the service life of solar modules, not only does the encapsulation material degrade, but the cells themselves and their electrical connectors are also affected by a variety of degradation effects. In particular, the interaction of the different layers of the solar modules plays a role so that the respective degradation chain depends on the selected material combination. In this chapter, the most important degradation mechanisms of the PERC solar cell will be briefly presented, whereby degradation due to radiation and degradation due to corrosion are of particular importance for this work.

Potential induced degradation (PID)

Even though PID effects only play a subordinate role in this work, this form of degradation should nevertheless be mentioned briefly, as its manifestation is strongly dependent on the encapsulation and backsheet materials used [185]. As the name "potential induced degradation" suggests, this effect is dependent on a potential difference (voltage) [186]. Solar modules are connected in series during operation in order to generate a high output voltage, whereby the frame is usually grounded [186]. Depending on the inverter type, a high potential difference can arise between the frame and the solar cell on the external solar modules of a string [186]. Depending on the wiring and the type of solar cell, there are different types of PID [186]. On the one hand, PID can be triggered by corrosion of the cell connectors, dissolution of the anti reflective layer, and polarization effects [186, 187]. On the other hand, the semiconductor structure can change due to sodium ingress (shunting type PID-s) [186, 187]. In the following, only crystalline silicon (c-si) solar cells with PID-s will be discussed.

PID-s is the most common type of this degradation form in c-si modules and is associated with the reduction of the shunt resistance [186]. Large potential differences between the frame and the cell can lead to various types of leakage currents [186]. One type of leakage current causes sodium ions (Na^+) to diffuse from the front glass through the

anti reflective layer and reach the emitter [186, 187]. The Na^+ accumulates between the emitter and the anti-reflective layer due to the positive charge. Due to stacking faults in the semiconductor, there are prefabricated paths into which the Na^+ can continue to diffuse [186–188]. The accumulated ions create defect states in the p n junction [186, 187]. If the density of these states is high enough, hopping conduction can occur, and a shunt path is created [186, 187]. If the defect density is relatively low, Shockley Read Hall recombination (recombination through local defect states) occurs [186, 187].

Since the PID-s effect is strongly dependent on the Na^+ migration through the module and this, in turn, is influenced by the barrier properties of the individual module components, its magnitude depends on the selected material combination [17, 18, 185, 189]. On the one hand, a glass with a lower sodium concentration (e.g. quartz glass) can reduce PID-s effects [18, 189]. On the other hand, the choice of polymer layers is decisive. Encapsulants with higher volume resistivity reduce the effect [17, 18]. The moisture permeation rate of backsheets also plays an important role, as this can destroy the insulation properties in addition to degrading the encapsulant [18, 190].

Degradation by irradiance

Depending on the solar cells and module structure, degradation due to irradiance or light-induced degradation (LID) is a serious factor that influences the performance of solar modules [191–197]. In general, photons in the UV range are responsible for the degradation effects [194–197]. As explained in the previous chapter on the PERC cell structure and shown in Figure 18, the passivation layers are required to reduce carrier recombination and thus increase cell efficiency. Degradation analysis models show that a photon energy of 3.5 eV ($\approx$ 354 nm) is sufficient to destroy the Si-H bonds of the passivation layer and to reach the SiN-Si interface [194, 196]. The destruction of the Si-H bonds leads to an increase in the number of dangling bonds and thus to increased surface recombination at the emitter interface [196]. However, there are also considerations that the process is caused by defects in the bulk material [195]. The UV radiation generates charge carriers in the space charge zone [195]. During the separation of the charge carriers in the electric field, these change the charge state of the impurities during their transfer process [195]. This also changes the mobility of the impurities, and they can be converted into local defects in the bulk, leading to increased bulk combination [195].

For PERC cells, radiation-induced degradation generally leads to a reduction in J_{SC} and U_{OC} and thus to a loss of performance [194–197]. As this form of degradation is dependent on high-energy photons reaching the solar cell, its severity is also strongly dependent on the selected material combination [196, 197]. On the one hand, the choice of glass can influence the transmittance of photons [197]. On the other hand, the UV absorbers contained in the front encapsulant can effectively protect the cell from photon ingress [196, 197].

Degradation by corrosion

In this chapter, the main corrosion effect of this work will be briefly presented. This is not the corrosion of the Si semiconductor itself but the corrosion of the electrical contacts

or their interfaces. According to the current state of the literature, the corrosion of the Si layers can be attributed to a PID effect, which leads to delamination of the passivation layer [198, 199].

Like the other degradation effects, the corrosion of the solar cell is also dependent on the interaction of the other layers of the solar module. In general, this effect is the loss of contact between the cell and the electrical connector [200, 201]. Figure 19 shows scanning electron microscope (SEM) measurements and energy dispersive X-ray spectroscopy (EDX) of the contact point between the SI semiconductor and the Ag busbar of a PERC solar cell within this work before and after accelerated aging. The red rectangle in the aged sample shows a cavity between the semiconductor and the silver busbar. As a result, the charge carriers can only leave the semiconductor via the intact areas, and the series resistance increases [172, 201].

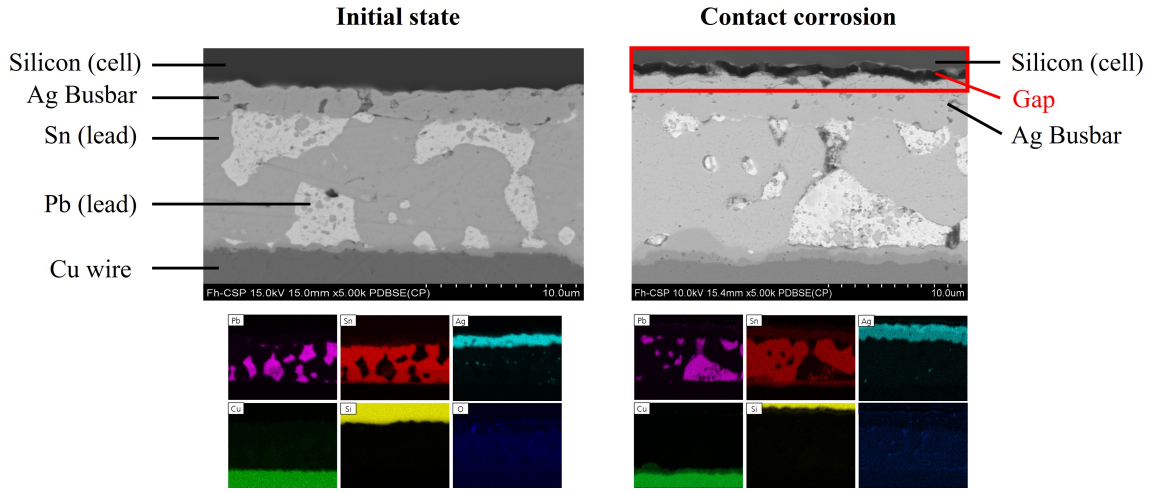

Figure 19: SEM and EDX images of the electrical connector of a PERC solar cell in the initial state (left) and after accelerated aging (right). The red rectangle marks the gap formation between the solar cell and the silver busbar.

The reason for the formation of the cavities is a complex interaction between several reaction partners. The degradation chain begins with the formation of acetic acid [172, 200, 201]. As described in subsubsection 2.1.3, this can be formed either by Norrish type II reactions or hydrolysis of the EVA encapsulant [31, 108–112]. Consequently, the reaction chain is not only dependent on the EVA itself but also on the barrier properties of the (permeable) backsheet, as these determine the penetration rate of moisture since diffusion from the edges of the module takes many orders of magnitude longer [202]. The screen-printed silver contacts usually contain silver particles, glass frits, solvents, additives, and surfactants [200]. The commonly used lead glass frits contain lead oxide, which is decomposed by acetic acid [200]. Lead acetate and water are formed according to the following reaction equation [200]

$$\mathrm{PbO} + 2\mathrm{CH_3COOH} \rightarrow (\mathrm{CH_3COO})_2\mathrm{Pb} + \mathrm{H_2O}. \tag{33}$$

This process breaks the connection between the Ag busbar and the cell and creates the cavity shown in Figure 19. It has been observed that the connection between busbar and cell is maintained locally by Ag columns and leads to an increase in series resistance [201]. In addition, it is assumed that the electrons can tunnel through the dissolved silver nanoparticles from the glass layer, which leads to a reduction of the FF [201]. If this degradation continues, J_{SC} also decreases, as the electronic properties of the Ag columns change [201]. However, the exact process behind this observation is still unclear [201].

2.3. Accelerated lifetime testing (ALT)

Since 1975, efforts have been made by various test laboratories, research institutes, and universities to develop suitable accelerated aging procedures to test PV modules [203]. Based on this, standard test procedures have gradually been developed to detect potential sources of error at an early stage [203]. Some of these test procedures are very specific and only relevant for a particular type of module (e.g., light soaking tests for thin film modules) [203]. In general, it is difficult to draw conclusions about the real service life of solar modules from these experiments, especially since most tests only include a few stress factors at a time [203]. Nevertheless, attempts are often made to calculate acceleration factors (AF) for various processes [204]. These AF are usually only valid for one process, as the chemical and physical interactions of different processes differ [204]. Furthermore, an AF is only valid for a defined material or combination of materials so that no universal statements can be made [204].

Various test procedures have become established for solar modules [204]. On the one hand, these are procedures for the complete module [48, 203, 204]. On the other hand, individual components (e.g., the encapsulant) are aged [49, 204–210]. There are a number of potential degradation effects that should be assessed before a module is used while the impact of various stress factors on module reliability is evaluated [204]. In general, the influence of temperature and humidity (Damp Heat (DH) tests), temperature cycles (thermal cycle test), solar irradiance (UV test), frost (humidity freeze test), wind and snow load (static mechanical load test), wind gusts (dynamic mechanical load test), hail (hail test), salt water and salt mist (salt mist spray test) are investigated [204].

As there are a large number of different test and qualification standards with respective sub-guidelines, the following chapter only refers to the aging procedures that were also used in the course of this work. The procedures were not used with the aim of qualifying a product or estimating the module service life. They were used to provoke aging effects in various components of the solar modules so that their reaction kinetics can be investigated in order to develop a holistic understanding of the aging of solar modules.

2.3.1. UV weathering

Accelerated aging using UV irradiation is typically carried out in special climate chambers at low relative humidities. The IEC 61215 standard defines the conditions for the

weathering of PV modules with relatively rough framework conditions, as the UV test within this standard is only used as preconditioning and defect provocation of the solar cell [48]. It is specified that the intensity between 280 nm to 400 nm should not exceed 250 W/m^2 and that a homogeneity of ± 15 % must be guaranteed [48]. In total, the modules must be irradiated with a dose of 15 kWh/m^2 in the wavelength range from 280 nm to 400 nm at a module temperature of 60 °C [48].

These specifications can be met by a variety of spectra and chambers. Figure 20 shows the spectra of a metal halide lamp and a xenon lamp that were mainly used within this work. The spectra are to be understood as examples, as they can be scaled depending on the lamp current used. However, the spectral distribution remains the same. It is obvious that the A3 spectrum is much more similar to natural sunlight, but both types of lamp would still be permissible according to IEC 61215 [48]. IEC 62788 was developed in order to define the framework conditions for this type of weathering more strictly and to develop an aging test for predicting long-term properties [49]. However, this weathering standard is only intended for the polymer materials in PV modules [49]. Nevertheless, it provides clearer guidelines regarding the choice of spectrum (UV-A lamps or xenon lamps with daylight filters), different chamber temperatures and significantly higher minimum doses [49].

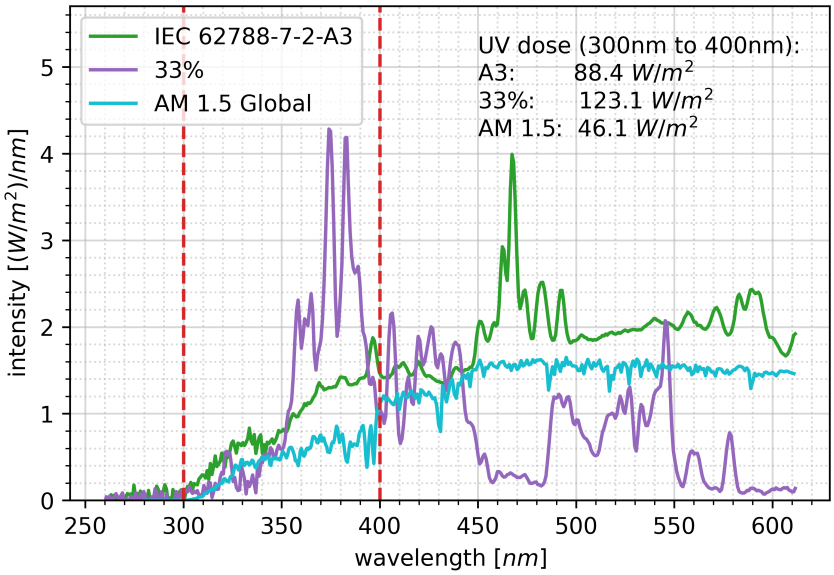

Figure 20: Exemplary spectra of a metal halide lamp (purple) and a xenon lamp with daylight filters (green) used in this work in comparison with the standard spectrum AM 1.5 Global (ASTM G173-03 reference spectra derived from SMARTS v. 2.9.2. provided by NREL). The lamp spectra are to be understood as examples. Their spectral resolution remains the same, but the lamp intensity was varied in the course of this work by the lamp current and the sample position.

Figure 21 shows all the cumulative UV aging doses used in this work in comparison

with the yearly UV dose of different positions on Earth. The exact aging conditions are given separately for each section of this work so that this presentation should only be understood as an overview. It should be noted that the cumulative dose does not contain any information about the spectral distribution. This can be particularly problematic if certain spectral ranges are neglected, as some interactions are only caused by certain wavelength ranges [58, 211, 212].

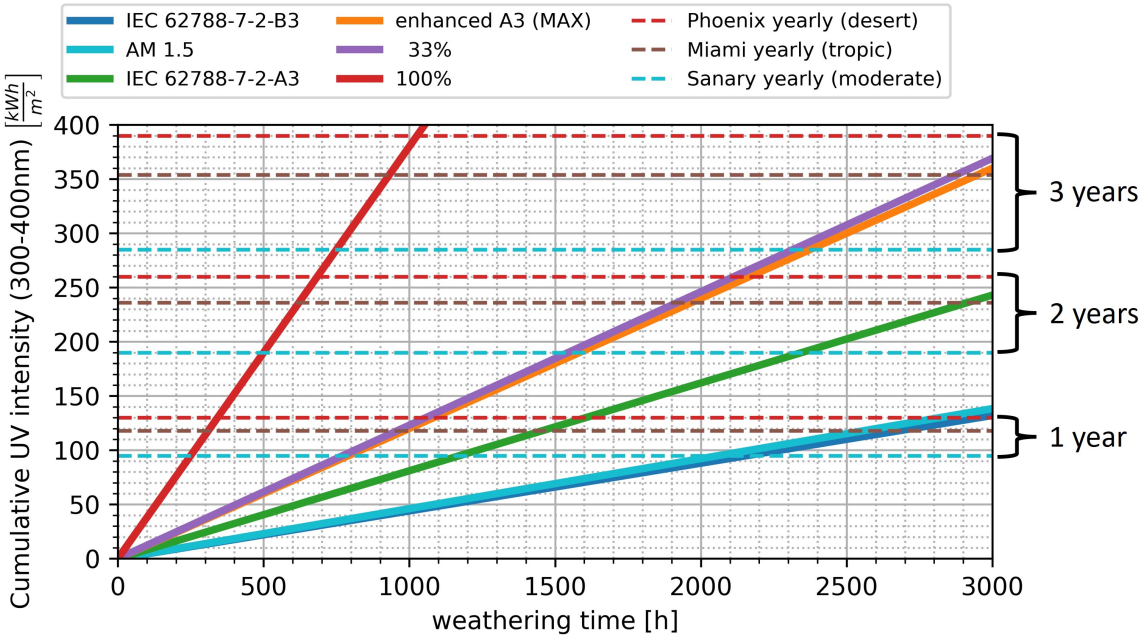

Figure 21: Cumulative UV dose of the weathering methods used in this work as a function of the weathering time. AM 1.5 corresponds to the standard solar spectrum, 33 % and 100 % are metal halide lamp spectra, A3 and enhanced A3 are xenon lamp spectra with daylight filter, and B3 corresponds to the spectrum of a UV-A fluorescence lamp. The dashed lines are annual UV doses from different locations around the world. Based on the data of [49].

2.3.2. Damp heat (DH) weathering

The standard DH test is also defined in IEC 61215, and it is used to qualify if solar modules are able to withstand the long term ingress of humidity [48]. It specifies storage of the solar modules at 85 °C ± 2 °C and 85 % relative humidity (r.h.) ± 5 % r.h. for at least 1000 h [48]. The DH test is probably the most widely used test of the accelerated aging methods [204]. Nevertheless, the results cannot be directly correlated with the performance of modules in outdoor use [203, 204]. Previous studies of the degradation effects that occur are often phenomenological in nature, although there are synergistic effects in conjunction with UV radiation [190, 213]. The effects of the test on the modules

are generally dependent on the polymer materials used and their water permeation rates [190, 204].

2.3.3. Combined stress tests

In general, there are two different ways to expose solar modules to several different stressors. Either sequential or parallel test methods are used [204, 214–216]. These aging procedures usually combine individual tests from IEC 61215 [204, 215, 216]. As the standard functions as a type approval, but there are still a large number of system failures, other test conditions are constantly being researched [216]. Many of these tests are only aimed at provoking a specific module fault (e.g. backsheet cracking), meaning that there are currently only a few approaches for a holistic, accelerated aging procedure [216].

In the course of this work, the conditions of UV weathering and DH weathering were combined. The aim is to investigate the effects of the parallel presence of stressors on solar modules. Different UV intensities of the metal halide lamp spectrum (see Figure 20) were used at 85 °C chamber temperature and 60 % r.h.

3. Degradation modes in solar modules for single stress factors

As described above, the effects of various stressors on solar modules have not yet been sufficiently researched. Although there is a lot of work on the degradation of individual materials, the findings from this can only be applied to multilayer systems such as solar modules to a limited extent. In addition, it is necessary to compare the influence of different environmental factors (i.e., UV aging and DH aging) in order to better understand the degradation effects caused.

In the following publication, the fundamental aging effects of UV and DH weathering on solar modules are therefore compared in a first step. The degradation of the cell, the encapsulant and the HALS contained in the EVA is discussed in dependence of the applied stressors. It should be pointed out again at this point that the EPR and Orbitrap MS measurements were carried out by colleagues from TotalEnergies OneTech in Solaize. The discussion of all results was done jointly by the three first authors.

RESEARCH ARTICLE

Solar RRL

www.solar-rrl.com

From Performance Measurements to Molecular Level Characterization: Exploring the Differences between Ultraviolet and Damp Heat Weathering of Photovoltaics Modules

Robert Heidrich, Nikola Babić,* Oscar Lacroix-Andrivet, Charles-Emmanuel Dutoit, Camille Bainier, Anton Mordvinkin, Ralph Gottschalg, Hervé Vezin, Carlos Afonso, and Simon Pondaven*

The degradation behaviors of the encapsulant and the imbedded additives significantly determine the reliability of solar modules. Nevertheless, a link between the degradation of the encapsulant, including the additive interactions, and the longevity of the overall module is rarely established until now. Herein, mini-modules containing ethylene-vinyl acetate copolymer (EVA) as encapsulant are subject to damp heat (DH) or ultraviolet (UV) weathering based on IEC 61215. Macroscopically, the degradation under both weathering types characterized by *I–V* measurements and electroluminescence (EL) measurements is diverging in dependence on the used stressor. Using electron paramagnetic resonance and orbitrap mass spectrometry, it is shown that deacetylation of the EVA occurs significantly for both types of weathering. In the case of DH, however, the mechanism of action of the UV stabilizer is hindered, so that strong encapsulant degradation is observed despite a lower energy input in comparison with UV. Furthermore, the produced acetic acid under DH weathering leads to the observed reduction in EL, an increase in series resistance, and, a reduction of the performance of the modules. The work carried out shows that the degradation of the solar modules is strongly dependent on the behavior of the UV stabilizer.

1. Introduction

Today, the increase in global energy demand as well as the need to reduce CO_2 emissions is driving the development of renewable energies, especially solar photovoltaics (PV). Since 2010, solar PV has shown an impressive learning curve and is now a mainstream energy source, which is the result of consistent cost reduction and technical performance improvements.[1] However, PV modules installed in the field are facing various climatic conditions: humidity, temperature cycling, ultraviolet (UV) exposure, mechanical stress, etc. that could be combined at very different intensity levels, leading to various degradation and failure scenarios.[2–5] With a mass share of ≈6.5%, polymer materials (encapsulants and backsheets) only make up a small proportion of a solar module.[6] Nevertheless, a large number of module defects can be attributed to the failure of polymer components.[7] Furthermore, the interaction of different polymer layers within a module can have a major influence on its degradation behavior.[4,8–10] Understanding diverse degradation modes

R. Heidrich, A. Mordvinkin, R. Gottschalg
Fraunhofer CSP
Otto-Eissfeldt-Strasse 12, 06120 Halle (Saale), Germany
E-mail: robert.heidrich@csp.fraunhofer.de

R. Heidrich, R. Gottschalg
Anhalt University of Applied Sciences
Bernburger Strasse 55, 06336 Koethen (Anhalt), Germany

The ORCID identification number(s) for the author(s) of this article can be found under https://doi.org/10.1002/solr.202400144.

DOI: 10.1002/solr.202400144

N. Babić, O. Lacroix-Andrivet, S. Pondaven
TotalEnergies OneTech
Centre de Recherche de Solaize (CRES)
Chemin du canal, BP 22, 69360 Solaize, France
E-mail: nikola.babic@totalenergies.com

N. Babić, C.-E. Dutoit, H. Vezin, S. Pondaven
Joint Laboratory—CR2ME: Centre de Résonance Magnétique Électronique pour les Matériaux et l' Énergie
59655 Villeneuve d'Ascq, France

O. Lacroix-Andrivet, C. Afonso
International Joint Laboratory—iC2MC: Complex Matrices Molecular Characterization
TRTG
BP 27, 76700 Harfleur, France

affecting PV modules, particularly those involving polymer materials, becomes imperative, enabling informed component selection and accurate quantification of performance losses. Surprisingly, there are only a few studies to date that correlate the degradation of polymer layers with the macroscopic degradation of a solar module (i.e., deterioration of electrical parameters).[9,11,12]

Solar modules are designed to last at least 25 years, although it has been shown in the past that this is only economical if an annual degradation rate of 0.73% is not exceeded.[13] However, depending on climatic conditions and material combinations in PV modules, annual degradation rates of well over 1% are possible, and earlier total failures can be expected at any time.[14,15] For these reasons, it is essential to test the modules thoroughly before using them in the field. Even though with IEC 62788-7-2, there is now a standard for testing polymer components,[16] the complete module is tested under the conditions defined in IEC 61215.[17] Typically, damp Heat (DH) and UV tests are carried out according to IEC 61215.[17] There are many studies that deal with the degradation of individual components of the solar module (e.g., cell degradation or degradation of polymer layers) as a function of the two types of weathering, however, an integral approach to understand the degradation of the complete module is often missing.[18–22]

Although new types of modules sometimes use polyolefin-based elastomers or thermoplastic polyolefins, ethylene-vinyl acetate copolymer (EVA) has been the main encapsulant used so far.[23,24] To date, the effects of these tests on the encapsulation material and, in this context, on the reliability of the overall module are not fully understood. The degradation of EVA is a complex process with various intermediate reactions, which can proceed differently depending on the external conditions.[15,24–27] In addition, the degradation of EVA is influenced by the additives contained in the encapsulant, whereby UV additives and antioxidants in particular are intended to protect the polymer.[28,29]

The given study is intended to close the abovementioned knowledge gaps. To achieve this goal, a combination of different analytical methods is used, ranging from macroscopic performance characteristics of the overall modules by electrical characterization and electroluminescence (EL) measurements to molecular analysis of the encapsulant by electron paramagnetic resonance measurements (EPR) and Orbitrap mass spectrometry (MS). Hindered amine light stabilizers (HALS) have a catalytic mechanism of action and one of their active intermediates is stable radicals called nitroxides. Being the analytic technique of choice for studying radicals, EPR is used to investigate the antioxidant activity of HALS under different weathering conditions. Concerning Orbitrap MS, it corresponds to a Fourier transform mass spectrometry (FTMS) technique suited for the characterization of complex matrices thanks to its high sensitivity, high mass accuracy, and very high resolution. It allowed us to characterize the HALS additive and the various forms of degradation of the base polymer at the molecular level. The combination of these different techniques provides a better understanding of encapsulant aging by linking performance test results to molecular markers.

C.-E. Dutoit, H. Vezin
Laboratoire Avancé de Spectroscopie pour les Interactions la Réactivité et l'Environnement (LASIRE)
Université Lille Nord de France
CNRS UMR8516
59655 Villeneuve d'Ascq, France

C. Bainier
TotalEnergies OneTech
R&D Power
7-9 Boulevard Thomas Gobert, 91120 Palaiseau, France

C. Afonso
Normandie Univ., COBRA, UMR6014 and FR3038
Université de Rouen
INSA de Rouen
CNRS, IRCOF
1 rue Tesnière, 76821 Mont-Saint-Aignan Cedex, France

2. Methodology

2.1. Sample Design

The used one-cell mini-modules correspond to the conventional structure of a solar module. The substrate was 3 mm float glass. The EVA has an UV cutoff (5% transmittance at 350 nm), a vinyl acetate content of 26–28%, and a thickness of 0.4–0.6 mm. A Meier ICOLAM 10/08 was used for lamination with the following parameters: the laminator was preheated to 55 °C. The samples were then placed in the laminator, which was evacuated for 6.5 min and heated to 80 °C. The modules were then pressed with 600 mbar and heated to 155 °C within 3 min. The temperature and pressure were maintained for a further 15 min. Finally, the laminator was cooled down to 55 °C within 30 min, whereby the 600 mbar pressure was kept constant.

The gel content after lamination is reported to be over 85% by the datasheet, while measurements of separate films show gel contents of ≈90%. Thus, no remaining crosslinking peroxides are expected. The EVA has a reported transmittance of over 91% and was used as front and back encapsulant. Solar cells were based on PERC technology with 5 busbars and 4 electrical contacts for *I*–*V* measurements. The backsheet is based on polyethylene terephthalate with a thickness of 320 µm. The moisture transmission rate of the backsheet is reported to be 1.9 g m^{-2} per day. After lamination, the edges of the mini-modules were sealed with an aluminum tape to simulate a frame and make it more difficult for moisture to penetrate.

The encapsulation material used was initially characterized by pyrolysis gas chromatography-mass spectrometry (PY-GCMS) for investigating the additive composition. The PY-GCMS setup has been described in detail in one of our previous publications.[30] However, in this work only a qualitative additive analysis was executed. **Table 1** lists the results of the additive analysis. A combination of crosslinking peroxide and crosslinking accelerator was used to enable the reported gel content after lamination. In addition, an adhesion promoter was admixed. For stabilization, a combination of an antioxidant, an UV absorber, and a HALS (UV stabilizer) was used.

2.2. Weathering

Two different types of weathering were performed for this study. UV weathering was conducted in CTS CSL-70/1500 climatic

ADVANCED SCIENCE NEWS
www.advancedsciencenews.com

Solar RRL
www.solar-rrl.com

Table 1. Results of the qualitative PY-GCMS analysis. Substances with ++ are certainly detected in significant amounts. For substances with +, only traces (small intensities) were found.

Name	Function	CAS	Amount
Luperox TBEC	Crosslinking peroxide	34443-12-4	++
TAIC	Crosslinking accelerator	1025-15-6	++
Silane A-174	Adhesion promoter	2530-85-0	+
BHT	Antioxidant	128-37-0	+
Cyasorb UV 531	UV absorber	1843-05-6	++
Tinuvin 770	HALS, UV stabilizer	52829-07-9	++

chambers. Here, the parameters were set to 60 °C chamber temperature, 5% relative humidity, and an integrated UV intensity of 175 ± 35 W m^{-2} (depending on the sample position in the chamber) between 300 and 400 nm. For example, lamp spectrum of the chamber and the intensity homogeneity of the lamps are displayed in the supporting information. The used parameters are in accordance with the UV preconditioning test MQT 10 of the IEC 61215-2.[17]

DH weathering was performed in a CTS CW + 40/8/8 chamber. The parameters were set to 85 °C chamber temperature and 85% relative humidity which are in accordance with the DH test MQT 13 of the IEC 61215-2.[17] The modules were characterized after 0, 500, 1000, 1500, and 2000 h, as described in **Table 2**. After the electrical characterization, 3 modules of every weathering step were removed for further analysis.

2.3. Characterization Methods

2.3.1. I–V Characterization and EL Measurements

The *I–V* characteristics were recorded using a Berger Lichttechnik solar simulator (flasher system). The tests were performed at 25 °C with 1000 W m^{-2} irradiated intensity (standard test conditions). The flasher corresponds to class A in the categories of homogeneity, spectral match, and temporal stability. The repeatability is less than 0.3% deviation. The flasher was calibrated with a reference module before each measurement series.

EL measurements were performed with a great eyes LumiSolar Professional system. A cooled GE2048 512 BI MID CCD sensor is installed in the camera. For the EL measurements, the modules were powered with 8.5 A.

Table 2. Sample list.

Aging type	Aging duration [h]	UV dose [kWh m^{-1}]
Native mini-module	0	0
Mini-modules aged under UV irradiation	UV-500	87.5
	UV-1000	175.0
	UV-2000	350.0
Mini-modules aged under DH	DH-500	0
	DH-1000	0
	DH-1500	0
	DH-2000	0

2.3.2. EPR Measurements

Sample Preparation and EPR Spectroscopy: EVA was sampled using scalpel by cutting out rectangles (2.5×20 mm) of the entire stack except the glass (backsheet, front and back layer of EVA, and solar cells). The samples were taken from two spots for each mini-module: the center of the mini-module, and the edge of the mini-module (the edge sample contained only the two layers of EVA and backsheet). Samples were placed in 5 mm quartz EPR tubes and EPR spectra were recorded at room temperature using a Bruker EMXnano EPR spectrometer (Bruker, Wissembourg, France) operating at X-band (9.61 GHz) with the following parameters: modulation frequency, 100 kHz; modulation amplitude 4.0 G; time constant, 20.48 ms; conversion time, 60.00 ms; center field, 3425.45 G; sweep width, 300 G; sweep time 45.0 s; microwave power, 10 mW; number of scans, 10; Pts/Mod. Amp, 10.00; and resolution 750 points. Data acquisition and processing were performed using Bruker Xenon software. The amount of nitroxide present in the sample is directly proportional to its EPR signal intensity. Since a similar spectral appearance of nitroxide was observed in all samples, the intensity was measured as the height of the central line and was normalized by the mass of the sample. For the shown set of samples, one sample per condition per time point was analyzed. Relative measurement error was calculated from three repetitions of 500 h UV sample and was found to be ±16%. It was used for other samples as a generic relative error.

Sample Preparation and EPR Imaging: Samples were prepared by cutting a rectangle (5.0×20 mm) of the entire solar mini-module (including the glass support). EPR imaging measurements were carried out on a conventional X-band Bruker ELEXSYS E580 spectrometer operating at about 9.5 GHz and room temperature. The microwave power and the modulation amplitude used were set to 5 mW and 10 G, respectively. The samples were placed into the magnet equipped with ZY two-axis field gradients. A gradient strength of 100 G cm^{-1} and a field-of-view of 20 and 15 mm have been used to record spatial–spatial and spectral–spatial images, respectively. Both images were performed using 402 projections and a size of 512×512 pixels corresponding to a pixel size of 0.0391 mm (0.0293 mm). The final images were reconstructed after a deconvolution of the recorded projections under a magnetic field gradient from a spectrum with field gradients turned off. Subsequently, a filtered back projection using the Fourier transform was applied. EPR images analysis and spectral simulations were done with the EasySpin package for MATLAB.[31]

2.3.3. Orbitrap MS Measurements

Sample Preparation Prior to MS Analyses: EVA pieces were sampled from the edge of the mini-modules using a scalpel. 1 mL of heptane for each 30 mg of EVA was placed in a glass vial. To solubilize a part of the EVA, the vials were treated for 1 h in an ultrasonic bath. The resulting solutions were then centrifugated at 4000 rpm for 5 min. Supernatants were then

collected to be analyzed by direct infusion on the Orbitrap instrument. A scheme of this procedure is displayed in Figure S1, Supporting Information.

MS Analyses: Orbitrap MS analyses were carried out using a Thermo Orbitrap QExactive Plus equipped with a commercially available atmospheric pressure chemical ionization (APCI) source. The instrument was calibrated before the analyses using the Thermo Scientific Pierce LTQ ESI positive ion calibration solution. Mass spectra were obtained on a mass range between m/z 100 and 1200 with an analysis duration of 6 min at 1 Hz resulting in 280 k resolution at m/z 200. The automated gain control target was set at 10^6, and the maximum injection time at 50. S-Lens RF was set at 100 to have a better sensitivity toward a high mass range. Indeed, this lens allows a 10-fold increase in the ion transfer efficiency in the MS/MS mode, and a threefold to fivefold increase for the full scan analysis. For the ionization source, a sheath gas and an auxiliary gas were set at 20 (a.u) and 10 (a.u), respectively, corona discharge was set at 4.5 µA, and the source temperature was 300 °C. MS data were treated using FreeStyle 1.6 software. Molecular formulae were attributed to each signal using a heteroatom tolerance set at a maximum of 2 nitrogen atoms and 10 oxygen atoms, with an error tolerance set at 2 ppm. Molecular maps and heteroatom class distribution were plotted using PyC2MC[32] and OriginPro softwares.

For the Kendrick mass defect (KMD) plots, KMD of molecules were calculated using the classical CH_2 base unit to obtain the Kendrick masses (KMs) using the following equations:

$$\mathrm{KM} = \text{observed IUPAC mass} \times \frac{\text{nominal mass of CH2 (14)}}{\text{IUPAC mass of CH2 (14.01565)}} \quad (1)$$

$$\text{Nominal KMaNKM} = \text{round (KM)} \quad (2)$$

$$\text{KM defect aKMD} = \text{aNKM–KM} \quad (3)$$

The nominal KM corresponds to the KM rounded to the nearest integer.

3. Results and Discussion

3.1. Electrical Characterization

To investigate the macroscopic degradation behavior of the modules, an electrical characterization was carried out for both types of weathering in 500 h steps. The behavior of the characteristic parameters: short circuit current I_{SC}, maximum power output P_{max}, open circuit voltage V_{OC}, fill factor FF, series resistance R_S, and efficiency η is discussed. The electrical characterization of the weathered mini-modules is displayed in **Figure 1**. Changes in the I_{SC}, P_{max}, V_{OC}, FF, and η vary from 1% to 4%. R_S increased significantly by ≈12% for the DH weathering. The differences in changes in the electrical parameter between UV exposure and DH exposure can be explained by diverging aging characteristics.

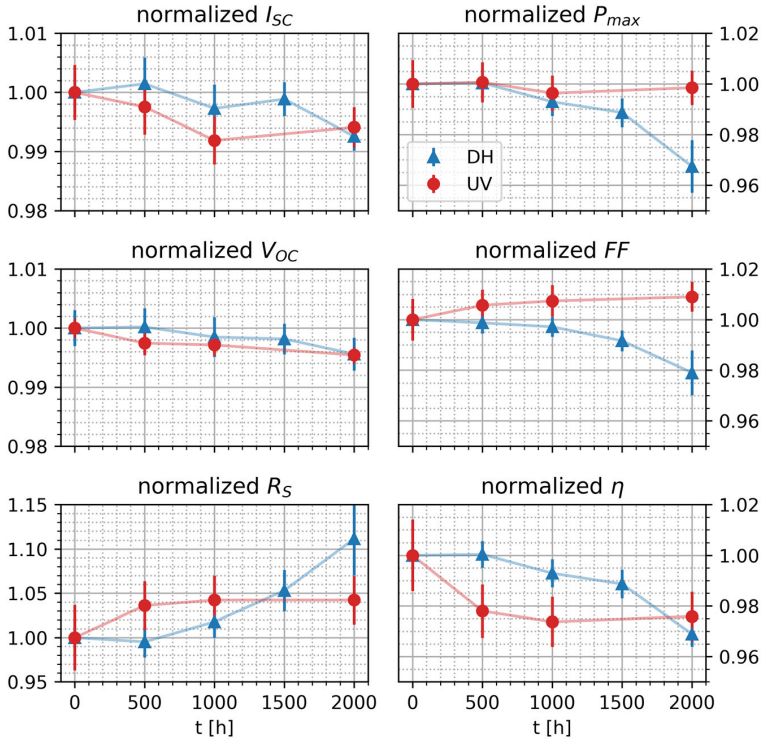

Figure 1. Electrical parameters of mini-modules under DH weathering (blue) and UV weathering (red) in dependence on the weathering time.

ADVANCED SCIENCE NEWS
www.advancedsciencenews.com

Solar RRL
www.solar-rrl.com

Considering the I_{SC} measurements, the UV weathering caused a higher degradation rate than the DH weathering. Within this work, the same encapsulant as in one of our previous weathering cycles was used.[24] Comparing the UV spectrum of the weathering chamber (see Figure S8, Supporting Information) with the previous weathering, especially the intensity of the 300–350 nm interval is less harmful for the UV aging carried out within this work. The previously weathered samples did not show changes in the optical properties determined by UV/VIS measurements and also the formed C=C bonds (which can lead to discoloration) occur only after 1750 h.[24] Thus, as the UV-aged modules of this work did not show browning and the degradation already started within 500 h, the decrease of I_{SC} is probably caused by the degradation of the passivation layer of the solar cell.[20,33,34] This is also in accordance with the constant V_{OC} decrease which is reported in the literature for the degradation of the passivation layer as well as the formation of defects in the bulk of PERC solar cells.[20,33–35] Witteck et al. reported that photons with wavelengths smaller than 353 nm may break Si—H bonds which leads to increased surface recombination.[33] As the used EVA (see Section 2.1) is also transmitting photons in that wavelength interval, the effect may also occur here. The small I_{SC} increase after 2000 h of weathering is most likely a result of deviations between the different sample batches and should not be over-interpreted as a general trend for the other weathering steps observed. However, the electrical parameters at the maximum power point stayed approximately constant for the UV weathering (not shown within this work), hence the minimal decrease of the P_{max} is most likely a result of the minor increase of the series resistance. Consequently, as P_{max} stays approximately constant while V_{OC} and I_{SC} are decreasing, the FF is increasing. As I_{SC} and V_{OC} decrease, but R_S increases, this is directly reflected in a reduction in efficiency of ≈2.25% after 2000 h of weathering.

In contrast to UV weathering, the data of the DH conditions indicate that the aging effects are probably not caused by the degradation of the passivation layer of the solar cell. While there is also a constant decrease of the I_{SC} and the V_{OC}, these changes are less pronounced as for the UV weathering. However, the P_{max} starts to decrease significantly after 1000 h of weathering which is probably caused by the simultaneously increasing R_S. Because I_{SC} and V_{OC} are only minimally decreasing while P_{max} is decreasing more severely, the FF is decreasing by ≈2% after 2000 h of weathering. After 2000 h, the R_S increased by ≈11% resulting in a η and P_{max} decrease of 3.5%. This R_S increase is probably caused by the corrosion of the solar cell contacts forced by a reaction with acetic acid.[22,36,37] The latter is either a result of the Norrish Type II reactions or hydrolysis of the EVA.[38–41] In both cases, this will lead to deacetylation of the acetate group. Thus, the deacetylation can be forced by high energy photons, elevated temperature, or/and the presence of water, and can be additionally catalyzed by the formed acetic acid.[42] In addition, further moisture ingress could act as a solvent and thus disperse the acetic acid which brings it to other reaction sites. This explains why the initial R_S increase is higher for the UV-weathered samples while forming a plateau after ≈500 h. The UV irradiance is splitting the acetate groups faster (Norrish Type II reaction), however, only a specific amount of moisture is present within the module and no additional moisture is diffusing inside due to the dry weathering conditions which prevents the autocatalytic reaction. In contrast, the hydrolysis-based process takes place more slowly at the beginning under DH conditions but does not slow down due to the constant penetration of moisture and its autocatalytic reaction.

This assumption is confirmed by the EL measurements displayed in **Figure 2**. For the UV weathering, no EL decrease was detected within 2000 h of weathering. For DH weathering, in contrast, the deacetylation starts slower, but the diffused-in moisture results in a constant R_S increase and a decrease of EL.[37] The water is two-dimensionally penetrating through the backsheet and migrating around the solar cell afterward while reacting with the electrical contacts.[43,44] Although the process of EL reduction starting from the edges of the module toward the center is described many times in the literature,[45,46] the exact cause of this path is still unclear. However, it is obvious

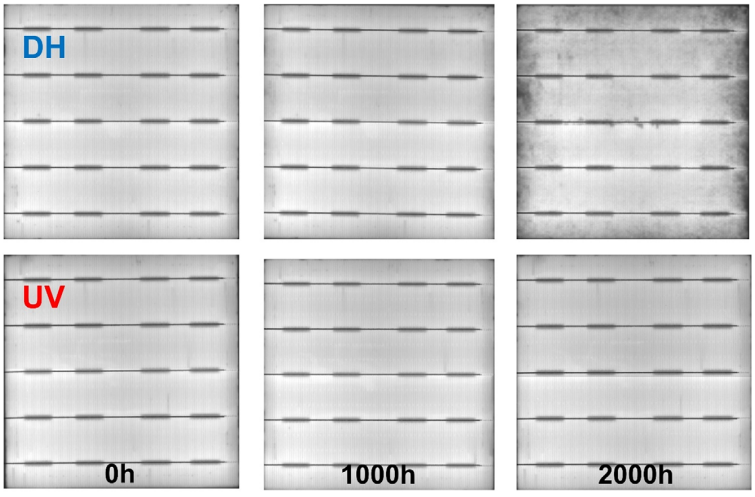

Figure 2. EL measurements of mini-modules under DH weathering (top, blue) and UV weathering (bottom, red) in dependence on the weathering time.

that the moisture penetrating from the rear at these points only has a short path to the top of the solar cell. The hydrolysis of the EVA then takes place almost simultaneously at the top and bottom of the edge area of the solar cell, so that the electrical contacts on both sides degrade resulting at the highest increase of R_S at these positions. Although Jankovec et al. have shown that the diffusion path of the moisture runs mainly via the backsheet,[43,44] diffusion from the edges can still be expected in the edge area, which should further intensify the effect.

3.2. EPR Study

HALS is used to delay the photo-oxidative degradation of an EVA encapsulant. These antioxidant additives act by catalytically inactivating free radicals produced by photo-oxidation through a complex mechanism involving nitroxide radical intermediates.[47–49] Being stable organic radicals, a method of choice for studying nitroxides is EPR spectroscopy.

Several species are involved in the mechanism of action of HALS, including stable nitroxide radicals (**Figure 3** and 12). HALS are added to polymers in their amine form (HN—NH). By reaction with radicals generated through photo-oxidation, amines are activated to nitroxide form (•ON—NH), which in reaction with a carbon-centered radical based on EVA fragments graft to it in the form of alkoxyamine (EVA-ON—NH). The same sequence of reactions can occur on the other amine moiety of HALS.[50]

In all analyzed samples, we observed a multiline EPR spectrum of nitroxide radicals which contains an unpaired electron spin $S = ½$ (Figure 5 and S1, Supporting Information). The overall shape, characterized by three-hyperfine lines, is dominated by the hyperfine interaction of the electron spin with the nuclear spin $I = 1$ of the ^{14}N nucleus. The EPR spectrum exhibits another typical feature of nitroxide radicals with reduced mobility: line broadening, especially of the high field line. It is well known that the EPR spectrum of nitroxides is highly dependent on their molecular mobility.[51] When in liquid solution, highly mobile nitroxides exhibit a symmetrical three-line EPR signal. In the solid state, depending on the degree of freedom, the appearance of the nitroxide radical EPR spectrum can vary.[52]

EasySpin package for MATLAB and a homemade program developed for such simulations have been used to quantify this motion. Considering an anisotropic rotational correlation time t_{corr}, with a long $t_{corr} = 14$ ns along x, a short $t_{corr} = 0.5$ ns along y, and an intermediate $t_{corr} = 2$ ns along z directions, the main features of the experimental signal are well reproduced (**Figure 4**). This result indicates that in its nitroxide form, HALS undergoes a slow motion in a quasi-rigid limit. While the appearance of EPR spectra of nitroxide HALS intermediates usually does not evolve over the course of polymer aging, their concentration may change, indicating HALS transformation. In a typical case of polymer aging, nitroxide radical intermediate accumulates in the initial phase of photooxidation, then peaks, and finally decreases as HALS are transformed into other forms.[53] The rate of peaking depends on the severity of oxidative conditions: harsher conditions (high temperature, intense light, presence of oxygen) cause nitroxide form to peak sooner.[54] Although HALS are still active as antioxidants in their grafted, alkoxylamine form (EVA-ON—NO-EVA), chemical degradation of the polymer accelerates only once the nitroxide intermediate has peaked, decreased, and stabilized at a low concentration.[55]

The set of samples analyzed by EPR spectroscopy consisted of four timepoints (0, 500, 1000, and 2000 h) for two aging conditions previously described (DH and UV), and two sampling positions for each: the center of the mini-module and the edge of the mini-module (Figure 7). For UV samples, it was observed that the concentration of nitroxides increases for both edge and center positions until 1000 h, when it peaks at the edges, but continues to increase in the center. Since the experiment was stopped at 2000 h, nitroxide concentration peaking in the center was not reached (**Figure 5**). In contrast, a different behavior is observed for DH conditions. The detected concentrations of nitroxide radicals are lower at both positions and for all timepoints, as compared to UV conditions. An increase in nitroxide concentration is observed until 1000 h for both positions, after which it seems to stagnate. Since DH conditions consisted of exposing mini modules only to high temperature and humidity without light irradiation, it is not surprising that HALS are not following the reaction scheme established for classical photo-oxidation conditions, which was observed for UV conditions. It is possible that the equilibria are shifted toward nonradical species of the Denisov cycle (Figure 3 and 12). Just as under

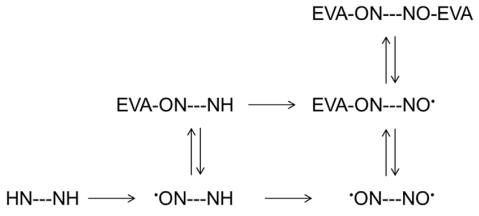

Figure 3. A schematic representation of chemical transformation of HALS during EVA aging. Only the functional groups of HALS (Tinuvin 770 UV stabilizer) are shown. They are introduced in their amine form (HN—NH) and get transformed to nitroxides on one (•ON—NH) or both sides (•ON—NO•) or alkoxyamines bound to the polymer (EVA-ON—NO• and EVA-ON—NO-EVA).

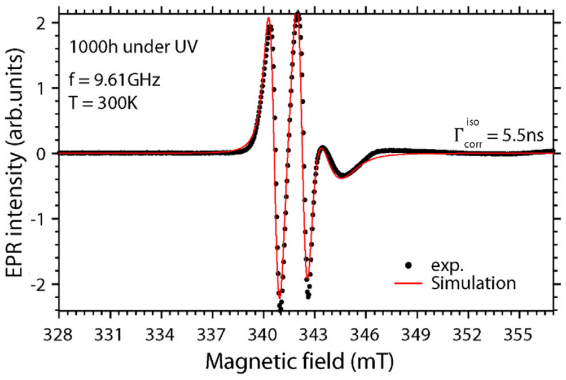

Figure 4. Experimental X-band cw-EPR spectrum of a sample taken from the edge of the mini-module after 1000 h of aging under "UV" conditions (black dots) and simulated spectrum (red line).

ADVANCED SCIENCE NEWS
www.advancedsciencenews.com

Solar RRL
www.solar-rrl.com

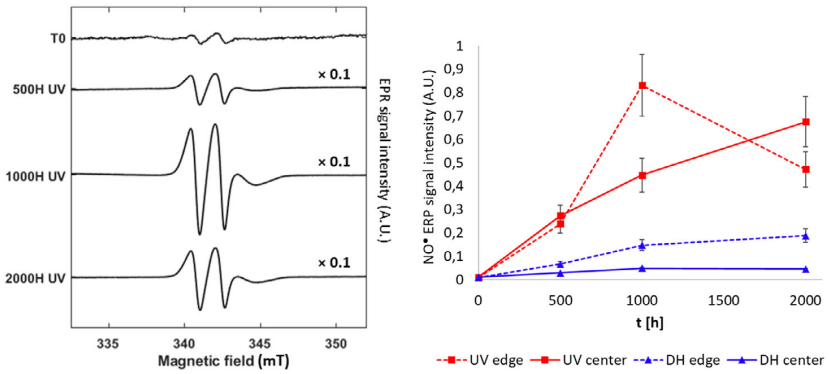

Figure 5. Left: EPR spectra of samples taken from the edge of the mini-module aged under "UV" conditions. EPR spectra of the full set can be found in Supporting Information (Figure S1). Right: graphical representation of nitroxide signal intensity measured by EPR in the entire set of samples.

UV conditions, a higher concentration of nitroxide radical was detected on the edge of the mini-module compared to its center. Differences in the level of exposure of EVA to oxygen and moisture are probably the cause of the differences in aging rate between the edge and center of the mini-module. Two effects may play roles here. The first is that oxygen and water diffuse toward EVA from the sides, affecting only outer several millimeters of EVA. The second is that oxygen and water diffuse through backsheet equally at all positions, but only on the edges affecting both layers of EVA, since in the center solar cells act as a barrier preventing exposure of the front EVA layer (Figure 7). More detailed information about the spatial distribution of nitroxides throughout the mini-modules was provided by EPR imaging.

EPR imaging experiment was performed on a sample taken from the mini-module aged during 1000 h, as it showed the highest difference in concentrations of nitroxide between edge and center. This experiment allows 2D mapping of the nitroxide radical within the sample, while the third spatial dimension (thickness of the mini-module) is averaged. In **Figure 6**, part C, we can observe that the concentration of nitroxide radical is higher toward the edge of the mini-module, and that it drops toward the center. More precisely, the concentration of nitroxide is low on the very edge of the mini-module since it was covered with a protective aluminum foil that blocked UV rays, and thus protected the EVA layer. The peak of the nitroxide radical concentration is found in the region of the mini-module in between the part protected by aluminum foil and the segment which contains silicon photovoltaic cells (the region in **Figure 7** indicated by dashed red arrow). While the aluminum foil protected both EVA layers from UV light, the front EVA layer of the center region was protected from oxygen and water diffusion through the backsheet by silicon cells that acted as a barrier. At the spot where the concentration of nitroxide peaked, EVA was exposed both to UV light and to oxygen and water diffusing through backsheet, which resulted in a higher rate of aging.

Spectral/spatial EPR imaging (Figure S3 and S4, Supporting Information) confirmed that the only observed paramagnetic species are nitroxide radicals.

3.3. Orbitrap MS

To characterize the difference of both aging conditions at the molecular level, encapsulants at the edge of the mini modules were analyzed by Orbitrap MS. Indeed, as it was demonstrated by EL and EPR analyses, the most variations were obtained at the edge compared to the center. In addition, sampling on the edge of the mini-module avoids the presence of silicon particles in the solutions after solvent extraction, which is preferable to avoid dirtying the instrument.

The mass spectrum obtained by APCI(+)-Orbitrap for the native mini-module is displayed in **Figure 8**. The mass spectra of samples after both UV and DH aging are presented in Figure S6, Supporting Information. The major signals obtained for each mass spectrum correspond to the protonated HALS $[C_{28}H_{52}N_2O_4 + H]^+$. Logically, this signal decreases progressively with both types of aging. It underlines that the HALS is consumed or is no longer found in its native form during aging. For the native sample, signals from EVA encapsulant can be observed below the HALS with Gaussian distributions between m/z 200 and 1000 as it can be observed in the enlargement in Figure 8. It is important to note that intact EVA polymers should be found at much higher masses that could not have been detected in the current mass range. The molecules that are observed in this study result from the extraction in n-heptane with ultrasonic bath, which probably allowed to solubilize small size chains or to fragment larger mass chains which then become detectable in the investigated mass range. Major ions of this Gaussian distribution correspond to hydrocarbon molecules (HC) with characteristic mass differences of CH_2 units corresponding to 14.01565 Da. Other EVA molecules with up to 4 VA units are observed below these HC major distributions. It is then assumed that the HC molecules correspond to the EVA polymer termination unit, or to several ethylene repeats that have solubilized in heptane using the current protocol. Finally, these compounds are used as reference for the native polymer signal. Interestingly, in the most aged samples (DH-2000 h and UV-2000 h), these distributions change in appearance, as the major hydrocarbon signals are no longer separated by

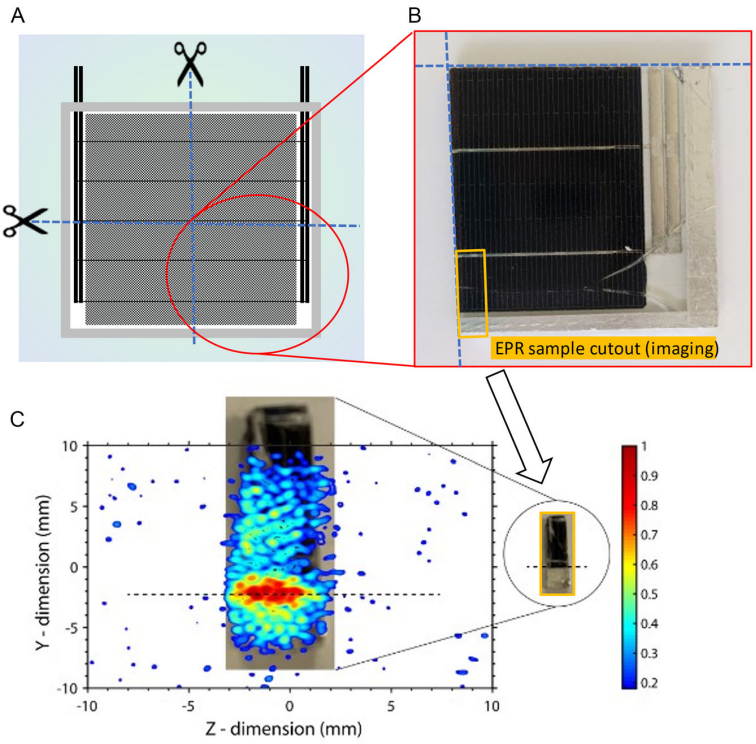

Figure 6. A) Schematic representation of the mini-module with indications of sampling for EPR spectroscopy. B) A quarter of the mini-module after 1000 h of aging under "UV" conditions with indication of the cutout of the sample for EPR imaging. C) EPR imaging: 2D map of the spatial distribution of nitroxide radical within a cutout piece of the mini-module (5.0 × 20 mm). The relative abundance of nitroxide radicals is presented as a color scale. The results were confirmed on a different sample (results presented in Supporting Information, Figure S2).

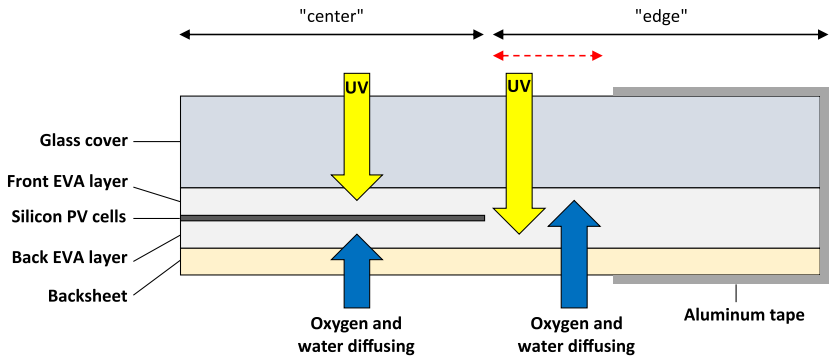

Figure 7. A cross-section of the PV module where we see both "edge" and "center" regions. We can observe that in the center region, the front EVA layer is only under the effect of UV, while the back layer is only under the effect of oxygen and water diffusing through the backsheet. The portion of "edge" region indicated by red arrow is influenced by both.

CH_2 mass differences, but by C_5H_8 gaps. Thus, it means that one additional unsaturation is obtained for each C_5H_8 unit. Such mass differences can be explained by the loss of the acetate group (and the corresponding formation of acetic acid) from the vinyl acetate unit during aging. Indeed, deacetylation of EVA is widely described in the literature through Norrish II reactions or hydrolysis.[38,56,57] This evidences that EVA was subjected to chemical modification with aging, with probable fragmentation of polymer

ADVANCED SCIENCE NEWS
www.advancedsciencenews.com

Solar RRL
www.solar-rrl.com

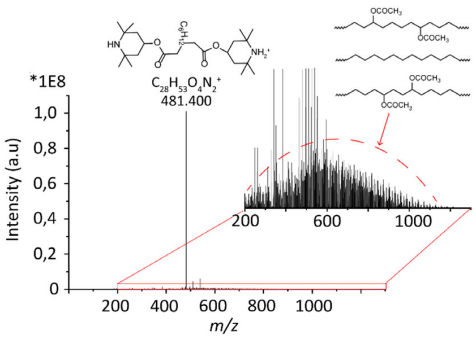

Figure 8. APCI(+)-Orbitrap mass spectrum obtained for the native mini-module sample, with its corresponding enlargement.

chains which were detached from the polymer network and then solubilized during the extraction process.

3.3.1. Focus on EVA Encapsulant

Double bond equivalent versus carbon number maps (DBE vs C#) are used to characterize this modification of encapsulant at the molecular level. To focus on the encapsulant, the major compound class HC is considered in **Figure 9** for the native and the different aging durations. O_1 and O_2 compound classes are also displayed in Figure S7, Supporting Information. These both compound classes are in a minority compared to the HC compound class, but they can also provide information on the polymer's state of degradation, particularly regarding oxidation. As described below (see **Figure 10**), these molecules do not correspond to complete EVA molecules but to small chains that were solubilized with the extraction process. For the native sample, molecules are observed between C10 and C70 with DBE values below 5. Significant differences are obtained after aging, regardless of the type of aging. Indeed, after aging, the distributions of HC, O_1, and O_2 compounds display molecules with higher DBE values up to 15 with both aging times. Major compounds after aging are separated by the C_5H_8 unit as discussed below (see Figure 10). For instance, distributions of HC compound class are almost identical between DH-2000 h and UV-2000 h, which underlines that the degradation of EVA occurs mainly by a loss of acetic acid on the vinyl acetate functions. It should be noted that the presence of O_1 and O_2 compounds could be coherent with Norrish III reaction forming ketones. Comparing both types of aging, it is interesting to note that these polyunsaturated markers are less abundant for UV-500 h and UV-1000 h. Indeed, for these two aging durations, major molecules are the same as those observed in the native sample. This trend is not observed for DH aging in which polyunsaturated markers are the most abundant molecules from DH-500 h. Although degradation of an EVA polymer seems to occur through deacetylation, these results highlight differences in aging kinetics with these two types of aging.

These aging kinetics are examined in detail with chemical class distributions in Figure 10. For DH and UV aging, the native HALS (O_4N_2) decreases from 60% to almost 10% of the relative natural abundance with UV and DH at 2000 h, underlining that it is consumed regardless of the aging conditions. Concerning the HC compound class, which mainly corresponds to the EVA degradation signals, the increase corresponds to the formation of the polyunsaturated markers through the deacetylation described above (Norrish II). The increase in relative abundance of this class is significantly greater in the DH (up to 65%) than in the UV (up to 45%). Concerning oxygen-containing compounds, it can be noticed that compound classes with more than 3 oxygen atoms only decrease in relative abundance with both types of aging. Furthermore, oxygen addition is not the major path of

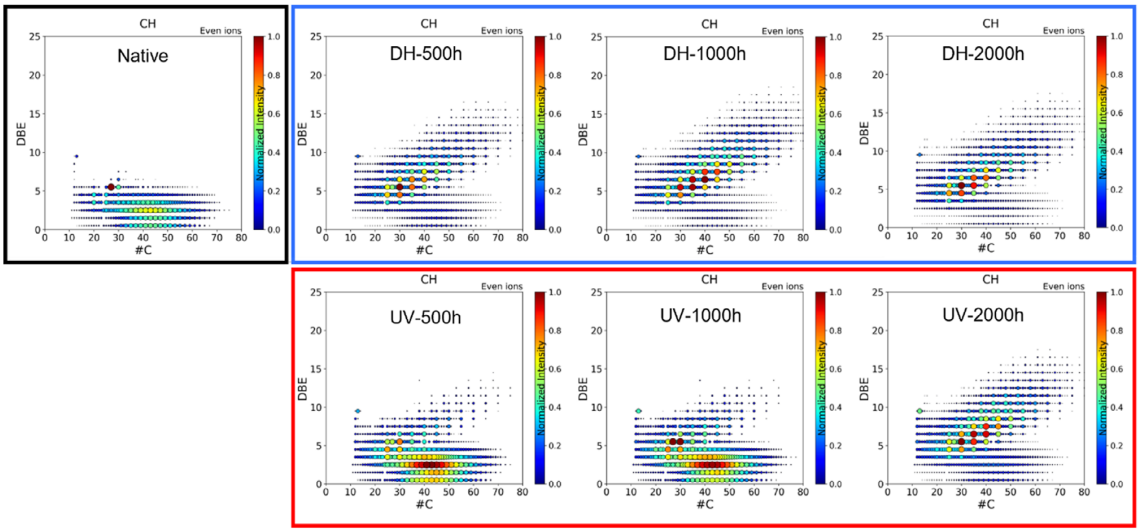

Figure 9. DBE versus C# maps of the HC compound class were obtained for the different mini-module samples.

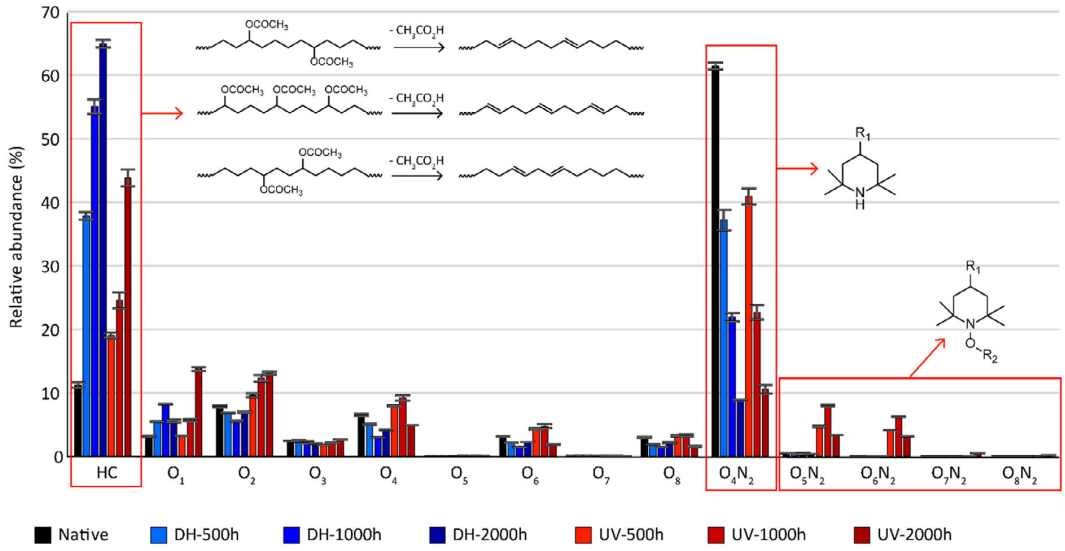

Figure 10. Compound class distributions were obtained with APCI(+)-Orbitrap data for the native and aged samples. Error bars are obtained from standard deviation calculated with the analytical triplicate. For the structure of HALS molecule, R_1 corresponds to the rest of the HALS molecule ($C_{19}H_{34}O_4N$) and R_2 group corresponds to an EVA degradation product.

EVA degradation. The O_4, O_6, and O_8 compound classes correspond to EVA molecules including 2,3, and 4 EVA units, respectively. These compound classes decreased with aging which further proves deacetylation as the major polymer degradation pathway. Only O_1 and O_2 compound classes increase in relative abundance with aging, especially in UV aging, which seems coherent with the formation of ketones or aldehydes (Norrish III). However, these classes are still in the minority compared to the HC class. Interestingly, the occurrence of $N_2O_{5\text{-}8}$ compound classes is observed in UV aging while they are not detected in the DH aging. Both N_2O_5 and N_2O_6 compound classes first occurred at UV-500 h, increased in relative abundance at UV-1000 h, and then decreased between UV-1000 h and UV-2000 h with the occurrence of $N_2O_{7\text{-}8}$. This could be correlated with the lower increase in EVA degradation products at UV-500 h and UV-1000 h compared to DH.

To investigate the difference between UV and DH aging, KMD plots representing all the data of each sample are plotted in **Figure 11**. These diagram uses are based on CH2 units to represent homologous compounds varying only by CH_2 addition on horizontal lines. KMD plots are widely used to represent polymer data obtained by mass spectrometry.[58–62] As annotated in Figure 11, the major compound obtained for each sample corresponds to the HALS, and this compound decreases significantly in relative abundance with aging for both DH and UV conditions. The N_2O_X compound classes can easily be observed for UV aging using this representation. These compounds seem to correspond to the interaction product between nitroxide from HALS and a piece of EVA degradation product. These products are then probably obtained by the trapping mechanism of HALS as it was described with the Denisov cycle (EVA-ON—NH). This suggests that the trapping mechanism of HALS did not occur in DH conditions. By correlating these observations with those obtained with the DBE versus C# maps focused on EVA degradation products, it can be assumed that the HALS reduced the EVA degradation in UV conditions, especially at UV-500 h and UV-1000 h of aging, as only a few EVA degradation products are observed. However, a decrease in the HALS efficiency seems to be observed from UV-2000 h as O_5N_2 and O_6N_2 compound classes decreased in relative abundance, and as the EVA degradation products significantly increased in relative abundance. As DH aging does not display any of these products, it evidences that the HALS does not work the same way in the presence of moisture. As the EVA degradation products are observed in significant abundance from the first point of aging at DH-500 h, it can be supposed that the HALS is deactivated in the presence of moisture or the absence of UV irradiation, preventing the trapping mechanism of HALS.

4. Summary of the Results and Discussion

In this study, three analytical techniques to investigate the aging of solar modules under DH and UV weathering conditions have been used. Macroscopically, the modules have been analyzed with *I–V* characterization and EL measurements. On the molecular level, the encapsulant (i.e., the EVA polymer and the HALS additive) was analyzed by EPR and orbitrap mass spectrometry. The results indicate a difference in the aging behavior of the solar modules under different weathering conditions as well as topological variations in the aging rate within the modules. The electrical performance decrease of the solar modules is related to the degradation of the passivation layer and the degradation of the encapsulant which leads to the corrosion of the electrical

ADVANCED SCIENCE NEWS
www.advancedsciencenews.com

Solar RRL
www.solar-rrl.com

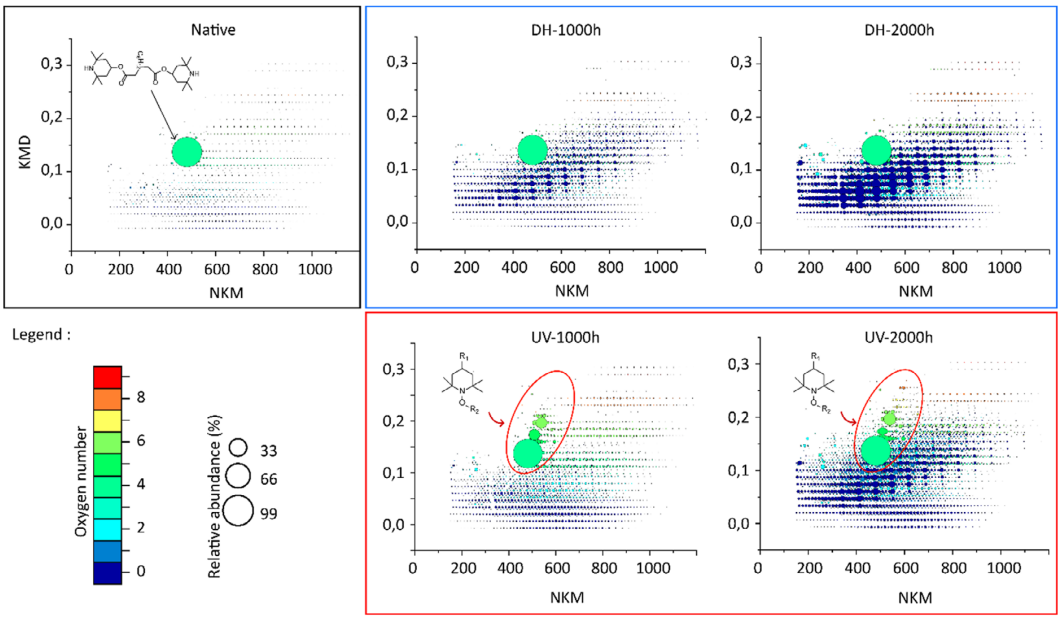

Figure 11. KMD plot obtained with APCI(+)-Orbitrap data for the native and aged samples. For the structure of HALS molecule, R_1 corresponds to the rest of the HALS molecule ($C_{19}H_{34}O_4N$) and R_2 group corresponds to an EVA degradation product.

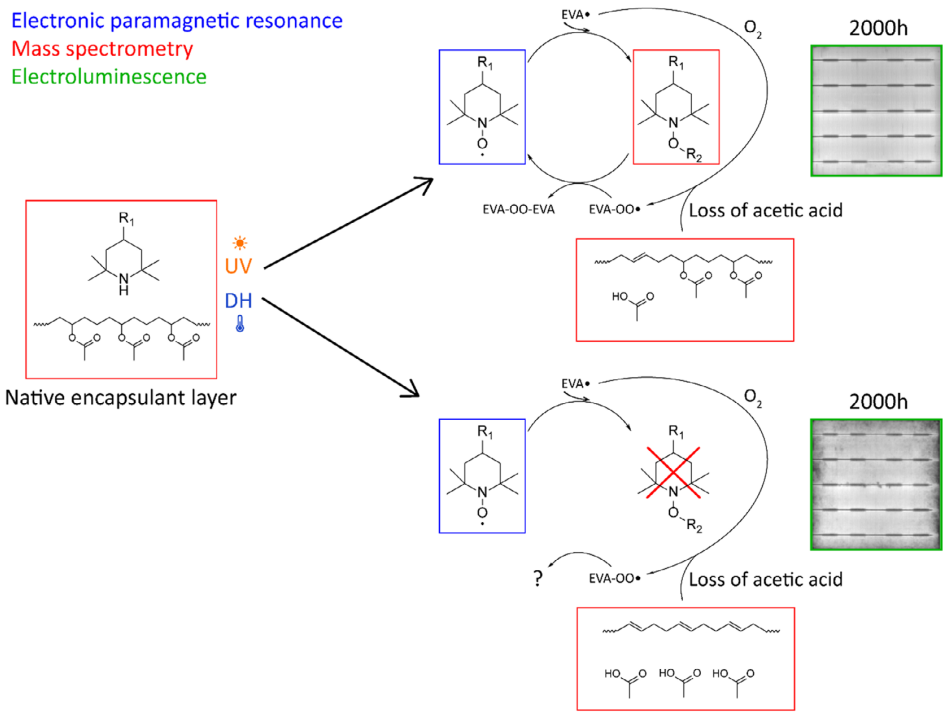

Figure 12. Summary diagram of the different results obtained with each technique for the two aging types. For the structure of HALS molecule, R_1 corresponds to the rest of the HALS molecule ($C_{19}H_{34}O_4N$), and R_2 group corresponds to an EVA degradation product.

contacts. Changes in short circuit current, maximum power output, open circuit voltage, fill factor, efficiency, and series resistance of the mini-modules exposed to UV and DH weathering were studied. UV weathering caused degradation of the passivation layer of the solar cell, while DH weathering caused a more severe degradation of the encapsulant resulting in the release of acetic acid and more pronounced contact damage (see Figure 1). EL measurements confirmed the difference in the degradation mechanisms between the two weathering conditions. It also indicated topological differences in the rate of performance loss, which was more pronounced at the edges (see Figure 2). This result was confirmed by the EPR analysis. For both aging conditions, a higher concentration of nitroxide was detected at the edges of the mini modules as compared to the center (see Figure 5 and 6), indicating faster aging at the edges.

Orbitrap mass spectrometry covers a wide range of molecular descriptors as it is displayed in **Figure 12**. Orbitrap results indicate that HALS native amine form is consumed at approximately equal rates for both weathering types. In reaction with free radicals of the autoxidation process, HALS are initially converted to stable nitroxide radicals (˙ON—NH) (see Figure 3). Quantification of nitroxide radicals by EPR spectroscopy showed that their concentration was lower in DH than in UV samples for all respective aging time points. This result suggested that HALS was engaged in different mechanisms in the two weathering conditions. Further transformation of HALS involves the reaction of nitroxide radical with a carbon-centered radical originating from autoxidation processes to yield alkoxyamine (EVA-ON---NH). Orbitrap mass spectrometry results confirmed the difference in the HALS functioning in the two aging conditions: polymer-grafted alkoxyamine intermediate was detected only in UV samples, suggesting uncommon HALS activity under DH conditions (see Figure 11 and 12). The common case of HALS activity with nitroxide peaking was detected at the edge of the mini-module under UV conditions (see Figure 5).[53]

Concerning EVA, degradation seemed to occur mainly through deacetylation for both aging conditions. However, the reason for the deacetylation is different. For UV weathering, this is caused by high-energy photons and Norrish-type reactions.[38,39] For DH weathering, the EVA is subject to hydrolysis.[40,41] Previous studies suggested that the autocatalytic deacetylation of EVA was responsible for the strong acetic acid formation, the discoloration of the encapsulants, and therefore also for the degradation of solar modules by corroding the electrical contacts.[36,63,64] Similar molecular distributions of polyunsaturated products of deacetylation were detected in both aging conditions by Orbitrap MS (see Figure 9).

However, a comparison of the relative abundance of these markers of deacetylation revealed their higher presence in DH samples (see Figure 10). Higher rates of deacetylation resulted in higher production of acetic acid that corroded contacts, and thus increased R_S and lowered P_{max} in DH samples (see Figure 1). EVA degradation under DH conditions seems to be autocatalytically hydrolysis driven[40,42] under realistic environmental conditions, in conjunction with radiation which generates more radicals,[24,28,39] this can lead to an increased degradation rate of the modules. Furthermore, moisture is probably required for the distribution of acetic acid in dry climates. If this is not the case, deacetylation itself has only minor effects on the module performance, as it was seen for the modules after UV weathering.

5. Conclusion

Although the separation of the vinyl acetate group could be confirmed as the main cause of EVA degradation for UV and DH weathering, the reasons and consequences for the respective solar modules are very different. Radicals created by photodegradation can be bound by the UV stabilizer under UV weathering and the effect on the encapsulant is only minimal. Minor reductions in the electrical parameters for this type of weathering result from the degradation of the cell or the passivation layers. However, the study carried out has shown that the UV stabilizer is hindered in its mechanism of action under DH weathering. Due to the lack of stabilization, the EVA could have strongly degraded under DH weathering by hydrolysis, although the energy introduced by the chamber temperature is significantly lower than photon energy from the UV range. The resulting acetic acid formation has subsequently led to corrosion of the contact fingers and thus to significant performance losses.

These findings can have far-reaching consequences for modules in the field. In very few climates can only one type of stressor be expected. This work and various literature sources have shown that additive-based stabilization of EVA is essential to ensure resistance to environmental influences. Consequently, further studies should investigate how antioxidants and amine-based stabilizers behave under combined stress conditions within the encapsulant in solar modules. Furthermore, hydrolysis of EVA is a serious problem for the lifetime of solar modules, the addition of hydrolysis-stabilizing additives in encapsulants should be considered. The microclimates created within such a module (e.g., by the diffusion of moisture) require a successive analysis of all components to understand the degradation behavior of the compound.

Supporting Information

Supporting Information is available from the Wiley Online Library or from the author.

Acknowledgements

R.H., N. B., and O.L.A. contributed equally to this work and share first authorship.

Open Access funding enabled and organized by Projekt DEAL.

Conflict of Interest

The authors declare no conflict of interest.

Data Availability Statement

The data that support the findings of this study are available from the corresponding author upon reasonable request.

ADVANCED SCIENCE NEWS
www.advancedsciencenews.com

Solar RRL
www.solar-rrl.com

Keywords

damp heat weathering, degradation, electron paramagnetic resonance, ethylene-vinyl acetate copolymer, mass spectrometry, ultraviolet stabilizer, ultraviolet weathering

Received: February 19, 2024
Revised: April 2, 2024
Published online:

[1] F. J. M. M. Nijsse, J.-F. Mercure, N. Ameli, F. Larosa, S. Kothari, J. Rickman, P. Vercoulen, H. Pollitt, *Nat. Commun.* **2023**, *14*, 6542.
[2] M. Aghaei, A. Fairbrother, A. Gok, S. Ahmad, S. Kazim, K. Lobato, G. Oreski, A. Reinders, J. Schmitz, M. Theelen, P. Yilmaz, J. Kettle, *Renewable Sustainable Energy Rev.* **2022**, *159*, 112160.
[3] D. C. Jordan, N. Haegel, T. M. Barnes, *Prog. Energy* **2022**, *4*, 022002.
[4] L. Koester, S. Lindig, A. Louwen, A. Astigarraga, G. Manzolini, D. Moser, *Renewable Sustainable Energy Rev.* **2022**, *165*, 112616.
[5] G. Oreski, J. S. Stein, G. C. Eder, K. Berger, L. Bruckman, R. French, J. Vedde, K. A. Weiß, *Prog. Energy* **2022**, *4*, 032003.
[6] M. Tao, V. Fthenakis, B. Ebin, B. Steenari, E. Butler, P. Sinha, R. Corkish, K. Wambach, E. S. Simon, *Prog. Photovoltaics* **2020**, *28*, 1077.
[7] M. Halwachs, L. Neumaier, N. Vollert, L. Maul, S. Dimitriadis, Y. Voronko, G. C. Eder, A. Omazic, W. Mühleisen, Ch Hirschl, M. Schwark, K. A. Berger, R. Ebner, *Renewable Energy* **2019**, *139*, 1040.
[8] A. Omazic, G. Oreski, M. Halwachs, G. C. Eder, C. Hirschl, L. Neumaier, G. Pinter, M. Erceg, *Sol. Energy Mater. Sol. Cells* **2019**, *192*, 123.
[9] B. Brune, I. Ortner, G. C. Eder, Y. Voronko, G. Oreski, K. A. Berger, K. Knöbl, L. Neumaier, M. Feichtner, *Prog. Photovoltaics* **2023**, *31*, 716.
[10] R. Heidrich, M. Lüdemann, A. Mordvinkin, R. Gottschalg, *IEEE J. Photovoltaics* January **2024**, *14*, 131.
[11] A. P. Patel, A. Sinha, G. Tamizhmani, *IEEE J. Photovoltaics* **2020**, *10*, 607.
[12] R. Heidrich, A. Mordvinkin, R. Gottschalg, in *2023 IEEE 50th Photovoltaic Specialists Conf. (PVSC)*, San Juan, PR, USA June **2023**, pp. 1–3.
[13] F. Prieto-Castrillo, N. Núñez, M. Vázquez, *Prog. Photovoltaics* **2020**, *28*, 1308.
[14] I. Kaaya, J. Ascencio-Vásquez, K.-A. Weiss, M. Topič, *Sol. Energy* **2021**, *218*, 354.
[15] A. Bala Subramaniyan, R. Pan, J. Kuitche, G. TamizhMani, *IEEE J. Photovoltaics* **2018**, *8*, 1289.
[16] IEC TS 62788-7-2, *Measurement Procedures for Materials used in Photovoltaic Modules - Part 7-2: Environmental Exposures - Accelerated Weathering Tests of Polymeric Materials*, International Electrotechnical Commission, Geneva, Switzerland **2017**.
[17] Terrestrial Photovoltaic (PV), *Modules – Design Qualification and Type Approval – Part 2: Test Procedures*, Vol. *IEC 61215-2:2021*, International Electrotechnical Committee, Geneva, Switzerland **2021**.
[18] K. Hara, *J. Photochem. Photobiol. A* **2022**, *425*, 113721.
[19] C. Peike, T. Kaltenbach, K.-A. Weiß, M. Koehl, *Sol. Energy Mater. Sol. Cells* **2011**, *95*, 1686.
[20] J. Lindroos, H. Savin, *Sol. Energy Mater. Sol. Cells* **2016**, *147*, 115.
[21] R. Asadpour, X. Sun, M. A. Alam, *IEEE J. Photovoltaics* **2019**, *9*, 759.
[22] A. Kraft, L. Labusch, T. Ensslen, I. Durr, J. Bartsch, M. Glatthaar, S. Glunz, H. Reinecke, *IEEE J. Photovoltaics* **2015**, *5*, 736.
[23] C. Barretta, G. Oreski, S. Feldbacher, K. Resch-Fauster, R. Pantani, *Polymers* **2021**, *13*, 271.
[24] R. Heidrich, C. Barretta, A. Mordvinkin, G. Pinter, G. Oreski, R. Gottschalg, *Sol. Energy Mater. Sol. Cells* **2024**, *266*, 112674.
[25] F. Pern, *Sol. Energy Mater. Sol. Cells* **1996**, *41–42*, 587.
[26] M. C. C. de Oliveira, A. S. A. Diniz Cardoso, M. M. Viana, V. de F. C. Lins, *Renewable Sustainable Energy Rev.* **2018**, *81*, 2299.
[27] M. Çopuroğlu, M. Şen, *Polym. Adv. Tech.* **2004**, *15*, 393.
[28] P. Klemchuk, M. Ezrin, G. Lavigne, W. Holley, J. Galica, S. Agro, *Polym. Degrad. Stab.* **1997**, *55*, 347.
[29] A. Jentsch, K.-J. Eichhorn, B. Voit, *Polym. Test.* **2015**, *44*, 242.
[30] R. Heidrich, A. Mordvinkin, R. Gottschalg, *Polym. Test.* **2023**, *118*, 107913.
[31] S. Stoll, A. Schweiger, *J. Magn. Reson.* **2006**, *178*, 42.
[32] M. Sueur, J. F. Maillard, O. Lacroix-Andrivet, C. P. Rüger, P. Giusti, H. Lavanant, C. Afonso, *J. Am. Soc. Mass Spectrom.* **2023**, *34*, 617.
[33] R. Witteck, B. Veith-Wolf, H. Schulte-Huxel, A. Morlier, M. R. Vogt, M. Köntges, R. Brendel, *Prog. Photovolt: Res. Appl.* **2017**, *25*, 409.
[34] V. Guiheneuf, F. Delaleux, S. Pouliquen, O. Riou, P.-O. Logerais, J.-F. Durastanti, *Sol. Energy* **2017**, *157*, 477.
[35] F. Ye, Y. Li, W. Deng, H. Chen, G. Liao, Z. Feng, N. Yuan, J. Ding, *Sol. Energy* **2018**, *170*, 1009.
[36] M. D. Kempe, G. J. Jorgensen, K. M. Terwilliger, T. J. McMahon, C. E. Kennedy, T. T. Borek, *Sol. Energy Mater. Sol. Cells* **2007**, *91*, 315.
[37] C. Peike, S. Hoffmann, P. Hülsmann, B. Thaidigsmann, K. A. Weiβ, M. Koehl, P. Bentz, *Sol. Energy Mater. Sol. Cells* **2013**, *116*, 49.
[38] F. J. Pern, *Angew. Makromol. Chem.* **1997**, *252*, 195.
[39] J. Jin, S. Chen, J. Zhang, *Polym. Degrad. Stab.* **2010**, *95*, 725.
[40] M. Patel, S. Pitts, P. Beavis, M. Robinson, P. Morrell, N. Khan, I. Khan, N. Pockett, S. Letant, G. Von White, A. Labouriau, *Polym. Test.* **2013**, *32*, 785.
[41] K. Hara, Y. Chiba, *J. Photochem. Photobiol. A* **2021**, *404*, 112891.
[42] B. Sultan, E. Sörvik, *J. Appl. Polym. Sci.* **1991**, *43*, 1737.
[43] M. Jankovec, F. Galliano, E. Annigoni, H. Y. Li, F. Sculati-Meillaud, L.-E. Perret-Aebi, C. Ballif, M. Topic, *IEEE J. Photovoltaics* **2016**, *6*, 1152.
[44] M. Jankovec, S. Mitterhofer, J. Slapsak, M. Topic, in *2020 47th IEEE Photovoltaic Specialists Conf. (PVSC)*, IEEE, Calgary, AB, Canada **2020**, pp. 1308–1312.
[45] M. Koehl, S. Hoffmann, S. Wiesmeier, *Prog. Photovoltaics Res. Appl.* **2017**, *25*, 175.
[46] J. Zhu, M. Koehl, S. Hoffmann, K. A. Berger, S. Zamini, I. Bennett, E. Gerritsen, P. Malbranche, P. Pugliatti, A. Di Stefano, F. Aleo, D. Bertani, F. Paletta, F. Roca, G. Graditi, M. Pellegrino, O. Zubillaga, F. J. C. Iranzo, A. Pozza, T. Sample, R. Gottschalg, *Prog. Photovoltaics Res. Appl.* **2016**, *24*, 1346.
[47] J. L. Hodgson, M. L. Coote, *Macromolecules* **2010**, *43*, 4573.
[48] S. Commereuc, S. Scheirs, V. Verney, J. Lacoste, *J. Appl. Polym. Sci.* **1998**, *69*, 1107.
[49] S. Commereuc, P. Lajoie, V. Verney, J. Lacoste, *Polym. Int.* **2003**, *52*, 576.
[50] K. A. Harrison, E. A. Haidasz, M. Griesser, D. A. Pratt, *Chem. Sci.* **2018**, *9*, 6068.
[51] E. Bordignon, in *eMagRes* (Eds: R. K. Harris, Wasylishen, R. L.)), John Wiley & Sons, Ltd, Chichester, UK **2017**, pp. 235–254.
[52] E. Etienne, A. Pierro, K. C. Tamburrini, A. Bonucci, E. Mileo, M. Martinho, V. Belle, *Molecules* **2023**, *28*, 1348.
[53] J. L. Gerlock, D. F. Mielewski, D. R. Bauer, *Polym. Degrad. Stab.* **1989**, *26*, 241.
[54] J. L. Gerlock, D. R. Bauer, L. M. Briggs, *Polym. Degrad. Stab.* **1986**, *14*, 53.
[55] J. Durmis, D. J. Carlsson, K. H. Chan, D. M. Wiles, *J. Polym. Sci. B Polym. Lett. Ed.* **1981**, *19*, 549.
[56] S. Jiang, K. Wang, H. Zhang, Y. Ding, Q. Yu, *Macro React. Eng.* **2015**, *9*, 522.
[57] B. K. Sharma, U. Desai, A. Singh, A. Singh, *J. Appl. Polym. Sci.* **2020**, *137*, 48268.

[58] H. Sato, S. Nakamura, K. Teramoto, T. Sato, *J. Am. Soc. Mass Spectrom.* **2014**, *25*, 1346.
[59] T. Fouquet, S. Nakamura, H. Sato, *Rapid Commun. Mass Spectrom.* **2016**, *30*, 973.
[60] T. Fouquet, H. Sato, *Mass Spectrom.* **2017**, *6*, A0055.
[61] T. N. J. Fouquet, R. B. Cody, Y. Ozeki, S. Kitagawa, H. Ohtani, H. Sato, *J. Am. Soc. Mass Spectrom.* **2018**, *29*, 1611.
[62] O. Lacroix-Andrivet, C. Castilla, C. Rüger, M. Hubert-Roux, A. L. Mendes Siqueira, P. Giusti, C. Afonso, *Energy Fuels* **2021**, *35*, 2165.
[63] A. W. Czanderna, F. J. Pern, *Sol. Energy Mater. Sol. Cells* **1996**, *43*, 101.
[64] G. A. Razuvaev, B. B. Troitskii, L. V. Chochlova, Z. B. Dubova, *J. Polym. Sci. B Polym. Lett. Ed.* **1973**, *11*, 521.

4. Quantification of polymer additives in photovoltaic encapsulants

In the previous chapter, a number of insights were gained into the degradation of solar modules as a function of UV or DH weathering. It was shown that the polymer degradation for both types of weathering is mainly due to the cleavage of the vinyl acetate group. However, this occurs in different ways (hydrolysis vs. Norrish reactions). Furthermore, it was observed that the UV stabilizer (HALS) follows the expected Denisov cycle under UV weathering. Under DH weathering, the HALS base molecule also degrades, but the working cycle of the UV stabilizer could not be detected. Since no hydrolysis stabilizers were used, the EVA is strongly degraded under DH weathering. Under UV weathering, the combination of UV absorber and UV stabilizer could significantly delay the degradation reactions of the encapsulant.

The previous publication has shown that the degradation of the encapsulant is strongly dependent on the additives contained. In order to investigate this dependence further and to derive possible degradation models, it is therefore necessary to quantify the embedded polymer additives. Currently, there is no suitable approach for quantifying polymer additives in the PV sector. Consequently, two methods for quantifying additives in PV encapsulants are presented below.

4.1. Quantification by pyrolysis gas chromatography mass spectrometry (PY-GCMS)

4.1.1. Quantification of UV additives in EVA and POE

Polymer Testing 118 (2023) 107913

Contents lists available at ScienceDirect

Polymer Testing

journal homepage: www.elsevier.com/locate/polytest

Quantification of UV protecting additives in ethylene-vinyl acetate copolymer encapsulants for photovoltaic modules with pyrolysis-gas chromatography-mass spectrometry

Robert Heidrich [a,b,*], Anton Mordvinkin [a], Ralph Gottschalg [a,b]

[a] Fraunhofer CSP, Otto-Eißfeldt-Straße 12, Halle (Saale), 06120, Germany
[b] Anhalt University of Applied Sciences, Bernburger Str. 55, Koethen (Anhalt), 06366, Germany

ARTICLE INFO

Keywords:
EVA
Additives
GC–MS
Qualitative analysis
Quantitative analysis
UV absorber
UV stabilizer

ABSTRACT

Reliability of polymeric encapsulants is being assured using suitable additives. Especially UV absorbers and UV stabilizers are important to protect the encapsulants from solar radiation. Identifying the additives and their quantities is essential for quality control and lifetime predictions. In this work a new method for quantitative additive characterization by pyrolysis-gas chromatography-mass spectrometry (PY-GCMS) is presented. A general workflow for qualitative analysis and additive quantification is proposed which is based on solvent-free sample preparation. A series of polymer film samples has been prepared with different additive concentrations for method development and validation. Using the two-step thermo desorption extraction all admixed additives can be detected. Furthermore, it was shown that the desorption behavior of the UV protecting additives dissolved in n-hexane strongly differs from the desorption of additives bound inside the polymer matrix. Thus, the use of reference samples is required for calibration. Finally, using verification samples as well as one commercial polymer film, the determination of the mass fractions of the studied UV absorber and UV stabilizer was shown to be possible with high accuracy. While this work is focused on ethylene-vinyl acetate copolymer (EVA) as encapsulant for photovoltaic modules, the derived methodology is very likely directly transferable to other encapsulant and additive compositions.

1. Introduction

Polymeric encapsulants find a broad field of application as protection against environmental influences. The photovoltaic (PV) industry has been using large amounts for many decades [1–3]. While the development of thermoplastic polyolefins (TPO) and polyolefin elastomers (POE) for photovoltaic applications is ongoing, the most common encapsulant in this field remains ethylene-vinyl acetate (EVA) [4–6]. Remarkably, the EVA composition did not change much over the past decades [1,2,7,8]. Czanderna and Pern addressed the challenges related to the use of EVA as encapsulant for PV purposes already in 1995. Nevertheless, it took many years until recent works finally drew attention to implications of EVA as encapsulant [2,9,10].

Typically, raw EVA is mixed with different additives enhancing properties and stability of the encapsulant [1,2,9]. The most important function is preventing the EVA from decomposition into acetic acid and formation of free radicals. This degradation mechanism is driven by the reaction of Norrish type 2 separating vinyl-acetate groups from the main polymer chain when a specific energy threshold is exceeded. This can be caused by the additional input of thermal or photon-induced (e.g., UV-irradiance) energy. In combination with moisture, the detached vinyl acetate forms acetic acid [2,11,12]. Acetic acid is known to corrode electrical contacts which leads to an increased series resistance of the solar module and subsequently to significant performance losses [13–16]. Apart from the corrosion of electrical contacts by acetic acid, the photothermal degradation of the polymer backbone leads to formation of chromophores resulting in browning of the encapsulant and therefore decreasing the module performance [11,17–20].

The main additives for suppressing photo-thermal degradation are UV absorbers and UV stabilizers. Typically, UV absorbers are hydroxybenzophenones which can absorb nearly all wavelengths below 300 nm. The mode of action of this class of UV absorbers involves keto-enol tautomerism reactions absorbing high energy irradiance and dissipating the energy afterwards [21–24]. On the other hand, UV stabilizers (e.g., hindered amine light stabilizers (HALS)) do not absorb UV light and therefore can be admixed with lower concentrations than UV absorbers. UV stabilizers interact with free radicals according to the

* Corresponding author at: Fraunhofer CSP, Otto-Eißfeldt-Straße 12, Halle (Saale), 06120, Germany.
E-mail address: robert.heidrich@csp.fraunhofer.de (R. Heidrich).

https://doi.org/10.1016/j.polymertesting.2022.107913
Received 25 November 2022; Received in revised form 21 December 2022; Accepted 22 December 2022
Available online 27 December 2022

Denisov cycle either trapping or converting them to stable, less harmful molecules [21,25]. It is common to combine both additive types in practice for a synergetic effect. However, UV absorbers and UV stabilizers can degrade over time forming structures unable to fulfill the original purpose any longer [22,23,25].

Determining the additive composition and content is crucial to understand chemical interactions in polymer films leading to solar module degradation. However, there is currently no practical possibility to quantify the total additive content in PV encapsulants. While successful quantification attempts of additives have been carried out in the past, they require different types of solvents for the extraction of additives from the polymer matrix [26,27]. UV/VIS measurements were carried out in the past to determine the relative degradation of UV-absorbers due to changes in the absorption spectrum, but no absolute quantification measurements could be made [22,23]. Recent approaches using different GC–MS methods yield good qualitative additive analysis, however, they are not able to quantify the total additive amount [6,28–31].

In this work, PY-GCMS is used to determine the total mass fraction of the UV absorber Cyasorb UV 531 and the HALS Tinuvin 770 in EVA films based on ELVAX 150 W. PY-GCMS in general is not a new technique and was already used to qualitatively characterize PV encapsulants [31,32]. However, a recent study shows that quantification attempts, especially when addressed to more than one additive at once, are a rare subject and were mostly carried out for plasticizers [33]. The described procedure is carried out exemplary for the mentioned additives and the base polymer but could be expandable to other compositions. In total 15 different additive compositions with 3 film samples per composition have been prepared to derive calibration functions for quantification and for validation measurements. Furthermore, a commercial EVA film was analyzed showing additive mass fractions in the expected scale. Every EVA film was at least measured with double determination, thus considering local inhomogeneities in the additive distribution. The obtained results can allow a quick and convenient quality control of formulations of any polymer film. Furthermore, the quantification opens diverse possibilities to gain insight into polymer degradation mechanism.

2. Materials and methods

2.1. Additives and EVA

The quantification process was carried out for the UV absorber Cyasorb UV 531 and the hindered amine light stabilizer (HALS) Tinuvin 770. The resulting calibration functions were obtained using EVA films of own production. Different mass fractions of the UV absorber and HALS were varied with respect to the reference composition c_0 displayed in Table 1. This composition is typical for EVA encapsulants and can be found elsewhere [1,7,8]. The absolute additive mass fractions and the corresponding suppliers are listed in the supporting information. ELVAX 150 W was chosen as a base polymer with a vinyl-acetate content of 32 wt% which is common for EVA encapsulants. The used EVA features a rather low melting point of 63 °C which allows processing temperatures in the kneader and the hydraulic press below temperatures at which peroxides become activated. Antioxidants have not been additionally formulated because the raw ELVAX 150 W granulate already contained one, namely butylated hydroxytoluene (BHT), as validated by GC–MS measurements (see Fig. 3).

2.2. EVA film preparation

Preparation of EVA film samples was realized with a kneader and a hydraulic press instead of the more common extrusion to ensure a homogeneous additive distribution inside the polymer matrix. Furthermore, this allows the preparation of smaller samples without wasting large amounts of chemicals for stabilization of the extrusion process.

Table 1
Reference composition c_0 for the EVA films of own production.

Name	Function	Per hundred gram EVA [g]	CAS number
ELVAX 150 W	EVA matrix		
Cyasorb UV 531	UV absorber	0.3	1843-05-6
Tinuvin 770	HALS	0.13	52829-07-9
Luperox TBEC	Crosslinking agent	1.5	34443-12-4
Perkalink 301	Crosslinking accelerator	2.5	1025-15-6
Silan A 174	Adhesion promoter	1.2	2530-85-0

The chemicals were precisely weighed and placed into small sample containers before the kneader was filled in a two-step process. For the first step, approximately 25 g EVA was admixed with all the additives in the corresponding concentration. In the second step, another approximately 25 g EVA was given to the same sample container to transfer additive residues from the sample container to the kneader. This was necessary because the crosslinking additives were liquid at room temperature and partially sticking to the bottom and the edges of the sample containers. The kneading was carried out in the Rheomix 3000 kneader with RheoDrive 7 as stirring unit at 70 °C with 50 rpm for 5 min. Pictures of the kneader and the resulting polymer mixture can be found in the supporting information.

After the samples have been removed from the kneader, they were transferred to a Rucks KV 192.00 hydraulic press. A metallic frame with 1 mm thickness in combination with a layer stack of 7×120 µm PTFE films ensured a polymer film thickness of approximately 160 µm after the pressing process. For every run 3 chunks of the polymer mixture were placed inside the frame and pressed at 50 bar and 70 °C for 6 min. Due to the relatively low preparation temperatures and short time spans it was assumed, that the crosslinking additives were not activated. This consideration was confirmed by later GC–MS analysis (see Fig. 3, especially in comparison with Fig. 6) verifying large quantities of unreacted Perkalink 301 and Luperox TBEC. Furthermore, DSC measurements of a commercial EVA film using the same crosslinking additives show that the reaction starts above 120 °C and are displayed in the supporting information. Pictures of the pressing process and resulting polymer films can be found in the supporting information.

2.3. PY-GC–MS sample preparation

PY-GCMS samples were prepared with a punch and a hammer. Typically, sample masses of approximately 2 mg to 4 mg were used and weighed with a Mettler Toledo XS205DU allowing a resolution of 0.01 mg with a repeatability of 0.02 mg. For this reason, the weighing error was neglected for all polymer film samples.

2.4. PY-GC–MS

For the qualitative and quantitative analysis of the polymer film formulations a combination of the 3-step thermo desorption in the pyrolysis chamber, gas chromatography and mass spectrometry was used.

An EGA/Py-3030D from Frontier Laboratories Ltd. with the attached autosampler AS-1020E was used for a two-step thermo desorption and subsequent pyrolysis. As a carrier gas a constant flux of He was ensured. The first thermo desorption was carried out at a starting temperature of 100 °C and held for 3 min. After the first GC–MS measurement, the second thermo desorption step starting at 100 °C and increasing temperature with 30 °C/min until reaching the target temperature of 300 °C was executed. For the pyrolysis step, the samples were treated with 600 °C for 0.2 min, while this step was only performed to flush the column and remove residues from the system. The interface temperature at the inlet of the pyrolysis chamber was chosen to be 100 °C higher than the corresponding desorption temperature, respectively.

All desorption steps were carried out with help of a selective sampler SS-1010E from Frontier Laboratories Ltd. which prevents column contamination by undesirable fragmented components. Furthermore, a cryo-trap MJT-1035E can be used allowing a more precise separation of volatile components in the column.

Gas chromatograph was a Trace 1300 from Thermo Scientific with a He carrier gas. An Ultra ALLOY Capillary Column (length 30 m, internal diameter 0.25 mm, film thickness 0.25 μm) from Frontier Laboratories Ltd.was used for the separation of substances. For the different desorption steps, the following parameters have been used:

- first desorption: GC inlet temperature 280 °C; column flow 1.2 ml/min; purge flow 5 ml/min; split flow 25 ml/min; oven temperature at start 40 °C and hold for 1 min, then heating with 10 °C/min to 325 °C with subsequent plateau time of 20 min
- second desorption: GC inlet temperature 280 °C; column flow 1.2 ml/min; purge flow 5 ml/min; split flow 50 ml/min; oven temperature at start 40 °C and hold for 1 min, then heating with 10 °C/min to 325 °C with subsequent plateau time of 20 min
- pyrolysis: GC inlet temperature 280 °C; column flow 1.2 ml/min; purge flow 3 ml/min; split flow 50 ml/min; oven temperature at start 40 °C and hold for 2 min, then heating with 20 °C/min to 320 °C with subsequent plateau time of 14 min

An ISQ 7000 mass spectrometer from Thermo Scientific was coupled to the gas chromatograph. The m/z range was set from 29 to 800. The electron energy was set to 70 eV with an initial detector gain of 3×10^5. As an internal MS tune substance FC43 ($C_{12}F_{27}N$) was used while the corresponding $m/z = 219$ peak was tuned to an intensity of 2×10^7 for the quantification normalization. As a result, depending on the ion source condition the later detector gain varied between 1.8×10^5 to 2.8×10^5. The MS transfer line temperature was fixed at 320 °C with a ion source temperature of 300 °C. For the evaluation of different mass spectra, the database of the National Institute of Standards and Technology (NIST) was used.

3. Results and discussion

The MS was tuned before every measurement series for all measured pure substances or film formulations as it was described in Section 2 enabling the normalization of intensity values. In general, intensity values are defined as a peak area with the resulting units [counts/min]. All measured intensities have been normalized to the calibration value of the $m/z = 219$ ratio. This value was chosen for the sake of simplicity because Cyasorb UV 531 has a significant peak at $m/z = 213$. Thus, the transformation of all the intensities to a manageable scale for data evaluation was enabled. However, it should be mentioned that the intensities are strongly dependent on the condition of the ion source and the used MS parameters. To address this point, the dependence of measured intensities on different states of the ion source is displayed in the supporting information. All investigated substances produce MS spectra with a variety of different m/z ratios. The resulting shift of all these intensities by small changes of the ion source parameters (for instance due to residues) makes the use of calibration samples indispensable.

The quantification procedure was developed using the prepared EVA films as described in Section 2. Although first attempts using pure substance additives showed a linear dependence of the MS intensity and analyzed sample mass, they did not lead to a sufficient accuracy in the additive quantification. On the one hand the missing matrix interaction of the polymer backbone resulted in generally higher MS intensities in dependence on the analyzed additive. On the other hand, these values could not be corrected due to a missing reference. Therefore, the requirement of an offset correction forced a different approach. All the results regarding the pure substance measurements and the derived linear calibration functions can be found in the supporting information.

While the linear dependence between the additive mass fraction and MS intensity was shown for pure substances it cannot be directly employed for film samples due to interactions with the polymer matrix yielding increased binding energies. Instead, the initial calibration function obtained using polymer film samples was analyzed for linearity and employed as a first estimate which was later corrected by the reference samples.

Typically, quantitative GC–MS measurements use an internal standard for calibration which is partially adapted here. However, it is not possible to mix reference samples with known formulation and unknown samples in the same sample cup because one cannot distinguish if the additives are desorbing from the reference sample or the sample one wants to analyze. Also, using a single reference substance as an internal standard would miss the required matrix interactions and is not preferable. Therefore, the calibration samples must be measured separately. After sample preparation the calibration samples were analyzed between the unknown samples within one measurement series ensuring equal MS conditions.

Fig. 1 demonstrates the general workflow for the additive quantification of unknown polymer film samples. The subsequent chapters will address the different displayed steps for the quantification process. At first, the linear, initial calibration function estimates will be derived with polymer film samples with different additive concentrations. This step is only necessary once to ensure the linear dependence of the additive mass fraction and the MS intensity and can be presupposed for later measurements. Secondly, a qualitative analysis of the unknown samples will be carried out. Thirdly, the offset correction will be used to adjust the calibration function estimates for quantification. Then, the quantitative analysis will be carried out for verification film samples and one commercial EVA film.

3.1. Initial calibration function

Deriving an initial calibration function and examining the linear dependence of the MS intensity on the absolute mass fraction of the analyzed additive was realized by 10 different polymer film compositions. After extraction from the kneader, 3 samples of every concentration were put into the hydraulic press to build film samples. To account for local inhomogeneities, double PY-GCMS measurements of every film sample were performed. Therefore, a total of 6 samples for every concentration was prepared for the quantification purpose. Samples of around 1.5 mg to 4 mg were weighed in the Py-GCMS setup.

Due to the preparation process, it was not possible to weigh in equal sample masses within one concentration. This results in additional measurement points rather than a combination of mean values and statistical errors. The results are visualized in Fig. 2, while the corresponding calibration functions were fitted with the least-squares method leading to $f_C(m)$ for Cyasorb UV 531 and $f_T(m)$ for Tinuvin 770. The corresponding chromatogram can be seen in Fig. 3. Here, the Cyasorb UV 531 and Tinuvin 770 signals occur at approximately 27 min and 30 min, respectively.

$$f_C(m) = 9.2217 \cdot 10^2 \left[\frac{1}{\text{mg}}\right] \cdot m + 1.3649 \cdot 10^{-1} \quad (1)$$

$$f_T(m) = 6.8446 \cdot 10^2 \left[\frac{1}{\text{mg}}\right] \cdot m + 5.0440 \cdot 10^{-1} \quad (2)$$

In contrast to the pure substance measurements of Cyasorb UV 531 (see supporting information), all m/z ratios were used for the film samples. Compared to the previously derived calibration functions for pure substances, the slope is significantly smaller which is a result of less detected molecules extracted from the polymer matrix. This indicates that matrix interactions always should be considered. However, the intensity dependence remains linear allowing the use of calibration film samples for quantification.

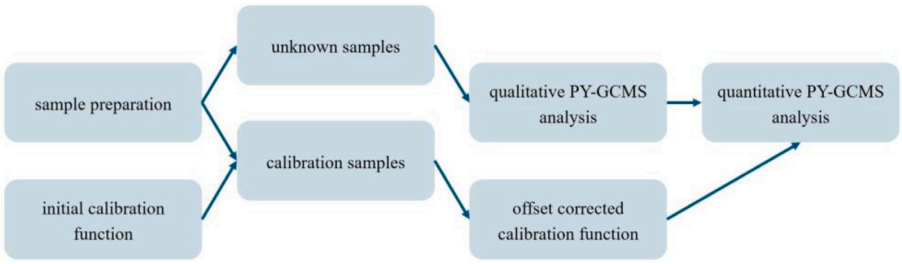

Fig. 1. Flowchart of the additive quantification process. Calibration samples were measured in between the unknown samples allowing an adjustment of the initial calibration function, obtained by polymer film samples with different additive concentrations.

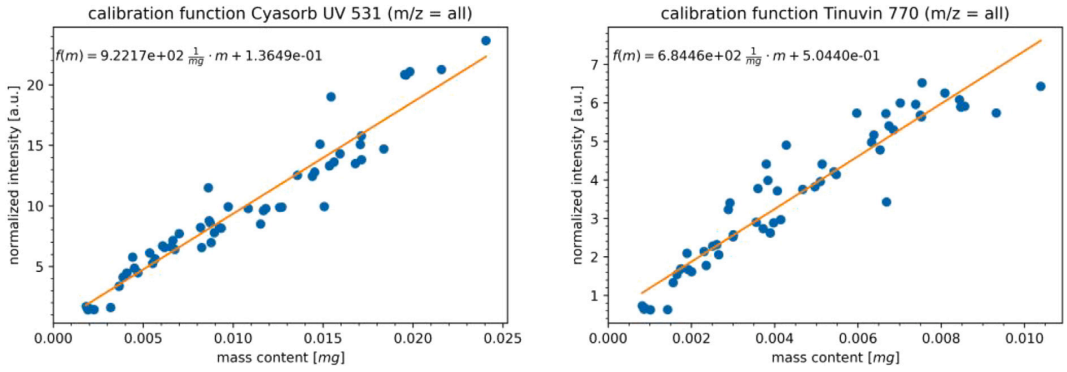

Fig. 2. Calibration functions for Cyasorb UV 531 (left) and Tinuvin 770 (right) based on EVA film samples. For Cyasorb UV 531 and Tinuvin 770 all m/z ratios were used for evaluation.

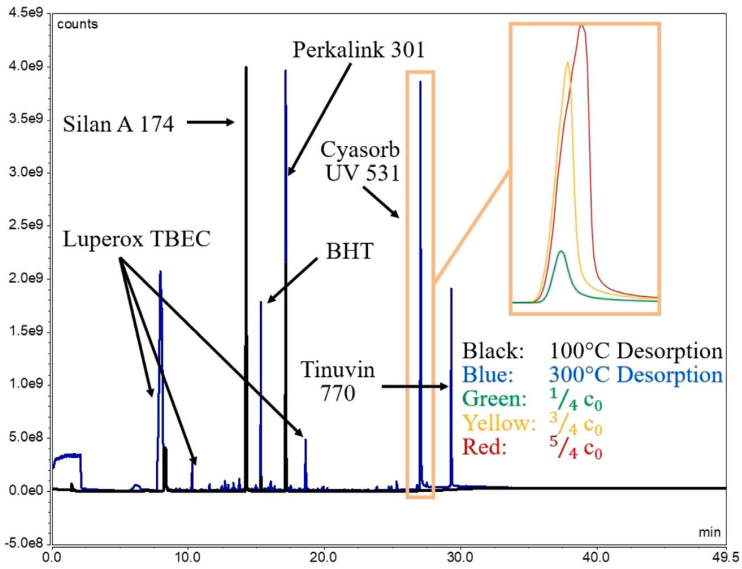

Fig. 3. Chromatogram and extracted additives of an exemplary EVA film prepared as described in Section 2. The used desorption temperatures are color coded. Furthermore, the Cyasorb UV 531 peak intensity is exemplary displayed for different additive compositions.

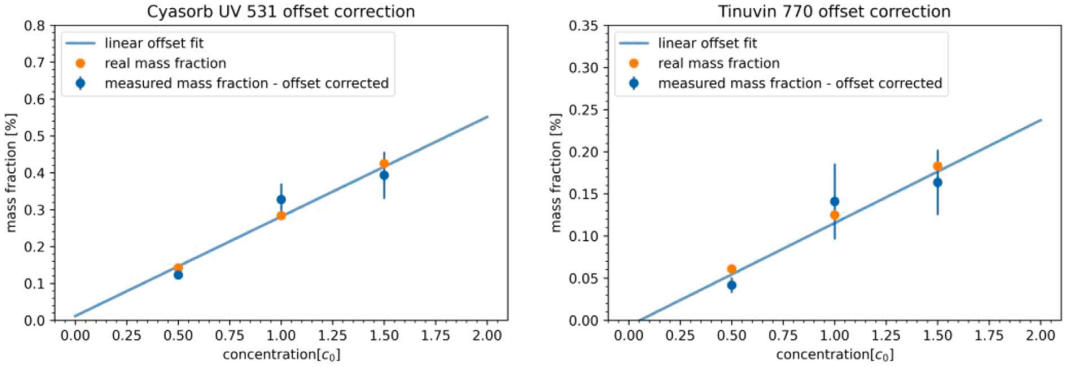

Fig. 4. Offset correction for quantification of Cyasorb UV 531 (left) and Tinuvin 770 (right) using polymer films with known additive density.

3.2. Qualitative analysis

The chromatogram resulting from the analyzed polymer films is shown in Fig. 3. All the additives listed in Table 1 are detectable after the extraction at the two desorption temperatures. Furthermore, for Cyasorb UV 531 an exemplary peak comparison for different additive contents is displayed. However, these peaks are not normalized to the sample mass at this point which explains the comparatively low difference between $3/4c_0$ and $5/4c_0$.

3.3. Offset correction

Fig. 4 shows the offset correction for the carried out quantification of Cyasorb UV 531 and Tinuvin 770. The abscissa shows the additive concentration in units of composition c_0 (see Table 1) while the corresponding additive mass fraction in the polymer film is represented in the ordinate. Here, $1/2c_0$, $1c_0$ and $3/2c_0$ were used for offset adjustments.

The initial calibration function estimates f_C and f_T were adjusted until the linear fit of the measured points was in good accordance with the inherent mass fractions. The offset correction resulted in the offset corrected calibration functions $f_{C_{oc}}$ and $f_{T_{oc}}$:

$$f_{C_{oc}}(m) = 1.4 \cdot 10^3 \left[\frac{1}{\mathrm{mg}}\right] \cdot m - 3.5 \tag{3}$$

$$f_{T_{oc}}(m) = 1.0 \cdot 10^3 \left[\frac{1}{\mathrm{mg}}\right] \cdot m - 0.3 \tag{4}$$

These functions were applied calculating the additive mass fractions mf of the calibration film samples using the linear standard expression, the weighed samples mass m_s and the determined absolute additive mass m

$$f(m) = tm + n \quad \text{and therefore} \quad mf = \frac{m}{m_s} = \frac{f(m) - n}{t} \cdot \frac{1}{m_s}. \tag{5}$$

As displayed as blue points in the graph, the results are showing good accordance with the real admixed mass fractions. In the next step, the adjusted calibration functions can be used to determine the additive content of unknown samples which have been measured in the same series as the calibration samples.

3.4. Quantitative analysis and validation

To validate the new quantification method another set of polymer film samples was prepared. 5 different compositions ($1/3c_0$, $2/3c_0$, c_0, $4/3c_0$, $5/3c_0$) with 3 films each were measured for the quantification purpose. The compositions are displayed in detail in the supporting information.

Fig. 5 displays the quantification results. The measurement points are mean values of the examined film samples while the error bar indicates the standard deviation. Investigating the measured mass fractions, the deviations from the real mass fractions are very small for Cyasorb UV 531. A comparatively high standard deviation for Tinuvin 770 is probably caused by inhomogeneities in the polymer film samples. Already the calibration samples for offset correction showed that the mixing of Tinuvin 770 for concentrations of $1c_0$ and above could be improved due to the relatively high standard deviation. Apart from the mentioned point, it is possible that molecules like Tinuvin 770 could change their desorption behavior above a critical concentration due to changing interactions with the polymer matrix. However, especially for mass fractions of $1c_0$ and below (i.e., the common use case for commercial EVA films), the measurements allow meaningful interpretations for further applications. In contrast to the results by pure substance measurements (see supporting information), the calibration functions based on polymer films produce values which are in accordance with the real mass fractions after offset correction.

Apart from the validation film samples, one commercial EVA film was evaluated in triple determination for independent validation. The resulting chromatogram is displayed in Fig. 6. The examined encapsulant film was laminated which explains the comparatively low peak intensity of the crosslinking additives and the adhesion promoter. However, the commercial EVA film shows the same additive composition as the samples of own production. Using the same reference samples for additive quantification as for the validation samples, the additive mass fraction of Cyasorb UV 531 was determined to be 0.277% and 0.073% for Tinuvin 770. In comparison with Table 1 where Cyasorb is listed with 0.284% and Tinuvin 770 with 0.123%, both additives are quantified in the expected scale. It must be mentioned that the admixed additive quantities can strongly vary between commercial samples. However, these results proof the possibility of the absolute UV additive quantification in commercial EVA films.

4. Conclusion

PY-GCMS measurements have been utilized to determine the mass fractions of the UV absorber Cyasorb UV 531 and the UV stabilizer Tinuvin 770 inside polymer films. While it is not possible to calibrate the Py-GCMS measurements by using only pure substances, the calibration functions developed from polymer films with subsequent offset correction show good accordance with the validation films. It was possible to quantify both UV additives within one measurement. Furthermore, the qualitative PY-GCMS analysis shows that all admixed additives can be detected with the used setup parameters. These results indicate that it is in principle possible to determine the content of

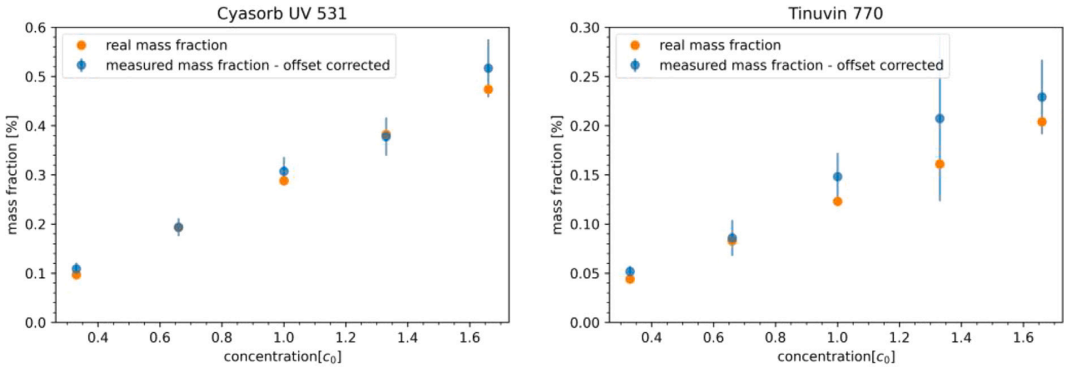

Fig. 5. Measured and real UV-absorber and UV-stabilizer mass fractions based on the EVA film sample derived calibration functions.

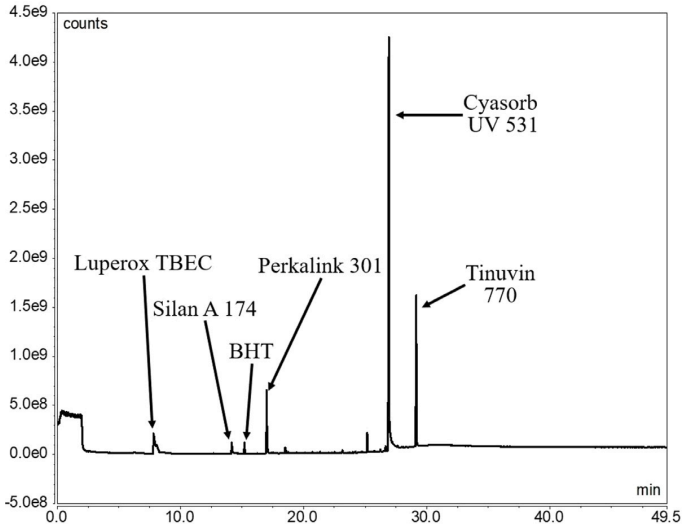

Fig. 6. Chromatogram and extracted additives of a commercial EVA film. Only the 300 °C desorption is displayed.

several additives within one measurement series using PY-GCMS. Nevertheless, the limitations of the measurement method have not yet been fully analyzed. In particular, limiting concentrations for the assumption of linearity should be investigated in the future. Further studies should investigate the possibility of additive quantification for different kinds of UV absorbers, HALS and antioxidants which are commonly used in PV encapsulants. In addition, cryogrinding should be considered as a possible approach for sample preparation. The resulting surface enlargement could improve the desorption behavior of the additives and reduce the influence of inhomogeneities. Therefore, the displayed results should be taken as a proof of concept stimulating the quantification of different kinds of additives. As an additional application, the amount of crosslinking additives before and after lamination could be studied as it has high influence on the degradation behavior of solar modules [34]. In general, these results allow various applications for developing additive diffusion models, solar module degradation models and quality control. Especially, analyzing encapsulants before manufacturing could prevent failures within the solar module lifetime.

CRediT authorship contribution statement

Robert Heidrich: Carried out the experiments, Analyzed the data, Discussed the results, Writing – original draft, Reviewed the manuscript. **Anton Mordvinkin:** Discussed the results, Reviewed the manuscript. **Ralph Gottschalg:** Discussed the results, Reviewed the manuscript.

Declaration of competing interest

The authors declare that they have no known competing financial interests or personal relationships that could have appeared to influence the work reported in this paper.

Data availability

Data will be made available on request.

Acknowledgments

We acknowledge support by the German Research Foundation (Deutsche Forschungsgemeinschaft DFG) - project number 491460386 - and the Open Access Publishing Fund of Anhalt University of Applied Sciences, Germany. Furthermore, we acknowledge funding by TotalEnergies.

Appendix A. Supplementary data

Supplementary material related to this article can be found online at https://doi.org/10.1016/j.polymertesting.2022.107913.

References

[1] E. Cuddihy, C. Coulbert, A. Gupta, R. Liang, Electricity from Photovoltaic Solar Cells: Flat-Plate Solar Array Project Final Report. Volume VII: Module Encapsulation, NASA, 1986.
[2] A. Czanderna, F. Pern, Encapsulation of PV modules using ethylene vinyl acetate copolymer as a pottant: A critical review, Sol. Energy Mater. Sol. Cells 43 (2) (1996) 101–181.
[3] G. Oreski, A. Omazic, G.C. Eder, Y. Voronko, L. Neumaier, W. Mühleisen, C. Hirschl, G. Ujvari, R. Ebner, M. Edler, Properties and degradation behaviour of polyolefin encapsulants for photovoltaic modules, Prog. Photovolt., Res. Appl. 28 (12) (2020) 1277–1288, http://dx.doi.org/10.1002/pip.3323.
[4] B. Adothu, F.R. Costa, S. Mallick, Damp heat resilient thermoplastic polyolefin encapsulant for photovoltaic module encapsulation, Sol. Energy Mater. Sol. Cells 224 (2021) 111024, http://dx.doi.org/10.1016/j.solmat.2021.111024.
[5] G. Oreski, A. Omazic, G.C. Eder, Y. Voronko, L. Neumaier, W. Mühleisen, C. Hirschl, G. Ujvari, R. Ebner, M. Edler, Properties and degradation behaviour of polyolefin encapsulants for photovoltaic modules, Prog. Photovolt., Res. Appl. 28 (12) (2020) 1277–1288, http://dx.doi.org/10.1002/pip.3323.
[6] C. Barretta, G. Oreski, S. Feldbacher, K. Resch-Fauster, R. Pantani, Comparison of degradation behavior of newly developed encapsulation materials for photovoltaic applications under different artificial ageing tests, Polymers 13 (2) (2021) http://dx.doi.org/10.3390/polym13020271.
[7] A. Beinert, C. Peike, I. Dürr, M.D. Kempe, G. Reiter, K.-A. Weiß, The influence of the additive composition on degradation induced changes in poly (ethylene-co-vinyl acetate) during photochemical aging, in: 29th European PV Solar Energy Conference and Exhibition, Amsterdam, 2014.
[8] C. Peike, L. Purschke, K.-A. Weiss, M. Köhl, M. Kempe, Towards the origin of photochemical EVA discoloration, in: 2013 IEEE 39th Photovoltaic Specialists Conference, PVSC, IEEE, 2013, pp. 1579–1584.
[9] A. Omazic, G. Oreski, M. Halwachs, G.C. Eder, C. Hirschl, L. Neumaier, G. Pinter, M. Erceg, Relation between degradation of polymeric components in crystalline silicon PV module and climatic conditions: A literature review, Sol. Energy Mater. Sol. Cells 192 (2019) 123–133, http://dx.doi.org/10.1016/j.solmat.2018.12.027.
[10] M. Halwachs, L. Neumaier, N. Vollert, L. Maul, S. Dimitriadis, Y. Voronko, G.C. Eder, A. Omazic, W. Mühleisen, C. Hirschl, M. Schwark, K.A. Berger, R. Ebner, Statistical evaluation of PV system performance and failure data among different climate zones, Renew. Energy 139 (2019) 1040–1060, http://dx.doi.org/10.1016/j.renene.2019.02.135.
[11] F. Pern, Ethylene-vinyl acetate (EVA) encapsulants for photovoltaic modules: Degradation and discoloration mechanisms and formulation modifications for improved photostability, in: Die Angewandte Makromolekulare Chemie: Applied Macromolecular Chemistry and Physics, Vol. 252. No. 1, Wiley Online Library, 1997, pp. 195–216.
[12] M.C.C. de Oliveira, A.S.A. Diniz Cardoso, M.M. Viana, V. de Freitas Cunha Lins, The causes and effects of degradation of encapsulant ethylene vinyl acetate copolymer (EVA) in crystalline silicon photovoltaic modules: A review, Renew. Sustain. Energy Rev. 81 (2018) 2299–2317, http://dx.doi.org/10.1016/j.rser.2017.06.039, URL https://www.sciencedirect.com/science/article/pii/S1364032117309851.
[13] C. Peike, S. Hoffmann, P. Hülsmann, B. Thaidigsmann, K.A. Weiß, M. Koehl, P. Bentz, Origin of damp-heat induced cell degradation, Sol. Energy Mater. Sol. Cells 116 (2013) 49–54, http://dx.doi.org/10.1016/j.solmat.2013.03.022.
[14] H. Xiong, C. Gan, X. Yang, Z. Hu, H. Niu, J. Li, J. Si, P. Xing, X. Luo, Corrosion behavior of crystalline silicon solar cells, Microelectron. Reliab. 70 (2017) 49–58.
[15] M.D. Kempe, G.J. Jorgensen, K.M. Terwilliger, T.J. McMahon, C.E. Kennedy, T.T. Borek, Acetic acid production and glass transition concerns with ethylene-vinyl acetate used in photovoltaic devices, Sol. Energy Mater. Sol. Cells 91 (4) (2007) 315–329, http://dx.doi.org/10.1016/j.solmat.2006.10.009.
[16] U. Weber, R. Eiden, C. Strubel, T. Soegding, M. Heiss, P. Zachmann, K. Nattermann, H. Engelmann, A. Dethlefsen, N. Lenck, Acetic acid production, migration and corrosion effects in ethylene-vinyl-acetate-(EVA-) based PV modules, in: 27th European Photovoltaic Solar Energy Conference and Exhibition, 2012, pp. 2992–2995.
[17] F. Pern, S. Glick, A. Czanderna, EVA encapsulants for PV modules: reliability issues and current R&D status at NREL, Renew. Energy 8 (1–4) (1996) 367–370.
[18] D. Berman, D. Faiman, EVA browning and the time-dependence of I–V curve parameters on PV modules with and without mirror-enhancement in a desert environment, Sol. Energy Mater. Sol. Cells 45 (4) (1997) 401–412, http://dx.doi.org/10.1016/S0927-0248(96)00087-6.
[19] D. Berman, S. Biryukov, D. Faiman, EVA laminate browning after 5 years in a grid-connected, mirror-assisted, photovoltaic system in the Negev desert: effect on module efficiency, Sol. Energy Mater. Sol. Cells 36 (4) (1995) 421–432, http://dx.doi.org/10.1016/0927-0248(94)00198-7.
[20] W.H. Holley, S.C. Agro, J.P. Galica, L.A. Thoma, R.S. Yorgensen, M. Ezrin, P. Klemchuk, G. Lavigne, Investigation into the causes of browning in EVA encapsulated flat plate PV modules, in: Proceedings of 1994 IEEE 1st World Conference on Photovoltaic Energy Conversion - WCPEC, a Joint Conference of PVSC, PVSEC and PSEC, IEEE, 1994, pp. 893–896, http://dx.doi.org/10.1109/WCPEC.1994.520105.
[21] F.P. Cortolano, Antioxidants and UV stabilizers: A summary of their utilization in PVC, J. Vinyl Technol. 15 (2) (1993) 69–75.
[22] F. Pern, Factors that affect the EVA encapsulant discoloration rate upon accelerated exposure, Sol. Energy Mater. Sol. Cells 41 (1996) 587–615.
[23] J.E. Pickett, J.E. Moore, Photodegradation of UV absorbers: kinetics and structural effects, in: Die Angewandte Makromolekulare Chemie: Applied Macromolecular Chemistry and Physics, Vol. 232, No. 1, Wiley Online Library, 1995, pp. 229–238.
[24] F. Pern, S. Glick, A. Czanderna, Review of the photothermal stability of EVA pottants: Effects of formulation on the discoloration rate and mitigation methods, in: AIP Conference Proceedings, Vol. 462, No. 1, American Institute of Physics, 1999, pp. 599–604.
[25] J.L. Hodgson, M.L. Coote, Clarifying the mechanism of the Denisov cycle: how do hindered amine light stabilizers protect polymer coatings from photo-oxidative degradation? Macromolecules 43 (10) (2010) 4573–4583.
[26] M. Monteiro, C. Nerín, C. Rubio, F. Reyes, A GC/MS method for determining UV stabilizers in polyethyleneterephthalate bottles, J. High Resol. Chromatogr. 21 (5) (1998) 317–320.
[27] T. Riley, T. Prater, J. Gerlock, J. DeVries, D. Schuetzle, Quantitative determination of paint additives with fast atom bombardment mass spectrometry, Anal. Chem. 56 (12) (1984) 2145–2147.
[28] S.-H. Im, S.-S. Choi, Analysis of polymeric UV absorber (Tinuvin 213) using LDI-TOFMS: Solvent effect in sample preparation, Bull. Korean Chem. Soc. 32 (6) (2011) 2093–2096.
[29] C.W. Klampfl, M. Himmelsbach, Advances in the determination of hindered amine light stabilizers–A review, Anal. Chim. Acta 933 (2016) 10–22.
[30] Y. Zhang, Z. Du, A. Li, A. Tu, W. Yu, J. Zou, Rapid qualitative and semi-quantitative determination of polymer additives in polymer matrix by electrospray ionization-triple quadrupole mass spectrometry with accelerated solvent extraction (ASE–ESI-MS/MS), Anal. Methods 5 (19) (2013) 5112–5120.
[31] I. Hintersteiner, L. Sternbauer, S. Beissmann, W.W. Buchberger, G.M. Wallner, Determination of stabilisers in polymeric materials used as encapsulants in photovoltaic modules, Polym. Test. 33 (2014) 172–178, http://dx.doi.org/10.1016/j.polymertesting.2013.12.004.
[32] C. Perez Locas, V.A. Yaylayan, Isotope labeling studies on the formation of 5-(hydroxymethyl)-2-furaldehyde (HMF) from sucrose by pyrolysis-GC/MS, J. Agricult. Food Chem. 56 (15) (2008) 6717–6723, http://dx.doi.org/10.1021/jf8010245.
[33] F. Akoueson, C. Chbib, S. Monchy, I. Paul-Pont, P. Doyen, A. Dehaut, G. Duflos, Identification and quantification of plastic additives using pyrolysis-GC/MS: A review, Sci. Total Environ. 773 (2021) 145073, http://dx.doi.org/10.1016/j.scitotenv.2021.145073.
[34] G. Oreski, A. Rauschenbach, C. Hirschl, M. Kraft, G. Eder, G. Pinter, Crosslinking and post-crosslinking of ethylene vinyl acetate in photovoltaic modules, J. Appl. Polym. Sci. 134 (23) (2017).

POE

Following the same principle as in the previous publication, the procedure was extended to POE encapsulants. In addition, the PY-GCMS method was simplified to a one-step method so that only the second thermo desorption step from the previous work was used. The films were prepared as described in the previous chapter (and shown in Appendix B). However, DOW ENGAGE PV 8669 was used as the polymer matrix, which is an ethylene-octene copolymer. The additive mass contents used in the different POE films are listed in Appendix C and are similar to the values from the previous chapter. Since the quantification principle was validated with the previous publication, only 6 different concentrations were produced for the POE encapsulant. Of these concentrations, 3 were used to determine the calibration curve, and 3 were used for validation.

Figure 22 shows the offset correction described in the previous publication for the samples $1/4c_0$, $3/4c_0$ and $5/4c_0$ for the UV absorber Cyasorb UV 531 and the UV stabilizer Tinuvin 770. An additional measuring point at $0c_0$ was generated by assuming that the signal intensity must correspond to 0.

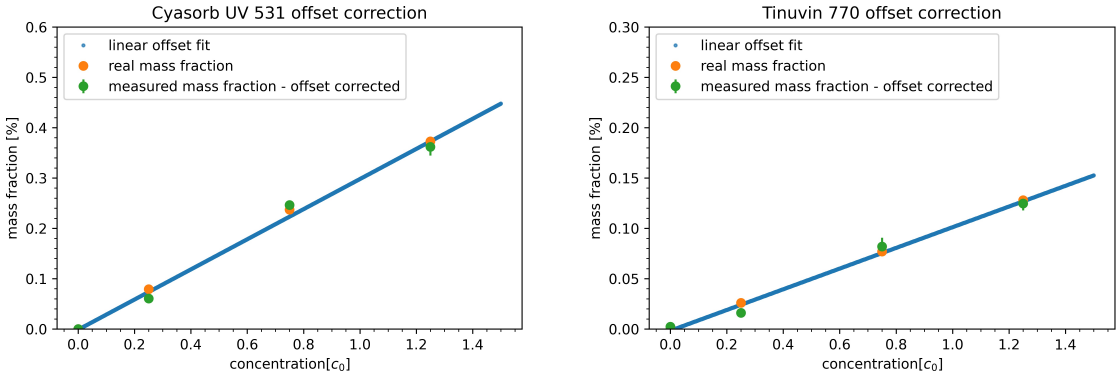

Figure 22: Calibration functions for the UV absorber Cyasorb UV 531 (left) and Tinuvin 770 (right). The methodology is in accordance with [51]. The error bars indicate the standard deviation of 3 measurements.

The data points show linear behavior yielding the offset corrected calibration functions $f_{C_{OC}}$ for Cyasorb UV 531 and $f_{T_{OC}}$ for Tinuvin 770

$$f_{C_{OC}}(m) = 1.45 \cdot 10^3 \left[\frac{1}{\text{mg}}\right] \cdot m \quad \text{and} \tag{34}$$

$$f_{T_{OC}}(m) = 1.60 \cdot 10^3 \left[\frac{1}{\text{mg}}\right] \cdot m - 0.15. \tag{35}$$

If one compares Equation 34 and Equation 35 with the calibration functions from the previous publication, one will notice significant deviations. The mass spectrometer was calibrated in the same way, but it cannot be assumed that the ion source was in the same condition (see the detailed discussion of the influence of the ion source in Appendix B). Furthermore, the polymer matrix can have a significant influence on the desorption

behavior of the molecules. Consequently, it is imperative that the additive structure and the polymer matrix correspond as closely as possible to the material to be quantified.

Figure 23 shows the quantification of the validation samples $1/2c_0$, $1c_0$ and $3/2c_0$ using Equation 34 and Equation 35 as explained in the previous publication. The data show that it is also possible to quantify the UV additives in a POE matrix. In particular, the results of $1/2c_0$ and $1c_0$ show good agreement with the expected mass ratios. For both additives, the mass fraction of the $3/2c_0$ sample is predicted too low, but is still almost within the tolerable range of the standard deviation. This could be explained by the fact that the intensity measured by the mass spectrometer is not necessarily linearly dependent on the molecule concentration over the entire mass range. This means that the choice of calibration samples must be made according to the expected mass ratios. However, for the mass range up to $1c_0$, which is of interest for PV encapsulants, the quantification method shows good agreement with the samples used and can be used for the quantification of UV additives.

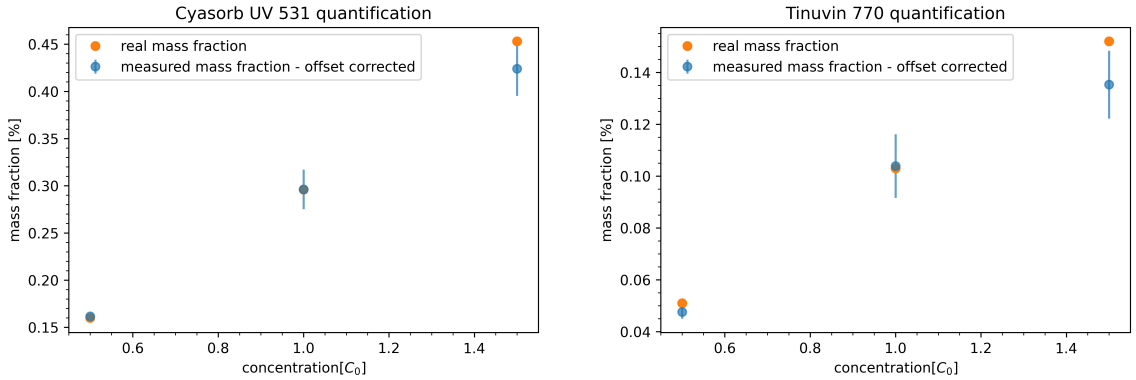

Figure 23: Quantification of the UV Absorber Cyasorb UV 531 (left) and the UV Stabilizer Tinuvin 770 (right). The methodology is in accordance with [51]. The error bars indicate the standard deviation of 3 measurements.

4.1.2. Quantification of crosslinking additives in EVA

This chapter is a section of a work on the crosslinking behavior of EVA depending on the crosslinking additives used and has been accepted for publication [217].

As described in subsection 2.1, the crosslinking additives also play an important role for the encapsulants by initiating the crosslinking reaction, which defines gel content and thus the mechanical properties [63, 64]. Consequently, the approach described in the previous chapters was extended to crosslinking additives. In the following, the crosslinking peroxide Luperox TBEC and the crosslinking accelerator Perkalink 301 (TAIC) are quantified by PY-GCMS. The production of the calibration samples was carried out in the same way as for the previous work and is shown in Appendix B.

Luperox TBEC

The polymer films with the variation in crosslinking peroxide content were also quantified

using only the second thermo desorption stage of the previous publication. All films with the corresponding additive quantities are listed in Appendix C. A chromatogram of the 300 °C desorption step for different mass contents of Luperox TBEC is shown in Figure 24. All other additives correspond to the film composition of the previous publication, while BHT was already admixed in the ELVAX 150W polymer granulate.

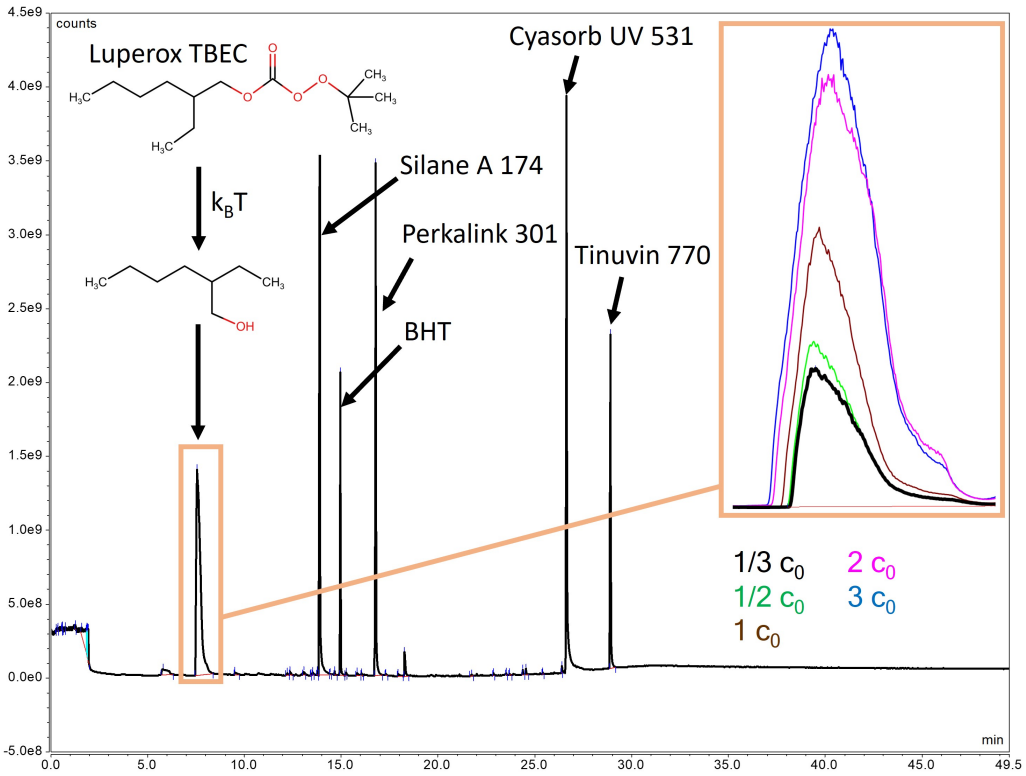

Figure 24: Chromatogram of the 300 °C desorption with all admixed additives and the thermal decomposition of Luperox TBEC with the detected fragment. Different contents of the Luperox TBEC fragment are color coded and in accordance with Appendix C. However, the integrals are not normalized to the sample mass at this point, which could lead to the impression of non-linearity.

As displayed in the chromatogram, Luperox TBEC cannot be detected directly. As a peroxide, it is thermally unstable and decomposes at the 300 °C desorption stage. However, the fragment 1-hexanol, 2-ethyl- is formed during the thermal decomposition of Luperox TBEC and is in a stoichiometric ratio to the base molecule. Consequently, the decomposition product can be correlated with the mass fraction of the crosslinking peroxide and used for quantification. Originally, this film series was also intended to quantify the crosslinking accelerator Perkalink 301. However, the mass fractions of the Perkalink 301 variation were deviating too much from real foil compositions, and the calibration function is only linear in a small measuring range. Consequently, the quantification of Perkalink 301 was not possible with this foil series. However, the films with the Perkalink 301 variation (but similar Luperox TBEC content) were used to

validate the quantification of Luperox TBEC. The results are shown in Figure 25.

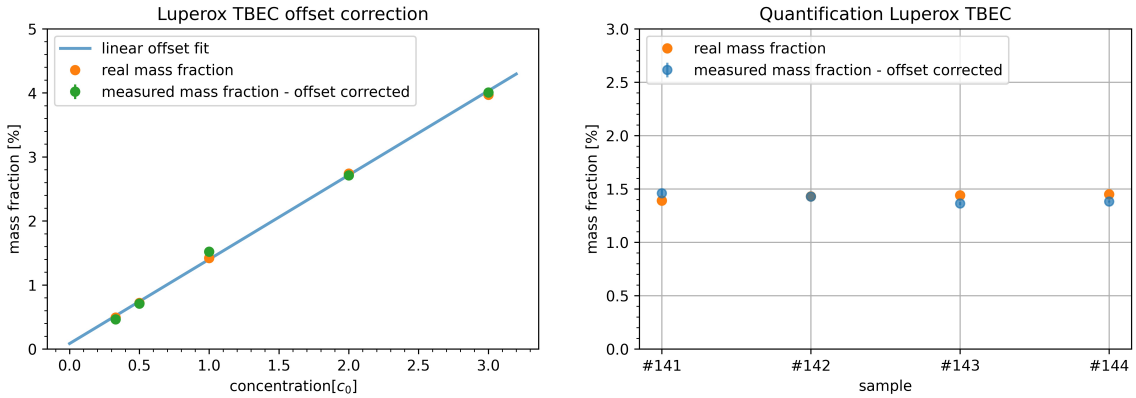

Figure 25: Calibration function for the crosslinking peroxide Luperox TBEC (left) and the calculated mass fractions of the validation samples (right). The methodology is in accordance with [51]. The error bars indicate the standard deviation of 3 measurements.

As shown in the graph, the offset corrected calibration function for Luperox TBEC $f_{L_{OC}}$ shows linearity over a wide range of mass fractions. It can be calculated using

$$f_{L_{OC}}(m) = 0.55 \cdot 10^3 \left[\frac{1}{\text{mg}}\right] \cdot m - 9.0. \tag{36}$$

If Equation 36 is used to calculate the mass fractions of the validating films (Appendix C), there is very good agreement with the real Luperox TBEC fractions. Thus, it could be shown that the quantification of crosslinking peroxides in EVA is possible, in principle, with good accuracy. Furthermore, stoichiometrically dependent decomposition products of the base molecules are sufficient for this approach.

Perkalink 301 (TAIC)

As the last additive in this work, the crosslinking accelerator Perkalink 301 was quantified using PY-GCMS. The Peak is also shown in Figure 24, whereas Perkalink 301 desorbs as a complete molecule. As before, the approach corresponds to the previously presented publication, and all concentrations used are listed in Appendix C. For the quantification of Perkalink 301, 3 samples were used for calibration and 3 samples for verification. As there is no literature on the mass content of crosslinking accelerators in EVA encapsulants, a variety of different concentrations were investigated. The peak integrals of the self-produced films with different mass fractions of Perkalink 301 were repeatedly compared with commercial samples (for example, the film of the previous chapter) until they were in approximately the same order of magnitude. The result of this iterative approach is shown with the last film series in Figure 26.

As shown in the graph of the calibration function, Perkalink 301 also shows sufficient linearity in the interval of the mass fractions analyzed. The offset corrected calibration function $f_{P_{OC}}$ for Perkalink 301 can be derived from the measurement data as

$$f_{POC}(m) = 4.25 \cdot 10^2 \left[\frac{1}{\text{mg}}\right] \cdot m - 0.9. \tag{37}$$

Using Equation 37, the mass fractions of Perkalink 301 in the validation samples were quantified. As displayed in the graph, the mass fractions of the $1/2c_0$ and $1c_0$ samples could be accurately determined. For the $3/2c_0$ sample, there is a significant deviation, which could be attributed to a non-linearity for larger mass ratios of the calibration curve. As it will be seen in the following chapter, mass fractions of less than 0.15 % Perkalink 301 are added to commercial polymer films. The accuracy of the calibration function for this mass range is sufficient, and the crosslinking accelerator could also be successfully quantified using this measurement method.

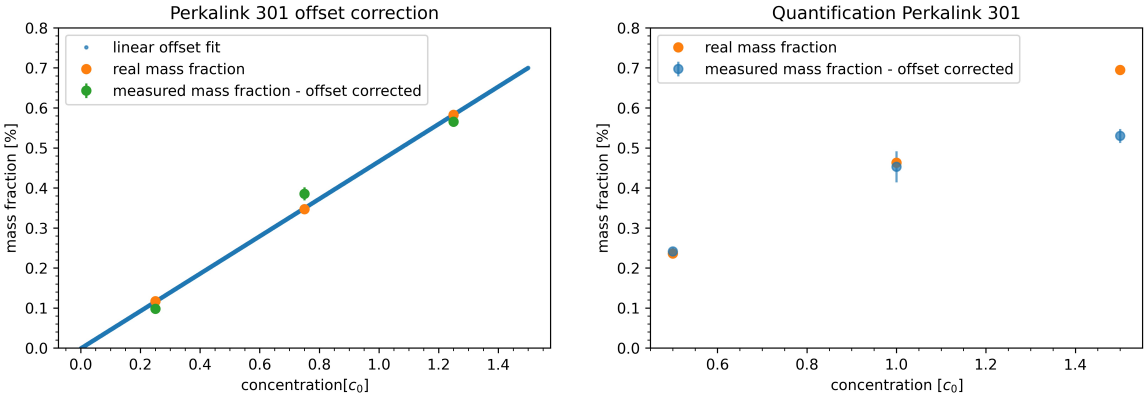

Figure 26: Calibration function for the crosslinking accelerator Perkalink 301 (left) and the calculated mass fractions of the validation samples (right). The methodology is in accordance with [51]. The error bars indicate the standard deviation of 3 measurements.

Quantification of crosslinking additives in commercial films

As mentioned above, there is no reliable literature on the mass content of additives currently used in commercial encapsulation films for solar modules. There are a few publications, but these generally refer to mass fractions from the Flat-Plate array project, which dates back almost 40 years [29, 61, 62]. Furthermore, as the crosslinking accelerator was not yet in use at that time, there is a lack of data on it in more recent literature [29, 61, 62].

In the course of this work, it was possible to determine the mass fractions of various additives in commercial films. The results of the publication showed that the commercial film contains a UV absorber content of 0.284 % and a UV stabilizer content of 0.073 % [51]. These mass fractions correspond approximately to the formulation in the Flat-Plate array project [29].

By using the calibration samples produced, it was also possible to quantify the crosslinking peroxide Luperox TBEC and the crosslinking accelerator Perkalink 301 in commercial EVA films. The results are shown in Figure 27. In the various EVA films, Luperox

TBEC contents between 0.6 % and 1.25 % mass content were detected. It should be noted that the only difference between EVA 4 and EVA 5 was the presence of an UV absorber. Perkalink 301 was detected in the encapsulants with mass fractions of approximately 0.06 % to 0.125 %. This means that partially significantly lower amounts of crosslinking peroxide are used in EVA films today (see 1.5 % to 3.0 % in the flat-plate array project) [29, 61, 62]. Furthermore, significantly less crosslinking accelerator is used than crosslinking peroxide. This supports the consideration from subsection 2.1, in which the crosslinking accelerator provides bonds between the polymer chains during peroxide crosslinking processes by hydrogen abstraction [65, 67–70, 72, 73]. Since the crosslinking accelerator must also react with the radicals of the crosslinking peroxide, at least 2 Luperox TBEC molecules are required to link two polymer chains by means of one Perkalink 301 molecule. Since it cannot be assumed that the polymer chains and crosslinking accelerator molecules are always perfectly arranged, significantly more crosslinking peroxide than crosslinking accelerator is required to initiate crosslinking, which is seen in the corresponding mass fractions.

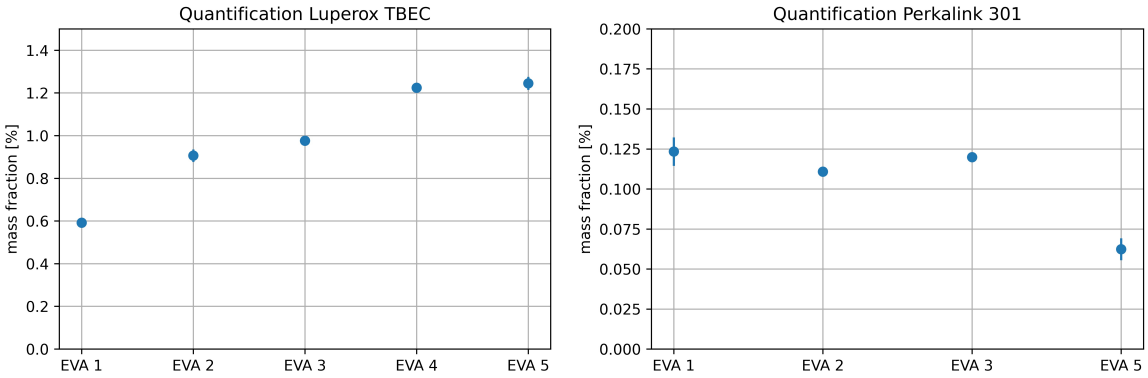

Figure 27: Quantification of the crosslinking peroxide Luperox TBEC (left) and the crosslinking accelerator Perkalink 301 (right) in different commercial EVA films. The original trade names have been replaced by general terms. The methodology is in accordance with [51]. The error bars indicate the standard deviation of 3 measurements.

4.2. Quantification of UV absorbers by UV/VIS spectrophotometry

The following chapter deals with the change in the optical properties of EVA films in dependence on the admixed UV absorber concentration. It can be shown that the mass content of different UV absorbers in unknown EVA samples can be determined using calibration samples and carrying out transmission and reflection measurements using UV/VIS spectrophotometry. The results of these analyses were further developed into a patent application with a potential measuring device for non-destructive analysis of the UV absorber concentration. However, this application had not been granted at the time this thesis was written. Thus, the structure of the following chapter is based on

the structure of a paper, as the analyses can be published on their own. It has its own introduction, methodology, results, discussion, and conclusion section. However, these have been brought into line with the other chapters of this thesis and are based on the same bibliography.

4.2.1. Introduction

In most cases, polymer films must be provided with additives in order to be usable for their specialized field of application. In the photovoltaic industry, ethylene-vinyl acetate copolymers (EVA), polyolefins (POE), and thermoplastic polyolefins (TPO) are typically used as encapsulation materials [84]. Crosslinking additives, UV absorbers, UV stabilizers, and antioxidants are added to these polymer films [29, 35, 61, 62, 84]. The used amount and homogeneous distribution of the additives significantly determine the lifetime of the polymer films and thus the degradation behavior of the solar modules [34, 35, 218].

A recently developed measurement technique allows the quantification of UV additives in EVA encapsulants by pyrolysis-gas chromatography-mass spectrometry (see previous publication) [51]. However, this method is cumbersome and can only examine small sample areas. The method presented here uses the absorption behaviors of the UV absorbers Cyasorb UV 531 and Tinuvin 329 to determine their additive concentration. The method is fast, requires no chemicals, and is non-destructive. It makes use of significant absorption or reflection peak changes in dependence on the additive concentration, like the peak of the Cyasorb UV 531 benzophenone molecule at 265 nm. This peak has been observed in the literature [32, 219]. However, it has never been correlated with the concentration of the UV absorber or used for quantification. In addition, other UV absorbers could be investigated in dependence on the presence of characteristic peaks. Thus, the method can be easily adjusted by using different wavelengths.

Because of these properties, it is potentially possible to perform an inline measurement within the production environment of polymer films. In this way, a film manufacturer can investigate in situ whether the added UV absorber content complies with the specifications and is homogeneously distributed. If the feeding units and the flow behavior of other additives are similar to that of the UV absorber, it could also be concluded that the distribution of the other additives is homogeneous/inhomogeneous. Additionally, it is possible to determine the UV absorber content in manufactured solar modules by reflection measurements, which opens possibilities for another field of application.

4.2.2. Methdology

For UV absorber quantification, samples were prepared for calibration and verification as in the approach above using PY-GCMS. In this section, the UV absorbers Cyasorb UV 531 and Tinuvin 329 are quantified. The concentrations of Cyasorb UV 531 contained in the films correspond to the previously listed publication (see subsubsection 4.1.1 [51]) on quantification using PY-GCMS and can be found in Appendix B. All concentrations used for the experiments with Tinuvin 329 are listed in Appendix C.

For transmission measurements, the 3 films of each concentration were prepared using a kneader and hydraulic press as in the previous section. The procedure is shown in [51] and Appendix B. Coupon samples were prepared for reflectance measurements. The lamination of the coupons and the measuring device parameters are explained below.

Coupon preparation

The encapsulants were manufactured to coupons (glass / encapsulant / encapsulant / backsheet). The used backsheet is a mono film on the basis of PET with coating. The backsheet is fluorine-free and was used for all coupons. Thus, the influence of the backsheet should be equal for all samples. The glass used was 3 mm thick, tempered, and a low-iron type. A transmission measurement of the plain glass can be found in subsection 5.1 or [52]. As shown in the graph, the transmission rate is also high in the UV region.

The lamination parameters were the same for all coupon compositions. A Meier ICOLAM 10/08 laminator was used for lamination. The laminator was pre heated to 55 °C. Afterwards, all samples of one encapsulant batch were placed inside the laminator. The laminator was evacuated for 6.5 min and heated to 80 °C. Afterwards the coupons were pressed with 600 mbar and heated to 155 °C within 3 min. The temperature and pressure were held for an additional 15 min. Afterwards the laminator was cooled to 55 °C within 30 min still applying the 600 mbar pressure.

UV/VIS measurements

UV/VIS measurements were carried out in a Perkin Elmer Lambda 1050. As Light source a deuterium / wolfram lamp was used while the detector was a InGaAs / PbS semiconductor with photo multiplier. The device was used in transmission and reflection mode with an integration sphere in a wavelength interval of 200 nm to 700 nm (transmission) or 300 nm to 700 nm (reflection). The monochromator increment was set to $\Delta\lambda = 1\,\text{nm}$. Measured data was saved in *.asc* files and evaluated with python using the packages pandas, numpy, and matplotlib [220–222].

4.2.3. Observed effect and utilization

Results

In the beginning, UV/VIS measurements were carried out in transmission mode for the homemade film samples containing Cyasorb UV 531 with different additive concentrations. Measured transmission values have not been transformed into absorption values due to the potential scattering impact inside the polymer films, which is also wavelength dependent [223, 224]. As mentioned above, 3 film samples were prepared for every concentration, respectively. A comparison of all measured concentrations is displayed in Figure 28. Detailed evaluations in Figure 29 were executed with mean values while the error bars indicate the standard deviation of the 3 samples.

The graph shows that the Cyasorb UV 531 content has a diverse influence on the transmission behavior of polymer films. While the average transmission for all concentrations lays above 90 % after 400 nm, the behavior below these wavelengths is signifi-

cantly diverging. For $\frac{1}{4}c_0$, $\frac{1}{2}c_0$ and $\frac{3}{4}c_0$ additional peaks appear at approximately 315 nm. Furthermore, until reaching $2c_0$, a transmission peak at approximately 265 nm was detected and will be used later for quantification of the UV absorber content. Reasonable transmission values very only reached at $1c_0$ and above. Subsequent, the behavior at 50 % transmission and 265 nm will be evaluated.

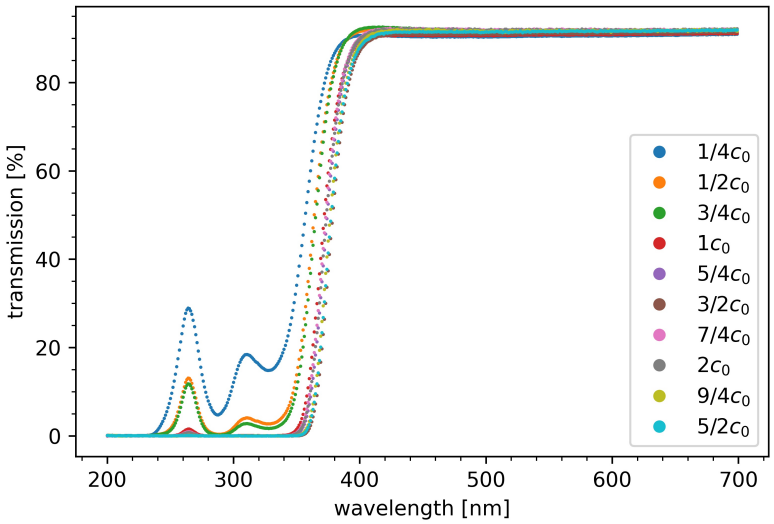

Figure 28: UV/VIS transmission measurements of all EVA film compositions containing Cyasorb UV 531 displayed in Appendix B. The transmission behavior is highly dependent on the UV-absorber content, which results in a characteristic peak at 265 nm and a shift in UV-cutoff.

For the sake of simplicity, the UV-cutoff comparison in dependence of UV-absorber concentration was executed at 50 % transmission and is displayed on the left side of Figure 29. The 50 % transmission value is already reached at approximately 354 nm for $\frac{1}{4}c_0$. For larger UV-absorber concentrations, this value is shifted towards higher wavelengths, while the behavior can not necessarily be described as linear. For $\frac{5}{2}c_0$ the 50 % transmission value was measured at approximately 376 nm which points out a total shift of 22 nm depending on the UV-absorber concentration.

The right picture of Figure 29 shows the transmission behavior at 265 nm in dependence of the UV absorber content. As it was already seen in Figure 28, the transmission decreases with a larger content of UV-absorber. The dependence on the UV absorber mass fraction m_f can be described with

$$T(m_f) = e^{-\tilde{B}m_f} \tag{38}$$

with an empiric value of $\tilde{B} = 12.5\left[\frac{1}{\%}\right]$. This exponential relationship between UV absorber concentration and transmission behavior is explained in the following section using an analytical approach.

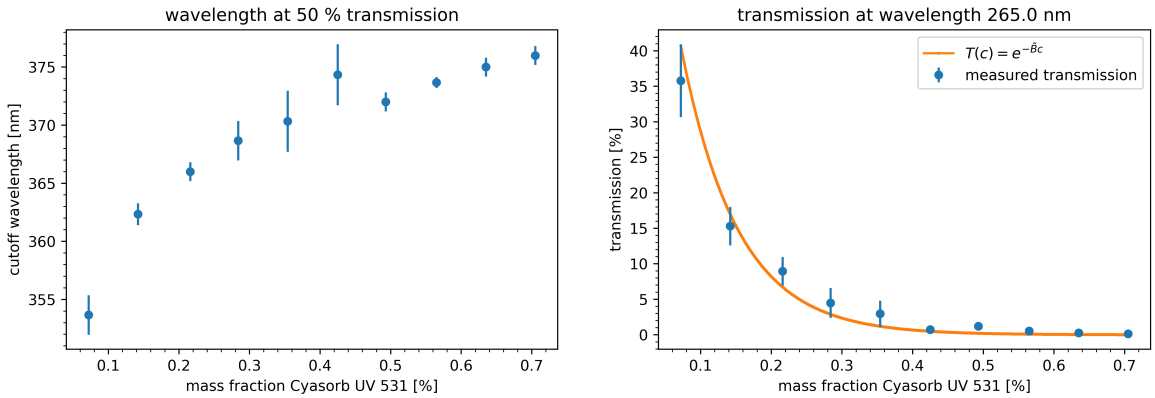

Figure 29: Wavelength at 50 % transmission value (left) and transmission behavior at the characteristic 265 nm peak (right) in dependence of the Cyasorb UV 531 mass fraction. The cutoff wavelength shows a non-linear dependence on the UV-absorber mass fraction. The transmission values at the characteristic 265 nm peak have been approximated with an exponential function.

Discussion

The transmission behavior of the polymer films is strongly influenced by modulations of the Cyasorb UV 531 mass fraction between 0.07 % and 0.7 %. A sufficient UV-cutoff was only reached for UV absorber contents of $1c_0$ and above. Especially the additional formed transmission peak at 265 nm shows that the UV-irradiance is damped in a non linear way. This peak has already been reported by Pern et al. in the absorption spectrum of Cyasorb UV 531 in solution, which indicates it as a property of the UV absorber [32]. However, as already mentioned, the transmission values should not be transformed into absorption due to the impact of scattering effects [223, 224]. Furthermore, the transmission values enable the possibility of an approach for deriving the UV absorber mass fraction within polymer films. Modifying the Lambert-Beer Law [225], the differential intensity change $\mathrm{d}I$ should be dependent on the incoming photon intensity $I(\hbar, \omega)$, the effective area which is irradiated A, the polymer film thickness l, a scaling constant B and the differential change in mass fraction $\mathrm{d}m_f$ which yields

$$\mathrm{d}I = -I(\hbar\omega)BAl\mathrm{d}m_f. \tag{39}$$

For a constant wavelength of 265 nm, $I(\hbar, \omega)$ is not dependent on the photon energy anymore. Furthermore, BAl can be described with $\tilde{B}$ as a material (and machine) dependent scaling factor as the effective area stays constant and all film samples have approximately the same thickness. Solving the differential equation and using the normalized initial condition $I(m_f = 0) = I_0 = 1$ yields

$$I(m_f) = I_0 e^{-\tilde{B}m_f} \quad \text{and therefore} \quad \frac{I}{I_0} = T(m_f) = e^{-\tilde{B}m_f}. \tag{40}$$

A material dependent scaling factor $\tilde{B} = 12.5\left[\frac{1}{\%}\right]$ fits with the experimental values. It follows that one is able to calculate the UV-absorber mass fraction by

$$m_f = -\frac{\ln(T)}{\tilde{B}}. \tag{41}$$

B is most likely linked to the extinction coefficient and could be determined by using different polymer film thicknesses because the effective area A stays constant [226]. However, for the purpose of additive quantification, a derivation from the complex refractive index is not necessary. In addition, m_f is correlated to the UV-absorber molecule concentration, or rather the additive density inside the polymer matrix, but a description as a mass fraction is beneficial for the purpose of quantification, which will be carried out in the next step.

Figure 30 shows the UV/VIS spectrum of the verification film samples containing Cyasorb UV 531 and the application of Equation 41. As before, the displayed mass fractions are mean values from 3 polymer films with standard deviation as error bars. For mass fractions of $1c_0$ and below, the UV/VIS quantification function is in accordance with the real mass fraction of the polymer films. For mass fraction values much higher than $1c_0$, the function becomes inaccurate due to the very low transmittance values at 265 nm. This is a direct result of the strong slope of the $\ln(T)$ function for values smaller than 0.05. Nevertheless, utilizing the 265 nm transmission peak allows a very quick and non-destructive quantification of commonly used Cyasorb UV 531 contents inside polymer films. In addition, previous works have shown that commercial EVA films use UV absorber contents similar to $1c_0$ [29, 51, 61, 62].

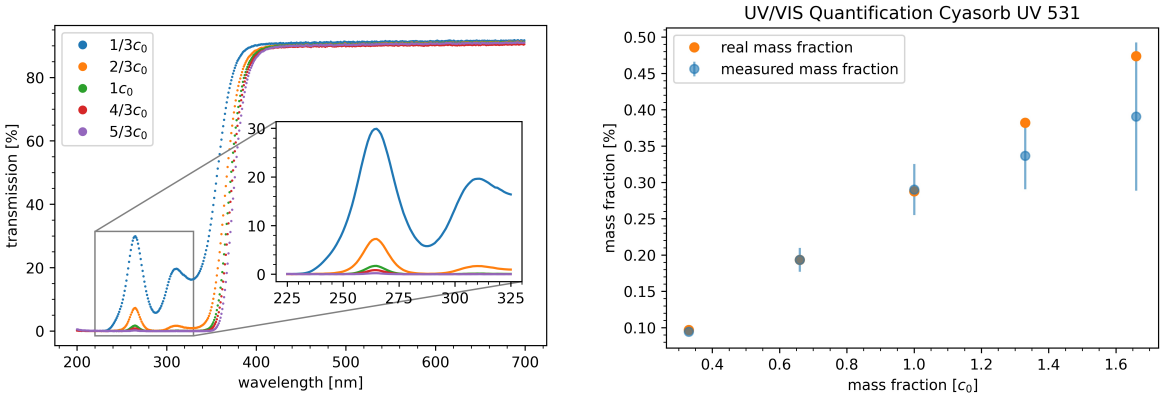

Figure 30: UV/VIS measurements of the verification film samples (left) and corresponding, calculated mass fractions (right).

To further verify the derived correlation, a second series of experiments containing 6 different concentrations of the UV absorber Tinuvin 329 was carried out. The results are displayed in Figure 31. In this case, the local maximum at 265 nm was not used, but the transmission behavior at 373 nm was investigated. As shown in the derivation of Equation 40, this approach is independent of the choice of wavelength interval as long

as only one wavelength is used. The scaling factor $\tilde{B}$ in this case is $\tilde{B} = 15\left[\frac{1}{\%}\right]$ and the expected exponential dependence is also given for the UV absorber Tinuvin 329. Consequently, the method can also be extended to other UV absorbers.

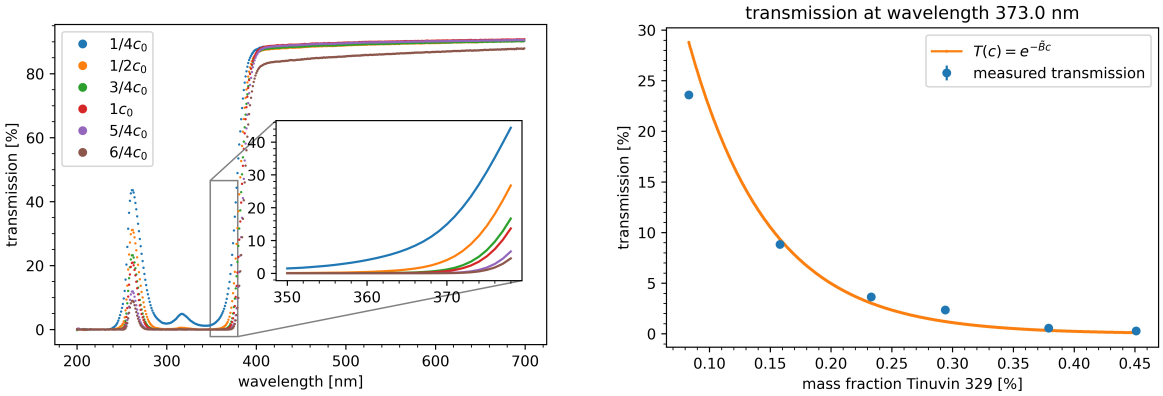

Figure 31: UV/VIS measurements in transmission mode of polymer film samples containing Tinuvin 329 (left) and the transmission values at 373 nm in dependence of the Tinuvin 329 concentration (right).

4.2.4. Extension to reflection measurements

The dependence of the optical properties of EVA films on the UV absorber concentration can be extended to reflectance measurements. For this purpose, coupons (glass / encapsulant / encapsulant / backsheet) were produced to simulate the structure of solar modules. The same concentrations were used as for the transmission measurements (see Appendix B). Figure 32 visualizes the reflection behavior of coupons containing EVA encapsulants with admixed Cyasorb UV 531.

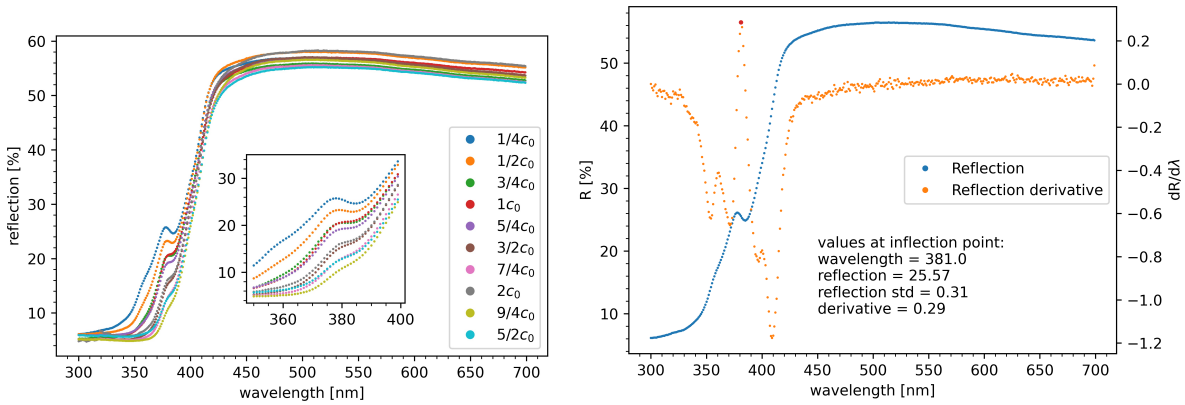

Figure 32: Reflection behavior of manufactured coupons (glass/EVA/EVA/backsheet) with different Cyasorb UV 531 content (left) and the 1/4 c_0 reflection curve with the first derivative (right).

The graph shows that the reflection behavior of the coupons changes significantly depending on the UV absorber concentration. With increasing UV absorber concentration, the UV cut-off also shifts to higher wavelengths, as was the case for the pure film samples and transmission measurements. In addition, the spectra show an inflection point at approximately 380 nm, whose reflectance value decreases with increasing Cyasorb UV 531 concentration. The first derivative was calculated in order to investigate the changes in reflection behavior in more detail. This allows the reflectance value at the inflection point to be analyzed for each UV absorber concentration. The results are shown in Figure 33 and show that the reflectance values are approximately linearly dependent on the UV absorber concentration. Consequently, a calibration function can also be derived for reflectance measurements, and the UV absorber content in unknown coupons (or solar modules) can be determined. The mass fraction of Cyasorb UV 531 in coupon samples can be determined by the reflection R at the inflection point with

$$m_f = -\frac{R - 25.94}{20.46}. \tag{42}$$

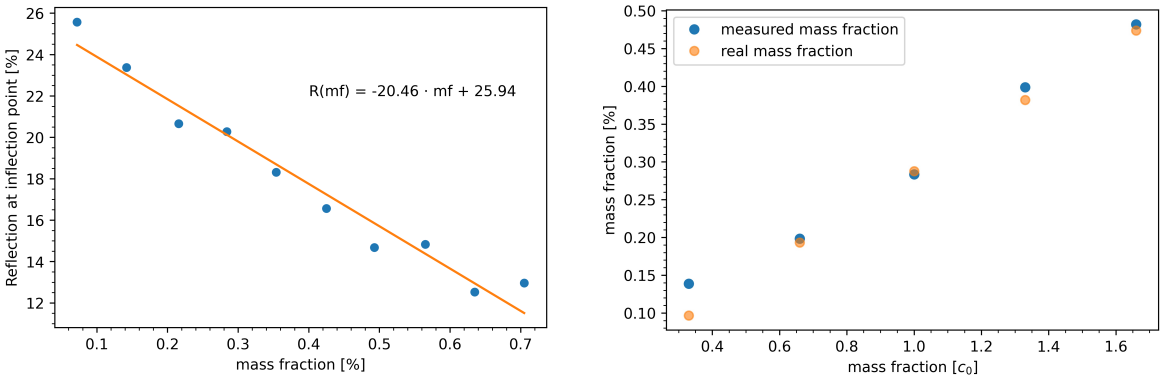

Figure 33: Calibration curve (left) and derived UV absorber concentration of the validation samples (right).

The quantification shows good agreement with the actual UV absorber concentrations contained, although in this case, no analytical model is used, and the correlation is purely empirical. An extension with an analytical approach would be conceivable but is considerably more complex due to the large number of interfaces. Consequently, this is not done at this time point, as the quantification can be carried out satisfactorily. However, it should be noted that the reflection behavior is strongly dependent on the glass and backsheet used. Consequently, it is essential that these match between the calibration sample and the unknown sample.

A second series of experiments with Tinuvin 329 as UV absorber was also carried out for the reflection measurements to further verify the quantification procedure. The same UV absorber concentrations as for the Tinuvin 329 transmission measurements have been used (see Appendix C) The results of the reflection measurements are displayed

in Figure 34. The measurements of the coupons do not show a characteristic inflection point. However, another significant point can easily be used for evaluation. In this case, the local minimum of the derivative at 393 nm was investigated. To derive the calibration function, the reflection values at 393 nm of samples 1/4 c_0, 3/4 c_0, and 5/4 c_0 were used to calculate the concentrations of Tinuvin 329 in the validation samples 2/4 c_0, 4/4 c_0 and 6/4 c_0. The results are visualized in Figure 35.

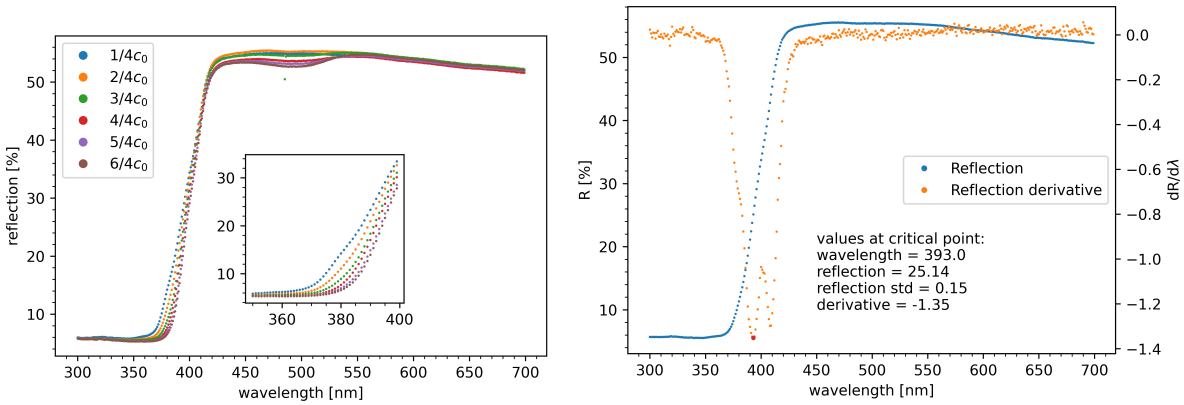

Figure 34: Reflection behavior of manufactured coupons (glass/EVA/EVA/backsheet) with different Tinuvin 329 content (left) and the 2/4 c_0 reflection curve with the first derivative (right).

In this case, the UV absorber concentration is calculated with

$$m_f = -\frac{R - 28.75}{24.97} \tag{43}$$

and also shows good agreement with the real admixed mass fractions of Tinuvin 329. By using further concentrations (as in the case of Cyasorb UV 531), the accuracy of the prediction can be significantly increased, but a well-founded statement is already possible with 3 concentrations.

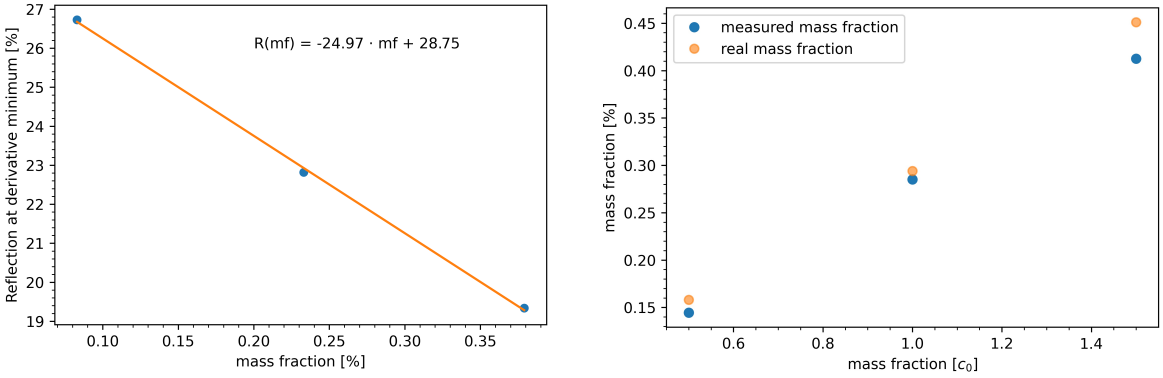

Figure 35: Calibration curve (left) and derived UV absorber concentration (right).

4.2.5. Conclusion

For the first time, the absolute mass contents of UV absorbers in encapsulants for photovoltaic modules were measured non-destructively using optical methods. This opens up a wide range of applications for potential evaluations. On the one hand, the production of polymer films can be monitored by using an inline-capable device to measure the UV absorber concentration and homogeneity during the manufacturing process. On the other hand, solar module manufacturers can test their modules quickly and non-destructively after lamination. Furthermore, changes in the optical properties of the encapsulants are often used as a measure of module solar module aging [205, 206, 219]. In this way, the degradation of the UV absorber can potentially be linked to degradation effects when its absolute concentration is analyzed as a function of weathering time.

5. Investigations of coupon samples under standardized UV weathering

5.1. Encapsulant degradation in dependence of the UV spectrum

The degradation effects under UV aging discussed in section 3 posed a problem. As described in subsection 2.3, the IEC 61215 standard only provides rough specifications for UV aging. The standard is considered more as a preconditioning test for the solar cell. As a result, IEC 62788-7-2 was created to better define the accelerated UV aging of polymers in the PV sector. Within this standard, however, two different lamp types (UV-A fluorescent lamps and xenon lamps with daylight filters) may be used. Both types of lamps have completely different spectra, so the degradation kinetics of encapsulants should also differ.

In many publications and standards, only the UV dose is usually discussed, and the spectral photon distribution is ignored. In the following work, using the method developed in section 4 for polymer additive quantification, it is shown that the degradation behavior of polymers depends more on the choice of the spectrum than on the intensity with the same spectral distribution. As a result, it is recommended that the current IEC 61215 and IEC 62788-7-2 standards be adapted, as misjudgments can have serious consequences for the long-term stability of solar modules.

Solar Energy Materials & Solar Cells 266 (2024) 112674

Contents lists available at ScienceDirect

Solar Energy Materials and Solar Cells

journal homepage: www.elsevier.com/locate/solmat

UV lamp spectral effects on the aging behavior of encapsulants for photovoltaic modules

Robert Heidrich [a,b,*], Chiara Barretta [c], Anton Mordvinkin [a], Gerald Pinter [d], Gernot Oreski [c], Ralph Gottschalg [a,b]

[a] Fraunhofer CSP, Otto-Eissfeldt-Strasse 12, Halle (Saale), 06120, Germany
[b] Anhalt University of Applied Sciences, Bernburger Strasse 55, Koethen (Anhalt), 06366, Germany
[c] Polymer Competence Center Leoben, Roseggerstrasse 12, Leoben, 8700, Austria
[d] Montanuniversitaet Leoben, Otto Gloeckel-Strasse 2, Leoben, 8700, Austria

ARTICLE INFO

Keywords:
EVA
POE
TPO
UV degradation
Spectroscopy
IEC 62788

ABSTRACT

Polymer encapsulants used in photovoltaic (PV) modules experience severe UV aging during more than 25 years of module's operation. However, the current standard qualification tests cannot provide a sufficient solution able to mimic the UV exposure in the field. IEC 61215 defines the requirements for UV stability of PV modules with very low cumulative UV dosage. While the new IEC 62788-7-2 imposes higher UV dosages on polymers films, the used UV testing procedure allows the use of either UV-A fluorescence lamps or xenon lamps, yielding different spectra. The given work compares the effect of different lamp spectra, based on IEC 62788-7-2, on the aging behavior of the encapsulant. For this purpose, coupons (glass/encapsulant/busbar/encapsulant/backsheet) using the common encapsulant ethylene-vinyl acetate copolymer (EVA) and the emerging encapsulants polyolefine (POE) and thermoplastic polyolefine (TPO) were manufactured. The samples were weathered under different UV conditions for a total duration of 2500 h with extraction times of 250 h. Photodegradation was observed for all encapsulants and weathering types. However, in general the weathering with UV-A lamps inflicted significantly less damage. The formation of unsaturated carbon bonds because of polymer backbone decomposition was only reported for xenon lamp weathering. The carried out experiments suggest that xenon lamps, providing more realistic accelerated aging, should be predominately used in the UV weathering standards in the PV industry, whose current versions are to be accordingly reconsidered.

1. Introduction

Polymers have a broad scope of application in the photovoltaic (PV) industry. In particular, the polymer films used in solar modules to protect them from environmental influences must meet stringent requirements to ensure an adequate module service life [1]. Different types of backsheets and encapsulants in combination with varying additive mixtures result in diverging degradation modes [2]. Remarkably, a large portion of PV module defects can be assigned to failures of the polymer parts [3]. The interactions between polymeric components further influence the degradation behavior [2,4,5]. Thus, testing the materials in advance to predict failures after some time in the field is crucial. Nevertheless, the general standard for testing PV modules, IEC 61215, only defines minimal requirements for UV weathering of solar modules, without setting too strict requirements to the UV lamp selection [6].

In the past, different standards of UV weathering of polymers were established [7–10]. Currently, only the IEC-62788-7-2 is dealing with UV weathering of polymers in the PV industry. Fig. 1 displays the spectral distribution of a xenon lamp and a UV-A fluorescence lamp which are both used within this standard [10]. In comparison with the solar spectrum (displayed as ASTM G173 AM 1.5) it is obvious that the xenon lamp spectrum is a more realistic approach than the UV-A lamp counterpart. The UV-A lamp spectrum only has a minor intensity in the mild UV region and does not contain any visible light. Hence, interactions which are induced by higher wavelengths will not occur [11,12]. Also overcoming the binding energy of aliphatic C–C bonds at 3.47 eV is less likely to happen due to the smaller intensity in that wavelength region [13]. However, the standard quotes that the use of UV-A lamps is in general possible. As a result, many recent works rely on the use of UV-A lamps to qualify the aging behavior of different polymers or just refer to fulfill the requirements of the

* Corresponding author at: Fraunhofer CSP, Otto-Eissfeldt-Strasse 12, Halle (Saale), 06120, Germany.
E-mail address: robert.heidrich@csp.fraunhofer.de (R. Heidrich).

https://doi.org/10.1016/j.solmat.2023.112674
Received 24 June 2023; Received in revised form 13 October 2023; Accepted 29 November 2023
Available online 9 December 2023

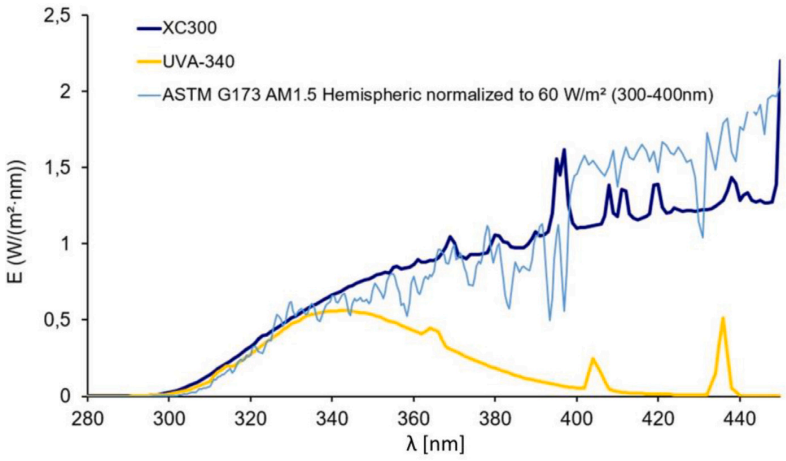

Fig. 1. Qualitative spectral distribution of the different lamps used for IEC 62788-7-2 in comparison with the ASTM G173 AM 1.5. To fulfill the weathering standard, the displayed intensities have to be adjusted in accordance with Table 1. The graph was provided by Atlas Material Testing Technology GmbH.

IEC 61215 because it is a comparatively cheap testing method [14–22]. While in general the use of standards is the best way to generate comparable data, the cross interpretation from the data generated by different lamp spectra could lead to false conclusions. Furthermore, differences between laboratories using the same standard have been reported in the past [23].

This work addresses this concern by investigating the impact of the used lamp (UV-A lamp and xenon lamp) spectrum on the common encapsulant ethylene vinyl acetate copolymer (EVA) and the emerging encapsulants polyolefine (POE) and thermoplastic olefine (TPO). The encapsulants are manufactured into coupons using the same mono layer backsheet on polyethylene terephthalate (PET) basis and busbars which enable realistic side reactions. Polymer degradation is a complex process including several intermediate reactions in dependence of the observed structure [24–27]. The carried out weathering based on IEC-62788-7-2 with a duration of 2500 h is comparatively mild and only inflicts minor damage to stabilized encapsulants. However, if significant distinctions in the encapsulant aging behavior in dependence of the different spectra already occur during this short time span, the conclusions to predict module lifetimes can be misinterpreted. Especially interactions which require only small amounts of reactants like the autocatalytic acetic acid decomposition in EVA could be underestimated when using an inadequate irradiation spectrum [28–30]. This work aims to clarify if the weathering with UV-A lamps is an appropriate procedure for UV aging or if the use of spectra which are more similar to the sun must be preferred.

Due to the large number of measurement results, the structure of the paper is briefly referred to for the sake of clarity. After the methodology part, the work is organized as follows: At the beginning, all encapsulants are analyzed by pyrolysis-gas chromatography-mass spectrometry (PY-GCMS) and Fourier-transform infrared spectroscopy (FTIR). In particular, the chemical structure of the POE and TPO encapsulants are of interest, since these material groups are not clearly defined. In addition, the additive structure of all encapsulants is determined. Subsequently, one chapter each deals with the degradation behavior of the different encapsulants using PY-GCMS, FTIR, evolved gas analysis (EGA)-FTIR and a principal component analysis (PCA). In the next section, all results are summarized and discussed together. The last part considers the consequences derived from the discussion for the UV weathering of PV components in the conclusion section of the work.

2. Materials and methods

2.1. Weathering parameters

Three runs of weathering with durations of 2500 h each were carried out. Table 1 lists all the corresponding parameters. Here, I is the lamp intensity at the sample position. The first two weathering runs are in accordance with IEC 62788-7-2 while the enhanced A3 weathering was used to compare two different xenon intensities [10]. The displayed abbreviations (Abbr.) will be used for all subsequent passages.

For B weathering, samples were aged in a UVTest^{TM} Fluorescent UV/Condensation Weathering instrument from Atlas Material Testing Technology LLC. UVA-340 lamps with the spectral distribution displayed in Fig. 1 were used. Chamber parameters were programmed as listed in Table 1. A and MAX weathering were carried out in an Atlas Xenotest 440 with B04 daylight filters. The spectrum is similar to the XC300 spectrum displayed in Fig. 1. All other chamber parameters were in accordance with Table 1.

As displayed in Table 1, some parameters remain unknown, as they are not adjustable. For the irradiation, the IEC 62788-7-2 standard claims that either the intensity at 340 nm or the integrated intensity between 300 nm and 400 nm needs to be adjusted [10]. In the presented work, the fluorescence weatherometer was programmed to the required 0.8 Wnm/m^2 at 340 nm while the xenon weatherometers used the integrated intensities of 81 W/m^2 (A) and 120 W/m^2 (MAX) between 300 nm and 400 nm. Spectrometer measurements of the xenon chambers is displayed in the supporting information. However, the spectra should be treated qualitatively as the spectrometer is not calibrated to the used chamber geometry.

The relative humidity was not controlled in the fluorescence weatherometer which is common for this type of machine and is no restriction to the standard [10]. As all samples are provided with white backsheets, the sample temperature is mainly dominated by the chamber temperature [19,31–33]. Previous studies showed that a BST of 75 °C for fluorescence lamps (B3) and a BST of 90 °C for xenon lamps (A3) will result in the approximately the same sample temperature for white specimens [10,34]. In the case of the fluorescence lamp which does not contain visible or infrared wavelengths, the sample temperature is expected to be approximately equal to the chamber temperature. The sample temperature during xenon weathering is highly dependent

Table 1
Used chamber parameters for all weathering runs.

Standard	Lamp type	Abbr.	I at 340 nm [(W/m^2)/nm]	$\int_{300nm}^{400\ nm} I\,d\lambda$ [W/m^2]	r.h. [%]	T_{Ch} [°C]	T_{BST} [°C]
62788-7-2-B3	fluorescence	B	0.8	n.a.	n.a.	n.a.	75
62788-7-2-A3	xenon	A	n.a.	81	20	65	90
enhanced A3	xenon	MAX	n.a.	120	20	65	90

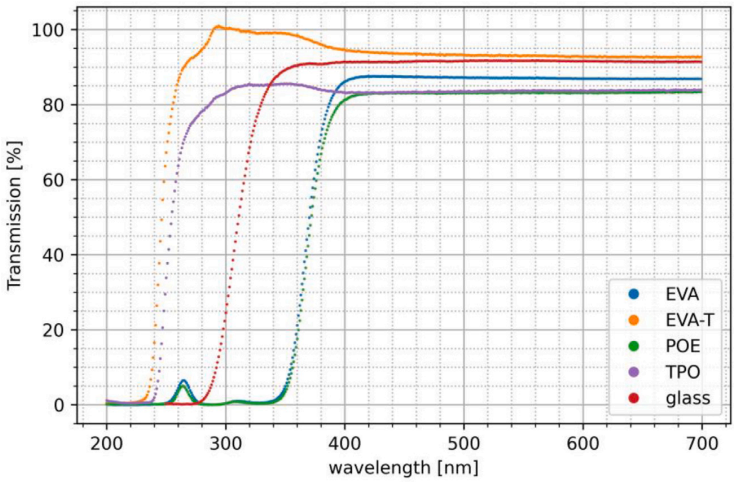

Fig. 2. UV/VIS measurements unlaminated encapsulant samples and the used glass. The measurements were carried out in a Perkin Elmer Lambda 1050. As Light source a deuterium/wolfram lamp was used while the detector was a InGaAs/PbS semiconductor with photo multiplier. The device was used in transmission mode with integration sphere in a wavelength interval of 200 nm to 700 nm. The monochromator increment was set to $\Delta\lambda = 1$ nm. Measured data was saved in *.asc* files and evaluated with python.

on the absorption behavior of the specimen and the chamber geometry (i.e., ventilation system etc.). However, previous studies showed, that clear and white samples only have a minimal increased sample temperature (i.e., +2 °C as maximum deviation) in comparison with the chamber temperature when using a xenon spectrum with daylight filters and 75 W/m^2 intensity at 340 nm [32,33]. Thus, the sample temperature was approximated to be 65 °C and equal between A and B weathering. For MAX weathering however, the sample temperature could be slightly higher due to the higher irradiation of longer wavelengths.

The first samples have been removed after 500 h. All following extractions took place with 250 h time steps.

2.2. Encapsulants and lamination

Four different types of encapsulants have been commercially purchased. All the following data was taken from the data sheets and not additionally tested (except the transmittance behavior). The used EVA sheets have an approximate thickness of 0.4 mm to 0.6 mm and vinyl acetate fractions of 26 % to 28 %. The gel content is above 85%. Two EVAs of the same base type were used and the difference between the materials is the absence (EVA-T) and presence (EVA) of an UV absorber. POE samples have an approximate thickness of 0.45 mm with a gel content of 50 % to 80 %. The UV cut off wavelength is specified at 360 nm. The TPO samples have an approximate thickness of 0.45 mm and a UV cut off wavelength below 300 nm. All samples within one batch were prepared close to each other. Thus, local inhomogeneities of the encapsulation roll were taken into account.

Fig. 2 lists the transmittance behavior of unlaminated encapsulants and the used glass. The glass used was 3 mm thick, tempered and a low-iron type. As shown in the graph, the transmission rate is also high in the UV region and the intensity maximum at 340 nm described in Fig. 1 should almost be completely transmitted to the rest of the coupon. The measurements also show a clear UV cutoff of the POE and EVA samples, confirming the data sheet specifications. The TPO and EVA-T samples are highly transparent in the high energy UV range up to about 260 nm.

The encapsulants were manufactured to coupons (glass/front encapsulant/busbar/back encapsulant/backsheet) as displayed in Fig. 3. Due to the use of different weatherometers, the corresponding sample size had to be adjusted. The used backsheet is a mono film on basis of PET with coating. The backsheet is fluorine-free and was used for all coupons. Thus, the influence of the backsheet should be equal for all samples. However, interactions between backsheet and encapsulant can vary in dependence of the used encapsulation material [21,35].

The lamination parameters were the same for all coupon compositions. Every lamination process was in accordance with the corresponding encapsulant data sheets. A Meier ICOLAM 10/08 laminator was used for lamination. The laminator was pre heated to 55 °C. Afterwards, all samples of one encapsulant batch were placed inside the laminator. The laminator was evacuated for 6.5 min and heated to 80 °C. Afterwards the coupons were pressed with 600 mbar and heated to 155 °C within 3 min. The temperature and pressure were hold for additional 15 min. Afterwards the laminator was cooled to 55 °C within 30 min still applying the 600 mbar pressure.

2.3. Sample preparation

After removal from the weatherometer, all test specimens were inspected for delamination, discoloration, cracking, or other degradation effects that would be apparent from visual inspection. The sample extraction was done by several steps. At first, the coupons were cut cautiously through the backsheet layer with a cutter knife around the busbar area. Afterwards, the busbar could be peeled off. In the next step the area around the newly formed region was cut in a rectangular shape

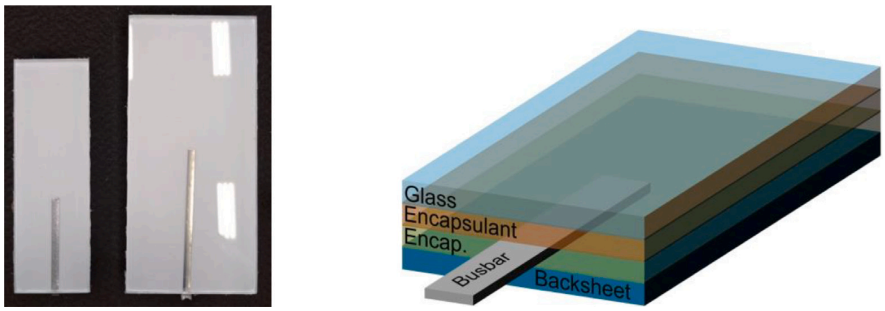

Fig. 3. Finished samples in both used dimensions (left) and schematic coupon structure (right).

until reaching the glass. At this point, all polymer materials at once were extracted with a chisel and peeled with hands or pliers. Due to the dent, which was created by the busbar, the glass side and backsheet side were always assignable for all encapsulant types. Pictures of the preparation process can be found in the supporting information.

2.4. Pyrolysis-gas chromatography-mass spectrometry (PY-GCMS)

For qualitative and quantitative analysis of the polymer and the additive composition a combination of pyrolysis, gas chromatography and mass spectrometry (PY-GCMS) was used. The PY-GCMS setup and settings are explained in detail in our previous work focusing on additive quantification [36]. An EGA/Py-3030D from Frontier Laboratories Ltd. pyrolysis oven with attached autosampler AS-1020E was used for a two-step thermo desorption. All desorption steps were carried out with the help of a selective sampler SS-1010E from Frontier Laboratories Ltd. which prevents column contamination by undesirable fragmented components. As gas chromatograph a Trace 1300 from Thermo Scientific with He carrier gas was used. The implemented column was an Ultra ALLOY Capillary Column (length 30 m, internal diameter 0.25 mm, film thickness 0.25 μm) from Frontier Laboratories Ltd. An ISQ 7000 mass spectrometer from Thermo Scientific was coupled to the gas chromatograph. The m/z range was set from 29 to 800. Every measurement was carried out in double determination. Samples were taken from the measurement spots of the FTIR measurements with a punch and a hammer. Thus, always the complete bulk material was analyzed with samples masses of 2 mg to 4 mg.

2.5. Fourier-transform infrared spectroscopy (FTIR)

FTIR measurements have been carried out with a Spectrum Two Fourier-Transform-Infrared-Spectrometer from Perkin Elmer. As ATR unit a Specac Quest^{TM} with diamond crystal was used. The Wavenumber range was set from 4000 cm^{-1} to 650 cm^{-1} with 4 cm^{-1} resolution. For every measurement the number of scans was set to 4. The raw data was computed with Python 3.9.7 using the standard libraries numpy, matplotlib and pandas [37–39]. Integrals were calculated using the numpy.trapz method (composite trapezoidal rule) [37]. For all samples, the glass side of the encapsulant was measured. In detail, the area next to the dent created by the busbar was used for triple determination.

2.6. Evolved gas analysis (EGA)-FTIR

A Frontier Fourier-Transform-Infrared-Spectrometer from Perkin Elmer was used for EGA-FTIR measurements. For Evolved Gas Analysis an EGA4000 module from Perkin Elmer was installed with a gas cell transfer line temperature of 280 °C. The system purge gas was nitrogen. Samples were prepared with sample masses of 9.5 mg to 10.5 mg. All samples have been treated with the same heating procedure. Starting at 40 °C and holding this temperature for 6 min. Afterwards the sample were heated to 600 °C with a heating rate of 10 K/min. IR scans were taken every 30 s using a wavelength interval from 4000 cm^{-1} to 600 cm^{-1} with 4 cm^{-1} resolution. Every measurement generated 5 different data sets: A time dependent Gram Schmidt profile, a temperature dependent Gram Schmidt profile, the thermogravimetric analysis (TGA) measurement, a time dependent FTIR measurement and a temperature dependent FTIR measurement. All raw data files were computed with Python 3.9.7 using the libraries numpy, matplotlib and pandas [37–39].

2.7. Principal component analysis (PCA)

PCA is a common approach for FTIR investigations and opens new possibilities for data interpretation [40–44]. The analysis was carried out on the raw data generated with the FTIR measurements. The data were computed with Python 3.9.7 using the libraries numpy, matplotlib, pandas and sklearn [37–39,45]. The complete FTIR spectra were sliced into regions of interest (e.g., wavelength intervals) before the PCA was carried out. Afterwards the data was scaled with the StandardScaler() package from sklearn [45]. The PCA of the desired and scaled regions was computed with the PCA() package from sklearn [45].

3. Results and discussion

Raw encapsulant samples have been analyzed with Pyrolysis-gas chromatography-mass spectrometry (PY-GCMS) in triple determination to investigate the admixed additive structure. The chromatograms are displayed in the supporting information while the setup is described in detail in [36]. Table 2 lists the results of the additive analysis. The EVA sample contains all common additives. As expected, the EVA-T sample is similar to the EVA sample except for the presence of an UV absorber. In contrast to the EVA encapsulants, the POE only uses minimal amounts of Luperox TBEC, no adhesion promoter and no UV stabilizer. While the TPO should not use any crosslinking additives by definition, the samples contained traces of a crosslinking agent and large amounts of crosslinking accelerator. In addition, the TPO is stabilized with Tinuvin 770 and minimal traces of Cyasorb UV 531 have been detected.

The initial chemical structure of the encapsulation polymers was determined and compared using FTIR measurements. All displayed FTIR curves are mean values of at least 3 measurements from different positions. The peak integration for the comparison of intensities is carried out after baseline subtraction by a linear approximation of the integral boundaries. As the 690 cm^{-1} to 750 cm^{-1} PE peak is facing the smallest changes during UV exposure, this peak integral was selected for normalization of effects of different contact between the sample and the ATR crystal [46]. Resulting diagrams showing the development of peak integrals are normalized to the initial state. Here, the error bars

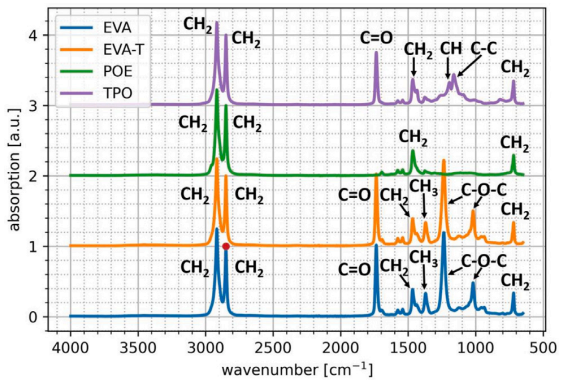

Fig. 4. Comparison of the FTIR spectra of the initial state for all used encapsulants. The red dot marks the 2850 cm^{-1} peak for normalization.

Table 2
Additive mixture of the investigated encapsulants. Additives with ++ are certainly detected in significant amounts, while for + only traces were found. Encapsulants with — do not contain the corresponding additive.

Name	Function	EVA	EVA-T	POE	TPO
Luperox TBEC	crosslinking agent	++	++	+	+
Silane A174	adhesion promoter	++	++	–	++
Perkalink 301	crosslinking accelerator	++	++	++	++
Cyasorb UV 531	UV absorber	++	–	++	+
Tinuvin 770	UV stabilizer	++	++	–	++

are the transformed standard deviation by Gaussian error propagation as displayed in the supporting information. A comparison of all encapsulants at the initial state is displayed in Fig. 4. For reasons of visual comparability, all intensities are normalized to the maximum of the 2850 cm^{-1} CH_2 peak marked with the red dot. The corresponding peaks are assigned in Table 3. In the tabular, the column "enc." represents the encapsulant where the corresponding peak was detected. In detail, E ≙ EVA, P ≙ POE, T ≙ TPO.

Since the material classes of PV encapsulants are often not clearly defined, especially for POE and TPO, an attempt was made to determine the chemical structure of all films. As expected, all encapsulants displayed in Fig. 4 have a PE-based backbone which is represented in the specific CH_2 peaks at 2920 cm^{-1}, 2850 cm^{-1}, 1465 cm^{-1}, 1370 cm^{-1} and 720 cm^{-1} [46]. EVA shows peaks which result from interactions with the bonds of the vinyl acetate groups (C=O, CH_3 and C-O-C) occurring at 1780 cm^{-1}, 1736 cm^{-1}, 1715 cm^{-1}, 1370 cm^{-1}, 1238 cm^{-1} and 1020 cm^{-1} [17,47]. The POE sample shows minor absorption of a C=O bond at 1700 cm^{-1}. Consequently, it may not be pure PE, but could have C=O side groups or the peaks correspond to additive interactions. The TPO sample shows a significant C=O peak at 1736 cm^{-1}. In addition, C-H (1200 cm^{-1}), C–C (1170 cm^{-1}) and C-O-C (1020 cm^{-1}) vibrations are found for the TPO sample. These intensities and the presence of C=O vibrations are most likely caused by ethyl acrylate moieties in the copolymeric backbone of the TPO sample resulting in ethylene ethyl acrylate copolymer as possible encapsulant [48,49].

All encapsulants show peaks at 1540 cm^{-1} and 1580 cm^{-1}. These intensities are probably caused by a superposition of several effects. For the encapsulants which contain the UV stabilizer Tinuvin 770 (EVA, EVA-T, TPO), these peaks could be generated by NH deformation vibrations of the functional amine group in the beginning and do not necessarily belong to the base polymer [46]. The mentioned absorption bands have been reported in the literature for different HALS and their nitro-degradation products [51–53]. For encapsulants which contain the UV absorber Cyasorb UV 531 (EVA, POE), the absorption by the

Table 3
FTIR peak assignment for the EVA, POE and TPO encapsulant [16,17,24,46,47,50].

waven. [cm^{-1}]	group	excitation	enc.
2920	CH_2	asymmetric stretching vibration	E,P,T
2850	CH_2	symmetric deformation vibration	E,P,T
1780	C=O	stretching vibration of γ-lactones	E,T
1736	C=O	stretching vibration	E,T
1715	C=O	stretching vibration of ketones	E,T
1720–1660	C=O	stretching vibration	P
1660–1550	C=C	stretching vibration	E,P,T
1580	NH	deformation vibration	E,T
1540	NH	deformation vibration	E,T
1465	CH_2	asymmetric deformation vibration	E,P,T
1370	CH_3	symmetric deformation	E,P,T
1238	C-O-C	stretching vibration	E,T
1200	C-H	skeleton vibration	T
1170	C-C	stretching vibration	T
1020	C-O-C	stretching vibration	E,T
960	CH	out of plane deformation vibration	E
910	C-H	deformation vibration (vinyl group)	E,T
820	C-C	skeleton vibration	T
810	CH_2	deformation vibration (vinyl group)	P
720	CH_2	skeleton rocking vibration	E,P,T

stretching vibration of the benzene rings will appear in the same region and was reported for benzophenone UV absorbers in the past [46,54,55]. In addition, for the initial state of the POE encapsulant, the 1580 cm^{-1} peak could be generated by dienes which can be formed before any photo oxidation occurred [27,56]. However, based on the peak intensity of the initial encapsulant samples, this explanation is assumed to be less likely than the vibration of the benzene ring. During the aging, the formation of C=C bonds is likely to occur for all encapsulants. In detail, due to deacetylation by Norrish type 2 reactions for EVA and as a result of photo oxidation (β-scission and subsequent Norrish type reactions) for POE and TPO [27,57,58].

3.1. EVA

As displayed in Table 2 the EVA samples contain the UV absorber Cyasorb UV 531 and the UV stabilizer Tinuvin 770. The previously developed quantification procedure for UV additives allows the investigation of the UV additive consumption during UV exposure [36]. Here, EVA was treated as an example and a similar additive degradation behavior is expected for the other encapsulants as they contain comparable additive compositions. However, it must be noted that only the unreacted form of Tinuvin 770 can be detected with the used quantification procedure. While hindered amine light stabilizers (HALS) are reacting in the complex Denisov cycle it cannot be excluded that resulting fragments keep shielding the base polymer albeit the measured content is zero [59–62].

Fig. 5 visualizes the results of the additive quantification. All data points were normalized to the initial value at $t = 0$ h. Error bars are the converted standard deviation as displayed in the supporting information. The UV absorber content varies between the different weathering times for all weathering types. However, excluding the values with the maximum deviations from the average (e.g., 2250 h and 2500 h for B weathering, 0 h for A weathering an 1500 h for MAX weathering), the UV absorber content is approximately constant during the weathering for all weathering types. The mentioned maximal deviations from the average are probably the result of local inhomogeneities as they appear inconsistently. Furthermore, the UV absorber is expected to react in reversible keto-enol tautomerism without decomposition [63–65]. Considering local inhomogeneities between the different samples (e.g., different weathering steps) and neglecting the spikes, none of the used UV spectra and intensities significantly consumed the UV absorber Cyasorb UV 531. Additional UV/VIS reflection measurements (see supporting information) showed no change in reflectance behavior, which also supports this statement.

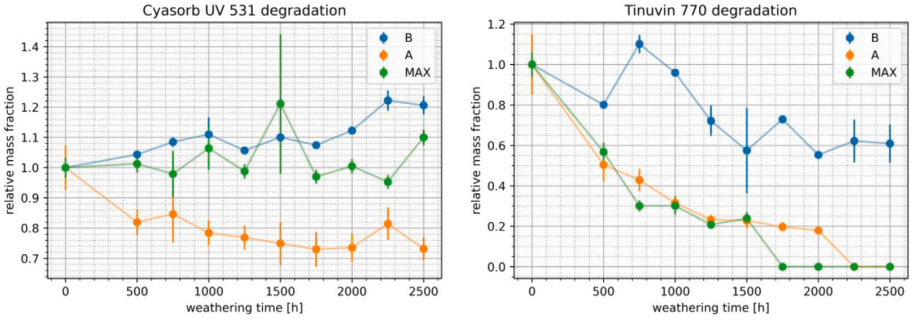

Fig. 5. Additive quantification of the UV absorber Cyasorb UV 531 (left) and the UV stabilizer Tinuvin 770 (right) in dependence of weathering time and weathering type for all EVA samples.

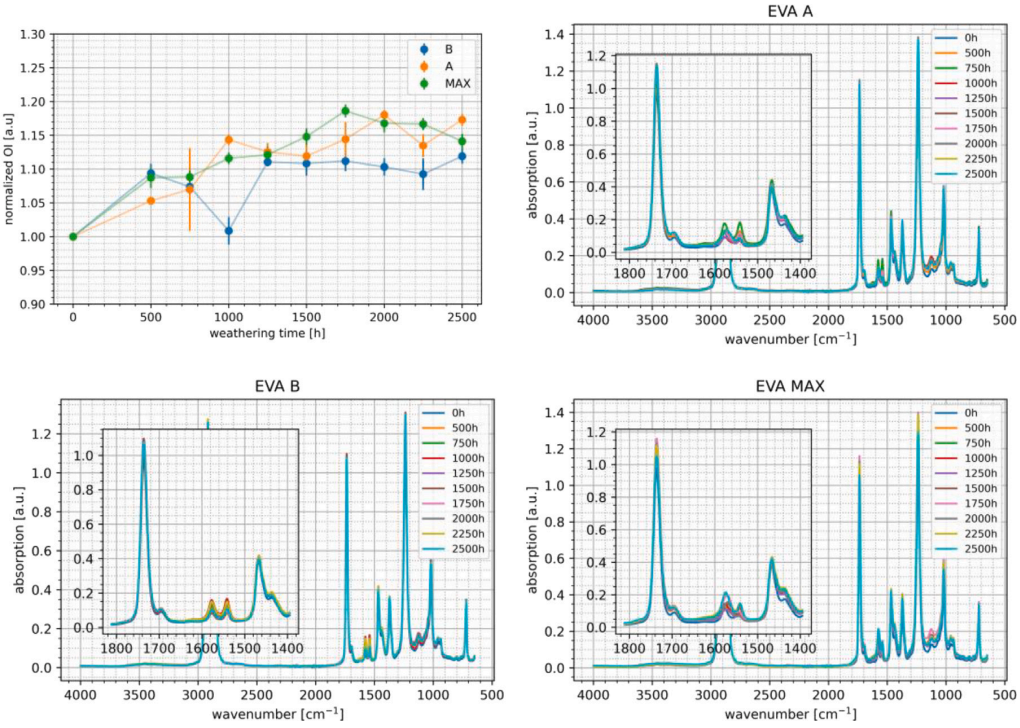

Fig. 6. FTIR measurements of the EVA samples aged under different UV conditions and the development of the calculated oxidation index (OI — top left plot) in dependence of the weathering time.

In contrast to the UV absorber, the base form of the UV stabilizer Tinuvin 770 significantly degrades. For B weathering these changes are less pronounced as for A and MAX weathering. While the increase in UV stabilizer content for 750 h and 1000 h is probably due to inhomogeneities, the content shows a decreasing trend until reaching 60% of the base concentration after 2500 h of weathering. For A and MAX weathering this behavior intensifies. Already after 500 h more than 40% of the initial UV stabilizer content is consumed. Afterwards the consumption velocity decreases until at 1500 h only 20% of the base concentration can be detected in the A and MAX samples. Until this point, the degradation was slightly increased for the MAX spectrum. After 1500 h the UV stabilizer content is fully consumed in the MAX samples. In the A samples it is further decreasing until 2000 h, afterwards it was also fully consumed.

The degradation behavior of Tinuvin 770 can be explained by the mode of action of the HALS amine. As only the base form of Tinuvin 770 can be analyzed and the molecules must react to trap radicals, the degradation kinetic is dependent on the UV stabilizer concentration [59–62]. Assuming a reservoir of radicals to react with, the degradation of the UV stabilizer should follow the first order kinetics resulting in an exponential decay of additive content. Especially for A and MAX weathering, this behavior is most pronounced in Fig. 5. Conversely this means that the B spectrum created significantly less radicals than the A and MAX spectrum which would lead to much smaller decomposition of the base polymer.

FTIR measurements of the EVA samples are displayed in Fig. 6. The degradation behavior of EVA under UV exposure is broadly discussed in the literature [17,25,26,28,47,57,66,67]. The oxidation index (OI) in the top left image is a useful measure to quantify effects of photo oxidation [17,26,67,68]. It was calculated using the ratio of the 1680 cm^{-1} to 1800 cm^{-1} C=O peak and the 690 cm^{-1} to 750 cm^{-1} CH_2 peak allowing

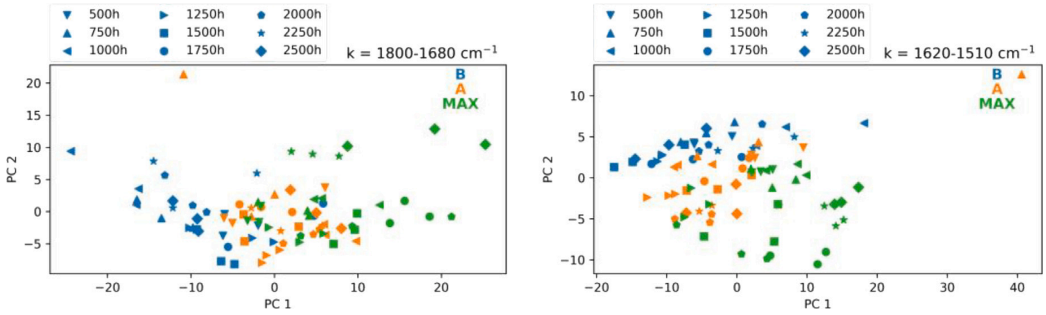

Fig. 7. PCA of the 1800 cm^{-1} to 1680 cm^{-1} peak (left) and the 1620 cm^{-1} to 1510 cm^{-1} peaks (right). The corresponding distribution of the weights of the principal components is displayed in the supporting information.

normalization of effects of different contact between the sample and the ATR crystal.

Approximating that changes in the polyethylene segments (CH_2 vibrations) of the base polymer can be neglected, most degradation effects can be observed by changes of the carbonyl group (C=O vibrations) [26,47,57,66,67]. Thus, the formation of lactones and ketones will result in an increase of the OI. Comparing the spectra in dependence of the used UV exposure, diverging behavior can be observed. While all exposure types show an increase in the OI, the smallest total changes with respect to chemical aging occur in the B spectrum. To more fully assess the changes in the C=O peak, difference spectra of spectral regions of interest were plotted and are listed in the supporting information. These show that hardly any ketone or lactone formation is observed under B weathering. Therefore, the fluorescence lamps seem to cause less damage to the vinyl acetate groups. Surprisingly, there is only a minor difference between the photo oxidation of the A and MAX spectrum. Both types of weathering show the formation of ketones and lactones in the difference spectra, but the change is more intense under MAX weathering, which could be due to possible temperature effects due to the higher irradiance. This finding emphasizes that the spectral distribution seems to be more relevant for photo oxidation of vinyl acetate groups than the integrated UV intensity at a given spectrum.

Apart from photo oxidation, further differences can be observed at the 1540 cm^{-1} and 1580 cm^{-1} peaks. In the B spectrum, these peaks are increasing until 1000 h and afterwards decreasing again. In the A spectrum, they are also increasing until 750 h and decrease afterwards. However, after 2000 h of weathering the 1540 cm^{-1} peak becomes smaller while the 1580 cm^{-1} peak becomes more pronounced. In the MAX spectrum, these peaks behave similar to the A spectrum. Here, both peaks are growing until 1000 h. Afterwards the 1540 cm^{-1} peak is decreasing, while the 1580 cm^{-1} peak is increasing.

The peak behavior can be explained by several effects considering the surface sensitive ATR-FTIR measurements and the HALS quantification by GCMS. In this consideration, the UV absorber is not taken into account, since its density is approximately constant and both NH signals always change simultaneously. The increase of the peak intensity in the B spectrum could be explained by HALS migration to the surface as it was reported in the literature [53]. After 1000 h the decrease is in accordance with the carried out quantification in Fig. 5. While for A and B weathering the migration of HALS can also occur, it was shown that the HALS content significantly decreased after 1000 h. Furthermore, the GCMS bulk measurements showed no UV stabilizer presence after 1750 h of weathering with MAX spectrum and 2250 h of A spectrum. Hence, the presence of both intensities and the broadening of the higher frequency peak suggest the formation of unsaturated C=C bonds and therefore a decomposition of the base polymer by the A and the MAX spectrum [24,26,46,50,67,69]. This consideration is also confirmed by the difference spectra (see supporting information). For the A and MAX weathering, the emergence of a C=C peak between 1660 cm^{-1} and 1580 cm^{-1} is observed after the intensity of the 1580 cm^{-1} NH peak has decreased. In addition, at 910 cm^{-1} a new peak occurs after 1750 h of MAX weathering and 2000 h of A weathering and belongs to vinyl hydrocarbon compounds containing C=C bonds [46]. These behaviors are more pronounced for MAX weathering than for A weathering. In contrast to the photo oxidation, the reactions of the 1540 cm^{-1} peak and the 1580 cm^{-1} peak are dependent on the used spectrum and the used intensity.

To further address small changes in the chemical aging behavior a PCA has been carried out comparing the behavior of the C=O peak, the NH peaks and the C=C peak while considering the weathering type. Fig. 7 visualizes the first two principal components (PC) while changes in PC 1 direction are more significant than changes in PC 2 direction. The distribution of weights of the PC is displayed in the supporting information. In addition, the graphs show color coded (A ≙ blue, B ≙ orange, MAX ≙ green) data points in dependence of used weathering type and symbol coded data points in dependence of weathering duration.

Considering the 1800 cm^{-1} to 1680 cm^{-1} C=O peak as indicator for most pronounced aging effects due to chemical changes of the vinyl acetate groups, the PCA shows clear results. The data points are clustered in dependence of weathering time and weathering type. However, the MAX data points show the widest spread. The most significant changes (PC 1 direction) occur in dependence of weathering type. Similar to the behavior of the OI, the data point overlap between the A and the MAX spectrum suggests that changes of the spectral distribution are more important than an increasing intensity with the same spectral distribution. Changes in PC 2 direction seem to be mainly caused by weathering while the MAX spectrum shows also shows changes in PC 1 direction which are caused by the aging. Due to the stated dependence on PC 1 and PC 2 direction it can be concluded that in the case of EVA, differences in the spectral distribution are more relevant than the total weathering time or intensity.

The PCA of the peaks at 1540 cm^{-1} and 1580 cm^{-1} also shows dependencies on weathering time and weathering type. As it was for the previous peak, the MAX spectrum also shows the widest spread here. However, an overlap with the B spectrum is also present. For these peaks, the most significant changes (PC 1 direction) occur due to weathering time. However, changes in PC 2 direction are mainly dependent on weathering type. In accordance with the data in Fig. 6, the peaks behave significant different in dependence of the used spectrum. As mentioned before this can be explained by a superposition of interactions with the NH bonds of the UV stabilizer and the formation of unsaturated C=C bonds due to base polymer degradation [24,26,46,50,67,69].

After the aging process, EGA FTIR measurements were used to investigate changes in the thermal decomposition behavior of samples which have been weathered for 2250 h. Fig. 8 is listing the results, showing a dependence on the used weathering type. Onset temperatures were

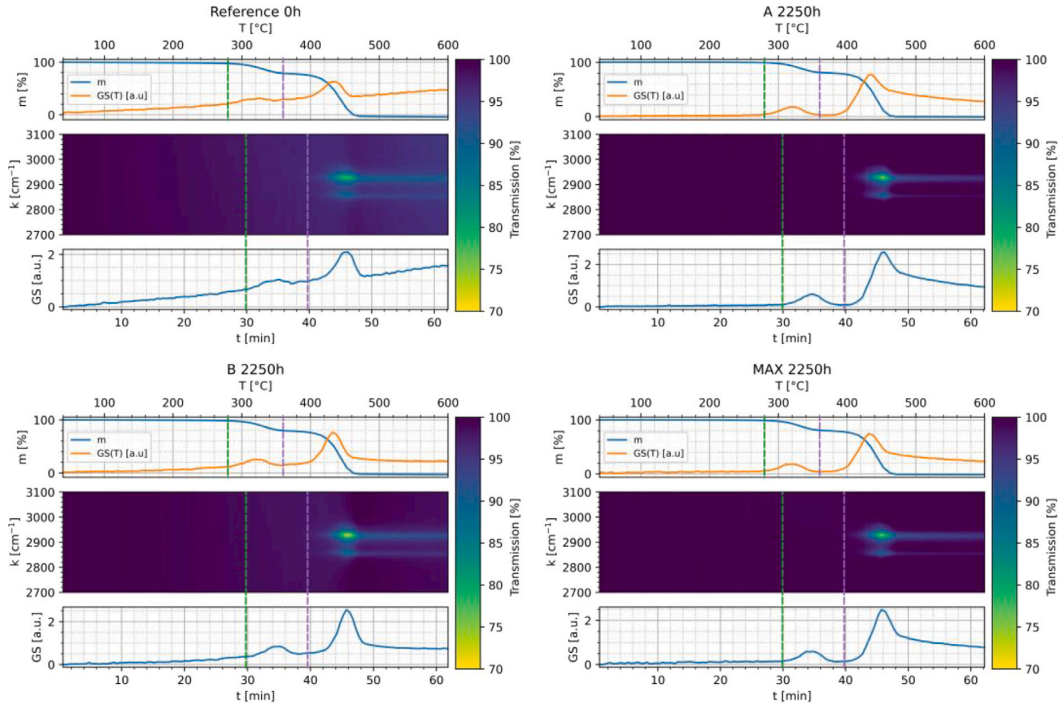

Fig. 8. EGA FTIR measurements of the EVA reference (0 h, top left), 2250 h A weathering (top right), 2250 h B weathering (bottom left) and 2250 h MAX weathering (bottom right).

defined as the point of significant mass change and correlated with the temperature dependent Gram Schmidt (GS) intensity. These changes were transferred in the GS time domain to visualize onset times in the time dependent EGA FTIR color map. As comparable changes only occur for the 2920 cm^{-1} and 2850 cm^{-1} peaks in the FTIR spectrum, this region was enlarged for the weathered samples. The complete spectrum can be found in the supporting information.

The TGA curves in Fig. 8 show the expected behavior. First, a mass loss starting approximately at 280 °C after 30 min (marked as green line in the plot) because of the release of acetic acid. Second, a mass loss starting at approximately 360 °C after 40 min (marked as purple line in the plot) as a result of the rupture of hydrocarbon chains [70]. Both decomposition steps are also visible in the FTIR color map (see supporting information for the color map version without zoom). The first weight loss step shows a transmission decrease at 1750 cm^{-1} (C=O interaction) and 1250 cm^{-1} (C-O-C interaction) because of the vinyl acetate decomposition (see supporting information). The weight loss step shows interactions at 2920 cm^{-1} and 2850 cm^{-1} (CH_2 vibrations) as a result of the basis polymer decomposition.

As visible in the pictures, the measured TGA behavior of both decomposition steps is not changing in comparison with the reference sample for all weathering types. However, comparing the intensity distribution of the 2920 cm^{-1} and 2850 cm^{-1} peaks an interesting observation can be made. In comparison with the B weathering and the reference sample, the peak center of the 2920 cm^{-1} peak is slightly shifted to earlier times for the A and MAX weathering resulting in a symmetric peak shape. These finding suggest a different decomposition behavior of the second weight loss step in dependence of weathering time and weathering type. Considering the previous FTIR measurements and the potential formation of unsaturated carbon bonds, the second weight loss step could contain a superposition of two effects which cannot be separated by a simple TGA measurement. Marcilla et al. showed that a superposition of C–C and C=C decomposition can occur in the second weight loss step of EVA [71–73]. The shift of the intensity maximum to earlier times (and therefore lower temperatures) for the A and MAX weathering is probably a result of the C=C bond decomposition. The double bonds produced in EVA chains by thermal photo oxidation render the polymer chains less thermally stable, because of the chain scission enabled by the transfer of the reactive hydrogen in the allylic position [74–76].

3.2. EVA-T

Fig. 9 is visualizing the FTIR measurements of the EVA-T samples. The OI in the top left image was calculated as it was done for the EVA samples. In general, the OI changes are comparable with the aging behavior of the EVA samples. However, the OI increase is less consistent in dependence of the weathering time. As it was for the EVA samples, the smallest change of the OI was also occurring in the B spectrum for the EVA-T samples. In addition, there is only a minor difference of the OI development in the A and MAX spectrum. Considering the difference spectra in the supporting information, the B weathering does not show significant changes. However, the A and MAX weathering generated peak shoulders at 1780 cm^{-1} and 1715 cm^{-1} indicating the formation of ketones and lactones.

In contrast to the minor changes of the OI and the coupled 1750 cm^{-1} C=O peak, the 1580 cm^{-1} and 1540 cm^{-1} peaks show a diverging behavior in dependence of weathering type and weathering time. For the B weathering, both peaks are continuous decreasing until they are nearly vanished after 2500 h. Similar but less pronounces as for the EVA samples, the A and MAX weathering result in a decrease of the 1540 cm^{-1} peak. After approximately 1500 h the double peak is broadening nearly merging to a single peak with the peak center at approximately 1570 cm^{-1}. This behavior is confirmed by the difference spectra displayed in the supporting information. For B weathering, only the decrease of both peaks is observable. A and MAX weathering show

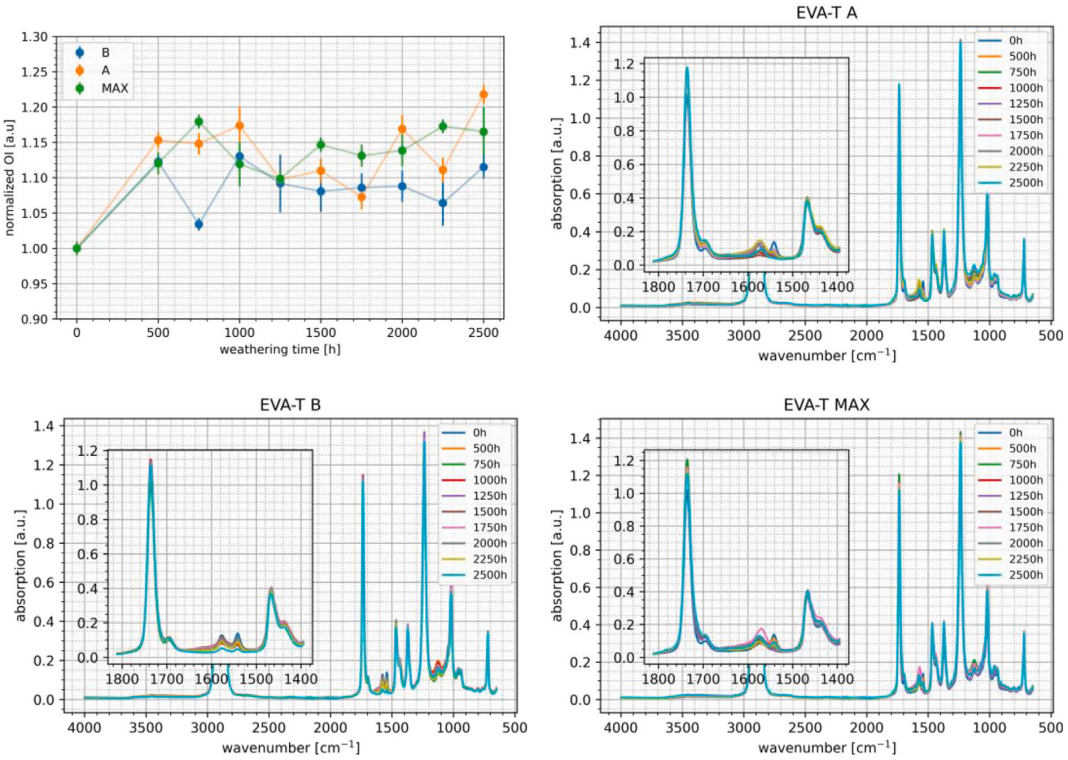

Fig. 9. FTIR measurements of the EVA-T samples aged under different UV conditions and the development of the calculated oxidation index (OI — top left plot) in dependence of the weathering time.

an increasing C=C peak between 1580 cm^{-1} and 1660 cm^{-1}. Additionally, the 910 cm^{-1} vinyl peak which was also occurring for the EVA samples is forming after 2000 h of A weathering and 1500 h of MAX weathering.

Considering that the difference between the EVA and EVA-T samples lays only in the missing UV absorber, the HALS degradation should occur in a similar way. This explains the continuous decrease of the 1540 cm^{-1} and 1580 cm^{-1} peak in the B spectrum whereas the intensity was probably too low to form C=C bonds and vinyl groups. In contrast, the A and MAX spectrum behave similar to results from the EVA samples. Here, the 1540 cm^{-1} peak is decreasing and both peaks merging to one. As previously discussed for EVA, this behavior could be a result of the formation of C=C bonds by base polymer degradation [24,26,46,50,67,69]. Considering the missing UV absorber in the EVA-T samples some remarks can be made. The OI of the EVA-T samples reaches higher values at the end of the weathering period for the A and MAX spectrum in comparison with the EVA samples. Here, the B weathering was leading to more or less the same result for both encapsulants. Also the emerging vinyl peaks at 910 cm^{-1} are more pronounced as in the case of EVA. Thus, photo oxidation seems to be minimally enhanced with missing UV absorber when using a xenon spectrum. However, the behavior of the 1580 cm^{-1} and 1540 cm^{-1} peaks is approximately equal suggesting similar effects regarding the C=C bond formation.

The PCA of the EVA-T samples is displayed in Fig. 10. The approach and the investigation of corresponding peaks are similar as it was done for the EVA samples. Investigating the 1800 cm^{-1} to 1680 cm^{-1} interval the trend which was observed for the EVA samples intensifies. Largest differences are occurring in dependence of the used spectrum. Especially for the B weathering, the observed differences in PC 1 direction are comparatively small. Here, the most variations can be observed in PC 2 direction because of the aging time. The A and MAX weathering show a much wider spread. Furthermore, the data points are overlapping much more with each other than with the B weathering which is not surprising considering the approximately similar OI development. However, the weathering time has a much higher influence on the absorbance values (changes in PC 1 direction) of the A and MAX weathering as it was for the B weathering. Also, for the EVA-T samples, the differences in the spectral distribution are probably more relevant than the total weathering time.

Also the 1620 cm^{-1} to 1510 cm^{-1} interval shows a similar trend in comparison with the EVA samples. The most significant changes for all weathering types occur in dependence of weathering time. However, in PC 2 direction the changes are clearly dependent on the weathering type. Here, the B weathering has a comparatively small spread. In contrast, the A and the MAX weathering are not clearly distinguishable. This is not surprising as the changes within the FTIR spectra behaved approximately similar. However, considering the missing UV absorber (in comparison with the EVA samples), the C=C bond formation in this absorption region could be affected and leading to a similar degradation behavior for the A and MAX weathering.

Fig. 11 is visualizing the EGA FTIR measurements of the EVA-T samples. The general thermal behavior of the reference sample is equal to the EVA reference resulting in the same onset and plateau temperatures. In addition, all previously discussed peaks and the characteristic decomposition of the vinyl acetate and PE groups are also observable [70]. Comparing the peak center of the 2920 cm^{-1} CH_2 peak with the reference, no time shift (temperature shift) is observable. In contrast to the B weathering, the A and MAX samples show the same peak shift to earlier times (temperatures) of the 2920 cm^{-1} intensity as it was the case for the EVA samples. Considering the similarities of the FTIR spectra development, the above discussed superposition of C–C

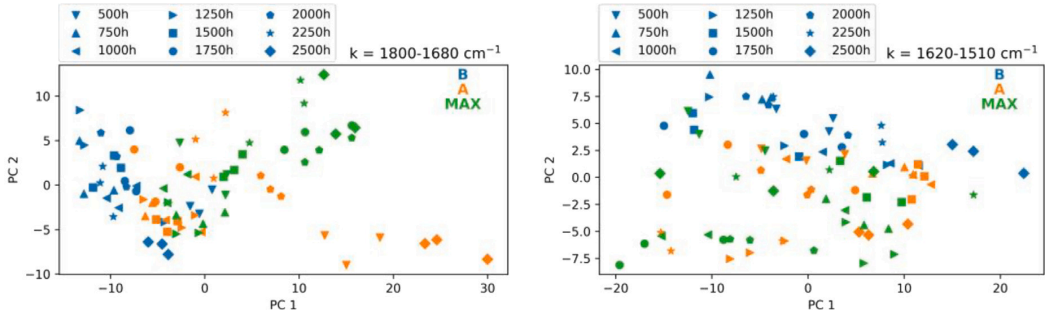

Fig. 10. PCA of the 1800 cm^{-1} to 1680 cm^{-1} peak (left) and the 1620 cm^{-1} to 1510 cm^{-1} peaks (right). The corresponding distribution of the weights of the principal components is displayed in the supporting information.

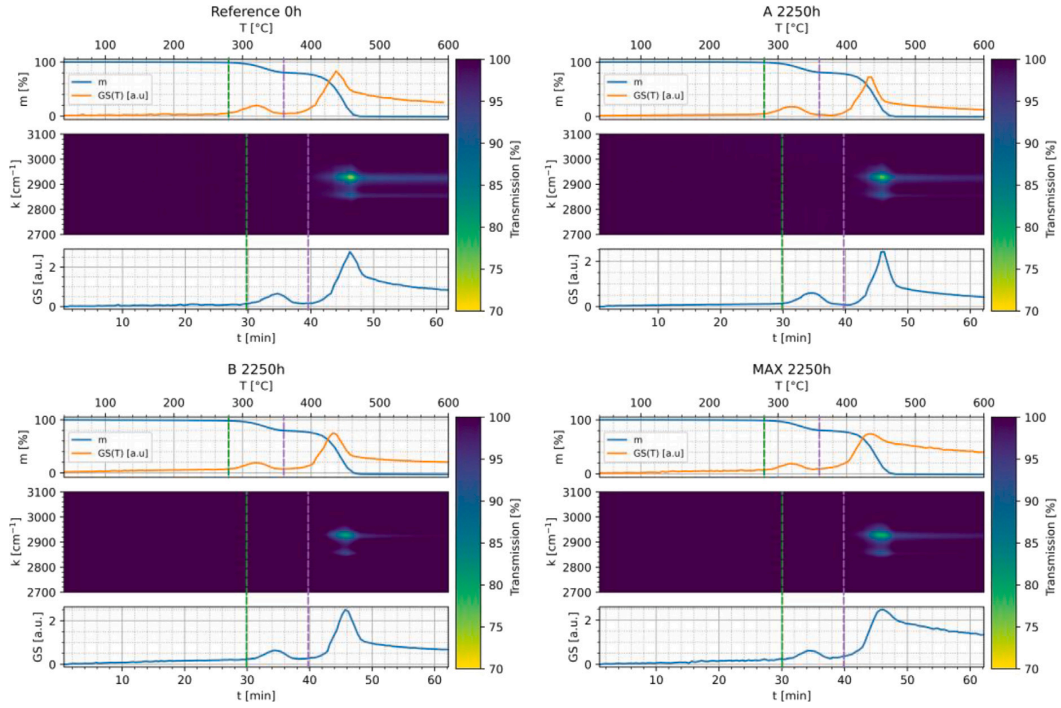

Fig. 11. EGA FTIR measurements of the EVA-T reference (0 h, top left), 2250 h A weathering (top right), 2250 h B weathering (bottom left) and 2250 h MAX weathering (bottom right).

and C=C decomposition is also conceivable for the EVA-T samples [71–73]. As a result, the EVA-T samples are more damaged by the A and MAX spectrum than by the B spectrum.

3.3. POE

The FTIR measurements are displayed in Fig. 12. The POE samples do not contain any vinyl acetate groups. Thus, discussing the degradation behavior with an OI is only possible when significant aging and the presence of oxygen occurred which was not the case within the weathering time. Also the difference spectra, displayed in the supporting information, do not show significant changes in the carbonyl region. Furthermore, comparing PE peak intensities with each other will not lead to interpretable results. For these reasons, the evaluation will focus on changes of the 1580 cm^{-1}, 1540 cm^{-1}, and 1465 cm^{-1} peaks. As mentioned in the beginning, the peaks occurring at 1580 cm^{-1} and 1540 cm^{-1} can be a result of several binding interactions. In the case of POE, they are most likely a result of formed C=C bonds by polymer degradation and C=C bonds of the benzene rings of Cyasorb UV 531 [24,27,46,50].

Investigating the 1620 cm^{-1} to 1510 cm^{-1} region, the absorption behavior is diverging between the different weathering methods. The B weathering is showing a pronounced double peak from the beginning of the weathering until 2500 h. However, the absorption value is decreasing until approximately 1500 h and increasing afterwards until the end of the weathering period. For the A weathering, this region shows a pronounced double peak which is decreasing until 1000 h. Afterwards the peaks are inconsistently increasing and decreasing until the end of the weathering period. However, after 1000 h, the 1580 cm^{-1} peak becomes broader nearly merging with the 1540 cm^{-1} peak at later weathering times. This behavior intensifies for the MAX weathering. The peaks are also decreasing until 1000 h with an increase afterwards, but the broadening of the 1580 cm^{-1} peak already starts after 500 h. The investigations are confirmed by the difference plots displayed in the

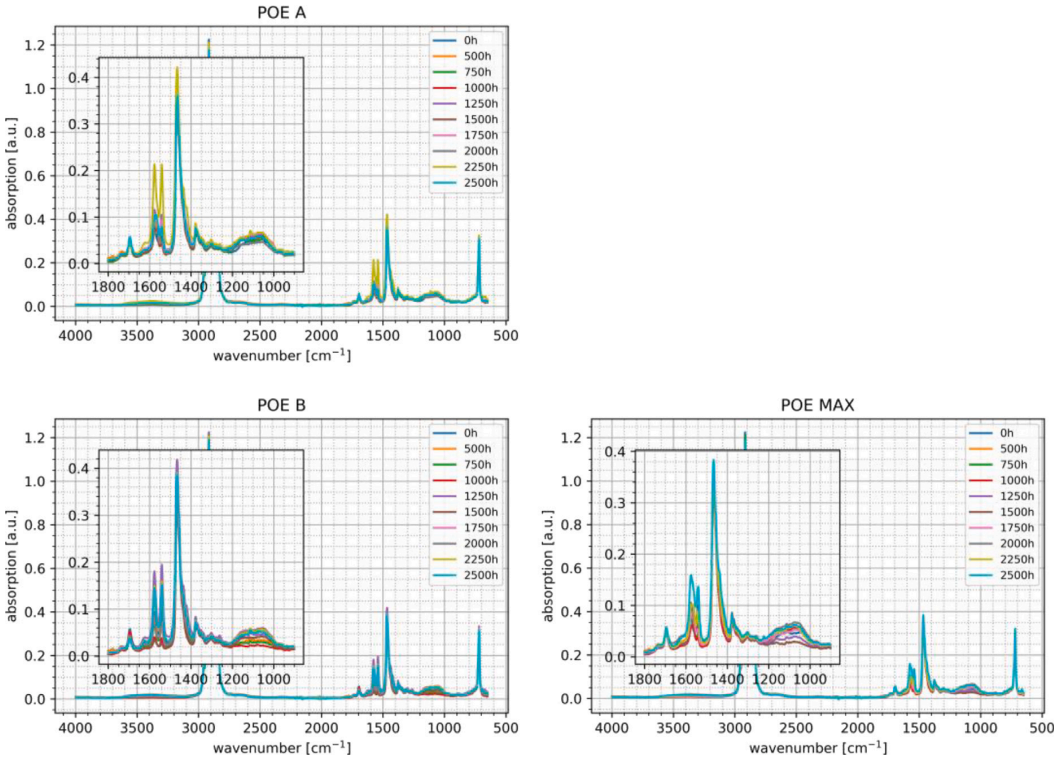

Fig. 12. FTIR measurements of the POE samples aged under different UV conditions in dependence of the weathering time.

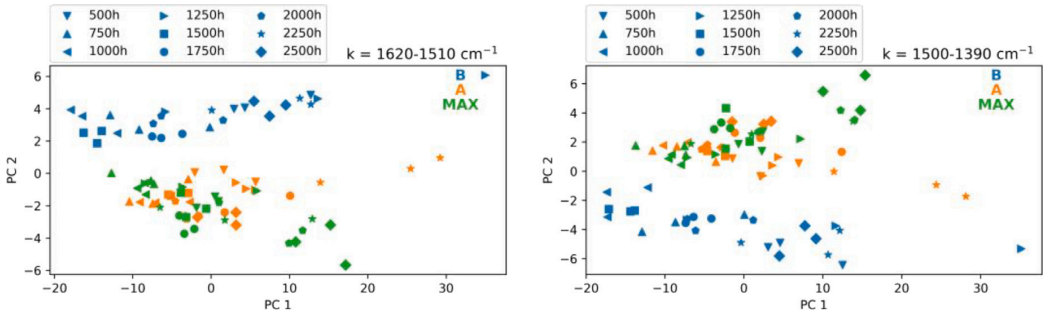

Fig. 13. PCA of the 1620 cm^{-1} to 1510 cm^{-1} peak (left) and the 1500 cm^{-1} to 1390 cm^{-1} peaks (right). The corresponding distribution of the weights of the principal components is displayed in the supporting information.

supporting information. Additionally, a peak at 810 cm^{-1} is emerging during MAX weathering and corresponds to vinyl compounds [46]. As previously argued, the peak emerging of the A and MAX weathering could be explained by the formation of C=C bonds. Thus, the B spectrum seems to inflect only minor damage to the POE encapsulant whereas the A and MAX spectrum force chemical aging processes to occur. In addition, these processes are dependent on the irradiation intensity because the MAX spectrum is forcing changes in the absorption values much faster than the A spectrum.

Fig. 13 shows the PCA of the 1620 cm^{-1} to 1510 cm^{-1} double peak area and the 1465 cm^{-1} PE peak. The latter was chosen to discuss changes in the PE base structure with respect to the CH_2 interactions. Considering the previous FTIR analysis, the PCA results show an expected behavior. The data is clustered in dependence of the weathering type and the weathering time while changes in PC 1 direction are more significant than changes in PC 2 direction.

Absorption values in the 1620 cm^{-1} to 1510 cm^{-1} interval show the most significant changes in dependence of weathering time. However, the second most significant changes occur in dependence of weathering type. Here, the data of the A and MAX weathering is clustered together while the B weathering is separated. A similar behavior can be observed for the 1465 cm^{-1} PE peak. Again, the most significant changes occur in dependence of the aging time. The data is also clustered in dependence of the weathering type representing the second most significant changes. Considering that the C=C formation must be a result of the PE degradation and is represented by changes of the 1465 cm^{-1} peak, the correlation between both investigated areas is not surprising. As it was the case for EVA, these finding suggests that the used weathering intensity within one xenon spectrum has less influence on the aging behavior of POE than using a different lamp spectrum. Thus, the result is in accordance with the previous reported C=C bond formation by FTIR which was mainly occurring for the A and MAX spectrum.

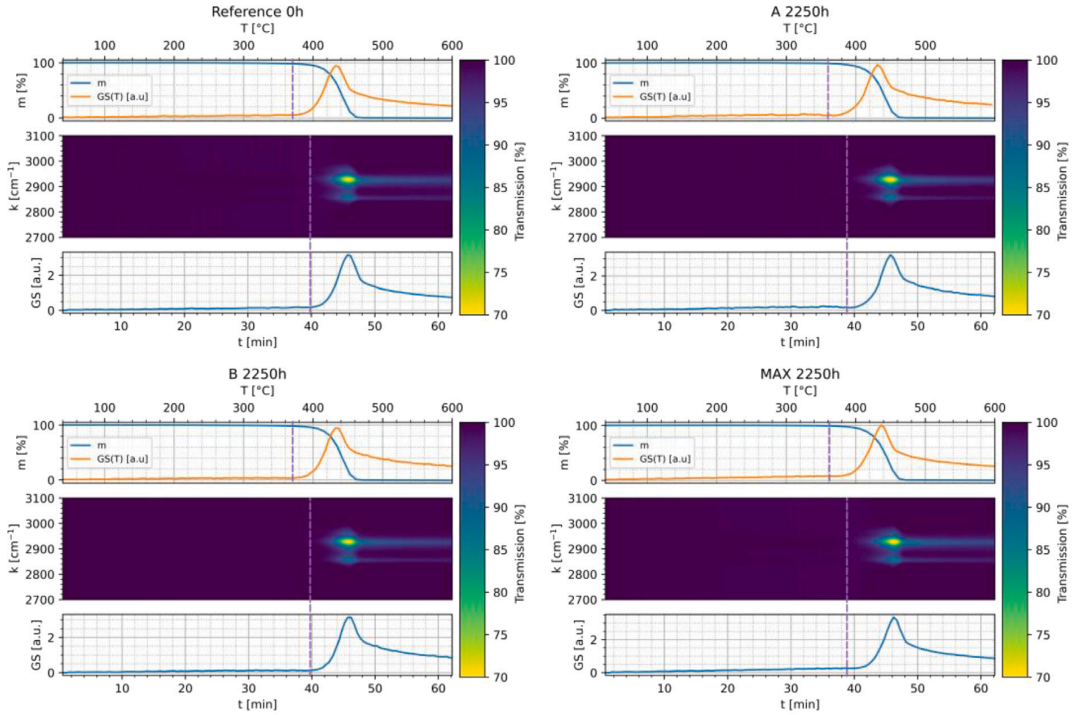

Fig. 14. EGA FTIR measurements of the POE reference (0 h, top left), 2250 h A weathering (top right), 2250 h B weathering (bottom left) and 2250 h MAX weathering (bottom right).

The EGA FTIR measurements are displayed in Fig. 14. As shown in Fig. 4 and Fig. 12, the POE samples mainly contain polyethylene groups. Thus, a single weight loss step showing the rupture of the hydrocarbon chains in the TGA analysis of the EGA FTIR is not surprising [70]. In Comparison with the EVA samples, the POE encapsulant shows a slightly higher thermal stability in the initial state starting to decompose at approximately 370 °C after 40 min (marked as purple line in the plot). The FTIR color map shows the 2920 cm^{-1} and the 2850 cm^{-1} CH_2 absorptions as most pronounce peaks, but also the 1465 cm^{-1} CH_2 absorption is visible.

Comparing the B weathering with the reference sample, the initial decomposition temperature did not change. However, the FTIR colormap shows minimal shift of the 2920 cm^{-1} peak center to later times. The A and MAX spectrum start to decompose at approximately 360 °C indicating a loss of thermal stability due to the weathering. As a result, the decomposition starts after approximately 39 min. Furthermore, the peak center of the 2920 cm^{-1} peak is shifted further to later times. As it was for the second weight loss step of the EVA measurements, the degradation probably also changed the decomposition behavior of the POE encapsulant. The earlier onset of the A and MAX weathering in combination with the peak center shift of the 2920 cm^{-1} peak to later times is most likely a result of the decomposition of smaller structures. Moieties containing C=C bonds which have been created by photo degradation decompose at first before saturated hydrocarbon chains are released. Here, the argumentation about the lowering the thermal stability of the polymer backbone by C=C bond formation is similar as for the EVA case [74–76].

3.4. TPO

Fig. 15 visualizes the FTIR measurements of the TPO samples. Chemical changes of the ethyl acrylate moieties, especially the C=O absorption at 1750 cm^{-1}, are used as a degradation marker. This approach assumes that photo oxidation occurs in a similar way as it happens for the EVA and EVA-T samples. In detail, changes of the C=O absorption behavior are caused by polymer chain decomposition. Thus, the OI in the top left image was also calculated using ratio of the 690 cm^{-1} to 750 cm^{-1} CH_2 peak and the 1680 cm^{-1} to 1800 cm^{-1} C=O peak. The OI development of the TPO samples behaves similar to the EVA samples resulting in the smallest changes for the B spectrum. The A and MAX weathering result in a higher increase of the OI, however, the difference between both weathering types is rather small. As it was the case for EVA, the OI is higher influenced by the spectral distribution than by changes of the intensity within the same spectrum. Considering the difference spectra (see supporting information), a broadening of the C=O peak and therefore the formation of ketone and lactone species was only found for A and MAX weathering.

The TPO samples show the most significant changes of the 1580 cm^{-1} and 1540 cm^{-1} peaks in dependence of weathering type. For the B weathering, both peaks are continuous decreasing in dependence of weathering time. This could be a result of UV additive decomposition or migration into the backsheet as it was the case for EVA [53]. However, no signs of C=C bond formation have been found. The A spectrum shows a double peak in the beginning. After 1000 h the 1540 cm^{-1} peak starts to decrease while the 1580 cm^{-1} peak is increasing. After 2000 h both peaks are nearly formed to a single peak with the maximum shifted to 1570 cm^{-1}. This behavior intensifies for the MAX spectrum. Here, the formation into a single peak starts at 750 h. Already after 1500 h both peaks are merged with the maximum shifted to 1570 cm^{-1}. This behavior is confirmed by the difference plots in the supporting information. For B weathering, no evidence of a emerging peak was found. However, for A and MAX weathering a significant peak between 1660 cm^{-1} and 1580 cm^{-1} is emerging. Additionally, the for EVA and EVA-T reported vinyl peak at 910 cm^{-1} can be observed after 2500 h of A weathering an 1750 h of MAX weathering [46]. As it was for the

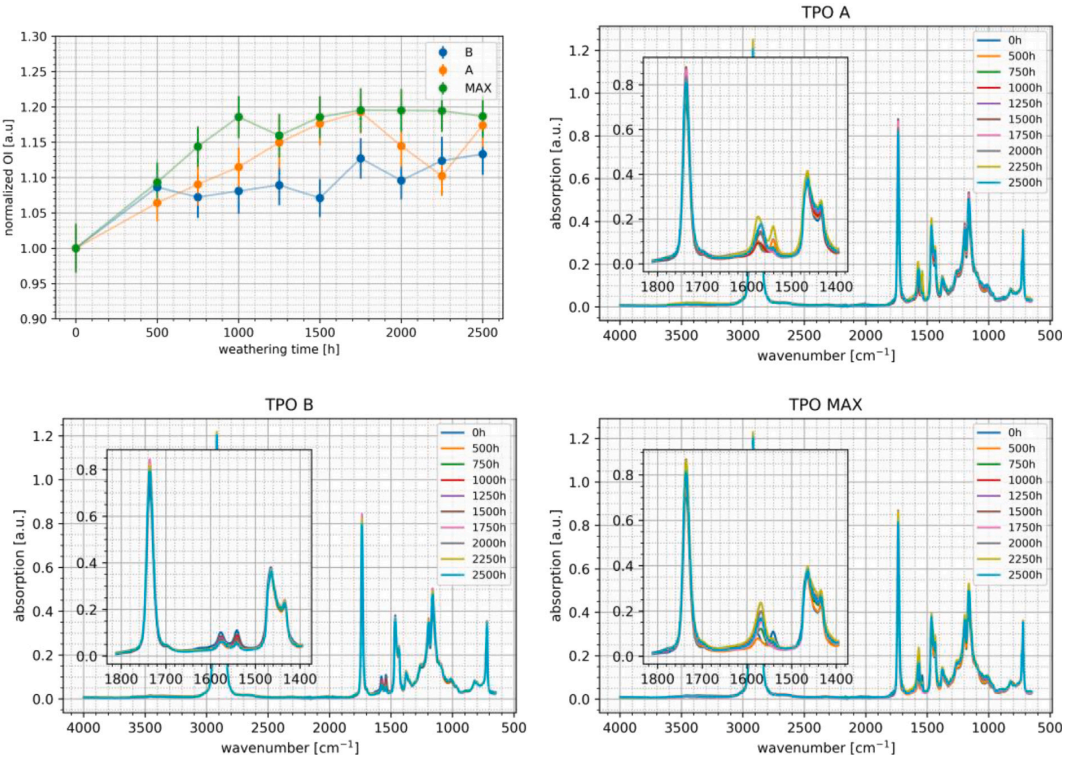

Fig. 15. FTIR measurements of the TPO samples aged under different UV conditions and the development of the calculated oxidation index (OI — top left plot) in dependence of the weathering time.

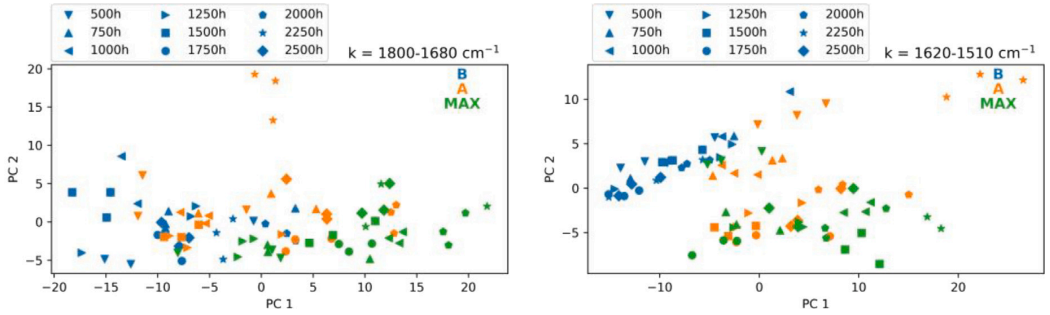

Fig. 16. PCA of the 1800 cm^{-1} to 1680 cm^{-1} peak (left) and the 1620 cm^{-1} to 1510 cm^{-1} peaks (right). The corresponding distribution of the weights of the principal components is displayed in the supporting information.

EVA and POE samples, the TPO samples probably show the formation of C=C bonds for the A and the MAX spectrum. In addition, this degradation is dependent on the used lamp intensity resulting in much faster changes after MAX weathering. Again, the B spectrum did only result in minor chemical aging of the encapsulant.

Fig. 16 visualizes the PCA of the TPO samples. The rather small differences of the OI development result in a wide spread of data points for all weathering types in the PCA of the 1800 cm^{-1} to 1680 cm^{-1} interval. While the PCA shows differences in dependence of weathering type and weathering time in PC1 direction, the data did not build clear clusters. However, the MAX spectrum did not overlap with the B spectrum, but with the A spectrum. As it was found for the EVA and POE samples, this further indicates that differences of the spectral distribution could be more important than intensity changes within the same spectrum.

As it was displayed in the FTIR measurements in Fig. 15, there are huge differences of the 1620 cm^{-1} to 1510 cm^{-1} interval in dependence of weathering type and weathering time. The PCA shows that the most significant changes occur in dependence of weathering type. However, changes within the B and MAX weathering are mainly driven by weathering time (spread in PC 1 direction). The impact of weathering time on changes of the spectrum is less pronounced for the A weathering (spread in PC 2 direction). Considering the clustering of the A and MAX spectrum the previously observed trend continues. Also, for the 1620 cm^{-1} to 1510 cm^{-1} interval, differences of the spectral distribution seem to have higher impact on chemical changes than different intensities within one spectrum.

Fig. 17 shows the EGA FTIR measurements of the TPO samples. As shown in Fig. 4 and Fig. 15 the TPO samples most likely contain ethyl acrylate moieties coupled to PE units. This results in intensities at

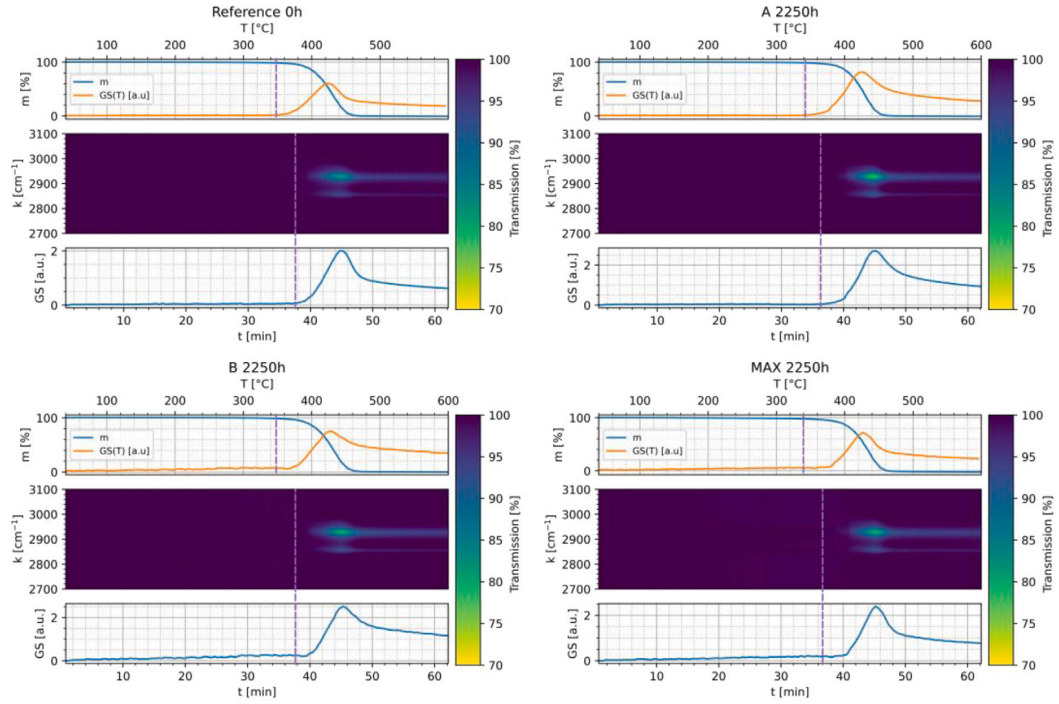

Fig. 17. EGA FTIR measurements of the TPO reference (0 h, top left), 2250 h A weathering (top right), 2250 h B weathering (bottom left) and 2250 h MAX weathering (bottom right).

2920 cm^{-1}, 2850 cm^{-1}, 1750 cm^{-1}, 1465 cm^{-1} and 1170 cm^{-1}. In contrast to the EVA samples, the TPO samples only show one weight loss step. If the TPO samples contain ethyl acrylate moieties, they are decomposing simultaneously with the PE units. In comparison with EVA and POE, the TPO samples show the lowest thermal stability starting to decompose at approximately 350 °C after 38 min (marked as purple line in the plot).

After B weathering, the onset temperature remains similar. However, the peak center of the 2920 cm^{-1} peak is shifted slightly to later times (similar to the POE results). While there was no evidence for C=C bond formations in the FTIR measurements, this shift could be a result of smaller structures which are released before larger PE fractions decompose. The A and MAX weathering resulted in a decrease of thermal stability with onset temperatures of approximately 340 °C after 37 min. Here, the peak center of the 2920 cm^{-1} peak is further shifted to later times like it was the case for the EVA and POE samples. Considering the data, the above discussed explanations for the peak shift of the EVA and POE encapsulants are most likely also valid for the TPO as it consists of the same PE backbone [74–76].

4. Summary of the results and discussion

A large number of coupons, imitating a typical PV-module composition, based on common encapsulant types (EVA, POE, TPO) were manufactured and aged using two UV lamp types (xenon and fluorescence), as required by the standard IEC62788-7-2 for a total weathering time of 2500 h. The sample analysis was carried out every 250 h to track chemical changes on the polymer and additive level. In general, all samples showed only minor degradation effects during the UV exposure brought about by a good stabilization in the studied PV encapsulants. However, the effects of the UV lamp spectra could be clearly recognized.

In this study total UV doses of 110 kWh/m^2 (B), 202.5 kWh/m^2 (A) and 300 kWh/m^2 (MAX) between 300 nm to 400 nm were applied. These doses equal 1.2 years (B), 2.1 years (A) and 3.4 years (MAX) of outdoor exposure in the example of Sanary, France (moderate climate, other sites can be also seen in Fig. 18) [10]. All observed effects are summarized in Table 4. Due to the combined characteristics of the weathering parameters defined by the standard, a clear distinction between thermally induced degradation and degradation forced by the UV irradiation is not possible.

None of the samples showed changes in the reflection behavior or browning effects. The observed delamination of the POE samples was associated with the missing adhesion promoter (see Table 2), which was the case only for the aging with a xenon lamp. A minor decrease in thermal stability was only observed for the POE and TPO samples after xenon weathering.

The quantitative UV additive analysis of the EVA samples has shown that the UV absorber content was not affected by the weathering conditions despite using glass which is transparent in the UV region (see Fig. 2). Thus, reversible keto-enol tautomerism of the UV absorber Cyasorb UV 531 is assumed [63–65]. In contrast to the UV absorber, the UV stabilizer showed severe consumption due to the underlying mode of operation [59–62]. For A and MAX weathering, the content of the base molecule was fully consumed which indicates enhanced radical formation in comparison with the B weathering.

An increase of the OI was found for the EVA, the EVA-T and the TPO samples and to be more intense after A and MAX weathering. In addition, the formation of significant peak shoulders of the carbonyl peak (C=O, 1750 cm^{-1}), indicating the formation of ketones and lactones, were detected only after xenon weathering [17,28,47,57,66]. Thus, the applied xenon spectra inflicted different changes to the ethyl acrylate and vinyl acetate group than the fluorescence spectrum.

The results of the EGA-FTIR measurements also show the different aging behavior of the encapsulants depending on the selected spectrum. As the measurements have shown, it can be assumed that

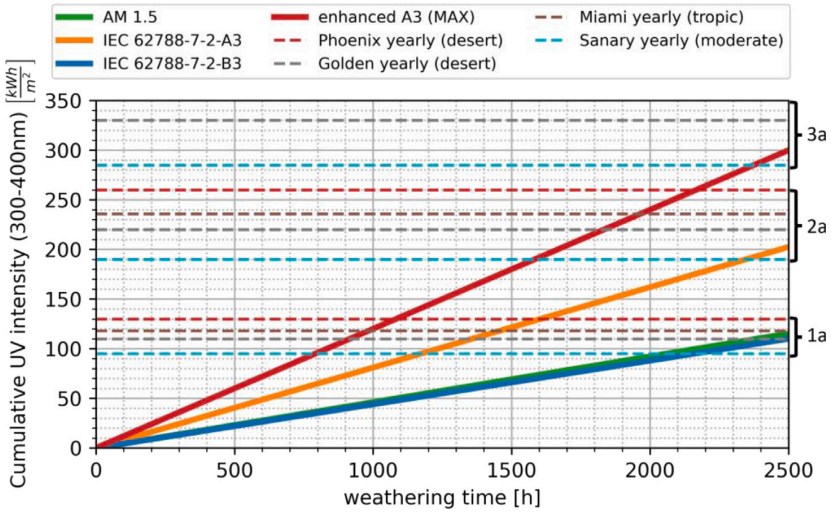

Fig. 18. Cumulative UV dose of the used weathering conditions in dependence of the weathering time. The dashed lines represent the cumulative UV dosage of 1 year (1 a), 2 years (2 a) and 3 years (3 a) at different locations. [10].

Table 4
Summary of the occurring effects within 2500 h of weathering for all encapsulant types and weathering parameter sets. Changes are indicated as follows: — no changes, ↑ increase, ⇑ strong increase, ↓ decrease, ⇓ strong decrease. The level of changes only represents the comparison within this study. The UV/VIS reflection measurements and the delamination of the POE samples are displayed in the supporting information (S.I.). All empty points have not been evaluated: The additive quantification was only carried out for the EVA encapsulants because the quantification procedure requires a set of calibration samples [36]. Due to minimal photo oxidation of the POE samples, the results of the OI were not interpretable.

Effect	EVA			EVA-T			POE			TPO		
	B	A	M	B	A	M	B	A	M	B	A	M
reflection (see S.I.)	–	–	–	–	–	–	–	–	–	–	–	–
browning	–	–	–	–	–	–	–	–	–	–	–	–
delamination (see S.I.)	–	–	–	–	–	–	–	↑	⇑	–	–	–
UV absorber content	–	–	–									
UV stabilizer content	↓	⇓	⇓									
oxidation index	↑	⇑	⇑	↑	⇑	⇑				↑	⇑	⇑
C=C bond formation	–	↑	⇑	–	↑	⇑	–	↑	⇑	–	↑	⇑
thermal stability	–	–	–	–	–	–	–	↓	↓	–	↓	↓

the xenon spectrum damages the encapsulants more severely. Consequently, smaller polymer fragments formed by UV radiation desorb already at lower temperatures. As discussed earlier, it is even possible that the desorption of C–C and C=C groups overlaps and explains the shift in measured peak intensity at similar desorption temperature [71–73].

The C=C bond formation was found for all encapsulants, but only after weathering with a xenon lamp. Considering the cumulative dosage mentioned above and displayed in Fig. 18, C=C bonds should have also been formed during the end of the B weathering if only the total UV dosage is relevant. However, as they appeared already after 750 h of A weathering (see the TPO FTIR results) but not during the whole duration of B weathering, the cumulative dosage is a misleading stress measure. Thus, considering an equal chamber temperature at B and A weathering, the differences in photo oxidation and C=C bond formation were caused by the applied lamp spectrum.

The formation of these C=C bonds is a result of the Norrish type 2 reactions in EVA and intramolecular hydrogen transfer followed by β-scission in POE [25,26,28,47,57,66,77]. As TPO contains ethyl acrylate moieties, the xenon spectrum can lead to the chain cleavage and the formation of groups containing C=C bonds and was proofed by the emerging 910 cm^{-1} peak [46,49].

In addition, the mentioned C=C peak formation as a result of polymer aging was observed in modules that were in the field for 18 and 21 years, respectively [69,78,79]. These modules contained EVA as encapsulant and a significant peak at approximately 1600 cm^{-1} occurred in both works. Consequently, it is necessary that realistic aging tests reflect this behavior. In the case of this work, weathering for 2500 h under B conditions did not lead to the formation of C=C bonds. At this time, it is not possible to determine the exact triggers for the failure of C=C bond generation under fluorescence weathering, but likely the reduced UV irradiation between 300 nm and 400 nm as well as missing visible light or infrared radiation component is partly responsible for the bond formation. Further basic research is needed in this area to clarify the exact cause of bond formation. Nonetheless, it can be assumed that the fluorescence spectrum under B conditions is unsuitable to realistically represent the aging of encapsulants with respect to the formation of C=C bonds.

5. Conclusion

The used accelerated aging tests cover less than 10% of the typical module's lifetime (see figure Fig. 18). Furthermore, other important stressors such as thermomechanical stresses, increased humidity, the influence of the system voltage and temperature fluctuations are missing. Nevertheless, already with the weathering methods used, a clear dependence of the aging behavior on the irradiation spectrum can be observed.

To ensure comparability between different laboratories, the use of standards is useful. However, a special care should be taken to ensure that the weathering tests can also represent real conditions. Furthermore, the given work has shown that for a weathering duration of 2500 h and the used sample compositions, strong deviations in aging behavior can be observed within the same standard depending on the choice of the spectrum. The typical statement that samples were weathered according to a standard should therefore be regarded with caution if no more detailed information on the spectrum is given or the cumulative UV dose is used.

While the IEC 62788-7-2 recommends weathering times up to 4000 h, the aging distinctions between the different lamp spectra were already clearly observable within 2500 h of weathering. On basis of the findings, the use of spectra similar to the natural sun spectrum (e.g., xenon lamps with daylight filters) should be considered as a

matter of choice for conducting realistic accelerated weathering studies. Especially, the insufficient UV dosage requirement imposed by the IEC 61215 should be reconsidered as this could lead to extreme overestimations in the assessed reliability of polymer encapsulants.

CRediT authorship contribution statement

Robert Heidrich: Writing – review & editing, Writing – original draft, Visualization, Validation, Software, Methodology, Investigation, Formal analysis, Data curation, Conceptualization. **Chiara Barretta:** Writing – review & editing, Validation, Methodology, Conceptualization. **Anton Mordvinkin:** Writing – review & editing, Validation, Supervision, Conceptualization. **Gerald Pinter:** Writing – review & editing, Supervision, Resources, Funding acquisition. **Gernot Oreski:** Writing – review & editing, Supervision, Resources, Funding acquisition, Conceptualization. **Ralph Gottschalg:** Writing – review & editing, Supervision, Resources, Funding acquisition, Conceptualization.

Declaration of competing interest

The authors declare that they have no known competing financial interests or personal relationships that could have appeared to influence the work reported in this paper.

Data availability

Data will be made available on request.

Acknowledgments

We acknowledge support by the German Research Foundation (Deutsche Forschungsgemeinschaft DFG) - project number 491460386 - and the Open Access Publishing Fund of Anhalt University of Applied Sciences. Furthermore, we acknowledge funding by TotalEnergies.

Appendix A. Supplementary data

Supplementary material related to this article can be found online at https://doi.org/10.1016/j.solmat.2023.112674.

References

[1] M. Aghaei, A. Fairbrother, A. Gok, S. Ahmad, S. Kazim, K. Lobato, G. Oreski, A. Reinders, J. Schmitz, M. Theelen, et al., Review of degradation and failure phenomena in photovoltaic modules, Renew. Sustain. Energy Rev. 159 (2022) 112160.

[2] A. Omazic, G. Oreski, M. Halwachs, G. Eder, C. Hirschl, L. Neumaier, G. Pinter, M. Erceg, Relation between degradation of polymeric components in crystalline silicon PV module and climatic conditions: A literature review, Sol. Energy Mater. Sol. Cells 192 (2019) 123–133.

[3] M. Halwachs, L. Neumaier, N. Vollert, L. Maul, S. Dimitriadis, Y. Voronko, G. Eder, A. Omazic, W. Mühleisen, C. Hirschl, et al., Statistical evaluation of PV system performance and failure data among different climate zones, Renew. Energy 139 (2019) 1040–1060.

[4] L. Koester, S. Lindig, A. Louwen, A. Astigarraga, G. Manzolini, D. Moser, Review of photovoltaic module degradation, field inspection techniques and techno-economic assessment, Renew. Sustain. Energy Rev. 165 (2022) 112616.

[5] B. Brune, I. Ortner, G.C. Eder, Y. Voronko, G. Oreski, K.A. Berger, K. Knöbl, L. Neumaier, M. Feichtner, Quantifying the influence of encapsulant and backsheet composition on PV-power and electrical degradation, Prog. Photovolt., Res. Appl. (2023).

[6] IEC 61215-2:2021 - Terrestrial photovoltaic (PV) modules - Design qualification and type approval - Part 2: Test procedures, Standard 2021, International Electrotechnical Commission, 2021.

[7] ISO 4892-1:2016-05, Plastics - Methods of Exposure to Laboratory Light Sources - Part 1: General Guidance, Standard 2016, International Organization for Standardization, 2016.

[8] ISO 4892-2:2013 + A1:20215, Plastics - Methods of Exposure to Laboratory Light Sources - Part 2: Xenon-arc Lamps, Standarad 2021, International Organization for Standardization, 2021.

[9] ISO 4892-3:2016 - Methods of Exposure to Laboratory Light Sources - Part 3: Fluorescent UV Lamps, Standard 2016, International Organization for Standardization, 2016.

[10] DIN IEC/TS 62788-7-2, Measurement Procedures for Materials Used in Photovoltaic Modules - Part 7-2: Environmental Exposures - Accelerated Weathering Tests of Polymeric Materials, Standard 2019, International Electrotechnical Commission, 2019.

[11] B. Rånby, Photodegradation and photo-oxidation of synthetic polymers, J. Anal. Appl. Pyrolysis 15 (1989) 237–247.

[12] S.J. Blanksby, G.B. Ellison, Bond dissociation energies of organic molecules, Accounts Chem. Res. 36 (4) (2003) 255–263.

[13] G.W. Ehrenstein, S. Pongratz, Resistance and Stability of Polymers, Carl Hanser Verlag GmbH Co KG, 2013.

[14] K.R. McIntosh, N.E. Powell, A.W. Norris, J.N. Cotsell, B.M. Ketola, The effect of damp-heat and UV aging tests on the optical properties of silicone and EVA encapsulants, Prog. Photovolt., Res. Appl. 19 (3) (2011) 294–300.

[15] J.C. Schlothauer, K. Grabmayer, G.M. Wallner, B. Röder, Correlation of spatially resolved photoluminescence and viscoelastic mechanical properties of encapsulating EVA in differently aged PV modules, Prog. Photovolt., Res. Appl. 24 (6) (2016) 855–870.

[16] B.K. Sharma, U. Desai, A. Singh, A. Singh, Effect of vinyl acetate content on the photovoltaic-encapsulation performance of ethylene vinyl acetate under accelerated ultra-violet aging, J. Appl. Polym. Sci. 137 (2) (2020) 48268.

[17] C. Barretta, G. Oreski, S. Feldbacher, K. Resch-Fauster, R. Pantani, Comparison of degradation behavior of newly developed encapsulation materials for photovoltaic applications under different artificial ageing tests, Polymers 13 (2) (2021) 271.

[18] K. Yamada, S. Kumagai, T. Shiratori, T. Kameda, Y. Saito, A. Watanabe, C. Watanabe, N. Teramae, T. Yoshioka, Combined UV-irradiation and pyrolysis-GC/MS approach for evaluating the deterioration behavior of ethylene vinyl acetate, Polym. Degrad. Stab. 190 (2021) 109623.

[19] D.C. Miller, J.G. Bokria, D.M. Burns, S. Fowler, X. Gu, P.L. Hacke, C.C. Honeker, M.D. Kempe, M. Köhl, N.H. Phillips, et al., Degradation in photovoltaic encapsulant transmittance: Results of the first PVQAT TG5 artificial weathering study, Prog. Photovolt., Res. Appl. 27 (5) (2019) 391–409.

[20] J. Morse, M. Thuis, D. Holsapple, R. Willis, M.D. Kempe, D.C. Miller, Degradation in photovoltaic encapsulant transmittance: Results of the second PVQAT TG5 artificial weathering study, Prog. Photovolt., Res. Appl. 30 (7) (2022) 763–783.

[21] D.E. Mansour, C. Barretta, L. Pitta Bauermann, G. Oreski, A. Schueler, D. Philipp, P. Gebhardt, Effect of backsheet properties on PV encapsulant degradation during combined accelerated aging tests, Sustainability 12 (12) (2020) 5208.

[22] A. Jentsch, K.-J. Eichhorn, B. Voit, Influence of typical stabilizers on the aging behavior of EVA foils for photovoltaic applications during artificial UV-weathering, Polym. Test. 44 (2015) 242–247.

[23] M. Koehl, A. Ballion, Y.-H. Lee, H.-S. Wu, K. Scott, S. Glick, P. Hacke, H.J. Koo, Ultraviolet radiation round-robin testing of various backsheets for photovoltaic modules, in: 2015 IEEE 42nd Photovoltaic Specialist Conference, PVSC, IEEE, 2015, pp. 1–4.

[24] F. Pern, Factors that affect the EVA encapsulant discoloration rate upon accelerated exposure, Sol. Energy Mater. Sol. Cells 41 (1996) 587–615.

[25] M.C.C. de Oliveira, A.S.A.D. Cardoso, M.M. Viana, V.d.F.C. Lins, The causes and effects of degradation of encapsulant ethylene vinyl acetate copolymer (EVA) in crystalline silicon photovoltaic modules: A review, Renew. Sustain. Energy Rev. 81 (2018) 2299–2317.

[26] M. Çopuroğlu, M. Şen, A comparative study of thermal ageing characteristics of poly (ethylene-co-vinyl acetate) and poly (ethylene-co-vinyl acetate)/carbon black mixture, Polym. Adv. Technol. 15 (7) (2004) 393–399.

[27] G. Grause, M.-F. Chien, C. Inoue, Changes during the weathering of polyolefins, Polym. Degrad. Stab. 181 (2020) 109364.

[28] A. Czanderna, F. Pern, Encapsulation of PV modules using ethylene vinyl acetate copolymer as a pottant: A critical review, Sol. Energy Mater. Sol. Cells 43 (2) (1996) 101–181.

[29] M.D. Kempe, G.J. Jorgensen, K.M. Terwilliger, T.J. McMahon, C.E. Kennedy, T.T. Borek, Acetic acid production and glass transition concerns with ethylene-vinyl acetate used in photovoltaic devices, Sol. Energy Mater. Sol. Cells 91 (4) (2007) 315–329.

[30] B. Adothu, F.R. Costa, S. Mallick, Damp heat resilient thermoplastic polyolefin encapsulant for photovoltaic module encapsulation, Sol. Energy Mater. Sol. Cells 224 (2021) 111024.

[31] D.R. Bauer, Interpreting weathering acceleration factors for automotive coatings using exposure models, Polym. Degrad. Stab. 69 (3) (2000) 307–316.

[32] J. Pickett, D. Gibson, S. Rice, M. Gardner, Effects of temperature on the weathering of engineering thermoplastics, Polym. Degrad. Stab. 93 (3) (2008) 684–691.

[33] J.E. Pickett, J.R. Sargent, Sample temperatures during outdoor and laboratory weathering exposures, Polym. Degrad. Stab. 94 (2) (2009) 189–195.

[34] S. Fowler, Effects of water spray on specimen temperature exposed during proposed xenon arc and fluorescent UV lamp weathering test cycles for backsheet materials", NREL PVMRW (2015).

[35] G. Oreski, G.C. Eder, Y. Voronko, A. Omazic, L. Neumaier, W. Mühleisen, G. Ujvari, R. Ebner, M. Edler, Performance of PV modules using co-extruded backsheets based on polypropylene, Sol. Energy Mater. Sol. Cells 223 (2021) 110976.
[36] R. Heidrich, A. Mordvinkin, R. Gottschalg, Quantification of UV protecting additives in ethylene-vinyl acetate copolymer encapsulants for photovoltaic modules with pyrolysis-gas chromatography-mass spectrometry, Polym. Test. (2022) 107913.
[37] C.R. Harris, K.J. Millman, S.J. van der Walt, R. Gommers, P. Virtanen, D. Cournapeau, E. Wieser, J. Taylor, S. Berg, N.J. Smith, R. Kern, M. Picus, S. Hoyer, M.H. van Kerkwijk, M. Brett, A. Haldane, J.F. del Río, M. Wiebe, P. Peterson, P. Gérard-Marchant, K. Sheppard, T. Reddy, W. Weckesser, H. Abbasi, C. Gohlke, T.E. Oliphant, Array programming with NumPy, Nature 585 (7825) (2020) 357–362.
[38] J.D. Hunter, Matplotlib: A 2D graphics environment, Comput. Sci. Eng. 9 (3) (2007) 90–95.
[39] Wes McKinney, Data structures for statistical computing in python, in: S. van der Walt, J. Millman (Eds.), Proceedings of the 9th Python in Science Conference, 2010, pp. 56–61.
[40] P. Yu, Applications of hierarchical cluster analysis (CLA) and principal component analysis (PCA) in feed structure and feed molecular chemistry research, using synchrotron-based Fourier transform infrared (FTIR) microspectroscopy, J. Agricult. Food Chem. 53 (18) (2005) 7115–7127.
[41] F. Gaston, N. Dupuy, S.R. Marque, M. Barbaroux, S. Dorey, FTIR study of ageing of γ-irradiated biopharmaceutical EVA based film, Polym. Degrad. Stab. 129 (2016) 19–25.
[42] E. Lazzari, T. Schena, M.C.A. Marcelo, C.T. Primaz, A.N. Silva, M.F. Ferrao, T. Bjerk, E.B. Caramao, Classification of biomass through their pyrolytic bio-oil composition using FTIR and PCA analysis, Ind. Crops Products 111 (2018) 856–864.
[43] M. Bredács, C. Barretta, L. Castillon, A. Frank, G. Oreski, G. Pinter, S. Gergely, Prediction of polyethylene density from FTIR and Raman spectroscopy using multivariate data analysis, Polym. Test. 104 (2021) 107406.
[44] M. Bredács, E. Kanatschnig, A. Frank, G. Oreski, G. Pinter, S. Gergely, Identifying active and degraded phenolic antioxidants in aged PE with IR-microscopy, Polym. Degrad. Stab. (2023) 110345.
[45] F. Pedregosa, G. Varoquaux, A. Gramfort, V. Michel, B. Thirion, O. Grisel, M. Blondel, P. Prettenhofer, R. Weiss, V. Dubourg, J. Vanderplas, A. Passos, D. Cournapeau, M. Brucher, M. Perrot, E. Duchesnay, Scikit-learn: Machine learning in Python, J. Mach. Learn. Res. 12 (2011) 2825–2830.
[46] G. Socrates, Infrared and Raman Characteristic Group Frequencies: Tables and Charts, John Wiley & Sons, 2004.
[47] N.S. Allen, M. Edge, M. Rodriguez, C.M. Liauw, E. Fontan, Aspects of the thermal oxidation, yellowing and stabilisation of ethylene vinyl acetate copolymer, Polym. Degrad. Stab. 71 (1) (2000) 1–14.
[48] L. Wang, W. Dong, Y. Xu, Synthesis and characterization of hydroxypropyl methylcellulose and ethyl acrylate graft copolymers, Carbohydr. Polymers 68 (4) (2007) 626–636.
[49] G. Oreski, G. Wallner, Evaluation of the aging behavior of ethylene copolymer films for solar applications under accelerated weathering conditions, Sol. Energy 83 (7) (2009) 1040–1047.
[50] Y. Shindo, B. Read, R. Stein, The study of the orientation of polyvinyl chloride films by means of birefringence and infrared, visible, and ultraviolet dichroism, Die Makromolekulare Chem.: Macromol. Chem. Phys. 118 (1) (1968) 272–312.
[51] S. Falicki, D. Gosciniak, J. Cooke, D. Carlsson, Secondary and tertiary piperidinyl compounds as stabilizers for γ-irradiated polypropylene, Polym. Degrad. Stab. 43 (1) (1994) 1–7.
[52] R. Singh, A. Patwa, S. Desai, J. Pandey, S. Solanky, A. Vishwa Prasad, Synthesis of new polymeric hindered amine light stabilizers: Performance evaluation in styrenic polymers, J. Appl. Polym. Sci. 90 (4) (2003) 1126–1138.
[53] G. Oreski, G.M. Wallner, R. Lang, Ageing characterization of commercial ethylene copolymer greenhouse films by analytical and mechanical methods, Biosyst. Eng. 103 (4) (2009) 489–496.
[54] J. Lustoň, Z. MaŇásek, R. Palovčík, Polymeric UV absorbers of the 2-hydroxybenzophenone type. III. Tertiary amine catalyzed polymerization of 2-hydroxy-4 (2, 3-epoxypropoxy) benzophenone, J. Macromol. Sci.—Chem. 9 (8) (1975) 1413–1431.
[55] G. Maggioni, A. Tessarollo, S. Carturan, Study of the effects of incorporation of UV-absorbing compound in parylene C films, Mater. Chem. Phys. 149 (2015) 530–538.
[56] R. Geetha, A. Torikai, S. Nagaya, K. Fueki, Photo-oxidative degradation of polyethylene: Effect of polymer characteristics on chemical changes and mechanical properties. Part 1—Quenched polyethylene, Polym. Degrad. Stab. 19 (3) (1987) 279–292.
[57] J. Jin, S. Chen, J. Zhang, UV aging behaviour of ethylene-vinyl acetate copolymers (EVA) with different vinyl acetate contents, Polym. Degrad. Stab. 95 (5) (2010) 725–732.
[58] K. Rajakumar, V. Sarasvathy, A. Thamarai Chelvan, R. Chitra, C. Vijayakumar, Natural weathering studies of polypropylene, J. Polym. Environ. 17 (2009) 191–202.
[59] E. Denisov, The role and reactions of nitroxyl radicals in hindered piperidine light stabilisation, Polym. Degrad. Stab. 34 (1–3) (1991) 325–332.
[60] E.N. Step, N.J. Turro, P.P. Klemchuk, M.E. Gande, Model studies on the mechanism of HALS stabilization, Die Angew. Makromolekulare Chem.: Appl. Macromol. Chem. Phys. 232 (1) (1995) 65–83.
[61] J.L. Hodgson, M.L. Coote, Clarifying the mechanism of the denisov cycle: How do hindered amine light stabilizers protect polymer coatings from photo-oxidative degradation? Macromolecules 43 (10) (2010) 4573–4583.
[62] M.R. Paine, G. Gryn'ova, M.L. Coote, P.J. Barker, S.J. Blanksby, Desorption electrospray ionisation mass spectrometry of stabilised polyesters reveals activation of hindered amine light stabilisers, Polym. Degrad. Stab. 99 (2014) 223–232.
[63] F. Pern, Ethylene-vinyl acetate (EVA) encapsulants for photovoltaic modules: Degradation and discoloration mechanisms and formulation modifications for improved photostability, Die Angew. Makromolekulare Chem.: Appl. Macromol. Chem. Phys. 252 (1) (1997) 195–216.
[64] N.A. Shaath, Ultraviolet filters, Photochem. Photobiol. Sci. 9 (2010) 464–469.
[65] J. Zawadiak, M. Mrzyczek, Influence of substituent on UV absorption and keto–enol tautomerism equilibrium of dibenzoylmethane derivatives, Spectrochim. Acta Part A: Mol. Biomol. Spectrosc. 96 (2012) 815–819.
[66] N.S. Allen, M. Edge, M. Rodriguez, C.M. Liauw, E. Fontan, Aspects of the thermal oxidation of ethylene vinyl acetate copolymer, Polym. Degrad. Stab. 68 (3) (2000) 363–371.
[67] M. Çopuroğlu, M. Şen, A comparative study of UV aging characteristics of poly (ethylene-co-vinyl acetate) and poly (ethylene-co-vinyl acetate)/carbon black mixture, Polym. Adv. Technol. 16 (1) (2005) 61–66.
[68] J. Almond, P. Sugumaar, M.N. Wenzel, G. Hill, C. Wallis, Determination of the carbonyl index of polyethylene and polypropylene using specified area under band methodology with ATR-FTIR spectroscopy, e-Polymers 20 (1) (2020) 369–381.
[69] H. Han, H. Yan, X. Wang, K. Zhang, J. Huang, Y. Sun, J. Liu, P.J. Verlinden, P. Altermatt, Z. Liang, et al., Analysis of the degradation of encapsulant materials used in photovoltaic modules exposed to different climates in China, Sol. Energy 194 (2019) 177–188.
[70] Y. Soudais, L. Moga, J. Blazek, F. Lemort, Coupled DTA–TGA–FT-IR investigation of pyrolytic decomposition of EVA, PVC and cellulose, J. Anal. Appl. Pyrolysis 78 (1) (2007) 46–57.
[71] A. Marcilla, A. Gomez, J. Reyes-Labarta, MCM-41 catalytic pyrolysis of ethylene–vinyl acetate copolymers: Kinetic model, Polymer 42 (19) (2001) 8103–8111.
[72] A. Marcilla, A. Gomez, S. Menargues, J. Garcia-Martinez, D. Cazorla-Amoros, Catalytic cracking of ethylene-vinyl acetate copolymers: Comparison of different zeolites, J. Anal. Appl. Pyrolysis 68 (2003) 495–506.
[73] A. Marcilla, A. Gomez, S. Menargues, TG/FTIR study of the thermal pyrolysis of EVA copolymers, J. Anal. Appl. Pyrolysis 74 (1–2) (2005) 224–230.
[74] D.D. Jiang, G.F. Levchik, S.V. Levchik, C.A. Wilkie, Thermal decomposition of cross-linked polybutadiene and its copolymers, Polym. Degrad. Stab. 65 (3) (1999) 387–394.
[75] V. Kholodovych, W.J. Welsh, Thermal-oxidative stability and degradation of polymers, in: Physical Properties of Polymers Handbook, Springer, 2007, pp. 927–938.
[76] M. Gagliardi, P. Lenarda, M. Paggi, A reaction-diffusion formulation to simulate EVA polymer degradation in environmental and accelerated ageing conditions, Sol. Energy Mater. Sol. Cells 164 (2017) 93–106.
[77] H. Bockhorn, A. Hornung, U. Hornung, D. Schawaller, Kinetic study on the thermal degradation of polypropylene and polyethylene, J. Anal. Appl. Pyrolysis 48 (2) (1999) 93–109.
[78] A. Sinha, D.B. Sulas-Kern, M. Owen-Bellini, L. Spinella, S. Uličná, S.A. Pelaez, S. Johnston, L.T. Schelhas, Glass/glass photovoltaic module reliability and degradation: A review, J. Phys. D: Appl. Phys. 54 (41) (2021) 413002.
[79] A.P. Patel, A. Sinha, G. Tamizhmani, Field-aged glass/backsheet and glass/glass PV modules: Encapsulant degradation comparison, IEEE J. Photovolt. 10 (2) (2019) 607–615.

5.2. UV additive diffusion and the impact on polymer degradation

In the previous work, it was shown that irradiation with xenon lamps with daylight filters is the more realistic option for accelerated UV aging, as it provokes effects from free-field weathering. In addition, the use of the additive quantification method provided initial insights into the degradation kinetics of UV additives.

These findings will be further developed in the following publication. The aim is to investigate how UV additives in EVA behave when irradiated by xenon lamps with daylight filters. Not only the degradation of the encapsulant will be investigated, but also the migration behavior of the additives. Solar modules are multilayer systems and additives are only bound by Van der Waals interaction. Consequently, it is expected that they can migrate, but it is unknown to what extent.

Thus, the following publication contains numerical simulations of UV absorber diffusion. The numerical procedure used could only be mentioned briefly in the paper but deserves a detailed explanation to enable an understanding of the simulations. Starting with the diffusion equation presented in subsubsection 2.1.2

$$\frac{\partial u(x,t)}{\partial t} = D\frac{\partial^2 u(x,t)}{\partial x^2}. \tag{44}$$

Solving Equation 44 can be achieved by using the forward time-centered space (FCTS) scheme [227]. Using the FCTS scheme, the partial derivatives transform to

$$\frac{\partial u(x,t)}{\partial t} \approx \frac{u(x,t+\Delta t) - u(x,t)}{\Delta t} \quad \text{and} \tag{45}$$

$$\frac{\partial^2 u(x,t)}{\partial x^2} \approx \frac{u(x+\Delta x,t) - 2u(x,t) + u(x-\Delta x,t)}{\Delta x^2}. \tag{46}$$

Thus, using Equation 45 and Equation 46 to approximate Equation 44 yields

$$u(x,t+\Delta t) = \frac{D\Delta t}{\Delta x^2}\left(u(x+\Delta x,t) - 2u(x,t) + u(x-\Delta x,t)\right) + u(x,t). \tag{47}$$

Solving Equation 47 numerically is possible by discretizing the grid. The concentration at a specific grid point j at the next time step $t = n+1$ is thus given by the neighboring grid points

$$u_j^{n+1} = u_j^n + \frac{D\Delta t}{\Delta x^2}\left(u_{j+1}^n - 2u_j^n + u_{j-1}^n\right) \tag{48}$$

yielding the stability condition

$$\Delta t \leq \frac{\Delta x^2}{2D} \quad [228]. \tag{49}$$

To fit the experimental data in the following publication, Dirichlet boundary conditions have been used for the left boundary and Neumann boundary conditions have been used for the right boundary. For the left boundary, it follows that

$$u_0^n = \alpha \tag{50}$$

for all time points n while $\alpha > 0$. To apply Neumann boundary conditions at the boundary $j = L$, the following relationship is necessary:

$$\frac{\partial u(L,t)}{\partial x} = 0 \approx \frac{1}{2\Delta x}\left(u_{L+1}^{n} - u_{L-1}^{n}\right). \tag{51}$$

Equation 51 requires a grid point $L+1$ which is out of grid. However, the space increment Δx will not equal 0, and thus, the concentration at $L+1$ equals the concentration at $L-1$ for Neumann boundary conditions. Using Equation 48 and Equation 51 yields

$$u_{L}^{n+1} = u_{L}^{n} + 2\frac{D\Delta t}{\Delta x^{2}}\left(u_{L-1}^{n} - u_{L}^{n}\right) \tag{52}$$

for the right boundary at $x = L$.

IEEE JOURNAL OF PHOTOVOLTAICS, VOL. 14, NO. 1, JANUARY 2024 131

Diffusion of UV Additives in Ethylene-Vinyl Acetate Copolymer Encapsulants and the Impact on Polymer Reliability

Robert Heidrich, Marius Lüdemann, Anton Mordvinkin, and Ralph Gottschalg

***Abstract*—The reliability of solar modules is largely determined by the encapsulation materials used and their inherent additive composition. Although the use of polymer additives generally leads to better encapsulant characteristics, the diffusion of these species must be considered. While UV additives protect the encapsulant from photo degradation, their interactions with other additives or with formed radicals can lead to undesirable effects such as browning. Within this work, the diffusion of UV additives and their impact on the degradation behavior of encapsulation material based on ethylene-vinyl acetate copolymer (EVA) is investigated. The fabricated test specimens (glass/EVA/PTFE/glass) were prepared with an artificially created UV additive concentration gradient and weathered under IEC 62788-7-2-A3 conditions. Test points with included UV additives showed no degradation effects, while test points without UV additives showed strong degradation. Surprisingly, the UV additives used could diffuse up to 4 cm within 1500 h weathering. They were able to effectively protect an area of 1.3 cm next to the concentration gradient. Therefore, minor inhomogeneities during the manufacturing process can probably be compensated by intrinsic UV additive diffusion. However, this simultaneously represents a high risk of reaction with residual crosslinking peroxides leading to the UV stabilizer depletion and eventually to browning.**

***Index Terms*—Additives, degradation, diffusion, encapsulant, ethylene-vinyl acetate (EVA), spectroscopy.**

I. Introduction

ENCAPSULATION polymer degradation by UV irradiance is known to be one of the key factors determining solar module longevity [1], [2], [3], [4]. Most commonly ethylene-vinyl acetate copolymer (EVA) is used as encapsulant for photovoltaic modules [5]. However, EVA can degrade by various reactions reducing the solar module reliability resulting in browning or the formation of acetic acid, which is corroding contacts and increasing the series resistance and thus seriously influencing the solar module performance [3], [6], [7], [8], [9], [10], [11], [12], [13]. Hence, shielding the encapsulation material by using appropriate additives is a necessary step to enhance the solar module lifetimes [14].

Additives have to fulfill a number of tasks and were used in EVA encapsulants for many decades [15]. While crosslinking additives are important to form a resilient network of polymer chains, unconsumed crosslinking peroxides can cause problems like browning when reacting with other additives [16], [17]. Typically, UV absorbers and UV stabilizers are used to increase the resistance against UV irradiation. Jentsch et al. [14] found that a combination of UV absorbing benzophenone-type molecules and radical trapping hindered amine light stabilizers (HALS) molecules has a synergy effect preventing the encapsulant from photo degradation. On the other hand, correlations between the presence of UV absorbers and browning of the encapsulant have been reported in the literature [6], [16], [18].

Additives can migrate due to diffusion processes [19], [20]. For most cases (e.g., neglecting external forces and convection effects), the description of additive migration by Fick's laws and deriving the general diffusion equation

$$\frac{\partial c}{\partial t} = \vec{\nabla} \cdot \left(D \vec{\nabla} c \right) \tag{1}$$

with c as the molecule concentration, t as the time and D as diffusion constant, is a sufficient approach [19]. In the past, several studies investigated the migration of small molecules in polymer films [21], [22], [23], [24], [25], [26]. Földes et al. [21], [22], [23] determined the diffusion coefficients of different antioxidants in polyolefin polymers. Reynier et al. [25] derived several diffusion coefficients for smaller different molecules and commercial additives in polypropylene. Thus, it is very likely that diffusion effects also occur in EVA layers of commercial solar modules. Furthermore, solar modules are complex physical objects consisting of different materials and various interfaces [3], [9]. Understanding potential interactions between these layers and also the possible migration of smaller species

Manuscript received 31 August 2023; revised 17 October 2023 and 9 November 2023; accepted 10 November 2023. Date of publication 27 November 2023; date of current version 18 December 2023. This work was supported in part by German Research Foundation (Deutsche Forschungsgemeinschaft DFG) under Grant 491460386, in part by the Open Access Publishing Fund of Anhalt University of Applied Sciences, and in part by TotalEnergies. *(Corresponding author: Robert Heidrich.)*

Robert Heidrich is with the Fraunhofer Center for Silicon Photovoltaics CSP, 06120 Halle (Saale), Germany, and also with the Anhalt University of Applied Sciences, 06366 Koethen (Anhalt), Germany (e-mail: robert.heidrich@csp.fraunhofer.de).

Marius Lüdemann and Anton Mordvinkin are with the Fraunhofer Center for Silicon Photovoltaics CSP, 06120 Halle (Saale), Germany (e-mail: marius.luedemann@imws.fraunhofer.de; anton.mordvinkin@csp.fraunhofer.de).

Ralph Gottschalg is with the Fraunhofer Center for Silicon Photovoltaics CSP, 06120 Halle (Saale), Germany, and also with the Anhalt University of Applied Sciences, 06366 Koethen (Anhalt), Germany (e-mail: ralph.gottschalg@csp.fraunhofer.de).

Color versions of one or more figures in this article are available at https://doi.org/10.1109/JPHOTOV.2023.3333198.

Digital Object Identifier 10.1109/JPHOTOV.2023.3333198

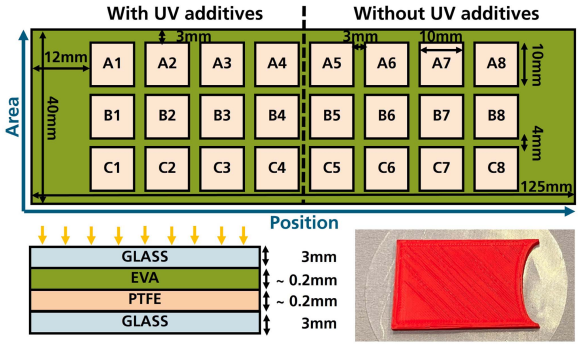

Fig. 1. Top: Sample geometry with all 24 extraction points. Repeatable sample extraction was enabled by using a 3D printed template. Bottom left: Sample cross section showing all used layers with approximate thicknesses and the path of irradiation. Bottom right: Cutting template with an elliptic opening.

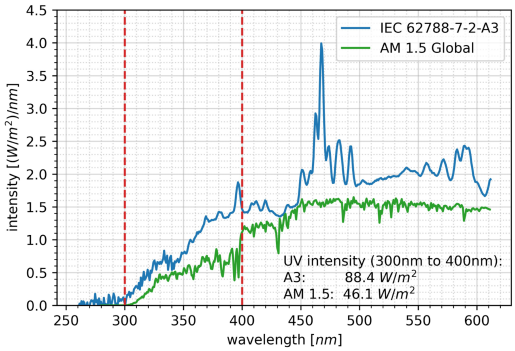

Fig. 2. Spectrum of the used xenon lamps with daylight filters in comparison with the standard spectrum AM 1.5 Global (ASTM G173-03 reference spectra derived from SMARTS v. 2.9.2. provided by NREL).

TABLE I
USED ENCAPSULANT COMPOSITIONS C1 (WITH UV ADDITIVES) AND C2 (WITHOUT UV ADDITIVES)

Name	Function	C1 [phr]	C2 [phr]	CAS
ELVAX 150W	EVA matrix	100	100	
Cyasorb UV 531	UV absorber	0.3	0	1843-05-6
Tinuvin 770	HALS	0.13	0	52829-07-9
Luperox TBEC	crosslinking agent	1.5	1.5	34443-12-4
Perkalink 301	crosslinking accel.	1.5	1.5	1025-15-6
Silane A 174	adhesion promoter	1.2	1.2	2530-85-0

The additive amounts are presented in grams per hundred gram EVA.

between different films is crucial for determining the longevity of the materials. On the one hand, this means that diffusion of additives from the initial site reduces the protection of the encapsulation material against environmental influences. On the other hand, initial inhomogeneities in the additive density could be compensated by diffusion effects.

This work aims to investigate the influence of UV additives on the degradation behavior of EVA films and to analyze potential diffusion effects. For this purpose, diffusion specimens, with 24 measurement points each, were manufactured. The weathering took place in rondel weatherometers under IEC 62788-7-2-A3 conditions. The newly developed quantification method for UV additives in EVA by pyrolysis-gas chromatography-mass spectrometry (PY-GCMS) will enable a time and spatially resolved determination of the corresponding UV additive concentration [27].

II. Materials and Methods

A. Used Materials and Sample Manufacturing

Fig. 1 visualizes the sample design. *Position* represents the sites 1 to 8 along the sample length. *Area* represents the sites A to C along the sample width. The EVA films have been manufactured in accordance with our previous work using a kneader and a hydraulic press [27]. Two different EVA types were prepared with a common additive structure while the presence of UV additives was varied [15], [18], [27], [28]. The formulations are displayed in Table I. After the pressing process, the samples were equally cut with the help of a template (see Fig. 1). Preliminary lamination experiments have shown that an elliptic form of the interface, where the different polymer films are laminated together, is beneficial as the EVA is flowing faster in the middle of the glass substrate.

Subsequently, two EVA films (one with, one without UV additives) were positioned on low iron, thermally hardened float glass and covered with a PTFE layer to enable the separation after weathering. After placing a second glass layer on top, the samples were laminated. An Meier ICOLAM 10/08 was used for lamination. The laminator was pre heated to 55 °C. Afterward, all samples were placed inside the laminator. The laminator was evacuated for 6.5 min and heated to 80 °C. Afterward, the coupons were pressed with 600 mbar and heated to 155 °C within 3 min. The temperature and pressure were hold for additional 15 min. In the last step the laminator was cooled to 55 °C within 30 min still applying the 600 mbar pressure.

After the lamination process aluminum tape was used to seal the edges of all glass laminates to exclude the influence of humidity and oxygen. Additionally, a template containing the openings as shown in Fig. 1 was 3D printed, allowing a reproducible sample extraction from the same points.

B. Weathering

The weathering was carried out in accordance with IEC 62788-7-2-A3 using an Atlas Xenotest 440 with Atlas B04 daylight filters. The chamber temperature was fixed at 65 °C (90 °C black standard temperature) with 20 % relative humidity. The Intensity at 340 nm was set to 0.8 $W/m^2/nm$. The measured spectrum is displayed in Fig. 2. Especially the UV interval of the xenon lamp with daylight filters behaves similar to the AM 1.5 Global, but the integrated intensity is increased by approximately the doubled amount. However, the spectrometer was not calibrated to the chamber geometry. Therefore, the measured (and integrated) intensities are slightly higher than displayed in the chamber parameters and should be understood qualitatively. All samples were irradiated with EVA as top layer in accordance with Fig. 1.

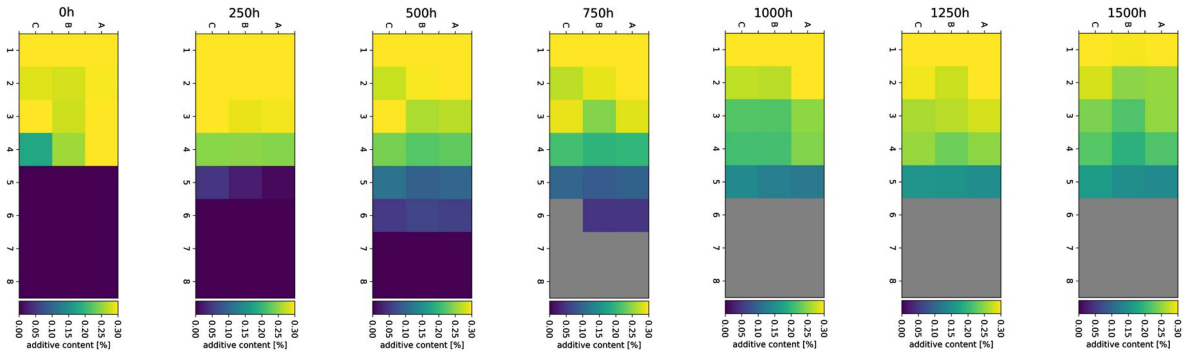

Fig. 3. Quantification of the UV absorber Cyasorb UV 531. The map positioning is in accordance with Fig. 1. Evaluation of the gray area and position combinations were not possible due to serious degradation.

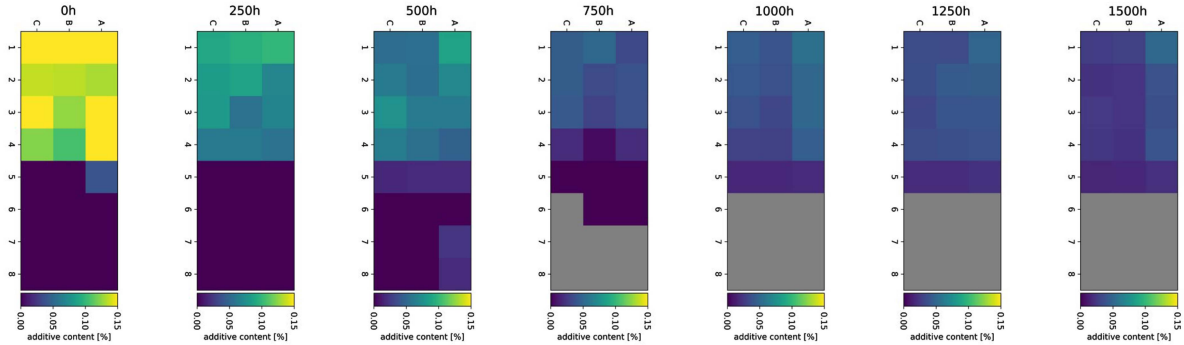

Fig. 4. Quantification of the UV stabilizer Tinuvin 770. The map positioning is in accordance with Fig. 1. Evaluation of the gray area and position combinations were not possible due to serious degradation.

C. Characterization Methods

1) Pyrolysis-Gas Chromatography-Mass Spectrometry (PY-GCMS): For qualitative and quantitative analysis of the polymer and the additive composition a combination of pyrolysis, gas chromatography and mass spectrometry (PY-GCMS) was used. The PY-GCMS setup and quantification procedure are explained in detail in our previous work focusing on additive quantification [27]. An EGA/Py-3030D from Frontier Laboratories Ltd. pyrolysis oven with attached autosampler AS-1020E was used for a two step thermo desorption. All desorption steps were carried out with the help of a selective sampler SS-1010E from Frontier Laboratories Ltd., which prevents column contamination by undesirable fragmented components. As gas chromatograph a Trace 1300 from Thermo Scientific with He carrier gas was used. The implemented column was an Ultra ALLOY Capillary Column (length 30 m, internal diameter 0.25 mm, film thickness 0.25 μm) from Frontier Laboratories Ltd. An ISQ 7000 mass spectrometer from Thermo Scientific was coupled to the gas chromatograph. The m/z range was set from 29 to 800.

2) Fourier-Transform Infrared Spectroscopy (FTIR): An Inventio spectrometer from Bruker was used for the FTIR analysis. The measurements were carried out in ATR mode using a transit platinum unit with diamond tip. The wavelength interval was set from 4000 cm^{-1} to 650 cm^{-1} with a resolution of 4 cm^{-1}.

III. Results and Discussion

A. Additive Diffusion

Figs. 3 and 4 are visualizing the quantitative PY-GCMS analysis of the UV absorber Cyasorb UV 531 and the UV stabilizer Tinuvin 770. Comparing the initial values with Table I, the UV stabilizer exaggerated in the samples during the initial state. This could either be caused by local inhomogeneities as a result of the kneader fabrication or by a general offset due to the calibration samples for PY-GCMS quantification [27]. However, comparing relative mass changes is possible with sufficient accuracy. Not all defined samples positions were analyzed until the end of the weathering time. The gray color in Figs. 3 and 4 symbolizes encapsulant position and area combinations, which were subject to severe degradation which impeded PY-GCMS measurements (see Fig. 9) and will be discussed in Section III-B. Due the diverging modes of operation of the UV absorber and the UV stabilizer, the mean content of both molecules relative to the total sample surface behaves differently and is shown for position 1 to 5 in Fig. 5.

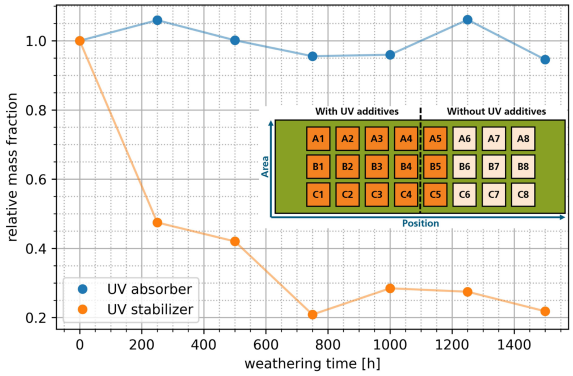

Fig. 5. Mean relative additive content of the UV absorber Cyasorb UV 531 and the UV stabilizer Tinuvin 770 for positions 1 to 5 (mean of all orange extraction points in the scheme). Considering Figs. 3 and 4, the total amount of the UV absorber in position 1 to 5 is preserved but redistributed. The total amount of the UV stabilizer is drastically decreasing within the first 250 h of weathering.

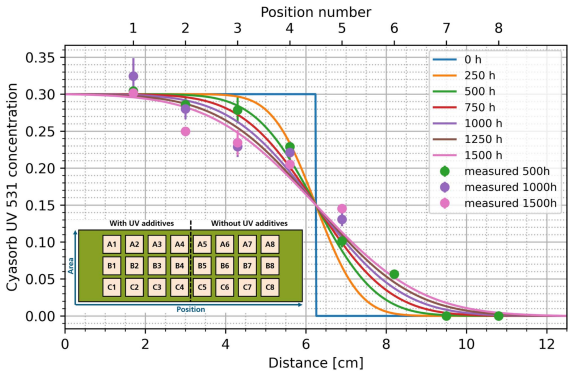

Fig. 6. Numerical solution of the diffusion equation for the UV absorber Cyasorb UV 531. The problem was simplified to a 1D simulation, and the measurement points are mean values of area A to C at the corresponding position. The error bars represent the standard deviation of the mean values.

Fig. 3 shows that UV absorber molecules start to diffuse significantly from position 4 as the concentration gradient is the highest, which is in accordance with general macroscopic Fickian diffusion [19]. After 250 h of weathering the UV absorber already diffused into position 6 and and is expected to diffuse further. However, further positions could not be analyzed due to the aforementioned polymer degradation. Due to the changing concentration gradient molecules from the positions 2 and 3 are predominantly compensating the concentration mismatch and after 1500 h only position 1 remained with approximately the initial concentration. Considering the mean relative additive content of position 1 to 5, which is displayed in Fig. 5, the total UV absorber content remains approximately constant. Therefore, the underlying keto-enol tautomerism works reversible for the applied weathering parameters and the total amount of the UV absorber is preserved but redistributed [7], [29], [30].

Thus, the general diffusion equation approach

$$\frac{\partial u(x,t)}{\partial t} = D\frac{\partial^2 u(x,t)}{\partial x^2} \tag{2}$$

was assumed for the UV absorber as displayed in (2) with $u(x,t)$ as UV absorber concentration and D as diffusion constant. The partial differential equation was solved numerically using an explicit forward in time and central in space (FTCS) approach with Dirichlet conditions for the boundary with UV additives and Neumann conditions for the boundary without UV additives. Both conditions have been chosen to match the observations as the initial concentration in position 1 remained constant while the additives cannot diffuse out of the sample on the other side. The effect of encapsulant thickness was not examined in this study as the numerical diffusion simulation was simplified to 1D for symmetry reasons, because no additional information could be gained in the case of a 2D observation. In the course of simplification to a 1D problem, the mean value of the areas A, B, and C for every position 1 to 8 was used. Fig. 6 shows the results of the numerical simulation and the real measured data points of the 500 h sample, the 1000 h sample and the 1500 h sample. When using a diffusion constant of $D = 5.5 \times 10^{-8}\,\mathrm{cm^2/s}$, the measured data points show a good agreement with the simulation. This value is in accordance with the work of Reynier et al. who determined the diffusion constant of Cyasorb UV 531 (Chimassorb 81) in polypropylene between $1.5 \times 10^{-10}\,\mathrm{cm^2/s}$ (40 °C) and $1.4 \times 10^{-8}\,\mathrm{cm^2/s}$ (70 °C) [25]. As the chamber and sample temperature (both temperatures should be approximately equal due to the transparent sample laminates [31], [32]) are approximately 65 °C during weathering, the used diffusion constant is in the correct order of magnitude. In addition, Földes et al. [21], [22], [23] determined similar diffusion coefficients for different antioxidants migrating in EVA. In accordance with the measured values, the graph shows that after 500 h the concentration in position 5 is increased to 1/3 of the initial concentration. After 1500 h of weathering, position 5 reached approximately half of the base concentration. Thus, under the used weathering parameters, the UV absorber is could be able to migrate approximately 4 cm within 1500 h of weathering.

However, the deviations of the measurements from the simulation could also be a result of an anomalous diffusion of the UV absorber. The normal diffusion and anomalous diffusion for the 1D case are displayed in (3) and (4). Assuming Fickian (normal) diffusion, the mean squared displacement

$$\langle r^2(t)\rangle = 2Dt \tag{3}$$

should allow particle movements of approximately 0.77 cm within 1500 h of weathering, which is significantly smaller than the measured data points and the simulation [33], [34]. Thus, D could be concentration dependent indicating a super diffusive behavior of the UV absorber [35], [36], [37], [38]. Following the anomalous diffusion approach

$$\langle r^2(t)\rangle = 2D_\alpha t^\alpha \tag{4}$$

with the anomaly parameter α for the measured data of the 500 h time step (and a mean square displacement of $2^2\,\mathrm{cm^2}$—see Fig. 6), the given diffusion constant of $5.5 \times 10^{-8}\,\mathrm{cm^2/s}$ would result in $\alpha = 1.21$ [38].

In order to exclude the influence of the PTFE layer on the diffusion behavior of the additives, samples from the same series were further weathered up to 2000 h. No additives were detected in the bulk measurements of the PFTE layers, but significant amounts were still found in the EVA. Consequently, the PTFE layer does not contribute to the transport of additives, neither on its surface nor within its volume. As an explanation for the anomalous diffusion, the incomplete EVA crosslinking can be responsible. Typically, EVA features a maximum gel content of 90 %, meaning that 10 % of the material can flow, which can accelerate the additive diffusion leading to the superdiffusion regime [39]. The vinyl acetate (VA) content can also play a role in this assumption. A lower VA content leads to higher crystallinity and lower glass transition temperature. Thus, the former would slow down, whereas the latter would boost the diffusion of additives in the polymer matrix [40], [41].

The migration of UV stabilizer molecules displayed in Fig. 4 behaves differently. While the migration due to the convectional transport associated with the material flow was already detected directly after the lamination (0 h sample), the diffusion effects are in general much less pronounced. In addition, after 250 h the initial concentration is approximately halved for all points, with position 4 showing the highest decrease. This could be explained by the reaction of the UV stabilizer with residual crosslinking peroxides which were not consumed during lamination and will be discussed in more detail in Section III-B. While the 500 h sample shows migration into position 5, this molecule diffusion is not detected for the 750 h sample. The observed behavior can be explained by a superposition of two effects. While the general concept of additive diffusion should also be applicable for Tinuvin 770, the migration of additives into new positions is probably counterbalanced by their reaction with radicals as their mode of action is not reversible [42], [43], [44], [45].

The molecular weight of the UV stabilizer Tinuvin 770 is 481 g/mol [46]. Földes et al. [22] found the diffusion coefficient of the antioxidant Irganox 1076 with a molecular weight of 531 g/mol to be $2.7 \times 10^{-8}\,\mathrm{cm^2/s}$ in EVA at 80 °C. As the molecular weight of the UV absorber Cyasorb UV 531 is 326 g/mol ($D = 5.5 \times 10^{-8}\,\mathrm{cm^2/s}$), it is conceivable that the diffusion coefficient of Tinuvin 770 is in the same order of magnitude as the previous mentioned additives [46]. As displayed in Fig. 5, the total UV stabilizer content is decreasing rapidly. Assuming a reservoir of formed radicals by UV irradiation (or nonconsumed crosslinking peroxide radicals), the degradation kinetics of the HALS should be dependent on their total amount as they need a reaction partner. Thus, the quantified HALS base form degrades with first order kinetics leading to an exponential decay of the total UV stabilizer concentration, which is observable in Fig. 5. As a result, the total Tinuvin 770 base form concentration decreased to approximately 20 % of the initial concentration after 1500 h of weathering. However, the decrease of molecular concentration (especially in position 1 to 4) does not necessarily mean the stabilizer is not functional anymore. As stated by Hodgeson et al. [44] the Denisov cycle is complex and even HALS fragments are able to bind radicals as long as the functional amine group is present.

TABLE II
FTIR Absorption Peak Assignment

waven. [$\mathrm{cm^{-1}}$]	group	excitation
3700-3100	OH	stretching vibration of hydroxyl groups
2920	CH_2	stretching vibration (PE)
2850	CH_2	deformation vibration (PE)
1900-1780	C=O	stretching vibration of γ-lactones
1736	C=O	stretching vibration (VA)
1715-1600	C=O	stretching vibration of ketones
1465	CH_2	stretching vibration (PE)
1370	CH_3	deformation vibration (VA)
1238	C-O-C	stretching vibration (VA)
1170	C-O-C	stretching vibration of aliphatic esters
1020	C-O-C	stretching vibration (VA)
960	CH	deformation vibration
720	CH_2	skeleton rocking vibration (PE)

Intensities belong to the polyethylene (PE) units, the vinyl acetate (VA) units or degradation products of the base polymer. The assignment is in accordance with [48], [49], [50], [8], [51], [52].

B. EVA Degradation in Dependence of UV Additive Presence

The EVA degradation was analyzed with ATR-FTIR measurements. All presented spectra are mean values of one position (e.g., the mean value of A1, B1, C1, etc.). Table II lists all assigned peaks with the corresponding functional group. Here, the peaks at 2920 $\mathrm{cm^{-1}}$, 2850 $\mathrm{cm^{-1}}$, 1465 $\mathrm{cm^{-1}}$, and 720 $\mathrm{cm^{-1}}$ belong to the polyethylene (PE) units. The peaks at 1736 $\mathrm{cm^{-1}}$, 1370 $\mathrm{cm^{-1}}$, 1238 $\mathrm{cm^{-1}}$, and 1020 $\mathrm{cm^{-1}}$ are assigned to the vinyl acetate (VA) units. The changes of the absorption bands in dependence of weathering time for the positions 3, 5, and 6 are displayed in Figs. 7 and 8. In addition, the oxidation index (OI) was calculated using the ratio of the wavenumber dependent absorption $A(k)$ of the 1736 $\mathrm{cm^{-1}}$ C=O peak and the 1465 $\mathrm{cm^{-1}}$ CH_2 peak [47]

$$OI = \frac{\int_{1600}^{1900} A(k)\mathrm{d}k}{\int_{1400}^{1500} A(k)\mathrm{d}k} \tag{5}$$

and displayed in the right image of Fig. 8.

Within 1500 h of weathering, position 3 did not show changes of the chemical structure. The OI remained approximately constant while small changes are probably rather a result of inhomegneities between the different samples than an aging effect. Considering the quantification of the UV additives in position 3, the UV absorber amount is still approximately 83 % of the initial concentration. Also, the UV stabilizer should be still functional, which has probably led to a suppression of degradation effects.

A similar result can be reported for position 5. The OI is slightly increased by approximately 20 % in comparison with the initial value after 1500 h of weathering. In addition, the broadening of the peak shoulder at 1715 $\mathrm{cm^{-1}}$ suggests the formation of ketones as a result of the degradation of the vinyl acetate entity [8], [49], [50], [51], [52]. However, considering the previously carried out quantification, the migration of UV additives was significantly damping the effects of photo degradation. Taking Fig. 6 into account, the UV absorber content in position 5 reached approximately 23 % of the initial concentration within 250 h. Based on the previous argumentation, it is conceivable that a similar amount of HALS additives also migrated to position 3, but was directly consumed by the formed

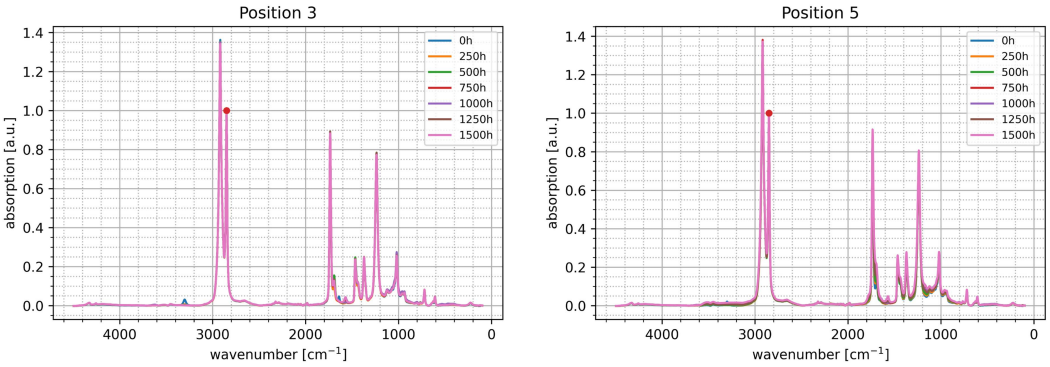

Fig. 7. FTIR measurements of the position 3 (left–with UV additives) and the position 5 (right – initially without UV additives) in dependence of weathering time. All spectra are mean values of the areas A, B, and C. The data was normalized to the 2850 cm^{-1} CH_2 peak (marked with the red dot).

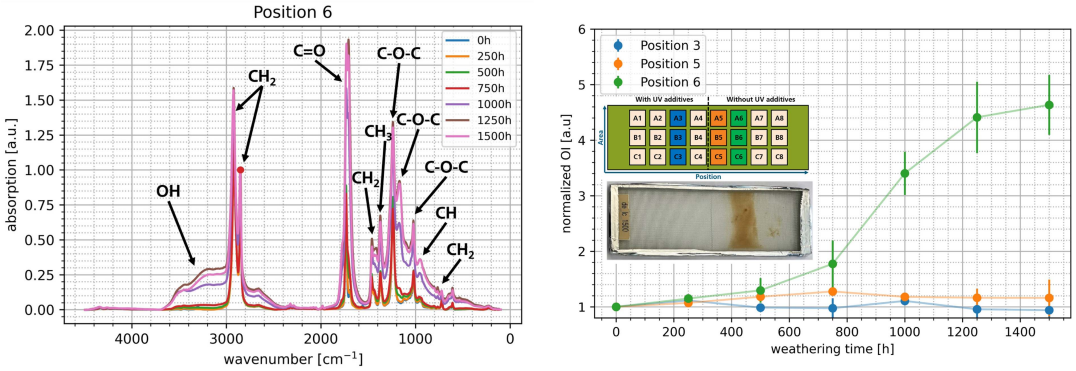

Fig. 8. FTIR measurements of the position 6 (left–without UV additives) and the development of the oxidation index (right) in dependence of weathering time. All data are mean values of the areas A, B, and C. The data was normalized to the 2850 cm^{-1} CH_2 peak (marked with the red dot) for the FTIR spectrum and to the initial oxidation index for the OI development.

radicals. Nevertheless, the migration UV additives forced by a concentration gradient was able to effectively prohibit photo degradation within 1.3 cm of lateral space.

Comparing these results with the spectrum of Position 6 in Fig. 8, the importance of UV additives becomes obvious. After 750 h of aging, the formation of several groups occurred. The formation of OH bonds can be found from 3700 cm^{-1} to 3100 cm^{-1}. These interactions are created by hydroperoxides or by hydroxyl groups as a result of hydroperoxide breakdown and are discussed in [49] and [50]. The peak shoulder from 1900 cm^{-1} to 1780 cm^{-1} is significantly broadened which is caused by γ-lactones [8], [49], [51]. These species are formed by the degradation of the VA units through the back-biting process [8], [49]. The other peak shoulder of the C=O peak from 1715 cm^{-1} to 1600 cm^{-1} is also broadened, which is caused by the generation of ketones [8], [49], [50], [51], [52]. They are either formed by Norrish type III reactions or due to the breakdown of hydroperoxides [8]. At 1170 cm^{-1}, a new peak was formed after 750 h of weathering. The C-O-C interaction is probably a result of the formation of aliphatic esters or as a result of the chain scission [8], [49], [51]. In addition, the absorption at 960 cm^{-1} intensified. These intensities are cause by CH out of plane bending. They occur in species like R-CH=CH-R which form during deacetylation [49]. In accordance with the changes in the spectra after 750 h of weathering, the OI started to increase significantly. After 1250 h of weathering the EVA was nearly totally degraded and a saturation of the OI increase occurred. The OI finally increased to approximately 4.6 times of the initial value after 1500 h due to ketone and lactone formation.

Fig. 9 visualizes the diffusion sample after 1500 h of weathering. Positions 1 to 5 do not show visual photo degradation. In position 6, severe browning occurred. However, these browning effects are not visible from position 7 to the end of the sample side without UV additives. Nevertheless, the removed samples from positions 6 to 8 were in a jellylike condition suggesting the destruction of the polymer network. In the literature, the presence of chromophores is correlated with the formation of

Fig. 9. Sample extracted after 1500 h of weathering. The sample extraction points with UV additives and without UV additives are in accordance with Fig. 1. Especially position 6 shows severe browning.

C=C and C=O bonds [1], [6], [7], [49], [53], [54]. While C=C bonds are also presented within the moieties generating the absorption intensities at 960 cm^{-1}, they should equally form in all positions without UV additives. Thus, the formed C=C bonds are probably no indication for the formation of chromophores, which are causing the browning effect.

On the other hand, several groups found correlations of additive presence and chromophore formation [6], [16], [18], [55], [56], [57], [58]. Considering the diffusion samples as displayed in Fig. 9, only the UV additives have been varied between both sides. Klemchuk et al. [16] proposed the formation of chromophore precursors if crosslinking peroxides are not fully consumed during lamination. The crosslinking peroxide reacts with the OH group of the benzophenone UV absorber creating a radical. In the next step, the created radical is interacting with another UV absorber radical to form a larger molecule, which can act as a chromophore [16]. Additionally, Oreski et al. [17] found that nonreacted crosslinking peroxides after lamination can cause browning effects during accelerated aging. Thus, the browning effect is most likely a result of the interactions with the UV absorber Cyasorb UV 531 [6], [16], [18], [58]. For the displayed diffusion samples two scenarios are conceivable while scenario 2) is considered more likely for the presented experiments.

1) The chromophores are formed by the reaction of the UV absorber Cyasorb UV 531 and radicals of the base polymer which are created by UV irradiance in the positions 5 to 8. In position 5, these radicals were neutralized by the UV stabilizer Tinuvin 770. However, the effective range of the UV stabilizer was limited to that position as it was discussed in Section III-A.
2) The chromophores are formed by the reaction of the UV absorber Cyasorb UV 531 with crosslinking peroxides, which were not consumed during the lamination process. During the weathering, the peroxides are radicalized by UV irradiation and react with the migrated UV absorber. This consideration could also explain why the UV stabilizer content was drastically reduced within the first 250 h of weathering (see Fig. 4) as it was consumed by the reaction with peroxide radicals. As in case 1), the effective range of the UV stabilizer was limited to the positions 1 to 5. Thus, the generation of browning effects is dependent on the migration behavior of the UV stabilizer which is in accordance with Fig. 6.

IV. Conclusion

The conducted experiments show the important role of UV additives within EVA encapsulants to prevent UV induced polymer degradation. Positions which have been stabilized by UV additives did not show degradation within 1500 h of weathering under IEC 62788-7-2-A3 conditions. Furthermore, inhomogeneities of the additive density can be balanced effectively by diffusion for distances of approximately 1.3 cm. Thus, positions which did not contain UV additives at the beginning were shielded for the full weathering duration when laying inside the effective distance. A synergy effect of the UV absorber and the UV stabilizer is likely to occur. Positions which have not been stabilized by the UV additives degrade significantly within 750 h of weathering. The formation of hydroxyl groups, ketones, lactones, and aliphatic esters was detected, and the oxidation index was strongly increased.

In total, the UV absorber is probably able to migrate approximately 4 cm within 1500 h of weathering. Considering the previous work by Reynier et al. and Földes et al., it is conceivable that molecules with comparable molecular weights can migrate similar distances when no other interaction occurs. Furthermore, the total UV absorber amount was conserved suggesting reversible keto-enol tautomerism. However, with the used weathering time of 1500 h within the conducted study, it is not possible to conclude whether the number or concentration of used UV-related additives is sufficient. Further experiments with longer weathering times and other combinations of stressors should be carried out to investigate the degradation behavior of the additives and polymers. In addition, the influence of the vinyl acetate content and the diffusion behavior of additives in POE and TPO encapsulants should be investigated at different temperatures and irradiation conditions. As discussed for anomalous diffusion, the microscopic structure of the respective material can have an influence on the migration behavior of different species.

The use of additives is a double edged sword. While the addition of additives is in general necessary for crosslinking reactions and to achieve a reasonable protection from UV irridiance, several interactions must be considered. On the one hand, the diffusion of additives can seemingly have a positive effect of leveling out the additive concentration screening with time the areas initially unprotected. On the other hand, if the crosslinking peroxide is not fully consumed during the lamination process, remnant molecules could decompose by UV irradiance forming radicals. These radicals probably significantly consume the UV stabilizer content. Moreover, they react with the UV absorber forming chromophores and therefore lead to severe browning effects. Thus, the lamination process or rather the crosslinking peroxide content has to be optimized when benzophenone UV absorbers are used. Either one needs to ideally consume all the peroxides during lamination or a sufficient amount of UV stabilizer needs to be added to trap remaining peroxide radicals.

The experiments within this work discussed effects within one EVA layer and while excluding humidity influences. A real solar module is much more complex as it contains several layers and interfaces with interaction potential. Furthermore, a combination of different stress factors like thermo-mechanical stresses, humidity, and UV irradiance can occur. Within a solar module lifetime, it is very likely that additives from different layers can migrate in the scale of several centimeters. This is especially problematic, when additives interact with each other or with radicals and should also be considered for the emerging EVA/polyolefin/EVA encapsulants. In the case of the UV absorber, the molecules could diffuse from the back side EVA into the front side EVA in solar modules. First, this could lead to a performance decrease because absorbed photons cannot reach the solar cell. Second, the migrated UV absorber molecules could react with radicals forming chromophores and reducing the solar module efficiency even more. Consequently, further studies should address the diffusion behavior of the additives at a coupon level and in solar modules as well as consider different film thicknesses.

References

[1] H. Han et al., "Analysis of the degradation of encapsulant materials used in photovoltaic modules exposed to different climates in China," *Sol. Energy*, vol. 194, pp. 177–188, 2019.

[2] A. Czanderna and F. Pern, "Encapsulation of PV modules using ethylene vinyl acetate copolymer as a pottant: A critical review," *Sol. energy Mater. Sol. cells*, vol. 43, no. 2, pp. 101–181, 1996.

[3] M. C. C. de Oliveira, A. S. A. D. Cardoso, M. M. Viana, and V. d. F. C. Lins, "The causes and effects of degradation of encapsulant ethylene vinyl acetate copolymer (EVA) in crystalline silicon photovoltaic modules: A review," *Renewable Sustain. Energy Rev.*, vol. 81, pp. 2299–2317, 2018.

[4] M. Halwachs et al., "Statistical evaluation of pv system performance and failure data among different climate zones," *Renewable Energy*, vol. 139, pp. 1040–1060, 2019.

[5] G. Oreski et al., "Properties and degradation behaviour of polyolefin encapsulants for photovoltaic modules," *Prog. Photovolt., Res. Appl.*, vol. 28, no. 12, pp. 1277–1288, 2020.

[6] F. Pern, "Factors that affect the EVA encapsulant discoloration rate upon accelerated exposure," *Sol. Energy Mater. Sol. Cells*, vol. 41, pp. 587–615, 1996.

[7] F. Pern, "Ethylene-vinyl acetate (EVA) encapsulants for photovoltaic modules: Degradation and discoloration mechanisms and formulation modifications for improved photostability," *Die Angewandte Makromolekulare Chemie: Appl. Macromol. Chem. Phys.*, vol. 252, no. 1, pp. 195–216, 1997.

[8] J. Jin, S. Chen, and J. Zhang, "UV aging behaviour of ethylene-vinyl acetate copolymers (EVA) with different vinyl acetate contents," *Polym. Degradation Stability*, vol. 95, no. 5, pp. 725–732, 2010.

[9] A. Omazic et al., "Relation between degradation of polymeric components in crystalline silicon PV module and climatic conditions: A literature review," *Sol. Energy Mater. Sol. Cells*, vol. 192, pp. 123–133, 2019.

[10] S. Chattopadhyay et al., "Visual degradation in field-aged crystalline silicon PV modules in India and correlation with electrical degradation," *IEEE J. Photovolt.*, vol. 4, no. 6, pp. 1470–1476, Nov. 2014.

[11] A. Sinha, O. Sastry, and R. Gupta, "Nondestructive characterization of encapsulant discoloration effects in crystalline-silicon pv modules," *Sol. Energy Mater. Sol. Cells*, vol. 155, pp. 234–242, 2016.

[12] C. Peike et al., "Origin of damp-heat induced cell degradation," *Sol. Energy Mater. Sol. Cells*, vol. 116, pp. 49–54, 2013.

[13] A. Kraft et al., "Investigation of acetic acid corrosion impact on printed solar cell contacts," *IEEE J. Photovolt.*, vol. 5, no. 3, pp. 736–743, May 2015.

[14] A. Jentsch, K.-J. Eichhorn, and B. Voit, "Influence of typical stabilizers on the aging behavior of EVA foils for photovoltaic applications during artificial UV-weathering," *Polym. Testing*, vol. 44, pp. 242–247, 2015.

[15] E. Cuddihy, C. Coulbert, A. Gupta, and R. Liang, "Flat-plate solar array project. Volume 7: Module encapsulation," 1986.

[16] P. Klemchuk et al., "Investigation of the degradation and stabilization of eva-based encapsulant in field-aged solar energy modules," *Polym. Degradation Stability*, vol. 55, no. 3, pp. 347–365, 1997.

[17] G. Oreski et al., "Crosslinking and post-crosslinking of ethylene vinyl acetate in photovoltaic modules," *J. Appl. Polym. Sci.*, vol. 134, no. 23, 2017.

[18] C. Peike, L. Purschke, K.-A. Weiss, M. Köhl, and M. Kempe, "Towards the origin of photochemical EVA discoloration," in *Proc. IEEE 39th Photovoltaic Specialists Conf.*, 2013, pp. 1579–1584.

[19] H. Frisch and S. A. Stern, "Diffusion of small molecules in polymers," *Crit. Rev. Solid State Mater. Sci.*, vol. 11, no. 2, pp. 123–187, 1983.

[20] J. Sax and J. Ottino, "Modeling of transport of small molecules in polymer blends: Application of effective medium theory," *Polym. Eng. Sci.*, vol. 23, no. 3, pp. 165–176, 1983.

[21] E. Földes and B. Turcsányi, "Transport of small molecules in polyolefins. I. diffusion of irganox 1010 in polyethylene," *J. Appl. Polym. Sci.*, vol. 46, no. 3, pp. 507–515, 1992.

[22] E. Földes, "Transport of small molecules in polyolefins. II. diffusion and solubility of irganox 1076 in ethylene polymers," *J. Appl. Polym. Sci.*, vol. 48, no. 11, pp. 1905–1913, 1993.

[23] E. Földes, "Transport of small molecules in polyolefins. iii. diffusion of topanol ca in ethylene polymers," *J. Appl. Polym. Sci.*, vol. 51, no. 9, pp. 1581–1589, 1994.

[24] S. X. Chen and R. T. Lostritto, "Diffusion of benzocaine in poly (ethylene-vinyl acetate) membranes: Effects of vehicle ethanol concentration and membrane vinyl acetate content," *J. Controlled Release*, vol. 38, no. 2–3, pp. 185–191, 1996.

[25] A. Reynier, P. Dole, and A. Feigenbaum, "Additive diffusion coefficients in polyolefins. ii. effect of swelling and temperature on the d= f (m) correlation," *J. Appl. Polym. Sci.*, vol. 82, no. 10, pp. 2434–2443, 2001.

[26] P. V. Yaneff, K. Adamsons, N. Cliff, and M. Kanouni, "Migration of reactable UVAS and HALS in automotive plastic coatings," *JCT Res.*, vol. 1, pp. 201–212, 2004.

[27] R. Heidrich, A. Mordvinkin, and R. Gottschalg, "Quantification of UV protecting additives in ethylene-vinyl acetate copolymer encapsulants for photovoltaic modules with pyrolysis-gas chromatography-mass spectrometry," *Polym. Testing*, vol. 118, 2023, Art. no. 107913.

[28] A. Beinert et al., "The influence of the additive composition on degradation induced changes in poly (ethylene-co-vinyl acetate) during photochemical aging," in *Proc. 29th Eur. PV Sol. Energy Conf. Exhib.*, Amsterdam, 2014.

[29] N. A. Shaath, "Ultraviolet filters," *Photochemical Photobiological Sci.*, vol. 9, pp. 464–469, 2010.

[30] J. Zawadiak and M. Mrzyczek, "Influence of substituent on uv absorption and keto–enol tautomerism equilibrium of dibenzoylmethane derivatives," *Spectrochimica Acta Part A: Mol. Biomol. Spectrosc.*, vol. 96, pp. 815–819, 2012.

[31] J. Pickett, D. Gibson, S. Rice, and M. Gardner, "Effects of temperature on the weathering of engineering thermoplastics," *Polym. Degradation Stability*, vol. 93, no. 3, pp. 684–691, 2008.

[32] J. E. Pickett and J. R. Sargent, "Sample temperatures during outdoor and laboratory weathering exposures," *Polym. Degradation Stability*, vol. 94, no. 2, pp. 189–195, 2009.

[33] A. Einstein, "Über die von der molekularkinetischen theorie der wärme geforderte bewegung von in ruhenden flüssigkeiten suspendierten teilchen," *Annalen der physik*, vol. 4, pp. 549–560, 1905.

[34] M. V. Smoluchowski, "Zur kinetischen theorie der brownschen molekularbewegung und der suspensionen," *Annalen der physik*, vol. 326, no. 14, pp. 756–780, 1906.

[35] C. M. Hansen, "Diffusion in polymers," *Polym. Eng. Sci.*, vol. 20, no. 4, pp. 252–258, 1980.

[36] S. Havlin and D. Ben-Avraham, "Diffusion in disordered media," *Adv. Phys.*, vol. 36, no. 6, pp. 695–798, 1987.

[37] F. Müller-Plathe, S. C. Rogers, and W. F. van Gunsteren, "Computational evidence for anomalous diffusion of small molecules in amorphous polymers," *Chem. Phys. Lett.*, vol. 199, no. 3–4, pp. 237–243, 1992.

[38] R. Metzler and J. Klafter, "The random walk's guide to anomalous diffusion: A fractional dynamics approach," *Phys. Rep.*, vol. 339, no. 1, pp. 1–77, 2000.

[39] M. Jaunich, M. Böhning, U. Braun, G. Teteris, and W. Stark, "Investigation of the curing state of ethylene/vinyl acetate copolymer (EVA) for photovoltaic applications by gel content determination, rheology, DSC and FTIR," *Polym. Testing*, vol. 52, pp. 133–140, 2016.

[40] M. Brogly, M. Nardin, and J. Schultz, "Effect of vinylacetate content on crystallinity and second-order transitions in ethylene—vinylacetate copolymers," *J. Appl. Polym. Sci.*, vol. 64, no. 10, pp. 1903–1912, 1997.

[41] J. S. Puente et al., "Segmental mobility and glass transition of poly (ethylene-vinyl acetate) copolymers: Is there a continuum in the dynamic glass transitions from PVAC to pe ?," *Polymer*, vol. 76, pp. 213–219, 2015.
[42] E. Denisov, "The role and reactions of nitroxyl radicals in hindered piperidine light stabilisation," *Polym. Degradation Stability*, vol. 34, no. 1–3, pp. 325–332, 1991.
[43] E. N. Step, N. J. Turro, P. P. Klemchuk, and M. E. Gande, "Model studies on the mechanism of hals stabilization," *Die Angewandte Makromolekulare Chemie: Appl. Macromol. Chem. Phys.*, vol. 232, no. 1, pp. 65–83, 1995.
[44] J. L. Hodgson and M. L. Coote, "Clarifying the mechanism of the denisov cycle: How do hindered amine light stabilizers protect polymer coatings from photo-oxidative degradation ?," *Macromolecules*, vol. 43, no. 10, pp. 4573–4583, 2010.
[45] M. R. Paine, G. Gryn'ova, M. L. Coote, P. J. Barker, and S. J. Blanksby, "Desorption electrospray ionisation mass spectrometry of stabilised polyesters reveals activation of hindered amine light stabilisers," *Polym. Degradation Stability*, vol. 99, pp. 223–232, 2014.
[46] A. Wypych and G. Wypych, *Databook of UV Stabilizers*. Scarborough, ON, Canada: ChemTec Publishing, 2020.
[47] J. Almond, P. Sugumaar, M. N. Wenzel, G. Hill, and C. Wallis, "Determination of the carbonyl index of polyethylene and polypropylene using specified area under band methodology with ATR-FTIR spectroscopy," *e-Polymers*, vol. 20, no. 1, pp. 369–381, 2020.
[48] G. Socrates, *Infrared and Raman Characteristic Group Frequencies: Tables and Charts*. Hoboken, NJ, USA: John Wiley & Sons, Inc., 2004.
[49] N. S. Allen, M. Edge, M. Rodriguez, C. M. Liauw, and E. Fontan, "Aspects of the thermal oxidation, yellowing and stabilisation of ethylene vinyl acetate copolymer," *Polym. Degradation Stability*, vol. 71, no. 1, pp. 1–14, 2000.
[50] G. Oreski, G. M. Wallner, and R. Lang, "Ageing characterization of commercial ethylene copolymer greenhouse films by analytical and mechanical methods," *Biosyst. Eng.*, vol. 103, no. 4, pp. 489–496, 2009.
[51] B. Ottersböck, G. Oreski, and G. Pinter, "Comparison of different microclimate effects on the aging behavior of encapsulation materials used in photovoltaic modules," *Polym. Degradation Stability*, vol. 138, pp. 182–191, 2017.
[52] C. Barretta, G. Oreski, S. Feldbacher, K. Resch-Fauster, and R. Pantani, "Comparison of degradation behavior of newly developed encapsulation materials for photovoltaic applications under different artificial ageing tests," *Polymers*, vol. 13, no. 2, 2021, Art. no. 271.
[53] Y. Shindo, B. Read, and R. Stein, "The study of the orientation of polyvinyl chloride films by means of birefringence and infrared, visible, and ultraviolet dichroism," *Die Makromolekulare Chemie: Macromol. Chem. Phys.*, vol. 118, no. 1, pp. 272–312, 1968.
[54] A. P. Patel, A. Sinha, and G. Tamizhmani, "Field-aged glass/backsheet and glass/glass PV modules: Encapsulant degradation comparison," *IEEE J. Photovolt.*, vol. 10, no. 2, pp. 607–615, Mar. 2020.
[55] J. H. Wohlgemuth, M. D. Kempe, and D. C. Miller, "Discoloration of PV encapsulants," in *Proc. IEEE 39th Photovolt. Specialists Conf.*, 2013, pp. 3260–3265.
[56] D. C. Miller et al., "Degradation in photovoltaic encapsulant transmittance: Results of the first PVQAT TG5 artificial weathering study," *Prog. Photovolt.: Res. Appl.*, vol. 27, no. 5, pp. 391–409, 2019.
[57] Y. Lyu et al., "Fluorescence imaging analysis of depth-dependent degradation in photovoltaic laminates: Insights to the failure," *Prog. Photovolt.: Res. Appl.*, vol. 28, no. 2, pp. 122–134, 2020.
[58] N. Pinochet, R. Couderc, and S. Therias, "Solar cell UV-induced degradation or module discolouration: Between the devil and the deep yellow sea," *Prog. Photovolt., Res. Appl.*, 2023.

6. Spatially resolved degradation analysis of solar modules

6.1. Solar module degradation under harsh weathering conditions

The previous publications have shown that different stressors lead to different degradation mechanisms in the encapsulant. This has a direct influence on the solar cell and, consequently, on the entire solar module. It was also shown that the use of UV-A fluorescent lamps leads to unrealistic aging behavior and that the long-wave components of the lamp spectrum also trigger degradation mechanisms in various PV encapsulants. Furthermore, it was observed that the degradation of the encapsulants is strongly dependent on the presence of stabilizing additives.

The following work extends the previous findings. Solar modules are artificially aged by a combination of UV irradiation and DH conditions. The concentration of stabilizing additives is analyzed at different positions and correlated with the degradation of the encapsulant. In addition, the electrical performance data of the solar modules and electroluminescence measurements are correlated with the degradation behavior of the UV additives and the encapsulant.

Since the combination of UV and DH weathering in conjunction with a spatially resolved analysis of the encapsulant represents a novel approach, the individual aging conditions of the IEC 61215 standard were used as a guideline and combined. This was necessary as there was no suitable preliminary work for orientation. The UV irradiation and the DH conditions would cause significantly less damage if used individually (see subsection 5.1), but in combination, they have led to severe degradation.

The work is reprinted, with permission, from Robert Heidrich, Anton Mordvinkin, Ralph Gottschalg, and the IEEE 50th Photovoltaic Specialists Conference (PVSC).

Spatially Resolved Degradation Analysis of Solar Modules After Combined Accelerated Aging

Robert Heidrich[12], Anton Mordvinkin[1], and Ralph Gottschalg[12]

[1]Fraunhofer Center for Silicon Photovoltaics CSP, Halle (Saale), 06120, Germany
[2]Anhalt University of Applied Sciences, Koethen, 06366, Germany

***Abstract*— The degradation behavior of solar modules was investigated under combined damp heat and UV weathering conditions. A full electrical characterization, including electro luminescence measurements, shows a severe module degradation after 2000h, with power losses exceeding 60%. A chemical analysis of the encapsulation material on the basis of ethylene-vinyl acetate copolymer, extracted directly from the weathered modules, reveals a clear dependence of the encapsulant degradation on the position in the module and the weathering time. Remarkably, the consumption of the UV stabilizer in the encapsulant correlates to the degradation of the encapsulation material and finally to the degradation of the solar module. This finding emphasizes the relevance of the quality control of the encapsulant formulation for the module reliability.**

Keywords—accelerated aging, I-V, EL, GCMS, FTIR

I. Introduction

The degradation behavior of solar modules and encapsulation materials is mainly analyzed with help of the accelerated weathering. However, one mostly relies on individual stressors, e.g., damp heat (DH) and UV weathering, thus separating the water ingress and UV-driven degradation. A more realistic approach requires a combination of the UV irradiation with the moisture ingress. Furthermore, a solar module is a complex object for physical investigations consisting of several multi-component materials, including encapsulants and backsheets interacting at their interfaces. Thus, to address this complexity, the degradation of encapsulation materials must be studied enabling these interactions rather than weathering individual polymer films.

Considering the aforementioned points, the given work shows the analysis of one-cell mini modules, built using an EVA encapsulant and a PET-based backsheet, which were aged under combined DH and UV weathering conditions. The macroscopic analysis such as the electrical characterization and electro luminescence (EL) measurements were correlated with space-resolved polymer investigations both on the chain and additive level.

II. Results and Discussion

A. Electrical Characterization

Mini modules were weathered under combined damp heat (DH) and UV irradiation (UV) conditions for 2000h. The following parameters were used: 80°C chamber temperature, 60% relative humidity (r.h.) and 227.5 W/m^2 integrated UV intensity between 280nm and 380nm.

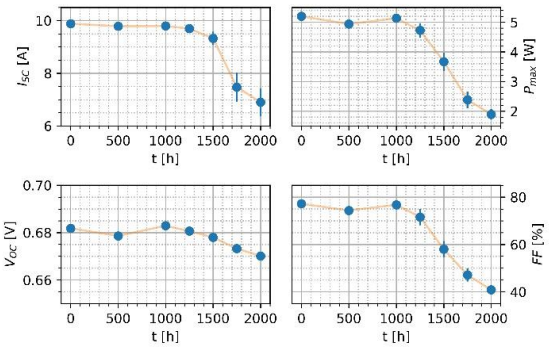

Figure 1: Electrical performance data of the one-cell mini modules weathered under combined UV and DH conditions.

Figure 1 shows the electrical characterization. An exemplary mini module after 2000h of the UV+DH weathering is visualized in Figure 2. The colored rectangles mark the positions for the EVA-sample extraction (Green: Backside EVA – middle of the module (m_m_b). Purple: Frontside EVA – top right corner of the module, on top of the electrical contact (t_r_f).). After approximately 1000h of weathering significant performance losses were detected. Within the next 1000h of weathering, the mini modules fully degraded with a total power loss of over 65%. While the series resistance was increasing, I-V curves suggest more complex degradation mechanism such as non-radiative recombination and surface short circuits. Furthermore, the mini modules showed prominent browning originating from the formation of chromophores [1]. Degradation effects regarding the encapsulation materials were investigated by several characterization methods on the polymer and additive levels.

Figure 2 demonstrates the EL images of a single solar module every 500h of weathering. The EL images show a significant decrease in the radiative recombination confirming the assumptions made due to the I-V curves. Non-radiative recombination effects are assumed to occur mainly due to the humidity-based degradation. Thus, the path of moisture ingress is visualized by the EL images, starting with the diffusion

2023 IEEE 50th Photovoltaic Specialists Conference (PVSC) | 978-1-6654-6059-0/23/$31.00 ©2023 IEEE | DOI: 10.1109/PVSC48320.2023.10359812

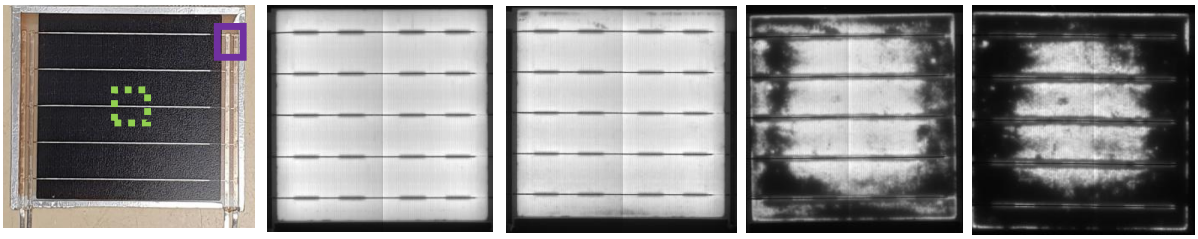

Figure 2: Left: Exemplary mini module after 2000h of weathering. The colored rectangles mark the position for the EVA-sample preparation. Middle left to right: Electro luminescence (EL) characterization every 500h of weathering.

through the backsheet, followed by the diffusion around the solar cell edges to the top of the cell. The moisture is known to interact with the EVA encapsulant leading to the formation of acetic acid and subsequently causing the decrease in EL [2].

The chemical analysis of the mini modules was performed destructively. Therefore, the data points for every weathering step were evaluated for different modules and include effects of inhomogeneities and local differences between samples.

B. GCMS measurements

The degradation behavior of additives within the encapsulant was investigated quantitatively with pyrolysis-gas chromatography-mass spectrometry (PY-GCMS) in dependence of the weathering time [3]. In particular, the content of the UV absorber Cyasorb UV 531 and the UV stabilizer Tinuvin 770 was of interest, serving as UV protectors. Figure 3 visualizes the PY-GCMS quantification in dependence of the weathering time and sample position in the module. The large difference of the initial UV absorber concentration can be caused by the local spatial inhomogeneities, introduced by the polymer film production. Furthermore, the degradation behavior

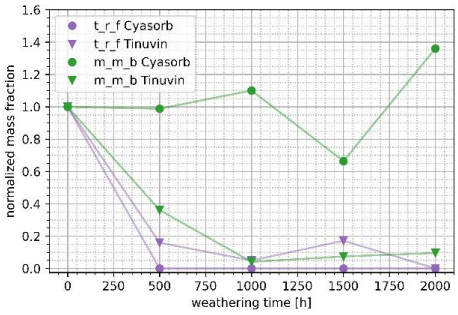

Figure 3: Consumption of the UV absorber Cyasorb UV 531 and the UV stabilizer Tinuvin 770 in dependence of the sample position and weathering (values normalized to the initial mass fraction).

strongly diverges in dependence of the sample position. While the concentration in the top EVA above the cell is already consumed after 500h of the UV irradiation, the concentration in the bottom EVA below the cell remains unchanged. Therefore, Cyasorb UV 531 becomes consumed in the course of photo degradation.

In contrast to the UV absorber, the UV stabilizer behaves nearly similar for the frontside and backside EVA. Thus, the UV irradiation seems to be not relevant for the degradation of the UV stabilizer. Tinuvin 770 as a hindered amine light stabilizer (HALS) reacts according to the Denisov cycle [4]. It degrades by interacting with free radicals, formed during the degradation, which results in the concentration-dependent reaction rate. Therefore, the data suggests that the radical formation is mainly driven by humidity rather than UV irradiation.

The solar modules showed a strong decrease in the power output after approximately 1000h of weathering, after the UV stabilizer was already consumed. Thus, it suggests that the degradation of the UV stabilizer can be considered as an early signature for the subsequent module degradation. After the free radicals cannot be neutralized by the UV stabilizer, the degradation of the mini modules intensifies leading to a significant power loss.

C. ATR -FTIR- measurements

The differences in the encapsulant degradation on the polymer level depending on the position and weathering time were investigated by ATR-FTIR measurements. Figure 4 shows the FTIR spectrum of EVA samples at the t_r_f and m_m_b positions. Especially the peaks at 1370 cm^{-1} (symmetric deformation of CH3), 1465 cm^{-1} (asymmetric deformation vibration of CH2), 1715 cm^{-1} (C=O stretching vibration of ketones), between 1800 cm^{-1} and 1680 cm^{-1} (C=O stretching vibration) and between 3700 cm^{-1} and 3100 cm^{-1} (hydroxyl groups vibrations) will be discussed [5] [6] [7]. As a measure of the chain oxidation, carbonyl indices were calculated referring the C=O stretching vibration peak to the area of the 1465 cm^{-1} CH2 peak, thus normalizing away the effects of the variable ATR-crystal contact with the EVA sample. These results are shown in Figure 5.

Except for the largely growing hydroxyl peak after 2000h of weathering, the spectrum of the front side EVA shows minor changes. The large hydroxyl peak can be caused by hydroperoxides forming due to high energy irradiance. Because these peaks also occur by aging EVA in a hot-air fan oven, the presence of moisture is probably not required for the hydroxyl formation [5].

The degradation of the backside EVA differs strongly from the degradation of the frontside EVA, as it is affected only by the moisture ingress. The carbonyl index strongly increases after 1500h of weathering. Furthermore, the 1715 cm-1 peak becomes more pronounced. This appearance in combination with the emerging peak at approximately 1175 cm^{-1} indicates an

978-1-6654-6059-0/23/$31.00 ©2023 IEEE

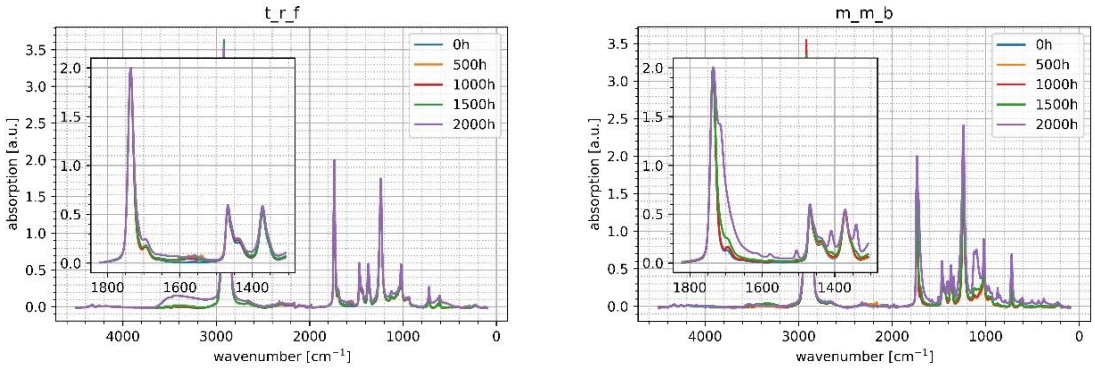

Figure 4: FTIR-ATR measurements in dependence of sample localization and weathering time.

increased presence of ketone carbonyl groups in the polymer chains, acting as chromophores [8] [9]. Considering that the 1715 cm-1 peak significantly increases after the UV stabilizer is consumed, it is conceivable that these reactions were prevented in the beginning. HALS amines trapped the formed radicals stopping the ketone formation.

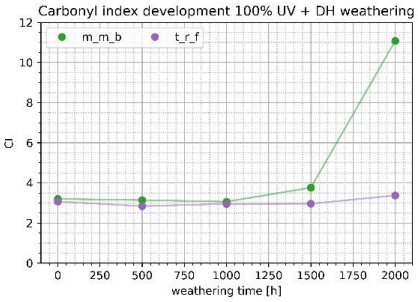

Figure 5: Change of the carbonyl index in dependence of sample localization weathering time.

III. Summary

Mini modules have been weathered under combined damp heat and UV conditions. The electrical characterization showed a performance decrease after approximately 1000h of combined weathering. A total power loss of approximately 65% occurred after 2000h. The I-V curve and EL images suggested the presence of non-radiative recombination centers. Furthermore, the EL images showed a moisture path which starts 2 dimensionally through the backsheet and crawling around the edges of the solar cell afterwards.

The degradation analysis of the encapsulant and the imbedded additives shows diverging results in dependence of the sample position. The UV absorber in the frontside EVA was already consumed after 500h of weathering while it stayed nearly unchanged in the backside EVA. The UV stabilizer degraded qualitatively similarly in the frontside and backside EVA and was completely consumed after approximately 1000h. The frontside EVA shows the formation of hydroperoxides due to the photo degradation which was not the case for the backside EVA. In the latter case, after the UV stabilizer was consumed, the moisture-driven formation of ketone carbonyl groups was observed because of radical forced polymer chain degradation.

These findings show that the occurring degradation reactions in the encapsulant are highly dependent on the position in the module. In addition, they occur after the UV stabilizer is fully consumed. Further studies should investigate the dependence of the UV stabilizer concentration as well as the dependence on weathering parameters on the encapsulant and module degradation. This finding emphasizes that the UV stabilizer can serve as an early-stage degradation marker for the module degradation. Further, it stresses that the quality control of the EVA formulation, especially the UV-stabilizer content, plays a key role for the solar module reliability.

[1] Pern, F. J. "Ethylene-vinyl acetate (EVA) encapsulants for photovoltaic modules: Degradation and discoloration mechanisms and formulation modifications for improved photostability." Die Angewandte Makromolekulare Chemie: Applied Macromolecular Chemistry and Physics 252.1 (1997): 195-216.

[2] Jankovec, Marko, et al. "In-situ monitoring of moisture ingress in PV modules using digital humidity sensors." IEEE journal of photovoltaics 6.5 (2016): 1152-1159.

[3] Heidrich, Robert, Anton Mordvinkin, and Ralph Gottschalg. "Quantification of UV protecting additives in ethylene-vinyl acetate copolymer encapsulants for photovoltaic modules with pyrolysis-gas chromatography-mass spectrometry." *Polymer Testing* (2022): 107913.

[4] Hodgson, Jennifer L., and Michelle L. Coote. "Clarifying the mechanism of the Denisov cycle: how do hindered amine light stabilizers protect polymer coatings from photo-oxidative degradation?." Macromolecules 43.10 (2010): 4573-4583.

[5] Allen, Norman S., et al. "Aspects of the thermal oxidation, yellowing and stabilisation of ethylene vinyl acetate copolymer." Polymer degradation and stability 71.1 (2000): 1-14.

[6] Sharma, Bhuwanesh K., et al. "Effect of vinyl acetate content on the photovoltaic-encapsulation performance of ethylene vinyl acetate under accelerated ultra-violet aging." Journal of Applied Polymer Science 137.2 (2020): 48268.

[7] Barretta, Chiara, et al. "Comparison of degradation behavior of newly developed encapsulation materials for photovoltaic applications under different artificial ageing tests." Polymers 13.2 (2021): 271.

[8] Jin, Jing, Shuangjun Chen, and Jun Zhang. "UV aging behaviour of ethylene-vinyl acetate copolymers (EVA) with different vinyl acetate contents." Polymer degradation and stability 95.5 (2010): 725-732.

[9] Çopuroğlu, Mehmet, and Murat Şen. "A comparative study of thermal ageing characteristics of poly (ethylene-co-vinyl acetate) and poly (ethylene-co-vinyl acetate)/carbon black mixture." Polymers for Advanced Technologies 15.7 (2004): 393-399

978-1-6654-6059-0/23/$31.00 ©2023 IEEE

6.2. Solar module degradation under moderate weathering conditions

The previous chapter has shown that the degradation of solar modules strongly depends on the polymer degradation and the consumption of the UV stabilizer. Furthermore, it was observed that the degradation reactions of the EVA vary at different points of the solar modules. The combination of UV and DH weathering used led to strong degradation, so the weathering was possibly over-accelerated.

In the following and final results chapter of this thesis, the previous weaknesses of the analysis are adjusted. A significantly lower irradiation dose is used for the combination of UV and DH weathering. In addition, polymer films and mini modules are aged in the same chamber to investigate the differences between single layer and multilayer systems. The additive consumption and the degradation reactions are successively analyzed at different points of the solar modules and in the films. In this way, a degradation model for the UV additives is derived. Afterwards, the degradation of the additives is correlated with that of the encapsulant. In the next step, the degradation of the encapsulant is linked to the deterioration of the electrical parameters. In many places, the results are compared directly with the previous work in order to develop a holistic understanding of the degradation chain of solar modules under the influence of combined stressors.

Spatially Resolved Degradation of Solar Modules in Dependence of the Prevailing Microclimate

Robert Heidrich, Anton Mordvinkin, and Ralph Gottschalg

***Abstract*—In this work, a holistic approach to analyze solar module degradation is undertaken. The degradation kinetics of UV additives in the ethylene-vinyl acetate copolymer (EVA) encapsulant are derived using a quantification method. In addition, minimodules are analyzed after combined accelerated aging (UV irradiation at 85°C and 60% relative humidity) at different positions. In this way, the local degradation reactions of the encapsulant are determined as a function of the prevailing stressors and additive consumption. These findings are correlated with the electrical characterization ($I - V$ and electroluminescence measurements) to expand the understanding of module degradation. Performance losses are mainly due to a combination of hydrolysis and Norrish type II reactions of the encapsulant, as acetic acid is produced in both cases corroding the electrical contacts. Independent of the local stressor, the UV stabilizer shows first-order degradation kinetics, which is directly linked to the degradation of the encapsulant and, thus, indirectly to cell degradation. It is shown that the UV stabilizer consumption is an early precursor of module degradation and could be utilized to evaluate the remaining lifetime of a PV module.**

***Index Terms*—Additives, degradation, encapsulant, ethylene-vinyl acetate copolymer (EVA), performance loss, spectroscopy.**

I. Introduction

SOLAR energy has become one of the most important energy sources of our time and will continue its success story in the near future [1]. Reliability and lifetime of the components are nowadays the main factors determining the costs of energy. There are several approaches to predict the long-term behavior of PV modules [2], [3], [4], [5], [6]. However, these are generally empirical without consideration of the underlying degradation mechanisms of the individual components of a module [2], [3], [4], [5].

The packaging materials used for solar modules determine their long-term behavior [7], [8], [9], [10]. In particular, the interaction of the individual encapsulant layers with the backsheet can have an influence on the degradation behavior of the modules [6], [11]. The additives contained in the various polymer layers, in turn, determine the degradation behavior of these layers [12], [13], [14]. In the end, an understanding of additive and polymer degradation and its influence on the degradation of the solar cell and the electrical connectors is essential for the development of a physics-based degradation model.

There is a large body of work dealing with the degradation of ethylene-vinyl acetate copolymer (EVA) [13], [14], [15], [16], [17], [18], [19], [20], [21], which is currently the most widely used encapsulant. There are also various studies on the degradation of different backsheets [22], [23], [24]. However, these materials are often only studied in isolation, although the degradation behavior in combination, especially with a solar cell, can be completely different. This can be explained by the fact that different microclimates occur within a PV module. Certain parts are more exposed to moisture than others and UV radiation does not reach all areas to the same extent. In addition, mobile species such as polymer additives can diffuse within or between the different layers [14]. Degradation effects such as PID are also heavily dependent on the combination of materials used [25], [26]. It is, therefore, to be expected that different degradation reactions take place depending on the position in a solar module.

The dependence of the degradation kinetics on the prevailing microclimate leads indirectly to the next problem. In most studies and weathering standards in the field of accelerated aging, a distinction is usually made between UV aging and damp heat (DH) aging [13], [14], [21], [27], [28], [29], [30]. Considering the different climatic conditions around the world, it is unrealistic to expose material combinations to only one type of stressor at a time. Although there has been some recent work in this direction, which has shown that field failures can be provoked, much research still needs to be done to develop optimal aging procedures [31], [32], [33].

This work is intended to investigate the influence of these microclimates, which arise under combined weathering conditions. It is an extension of our previously published work [34]. For this purpose, minimodules were produced in a conventional structure and aged at an accelerated rate. In addition, pure EVA films were weathered in the same chamber. Using a recently developed method for UV additive quantification, the degradation kinetics of UV absorber and UV stabilizer in EVA are to be derived [35]. Afterward, the additive consumption of the pure EVA films is compared with those in the module, enabling the correlation of UV additive degradation with the aging of the encapsulant and macroscopic effects, such as module performance. The minimodules are examined at different positions using Fourier-transform infrared spectroscopy (FTIR)

Manuscript received 11 March 2024; revised 14 April 2024; accepted 7 June 2024. This work was supported by TotalEnergies. *(Corresponding author: Robert Heidrich.)*

Robert Heidrich and Ralph Gottschalg are with the Fraunhofer Center for Silicon Photovoltaics CSP, 06120 Halle, Germany, and also with the Anhalt University of Applied Sciences, 06366 Koethen, Germany (e-mail: robert.heidrich@csp.fraunhofer.de; ralph.gottschalg@csp.fraunhofer.de).

Anton Mordvinkin is with the Fraunhofer Center for Silicon Photovoltaics CSP, 06120 Halle, Germany (e-mail: anton.mordvinkin@csp.fraunhofer.de).

Color versions of one or more figures in this article are available at https://doi.org/10.1109/JPHOTOV.2024.3414179.

Digital Object Identifier 10.1109/JPHOTOV.2024.3414179

to analyze the effect of the respective microclimate on the degradation reactions of the encapsulant. These are correlated to the electrical characterization of the modules to understand the degradation chain.

II. Materials and Methods

A. Minimodules

The single-cell minimodules used correspond to the conventional structure of a solar module with the dimension of approximately 20 cm × 20 cm. The front sheet used was 3-mm float glass. The EVA has a UV cut-off (50% transmittance at 365 nm), a vinyl acetate (VA) content of 26%–28%, and a thickness of 0.4–0.6 mm. The light transmission is reported to be over 91% by data sheet and the EVA was used as the encapsulation material for the front and back sides. A Meier ICOLAM 10/08 was used for lamination with the following parameters: The laminator was set to 55 °C. The samples were then placed in the laminator, which was evacuated for 6.5 min and heated to 80 °C. The modules were then pressed with 600 mbar and heated to 155 °C within 3 min. The temperature and pressure were maintained for a further 15 min. Finally, the laminator was cooled down to 55 °C within 30 min while the pressure of 600 mbar was kept constant. The gel content after lamination is specified in the data sheet with over 85% while measurements of separate films show gel contents of around 90%. This means that no remaining crosslinking peroxides are to be expected. The entire lamination process complies with the manufacturer's specifications for the EVA used. The solar cells are based on PERC technology with five busbars and four electrical contacts for $I-V$ measurements. The backsheet is based on polyethylene terephthalate (PET) with a thickness of 320 μm. The moisture permeability of the backsheet is specified with 1.9 g/m^2 per day. After lamination, the edges of the minimodules were sealed with an aluminum tape to simulate a frame and make it more difficult for moisture to penetrate while reducing edge effects.

B. Sample Preparation

For the measurements with pure EVA, an approx. 30 cm × 30 cm piece of film was laminated under the abovementioned conditions. Subsequently, 5 cm × 5 cm squares were cut out and aged in the climate chamber. Two film samples were available for each weathering step. For the PY-GCMS measurements, samples weighing approximately 4 mg (2–3 mm in diameter) were punched out. Consequently, the complete bulk was always measured in order to exclude surface effects. The PY-GCMS measurements were carried out in triple determination.

Sampling of the minimodules was carried out at various points in order to analyze aging effects in a spatially resolved manner. The different positions are shown in Fig. 4. The following nomenclature is used throughout the paper: t_r_f—front EVA on top of the inner interconnector at the top of the module, b_r_f—front EVA on top of the inner interconnector at the back of the module, m_m_b—back EVA in the middle of the module. For the b_r_f and t_r_f samples, the backsheet was cut in the area of the inner interconnector. Afterward, the interconnector was removed as a whole from the module. The front EVA remained on the glass and could be removed with a scalpel. For the m_m_b position, the backsheet was carefully removed layer by layer with a scalpel until the EVA layer on the back was visible. This was also carefully prepared with the scalpel to avoid contamination by the solar cell. PY-GCMS and FTIR measurements of the minimodules were carried out in double determination.

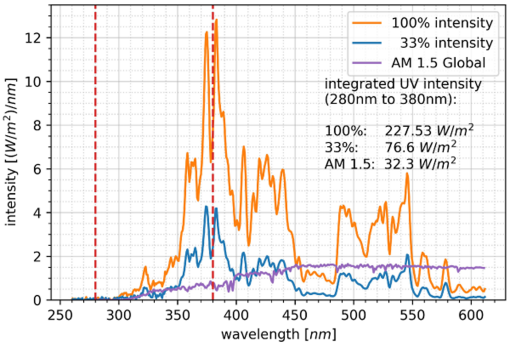

Fig. 1. Spectrum of the used metal halide lamps in comparison with the AM 1.5 global (ASTM G173-03 reference spectra derived from SMARTS v. 2.9.2. provided by NREL). The 100% weathering corresponds to the intensity used in our previous work [34].

C. Weathering

The weathering was carried out in CTS CSL −70/1500 UV climate chambers and was based on IEC 61215, but the parameters were varied [29]. A combination of DH and UV conditions was selected. The temperature was set to 85 °C and the relative humidity (r.h.) to 60%. The irradiation was realized by metal halide lamps, which were set with an integrated irradiance of 76.6 W/m^2 (33% weathering—this work) and 227.53 W/m^2 (100% weathering—previous work for comparison [34]) between 280 and 380 nm. The spectrum used is shown in Fig. 1, especially in the high-energy UV range, it is similar to the AM 1.5 global. The minimodules produced were weathered for a maximum of 2000 h. The electrical characterization was carried out every 250 h for all modules. After each weathering step, two modules were removed for destructive measurement procedures.

Temperature measurements at various positions inside modules with a comparable structure (same glass, same cell type, same encapsulant, and white backsheet) under the same weathering conditions show that the area below the solar cell reaches approximately 90 °C while b_r_f and t_r_f positions reach approximately 88 °C. Additionally, previous studies with xenon lamps have shown that the sample temperature of clear and white samples can be approximated by the chamber temperature during UV weathering [36], [37]. Thus, the temperature of the plain EVA films can be approximated by the chamber temperature.

D. Characterization Methods

1) I–V Characterization and Electroluminescence (EL) Measurements: The $I-V$ characteristics were measured with a Berger Lichttechnik solar simulator (Flasher system). The tests were carried out at 25 °C and an irradiance of 1000 W/m^2 (standard test conditions). The flasher corresponds to class A in the categories of homogeneity, spectral consistency, and temporal stability. The repeatability is less than 0.3% deviation. The flasher was calibrated with a reference module before each series

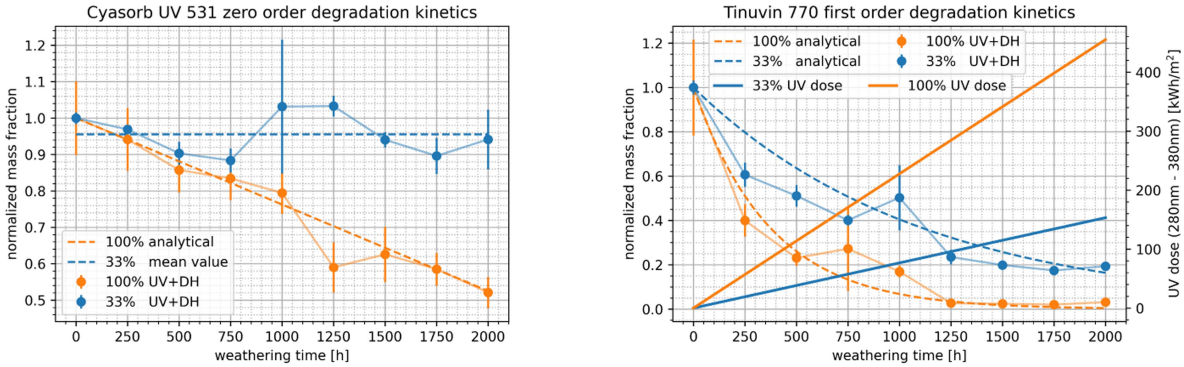

Fig. 2. UV additive quantification of the plain EVA films. Degradation kinetics of the UV absorber Cyasorb UV 531 (left) and the UV stabilizer Tinuvin 770 (right) and the corresponding integrated UV dose between 280 and 380 nm in dependence of the weathering time.

of measurements. The EL measurements were carried out with a greateyes LumiSolar Professional system. A cooled GE2048 512 BI MID CCD sensor is installed in the camera. For the EL measurements, the modules were powered with 8.5 A.

2) Pyrolysis-Gas Chromatography-Mass Spectrometry: For qualitative and quantitative analysis of the polymer and the additive composition, a combination of pyrolysis, gas chromatography, and mass spectrometry (PY-GCMS) was used. The PY-GCMS setup and settings are explained in detail in our previous works focusing on additive quantification [14], [35]. An EGA/Py-3030D from Frontier Laboratories, Ltd., pyrolysis oven with attached autosampler AS-1020E was used for thermo desorption. As gas chromatograph, a Trace 1300 from Thermo Scientific with He carrier gas was used. The implemented column was an Ultra ALLOY Capillary Column (length 30 m, internal diameter 0.25 mm, and film thickness 0.25 μm) from Frontier Laboratories, Ltd. An ISQ 7000 mass spectrometer from Thermo Scientific was coupled to the gas chromatograph. The m/z range was set from 29 to 800.

3) Attenuated Total Reflectance—Fourier-Transform Infrared Spectroscopy: An Inventio spectrometer from Bruker was used for the FTIR analysis. The measurements were carried out in ATR mode using a transit platinum unit with a diamond tip. The wavelength interval was set from 4000 to 650 cm^{-1} with a resolution of 2 cm^{-1} and eight scans.

III. Results and Discussion

A. UV Additive Consumption in Plain EVA Films

As stated in our previous work, the consumption of the UV stabilizer could be a potential marker for the degradation of solar modules [34]. However, the degradation behavior of UV additives in EVA films is currently not fully understood. Consequently, the consumption of the commonly used UV additives Cyasorb UV 531 (UV absorber) and Tinuvin 770 (UV stabilizer) was first investigated as a function of different radiation intensities in laminated EVA films. The degradation kinetics of both additives and the applied UV dose is visualized in Fig. 2. It must be mentioned that only the HALS base molecule can be detected with the PY-GCMS method used. All nitroxide forms resulting from the Denisov cycle remain unaffected by the analysis [38]. It is, therefore, a measure of how quickly the base molecule is consumed under given environmental conditions.

Analyzing the consumption of the UV absorber, a clear difference between both irradiation conditions is observable. For the 33% intensity, the UV absorber amount fluctuates around the mean value and no trend in degradation is observed. This indicates reversible keto-enol tautomerism [16], [39], [40]. In our previous work, we also found that similar intensities will not lead to the decomposition of the UV absorber [13], [14]. However, the 100% weathering shows a continuous decrease of UV absorber concentration until reaching approximately 52% of the initial concentration after 2000 h. This contrasts with the results of Pern [15] who reported an exponential degradation rate of Cyasorb UV 531 in cyclohexane, but in accordance with the work of Pickett and Moore[41], who reported zero-order degradation kinetics of Cyasorb UV 531 in PMMA films. In the case of the carried out weathering, the degradation kinetics of the UV absorber concentration N_C can be described by

$$\frac{\mathrm{d}N_C(t)}{\mathrm{d}t} = -IB_C(\varphi, T) \cdot \Theta(I) \tag{1}$$

with the UV intensity I and a chamber parameter B_C, which is dependent on the relative humidity φ and the temperature T and the Heaviside function Θ, which enables the degradation when a specific intensity threshold is passed. Equation (1) does not contain a dependence on the UV absorber amount $N_C(t)$ because the linear decrease of the mass fraction suggests a degradation kinetic, which is independent of the UV absorber concentration. Thus, (1) can be easily integrated and using the normalized initial condition $N_C(0) = 1$ yields

$$N_C(t) = 1 - IB_C(\varphi, T)t \cdot \Theta(I). \tag{2}$$

Using (2) with $B_C(\varphi, T) = 5.21 \times 10^{-6}$ m^2/J and $I = 227.53$ W/m^2 as integrated UV dose between 280 and 380 nm will lead to the displayed curve. However, the high intensity of the 100% weathering is unrealistic indicating that the UV absorber should not be consumed under outdoor irradiation.

In contrast to the UV absorber, the UV stabilizer degrades under both weathering conditions. This can be explained by the principle of work of the HALS functional groups. They react in the complex Denisov cycle trapping radicals; thus, they

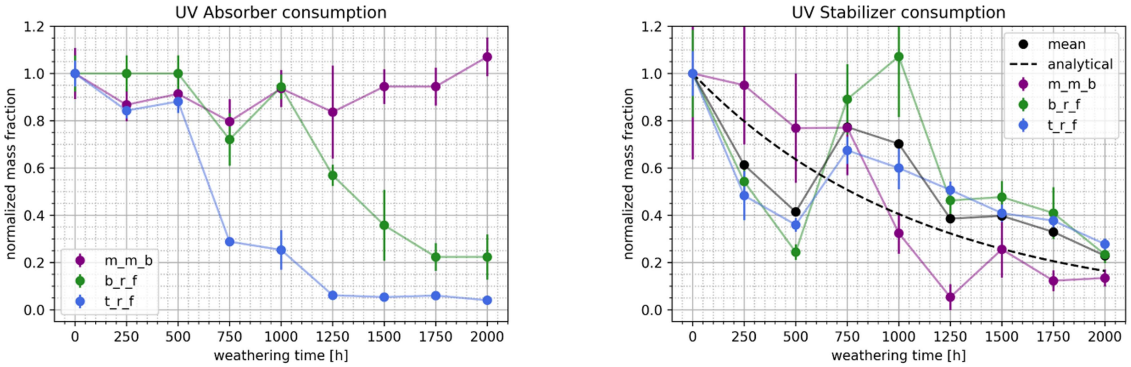

Fig. 3. UV additive quantification of the weathered mini modules. Left: Normalized development of the UV absorber content in dependence of weathering time while the standard deviation of the different samples is represented with the error bar. Right: Normalized development of UV stabilizer content at different positions with standard deviation as error bars, the mean curve of all positions and the analytical curve of (4) with the same chamber parameter as for the plain EVA films. The minimodules were aged with the 33% weathering conditions.

need a reaction partner and will be consumed in dependence of radical presence [38], [42], [43], [44]. The significantly higher consumption under the 100% weathering suggests an increased radical formation compared to the 33% weathering. For the 100% weathering, the HALS base form is nearly completely consumed after 1250 h, whereas for the 33% weathering, there is still about 20% of the base concentration present after 2000 h.

As observed in our previous work, the base form of the UV stabilizer is consumed exponentially [13], [14]. The exponential dependence can be explained by a reservoir effect. Assuming there is a reservoir of radicals for the HALS amines to react with, the decay is only dependent on the amount of HALS molecules $N_T(t)$ (pseudo first-order kinetics). This leads to

$$\frac{\mathrm{d}N_T(t)}{\mathrm{d}t} = -N_T I B_T(\varphi, T) \tag{3}$$

with the UV intensity I and the chamber parameter B_T. Using the normalized initial condition $N_T(0) = 1$ will lead to

$$N_T(t) = e^{-IB_T(\varphi,T)t}. \tag{4}$$

Using (4), the two UV intensities I_{33} and I_{100} and the molecule amounts $N_{T_{33}}$ and $N_{T_{100}}$ for the 100% and 33% weathering, the chamber parameter can be calculated analytically by

$$B_T(\varphi, T) = -\frac{\ln(N_{T_{33}} N_{T_{100}})}{(I_{33} + I_{100})\tilde{t}} \tag{5}$$

while the molecule amount of a specific time point $\tilde{t}$ must be evaluated. Using $B_T(\varphi, T) = 3.28 \times 10^{-9}$ m^2/J, $I_{100} = 227.53$ W/m^2 and $I_{33} = 76.60$ W/m^2 will lead to the displayed curves of the analytic solution of (4). Thus, for fixed humidity and temperature, the consumption of the UV stabilizer can be described sufficiently as a function of the UV intensity.

This can be observed, for example, at the measuring points of both curves for a radiation dose of approximately 120 kWh/m^2. This dose is reached after approximately 1500 h of 33% weathering and leads to a UV stabilizer concentration of approximately 20% of the initial concentration. With 100% weathering, this dose is reached after approximately 500 h and also leads to a UV stabilizer concentration of approximately 20%.

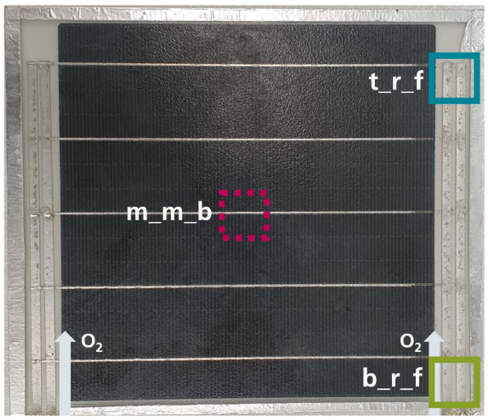

Fig. 4. Exemplary minimodule with encapsulant extraction point. The blue rectangle corresponds to the front EVA on top of the inner interconnector at the top of the module (t_r_f), the green rectangle corresponds to the front EVA on top of the inner interconnector at the bottom of the module (b_r_f) and the purple rectangle corresponds to the back EVA in the middle of the module (m_m_b). The arrows symbolize a possible oxygen pathway at the electrical connectors.

B. Spatially Resolved Solar Module Degradation

1) UV Additive Degradation: Minisolar modules have been aged under the same chamber conditions as the previously analyzed polymer films. The data of the 100% weathering were previously analyzed but are further evaluated and compared with the more realistic 33% weathering of this study [34]. An exemplary module with the encapsulant extraction points and the later used abbreviations is displayed in Fig. 4. The corresponding additive consumption in dependence of the weathering time for the 33% weathering is displayed in Fig. 3. The color code of the different positions is in accordance with Fig. 4.

Investigating the degradation behavior of the UV absorber in solar modules in comparison with the plain EVA films shows clear differences. In our previous works, dealing with coupon samples and for the plain EVA samples before, the UV absorber content stayed approximately constant or was fluctuating around the mean value due to inhomogeneities between different

samples [13], [14]. The same behavior can be observed for the backside sample of the module (m_m_b). However, for the front side of the module, the UV absorber content is significantly consumed. Especially for the top side of the module (t_r_f), the content is nearly completely vanished after 1250 h reaching only about 5% of the initial concentration.

As discussed in the weathering section, the temperature between the different positions within the module should be similar, only varying by $\pm$ 2 °C. Thus, the diverging behavior of front and back Cyasorb UV 531 consumption is most likely not the result of a temperature effect, because the temperature between front encapsulant and back encapsulant as well as the temperature of plain EVA is only minimally varying. Furthermore, it was shown that the moisture ingress of permeable backsheets is occurring 2-D for the whole backsheet area [45], [46]. Consequently, the m_m_b position should be penetrated by moisture at first, but this does not affect the UV absorber content. It is conceivable that the moisture diffused in over a certain period of time in combination with the UV radiation at positions b_r_f and t_r_f has led to the degradation of the UV absorber. The pure EVA films allow moisture to diffuse in and out quickly, but the layered structure of a solar module traps it. In addition, reactions with the electrical connector in combination with the stressors could lead to the observed behavior. The UV absorber could have been radicalized [47], bound to the connectors and, thus, is not desorbing anymore. Reactions of the UV absorber with excess crosslinking peroxide as in our previous work with another encapsulant are unlikely [14], as the encapsulant used here did not show discoloration or UV absorber degradation in any of our other work [13], [48]. At this stage, the exact cause of this degradation reaction is still unclear.

In contrast to the UV absorber, the UV stabilizer in the mini modules behaves similarly as in the plain EVA. Especially, the m_m_b position shows an exponential decrease. After 2000 h the UV stabilizer content decreased to 15%–25% of the initial content in dependence of the sample position. However, inhomogeneities and internal diffusion between the different sample positions and weathering steps probably resulted in the observed fluctuations [14]. Recently, it was found that the consumption of the HALS base molecule is similar for UV weathering and DH weathering under IEC 61215 [48]. Thus, the UV stabilizer content of all positions was combined in the right image of Fig. 3 using the mean value of the investigated positions. The dashed line represents the analytical solution of (4) using the same B_T as for the plain EVA samples. Except for the 750 and 1000 h weathering steps, which also showed the strongest deviations in comparison with the other weathering steps, the HALS consumption behaves similarly in the mini modules and the plain EVA films. Thus, assuming a reservoir of radicals and describing the UV stabilizer content with (4) seems to be sufficient for plain EVA films and EVA in minimodules when weathered under the same conditions.

2) EVA Degradation: The previously examined EVA positions (see Fig. 4) have been further characterized by attenuated total reflectance—Fourier-transform infrared spectroscopy (ATR-FTIR) measurements. The results are displayed in Fig. 5 (the color coding is in accordance with Fig. 4) while the corresponding peaks and functional groups are listed in Table I. As observable in the full spectrum (top left image), the encapsulant shows all characteristic EVA peaks while significant changes due to aging occur mainly in the region of 1800–1500 cm^{-1}. Thus, further evaluation focused on the mentioned wavenumber interval yielding significant differences regarding the EVA degradation in dependence on the observed position. The displayed graphs (except for the full spectrum) are difference plots, subtracting the initial FTIR spectrum after normalization using the 2850-cm^{-1} CH_2 peak.

TABLE I
FTIR ABSORPTION PEAK ASSIGNMENT

waven. [cm^{-1}]	group	excitation
2920	CH_2	stretching vibration (PE)
2850	CH_2	deformation vibration (PE)
1736	C=O	stretching vibration (VA)
1740-1660	C=O	stretching vibration (acetic acid)
1715-1650	C=O	stretching vibration of ketones
1660-1550	C=C	stretching vibration
1465	CH_2	stretching vibration (PE)
1370	CH_3	deformation vibration (VA)
1238	C-O-C	stretching vibration (VA)
1020	C-O-C	stretching vibration (VA)
960	CH	deformation vibration (VA)
770	CH	vibration of vinyl groups (-CH=CH-)
720	CH_2	skeleton rocking vibration (PE)

Intensities belong to the polyethylene (PE) units, the VA units or degradation products of the base polymer. The assignment is in accordance with the work in [13], [14], [18], [20], [21], [51], [52], and [53].

The b_r_f position shows two significant changes. The 1736-cm^{-1} peak is increasing in intensity and broadening suggesting ketone formation. This species can either be formed by Norrish type III reactions induced by photodegradation or during a breakdown reaction of hydroperoxides [19], [20], [49]. The peak with the center at 1570 cm^{-1} is probably the result of UV-induced Norrish type II reactions forming C=C bonds [17], [18], [20], [50]. The t_r_f position shows no ketone formation during aging. However, Norrish type II reactions with resulting C=C bond formation can be observed [17], [18], [20], [50]. Furthermore, the formation of a new C=C peak at 770 cm^{-1} was observed (not shown). The oxidation index (OI) was calculated using the peak ratio of the 1700 cm^{-1} C=O peak integral and the 720 cm^{-1} CH_2 peak integral as carried out in our previous work [13]. The OI development is visualized in Fig. 6. Only the b_r_f position shows a significant OI increase with ongoing weathering time. Thus, the assumed ketone formation for this position is validated. Although Norrish type III reactions or breakdown reactions of hydroperoxides can lead to ketone formation, the latter is more likely because, otherwise, ketones should have also formed at the t_r_f position, which was exposed to the same UV irradiance. The solar modules have not been sealed with aluminum tape at the electrical contacts (see Fig. 4). Consequently, oxygen diffused into the modules via this point and led to the reaction described at the b_r_f position. In accordance with our previous work, all photodegradation effects seem to be pronounced after approximately 1500 h of weathering, when most of the UV stabilizer is consumed (see Fig. 3) [34].

In comparison with the front encapsulant, the m_m_b position behaves differently. The vanishing peak with the center at approximately 1550 cm^{-1} is probably a vibration of NH groups of the HALS in the initial state [52], [54], [55]. This peak has also been reported in our previous work using the same commercial encapsulant [13]. Thus, it does not correlate with encapsulant degradation of the back EVA. However, the changes of the C=O peak from 1770 to 1600 cm^{-1} are probably a result of EVA

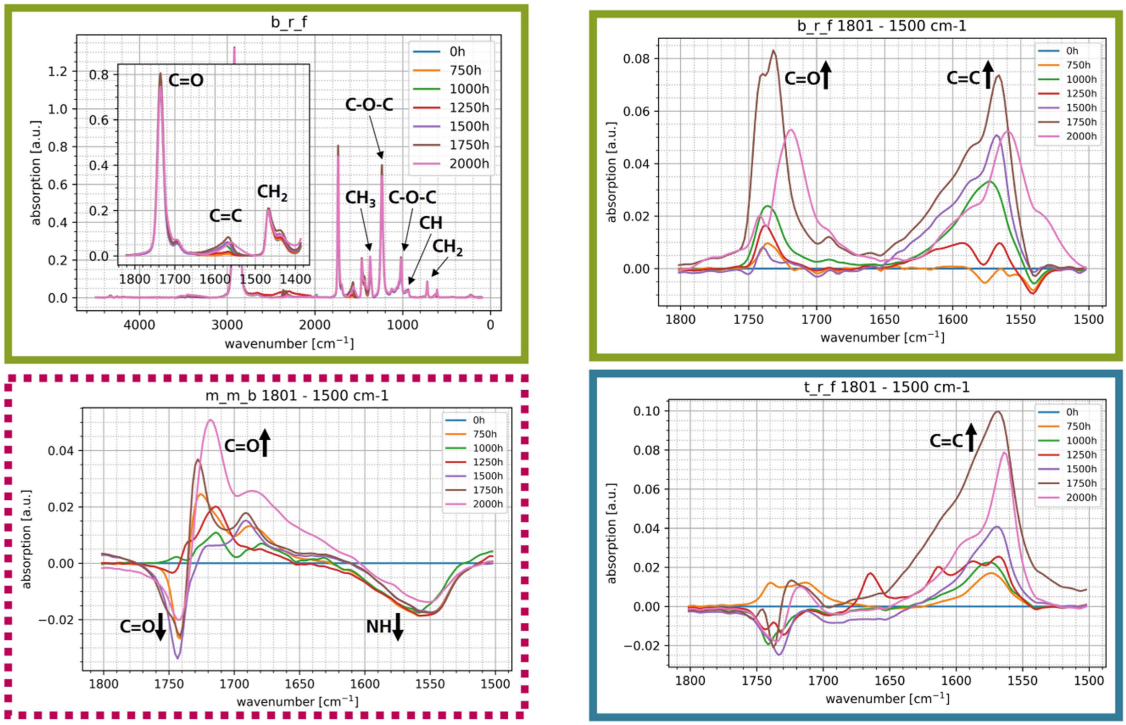

Fig. 5. ATR-FTIR measurements of the examined encapsulant positions. The color coding is in accordance with Fig. 4. The top left image shows a complete FTIR spectrum of the EVA encapsulant. The other images show difference spectra subtracting the initial spectrum after normalization. The minimodules were aged with the 33% weathering conditions.

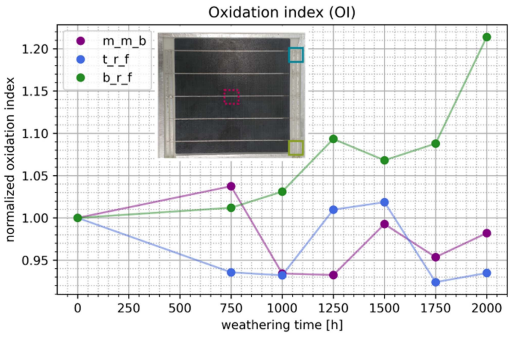

Fig. 6. Oxidation index (ratio of the 1700 cm^{-1} C=O peak integral and the 720-cm^{-1} CH_2 peak integral) in dependence of the position and weathering time. The color code corresponds to Fig. 4. The minimodules were aged with the 33% weathering conditions.

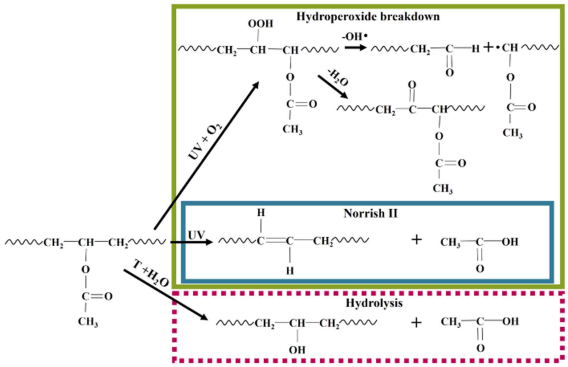

Fig. 7. Observed degradation reactions in dependence of the investigated position. The color code corresponds to Fig. 4. The degradation reactions are based on the work in [17], [18], [20], [27], [28], [49], [50], and [56].

hydrolysis [28], [56]. The decrease in intensity at approximately 1750 cm^{-1} and increase in intensity at approximately 1720 cm^{-1} indicate the formation of acetic acid and were observed for DH aged modules [27], [28]. The measured spectra are also in accordance with the absorbance of pure acetic acid as they show a pronounced C=O peak from 1740 to 1700 cm^{-1}, which can also create a shoulder from 1710 to 1660 cm^{-1} [51]. The UV stabilizer consumption of the m_m_b position is even stronger than for the front encapsulant samples as seen in the Py-GCMS results. For the front EVA, the effect is overlapped with the formation of double bonds observed in the same spectral region. However, as the hydrolysis of EVA does not result in radical formation like for photodegradation, the consumption of the UV stabilizer can probably not easily be correlated to the polymer degradation at this point.

The EVA inside the minimodules degrades differently in dependence of the investigated position and the environmental stressors. Thus, the microclimate at a specific position has a significant impact on the occurring degradation reactions. Fig. 7 visualizes the suggested reactions in dependence of the position

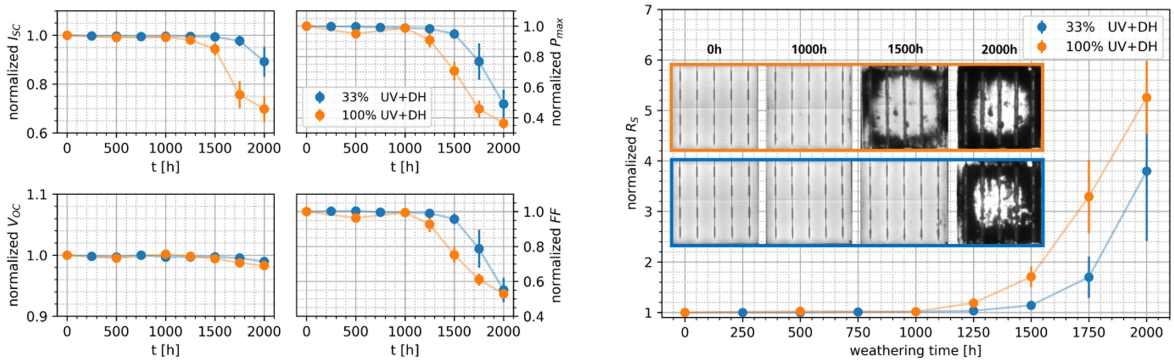

Fig. 8. Development of the electrical key parameters I_{SC}, V_{OC}, P_{max}, and FF (left) and increase in the series resistance R_S in combination with EL measurements (right).

inside the modules. These microclimate effects can possibly intensify for real-sized modules due to different diffusion distances of moisture and additives [14], [45]. Furthermore, they should be highly dependent on the used material combination, especially when combining encapsulant layers with different additive compositions or when using a diffusion-open / diffusion-inhibiting backsheet.

3) Electrical Characterization: The consumption of the UV additives in combination with encapsulant degradation and ingressed moisture led to the degradation of the solar cells. The electrical characterization of both weathering conditions is displayed in Fig. 8 while the comparison with our previous work (100%, orange) is color coded [34]. In comparison with the previous weathering, the 33% weathering shows a comparable behavior of short circuit current (I_{SC}) degradation, open-circuit voltage (V_{OC}) degradation, fill factor (FF) decrease and power decrease at the maximum power point (P_{max}). However, the degradation of all key performance parameters started later, after approximately 1500 h of weathering. Also, the increase in series resistance (R_S) and the decrease in electroluminescence (EL) follow the same pattern but shifted to later times. If Fig. 2 is taken into account, the degradation of the 100% weathering begins after about 230 kWh/m^2 and the degradation of 33% weathering after about 120 kWh/m^2. The combination of irradiation with humidity and temperature, therefore, plays a greater role than the pure UV dose.

While the encapsulant degradation shows a combination of UV (hydroperoxide breakdown and Norrish type II reactions) and DH (hydrolysis) induced degradation, the resulting performance loss of the solar modules can mainly be attributed to the DH effects. As reported by several groups in the literature, the performance loss of PERC-based solar modules induced by UV irradiation is minimal in comparison with the observed degradation [57], [58], [59]. In our previous work, in which we used the same module structure but carried out individual DH and UV weathering, only minimal damage occurred under pure UV aging despite the higher intensity [48]. In particular, FF, which shows a severe decrease, is nearly unaffected by sole UV aging [48], [58], [59].

However, the FTIR analysis showed the hydrolysis of EVA and Norrish type II reactions, both leading to the formation of acetic acid, especially after 1250 h. Thus, the increased R_S that results in a decrease in FF and P_{max} is induced by acetic acid. It was shown in the past that acetic acid corrodes electrical contacts of the solar cells, which leads to an increase in R_S and decrease in EL [60], [61], [62]. In accordance with the literature, this corrosion manifests itself macroscopically first in a drop in FF and in a second step with a reduction in I_{SC} [63]. This is due to the fact that the acetic acid dissolves the Ag-nanoparticles contained in the glass layer between the busbar and the cell [62], [63].

As shown in our previous work, the macroscopic degradation (e.g., performance loss) starts, when most of the UV stabilizer is consumed [34]. The UV stabilizer reached approximately 40% of the initial concentration after 1250 h of weathering, which is just before a significant decrease in the electrical parameters occurred. Although there is no direct link between UV stabilizer consumption and performance losses in the module, the behavior of the UV stabilizer is directly linked to the degradation of the encapsulant. Consequently, the degradation behavior of the UV stabilizer could be used to make assumptions about the expected solar module degradation, as this can be described using (4) or modifications of it.

The used DH conditions (85 °C and 60% r.h.) have a much smaller r.h. than the parameters used in the literature and the weathering standard IEC 61215; however, the examined modules show a significant faster degradation than in the literature [29], [61], [64]. Although the temperature is comparable and the UV irradiance inflicts only minor damage to the solar cell [36], [37], the combination of DH and UV weathering seems to be more severe for the solar modules than DH weathering with higher r.h. This can be explained by the fact that UV-induced Norrish type II reactions also produce acetic acid [18], [20]. Under normal UV aging conditions (low r.h.) there is little moisture available in the module. The acetic acid cannot dissociate and be transferred to all the locations by moisture. Furthermore, the autocatalytic effect is prevented when all the moisture in the module has been used up for hydrolysis [60].

Under combined conditions, after moisture diffusion around the cell [45], [46], sufficient moisture is also available for the acetic acid formed by UV radiation. Consequently, the damage to the modules is greater, although the individual conditions are less

intense than for sole UV weathering or sole DH weathering. This could also explain why the reduction in EL is particularly strong at the edges. The acetic acid produced by EVA hydrolysis can quickly reach the front and back contacts of the solar cell at these positions. Especially at the edges, this effect is superimposed with acetic acid formation due to UV-induced Norrish type II reactions. This means that the front and back contacts are more severely damaged at the edges than in the center, as the acetic acid (or moisture) has to travel a long diffusion path to the front contact in the center of the cell. In the field, however, it is always to be expected that more than one stressor will act simultaneously. This shows a further advantage for the use of the UV stabilizer as a degradation marker. The additive reacts to all forms of stressors, so that modeling is possible under different aging conditions.

IV. Conclusion

The degradation of solar modules is a complex process of various reactions and interactions between the different materials used. It has been shown that the degradation reactions at different points within a module can differ significantly depending on the prevailing microclimate. The UV additives, which are intended to protect the encapsulant from degradation, play a special role here. The UV absorber, which is not consumed in a pure foil, degrades quickly within solar modules if exposed to UV irradiance. On the other hand, the UV stabilizer follows pseudo first-order degradation kinetics, regardless of whether it is embedded in a pure film or in an encapsulant in the module. The derived analytical solution allows one to predict the consumption of the UV stabilizer depending on the used irradiance. Since the degradation behavior of the encapsulant is directly coupled to the consumption of the UV stabilizer base molecule, its degradation kinetics are suitable for modeling macroscopic module degradation.

The combination of UV and DH weathering conditions used caused significant damage to the modules within 1500 h, although the combination of conditions is milder than it would be in the respective individual parameters under IEC 61215. This is probably due to a synergy effect of the Norrish type II reactions with moisture penetration and the hydrolysis of the encapsulant. Both types of reaction lead to the formation of acetic acid, which corrodes the contacts of the solar cell and increases the series resistance. However, the combination of different stressors in the field is a realistic scenario. Consequently, future tests should consider that the combination of stressors can drastically accelerate the degradation behavior of solar modules. In addition, it was found that the hydrolysis of EVA has critical consequences for module reliability compared to photodegradation. Thus, stabilization against hydrolysis by means of suitable additives should be considered.

Although this work dealt with EVA as an encapsulant, various findings are transferable to novel polyolefin elastomer (POE)-based encapsulants. These use the same UV additives, so the UV stabilizer could also be used here for modeling. Furthermore, photo oxidation is also problematic for POE encapsulants, so that the influence of microclimates and the material combination of backsheet and encapsulant used can lead to different degradation reactions at different points within the solar modules.

Acknowledgment

The authors would like to thank Marius Lüdemann for his help with sample preparation.

References

[1] F. J. Nijsse et al., "The momentum of the solar energy transition," *Nature Commun.*, vol. 14, no. 1, 2023, Art. no. 6542.
[2] D. C. Jordan, C. Deline, S. R. Kurtz, G. M. Kimball, and M. Anderson, "Robust PV degradation methodology and application," *IEEE J. Photovolt.*, vol. 8, no. 2, pp. 525–531, Mar. 2018.
[3] A. B. Subramaniyan, R. Pan, J. Kuitche, and G. TamizhMani, "Quantification of environmental effects on PV module degradation: A physics-based data-driven modeling method," *IEEE J. Photovolt.*, vol. 8, no. 5, pp. 1289–1296, Sep. 2018.
[4] I. Kaaya, M. Koehl, A. P. Mehilli, S. de Cardona Mariano, and K. A. Weiss, "Modeling outdoor service lifetime prediction of PV modules: Effects of combined climatic stressors on PV module power degradation," *IEEE J. Photovolt.*, vol. 9, no. 4, pp. 1105–1112, Jul. 2019.
[5] J. Ascencio-Vásquez, I. Kaaya, K. Brecl, K.-A. Weiss, and M. Topič, "Global climate data processing and mapping of degradation mechanisms and degradation rates of PV modules," *Energies*, vol. 12, no. 24, 2019, Art. no. 4749.
[6] B. Brune et al., "Quantifying the influence of encapsulant and backsheet composition on PV-power and electrical degradation," *Prog. Photovolt.: Res. Appl.*, vol. 31, pp. 716–728, 2023.
[7] M. Halwachs et al., "Statistical evaluation of PV system performance and failure data among different climate zones," *Renewable Energy*, vol. 139, pp. 1040–1060, 2019.
[8] A. P. Patel, A. Sinha, and G. Tamizhmani, "Field-aged glass/backsheet and glass/glass PV modules: Encapsulant degradation comparison," *IEEE J. Photovolt.*, vol. 10, no. 2, pp. 607–615, Mar. 2020.
[9] D. C. Jordan, N. Haegel, and T. M. Barnes, "Photovoltaics module reliability for the terawatt age," *Prog. Energy*, vol. 4, no. 2, 2022, Art. no. 022002.
[10] G. Oreski et al., "Motivation, benefits, and challenges for new photovoltaic material & module developments," *Prog. Energy*, vol. 4, no. 3, 2022, Art. no. 032003.
[11] A. Omazic et al., "Relation between degradation of polymeric components in crystalline silicon PV module and climatic conditions: A literature review," *Sol. Energy Mater. Sol. Cells*, vol. 192, pp. 123–133, 2019.
[12] A. Jentsch, K.-J. Eichhorn, and B. Voit, "Influence of typical stabilizers on the aging behavior of EVA foils for photovoltaic applications during artificial UV-weathering," *Polym. Testing*, vol. 44, pp. 242–247, 2015.
[13] R. Heidrich et al., "UV lamp spectral effects on the aging behavior of encapsulants for photovoltaic modules," *Sol. Energy Mater. Sol. Cells*, vol. 266, 2024, Art. no. 112674.
[14] R. Heidrich, M. Lüdemann, A. Mordvinkin, and R. Gottschalg, "Diffusion of UV additives in ethylene-vinyl acetate copolymer encapsulants and the impact on polymer reliability," *IEEE J. Photovolt.*, vol. 14, no. 1, pp. 131–139, Jan. 2024.
[15] F. Pern, "Factors that affect the EVA encapsulant discoloration rate upon accelerated exposure," *Sol. Energy Mater. Sol. Cells*, vol. 41, pp. 587–615, 1996.
[16] F. Pern, "Ethylene-Vinyl acetate (EVA) encapsulants for photovoltaic modules: Degradation and discoloration mechanisms and formulation modifications for improved photostability," *Die Angewandte Makromolekulare Chemie, Appl. Macromol. Chem. Phys.*, vol. 252, no. 1, pp. 195–216, 1997.
[17] A. Czanderna and F. Pern, "Encapsulation of PV modules using ethylene vinyl acetate copolymer as a pottant: A critical review," *Sol. Energy Mater. Sol. Cells*, vol. 43, no. 2, pp. 101–181, 1996.
[18] N. S. Allen, M. Edge, M. Rodriguez, C. M. Liauw, and E. Fontan, "Aspects of the thermal oxidation, yellowing and stabilisation of ethylene vinyl acetate copolymer," *Polym. Degradation Stability*, vol. 71, no. 1, pp. 1–14, 2000.
[19] M. Çopuroğlu and M. Şen, "A comparative study of UV aging characteristics of poly (ethylene-co-vinyl acetate) and poly (ethylene-co-vinyl acetate)/carbon black mixture," *Polymers Adv. Technol.*, vol. 16, no. 1, pp. 61–66, 2005.

[20] J. Jin, S. Chen, and J. Zhang, "UV aging behaviour of ethylene-vinyl acetate copolymers (EVA) with different vinyl acetate contents," *Polym. Degradation Stability*, vol. 95, no. 5, pp. 725–732, 2010.

[21] C. Barretta, G. Oreski, S. Feldbacher, K. Resch-Fauster, and R. Pantani, "Comparison of degradation behavior of newly developed encapsulation materials for photovoltaic applications under different artificial ageing tests," *Polymers*, vol. 13, no. 2, 2021, Art. no. 271.

[22] N. Kim et al., "Study on the degradation of different types of backsheets used in PV module under accelerated conditions," *Sol. Energy Mater. Sol. Cells*, vol. 120, pp. 543–548, 2014.

[23] M. Knausz et al., "Degradation of photovoltaic backsheets: Comparison of the aging induced changes on module and component level," *J. Appl. Polym. Sci.*, vol. 132, no. 24, 2015, Art. no. 42093.

[24] A. Fairbrother, N. Phillips, and X. Gu, "Degradation processes and mechanisms of backsheets," in *Durability and Reliability of Polymers and Other Materials in Photovoltaic Modules*. Amsterdam, The Netherlands: Elsevier, 2019, pp. 153–174.

[25] V. Naumann et al., "Explanation of potential-induced degradation of the shunting type by Na decoration of stacking faults in Si solar cells," *Sol. Energy Mater. Sol. Cells*, vol. 120, pp. 383–389, 2014.

[26] F. ibne Mahmood and G. TamizhMani, "Impact of different backsheets and encapsulant types on potential induced degradation (PID) of silicon PV modules," *Sol. Energy*, vol. 252, pp. 20–28, 2023.

[27] K. Hara, S. Jonai, and A. Masuda, "Crystalline SI photovoltaic modules functionalized by a thin polyethylene film against potential and damp-heat-induced degradation," *RSC Adv.*, vol. 5, no. 20, pp. 15017–15023, 2015.

[28] K. Hara and Y. Chiba, "Spectroscopic investigation of long-term outdoor-exposed crystalline silicon photovoltaic modules," *J. Photochemistry Photobiol. A, Chem.*, vol. 404, 2021, Art. no. 112891.

[29] *Terrestrial Photovoltaic (PV) Modules - Design Qualification and Type Approval - Part 2: Test Procedures*, IEC Standard 61215-2:2021, *Int. Electrotechnical Commission, Geneva, Switzerland*, 2021.

[30] *Measurement Procedures for Materials Used in Photovoltaic Modules - Part 7-2: Environmental Exposures - Accelerated Weathering Tests of Polymeric Materials*, DIN IEC/TS 62788-7-2, Int. Electrotechnical Commission, Geneva, Switzerland, 2019.

[31] D. E. Mansour et al., "Effect of backsheet properties on PV encapsulant degradation during combined accelerated aging tests," *Sustainability*, vol. 12, no. 12, 2020, Art. no. 5208.

[32] M. Owen-Bellini et al., "Advancing reliability assessments of photovoltaic modules and materials using combined-accelerated stress testing," *Prog. Photovolt. Res. Appl.*, vol. 29, no. 1, pp. 64–82, 2021.

[33] P. Hacke et al., "Acceleration factors for combined-accelerated stress testing of photovoltaic modules," *Sol. RRL*, vol. 7, no. 12, 2023, Art. no. 2300068.

[34] R. Heidrich, A. Mordvinkin, and R. Gottschalg, "Spatially resolved degradation analysis of solar modules after combined accelerated aging," in *Proc. IEEE 50th Photovolt. Specialists Conf.*, 2023, pp. 1–3.

[35] R. Heidrich, A. Mordvinkin, and R. Gottschalg, "Quantification of UV protecting additives in ethylene-vinyl acetate copolymer encapsulants for photovoltaic modules with pyrolysis-gas chromatography-mass spectrometry," *Polym. Testing*, vol. 118, 2023, Art. no. 107913.

[36] J. Pickett, D. Gibson, S. Rice, and M. Gardner, "Effects of temperature on the weathering of engineering thermoplastics," *Polym. Degradation Stability*, vol. 93, no. 3, pp. 684–691, 2008.

[37] J. E. Pickett and J. R. Sargent, "Sample temperatures during outdoor and laboratory weathering exposures," *Polym. Degradation Stability*, vol. 94, no. 2, pp. 189–195, 2009.

[38] J. L. Hodgson and M. L. Coote, "Clarifying the mechanism of the Denisov cycle: How do hindered amine light stabilizers protect polymer coatings from photo-oxidative degradation ?," *Macromolecules*, vol. 43, no. 10, pp. 4573–4583, 2010.

[39] N. A. Shaath, "Ultraviolet filters," *Photochemical Photobiological Sci.*, vol. 9, pp. 464–469, 2010.

[40] J. Zawadiak and M. Mrzyczek, "Influence of substituent on UV absorption and keto–enol tautomerism equilibrium of dibenzoylmethane derivatives," *Spectrochimica Acta Part A, Mol. Biomol. Spectrosc.*, vol. 96, pp. 815–819, 2012.

[41] J. E. Pickett and J. E. Moore, "Photodegradation of UV absorbers: Kinetics and structural effects," *Die Angewandte Makromolekulare Chemie: Appl. Macromol. Chem. Phys.*, vol. 232, no. 1, pp. 229–238, 1995.

[42] E. Denisov, "The role and reactions of nitroxyl radicals in hindered piperidine light stabilisation," *Polym. Degradation Stability*, vol. 34, no. 1–3, pp. 325–332, 1991.

[43] E. N. Step, N. J. Turro, P. P. Klemchuk, and M. E. Gande, "Model studies on the mechanism of HALS stabilization," *Die Angewandte Makromolekulare Chemie, Appl. Macromol. Chem. Phys.*, vol. 232, no. 1, pp. 65–83, 1995.

[44] M. R. Paine, G. Gryn'ova, M. L. Coote, P. J. Barker, and S. J. Blanksby, "Desorption electrospray ionisation mass spectrometry of stabilised polyesters reveals activation of hindered amine light stabilisers," *Polym. Degradation Stability*, vol. 99, pp. 223–232, 2014.

[45] M. Jankovec et al., "In-situ monitoring of moisture ingress in PV modules using digital humidity sensors," *IEEE J. Photovolt.*, vol. 6, no. 5, pp. 1152–1159, Sep. 2016.

[46] M. Jankovec, S. Mitterhofer, J. Slapšak, and M. Topič, "Monitoring of lateral moisture ingress across the surface of a solar cell in PV modules," in *Proc. 47th IEEE Photovolt. Specialists Conf.*, 2020, pp. 1308–1312.

[47] P. Klemchuk et al., "Investigation of the degradation and stabilization of EVA-based encapsulant in field-aged solar energy modules," *Polym. Degradation Stability*, vol. 55, no. 3, pp. 347–365, 1997.

[48] R. Heidrich et al., "From performance measurements to molecular level characterization: Exploring the differences between UV and DH weathering of PV modules," *Sol. RRL*, vol. 8, 2024, Art. no. 2400144.

[49] M. Gardette et al., "Photo-and thermal-oxidation of polyethylene: Comparison of mechanisms and influence of unsaturation content," *Polym. Degradation Stability*, vol. 98, no. 11, pp. 2383–2390, 2013.

[50] M. C. C. de Oliveira, A. S. A. D. Cardoso, M. M. Viana, and V. D. F. C. Lins, "The causes and effects of degradation of encapsulant ethylene vinyl acetate copolymer (EVA) in crystalline silicon photovoltaic modules: A review," *Renewable Sustain. Energy Rev.*, vol. 81, pp. 2299–2317, 2018.

[51] G. Socrates, *Infrared and Raman Characteristic Group Frequencies: Tables and Charts*. Hoboken, NJ, USA: Wiley, 2004.

[52] G. Oreski, G. M. Wallner, and R. Lang, "Ageing characterization of commercial ethylene copolymer greenhouse films by analytical and mechanical methods," *Biosyst. Eng.*, vol. 103, no. 4, pp. 489–496, 2009.

[53] B. Ottersböck, G. Oreski, and G. Pinter, "Comparison of different microclimate effects on the aging behavior of encapsulation materials used in photovoltaic modules," *Polym. Degradation Stability*, vol. 138, pp. 182–191, 2017.

[54] S. Falicki, D. Gosciniak, J. Cooke, and D. Carlsson, "Secondary and tertiary piperidinyl compounds as stabilizers for γ-irradiated polypropylene," *Polym. Degradation Stability*, vol. 43, no. 1, pp. 1–7, 1994.

[55] R. Singh et al., "Synthesis of new polymeric hindered amine light stabilizers: Performance evaluation in styrenic polymers," *J. Appl. Polym. Sci.*, vol. 90, no. 4, pp. 1126–1138, 2003.

[56] M. Patel et al., "Thermal stability of poly (ethylene-co-vinyl acetate) based materials," *Polym. Testing*, vol. 32, no. 4, pp. 785–793, 2013.

[57] R. Witteck et al., "UV-induced degradation of PERC solar modules with UV-transparent encapsulation materials," *Prog. Photovolt. Res. Appl.*, vol. 25, no. 6, pp. 409–416, 2017.

[58] A. Sinha et al., "UV-induced degradation of high-efficiency silicon PV modules with different cell architectures," *Prog. Photovolt., Res. Appl.*, vol. 31, no. 1, pp. 36–51, 2023.

[59] U. Desai, B. K. Sharma, and A. Singh, "Assessment of the effect of accelerated ultraviolet aging on mini-PV modules encapsulated with different poly (ethylene-co-vinyl acetate) formulations," *J. Appl. Polym. Sci.*, vol. 140, no. 45, 2023, Art. no. e54676.

[60] M. D. Kempe et al., "Acetic acid production and glass transition concerns with ethylene-vinyl acetate used in photovoltaic devices," *Sol. Energy Mater. Sol. Cells*, vol. 91, no. 4, pp. 315–329, 2007.

[61] C. Peike et al., "Origin of damp-heat induced cell degradation," *Sol. Energy Mater. Sol. Cells*, vol. 116, pp. 49–54, 2013.

[62] A. Kraft et al., "Investigation of acetic acid corrosion impact on printed solar cell contacts," *IEEE J. Photovolt.*, vol. 5, no. 3, pp. 736–743, May 2015.

[63] M. Köntges et al., *Assessment of Photovoltaic Module Failures in the Field: International Energy Agency Photovoltaic Power Systems Programme: IEA PVPS Task 13, Subtask 3: Report IEA-PVPS T13-09: 2017*. Paris, France: Int. Energy Agency, 2017.

[64] M. Koehl, S. Hoffmann, and S. Wiesmeier, "Evaluation of damp-heat testing of photovoltaic modules," *Prog. Photovolt. Res. Appl.*, vol. 25, no. 2, pp. 175–183, 2017.

7. Discussion of the main findings

7.1. Behavior of polymer additives under stress conditions

In the course of this work, the degradation and diffusion of UV absorbers (mainly the benzophenone-based UV Absorber Cyasorb UV 531) and UV stabilizers (mainly the hindered amine light stabilizer Tinuvin 770) could be observed. The additives were analyzed in pure polymer films, in coupon samples and in mini modules. Depending on the sample type, the behavior of the additives can differ significantly. The most important findings are discussed below.

7.1.1. UV absorber

Studies on the degradation of benzophenone-based UV absorbers in PV encapsulants have been carried out for at least 30 years [32, 40, 41]. However, the understanding has so far been inadequate, as the experiments have mostly been carried out on pure polymer samples without a realistic module structure [32, 40–42, 83, 229]. Within this work, the degradation and diffusion behavior of the benzophenone-based UV absorber Cyasorb UV 531 was comprehensively investigated in order to gain a fundamental understanding of its long-term behavior within a solar module. The additive quantification method developed in this work allows the proportion of UV absorbers to be determined directly for the first time. Up to this point, the behavior of the UV absorber was always determined via changes in the transmission behavior of the polymers [40–42, 84, 205, 206, 219]. However, this indirect measurement does not allow any general statements to be made about the behavior of the UV absorber.

UV absorber degradation in dependence of the UV intensity and spectrum

In subsection 5.1, subsection 5.2, and subsection 6.2, the degradation behavior of the UV absorber was investigated at different UV intensities and spectral distributions. When using a xenon spectrum with daylight filters (see Figure 20), no degradation of the UV absorber was observed in coupon samples up to a UV intensity of $120\,\mathrm{W/m^2}$ between 300 nm to 400 nm. The same applies when using UV-A fluorescent lamps, which, however, have a significantly lower radiation intensity. This is in contrast to the investigations of Pickett et al., who observed first or zero order degradation kinetics in a comparable weathering setup with lower irradiation intensity [40, 41]. In the case of the coupon samples from subsection 5.1 and subsection 5.2, the stability could be explained by the fact that the glass absorbs part of the radiation (see the transmission spectrum in subsection 5.1). However, the UV cutoff of the used glass is at approximately 290 nm, so a significant portion of the UV radiation is transmitted into the encapsulant.

When using metal halide lamps (see the spectrum in Figure 20) with an irradiation intensity of approximately $77\,\mathrm{W/m^2}$ (similar to the work of Pickett et al. [40, 41]) between 280 nm to 380 nm, similar behavior of the UV absorber can be observed. Even in pure EVA films, without protective glass, the UV absorber is stable and does not degrade. In addition, the experiments were carried out under increased humidity (85 °C

and 60 % r.h.), and no UV absorber degradation under combined UV and DH conditions could be detected. If the irradiation intensity is increased to approximately 228 W/m^2, the UV absorber degrades with zero-order kinetics. The observed degradation kinetics can presumably be explained by the fact that the matrix is highly absorbent [40]. Thus, only the uppermost polymer layers contribute to the absorption of UV radiation, and the lower layers are completely protected. Gradually, the UV absorber in the upper layers is degraded, and the layers below begin to absorb the radiation.

For the UV intensity and spectral distribution to be expected for solar modules in the field, the results mean that the UV absorber should not degrade due to the solar irradiation itself. In particular, the weathering standard IEC 62788-7-2 used in this work assumes a spectral distribution similar to the solar spectrum and amplifies this significantly [49]. No degradation of the UV absorber was observed in coupon samples within this work. As other studies have nevertheless observed changes in the transmission behavior of the encapsulants at similar irradiation doses [40, 41, 205, 206, 219], these changes are most likely due to other interactions, which will be discussed in more detail below.

UV absorber diffusion

In subsection 5.2, the migration behavior of UV additives was investigated under IEC 62788-7-2-A3 conditions [49, 53]. As previously described, the UV absorber molecules are not degraded under these weathering conditions, and the total number is approximately maintained. Due to the large concentration gradient at the interface, a significant fraction of the UV absorber molecules were able to migrate a lateral distance of approximately 2 cm within 500 h. As mentioned in subsubsection 2.1.2, Fickian diffusion was assumed to simulate the migration process of the UV absorber molecules. A diffusion constant of $D = 5.5 \times 10^{-8}\,cm^2/s$ was used to approximate the measured values, which is in the same order of magnitude of different additives of this molecule size in different works [46, 90–92]. However, the real diffusion was more pronounced than calculated by the simulation. It can therefore be assumed that the diffusion constant is concentration-dependent, which leads to super diffusive behavior [230–233]. This behavior can be explained by the fact that EVA typically reaches gel contents of about 90 % in the crosslinked state [234]. This means that 10 % of the material can partially flow, and thus, the diffusion process of the additives can be enhanced.

These results have various consequences for solar modules. Based on the measurement data and simulations, it can be assumed that UV absorbers can diffuse a lateral distance of 4 cm within 1500 h under IEC 62788-7-2-A3 conditions within an EVA layer with an existing concentration gradient. In many cases, however, encapsulants without a UV absorber (glass side of the module) are combined with encapsulants with a UV absorber (backsheet side of the module). Particularly at the edge and between the electrical connectors, diffusion of UV absorbers is likely due to the resulting concentration gradients. From these points, the molecules can then migrate laterally again and lead to altered transmission properties in the front EVA. In this context, the diffusion of backsheet additives into the encapsulant and from the encapsulant into the backsheet would also be

conceivable. In addition to the altered transmission properties, the reaction of the UV absorber molecules with radicals also plays an important role. The potential of these degradation reactions is greatly increased by the diffusion of the UV absorber molecules and is discussed in detail in the following chapter.

UV absorber degradation in dependence of the encapsulant environment

As previously described, some studies have observed changes in the optical properties of the encapsulants and correlated these with the degradation of the UV absorber or chromophore formation, although similar spectra and UV doses were used as in this work [40, 41, 205, 206, 219]. Except for the weathering series with metal halide lamps at 228 W/m^2 between 280 nm to 380 nm no UV absorber degradation was observed in pure film samples within this work. Interestingly, the surrounding material of the encapsulant (and thus also the surrounding material of the UV absorber) influences its degradation behavior, leading to differences between experiments with plain encapsulant films and experiments with multi layer compositions.

Although the total number of UV additives remained approximately constant in the diffusion experiments in subsection 5.2, the degradation of some of the benzophenone molecules can be observed indirectly. Areas of the test specimens that were not initially protected by UV additives were damaged by photo degradation with the formation of radical species [31, 108, 109]. The diffusion of the UV absorbers into the area with high radical density led to the reaction of UV absorber molecules with radicals [34]. As a result, chromophores were formed by degradation of the UV absorbers [34]. This also explains why various studies have found a correlation between UV absorber presence and encapsulant browning [32, 34, 61, 98, 205, 235, 236].

In subsection 6.1 and subsection 6.2, it was found that the UV absorber in the EVA in solar modules behaves differently than in individually aged EVA films. Although the UV absorber in pure films decreases linearly even at a high irradiation intensity of 228 W/m^2 and was only consumed by 50 % within weathering time of 2000 h, it is already completely degraded in solar modules under the same conditions in the front EVA after 500 h. In the experiments with 77 W/m^2, the UV absorber content in pure films remains constant but degrades almost completely in the front EVA of solar modules aged under the same conditions after 1250 h. For both series of experiments, no degradation of the UV absorber in the backside EVA was observed. Due to the chamber conditions, it can be assumed that the temperature on the top and bottom of the solar cell inside the solar module is almost the same. Furthermore, the diffusion-open backsheet allows water to penetrate into the back EVA [202]. It can therefore be concluded that the degradation of the UV absorber in solar modules is neither dependent on water permeation itself nor on moderate module temperatures (up to 90 °C). Since the degradation only occurs in the front EVA of the solar modules but was not observed in coupon samples (see subsection 5.1), it is probably caused by interactions with the electrical connectors or the solar cell. However, it is conceivable that the combination of hydrolysis (after water diffusion to the front side) in combination with UV degradation led to radicalization of the UV absorber and the molecules were subsequently bound to the solar cell or

electrical connectors and no longer desorbed during the PY-GCMS measurement [30, 31, 34, 108–113]. Nevertheless, the exact cause of UV absorber degradation in solar modules must be clarified in the future, as it can have a significant impact on module service life and influence optical properties. Based on the analyses carried out, however, it is imperative to avoid evaluating the stability of the UV absorber in the individual encapsulant, as the degradation behavior in the solar module is completely different.

7.1.2. UV stabilizer

Investigations into UV stabilizer (HALS) degradation in the PV field have so far been a subordinate topic [29, 35], although this type of analysis is a standard procedure in general polymer oxidation research [37, 39, 237–241]. As shown at the beginning of this work in section 3, the degradation of the HALS amines can be investigated either directly by orbitrap mass spectrometry or indirectly by electron paramagnetic resonance (EPR). However, both methods are qualitative approaches. In contrast, the quantification method for UV additives developed in this work offers for the first time the possibility to derive the degradation kinetics of UV stabilizers directly, as the additive content can be quantified in absolute numbers. Thus, the degradation of the HALS base molecule Tinuvin 770 was studied within this work as a function of different environmental parameters.

UV stabilizer degradation in dependence of the applied stressor

section 3, subsection 5.1, subsection 5.2, subsection 6.1 and subsection 6.2 have investigated the degradation of the UV stabilizer Tinuvin 770 in EVA under different environmental conditions. Analyses were carried out in pure film samples, in coupons and also in mini modules. As HALS act as a radical scavenger, previous studies on its degradation have generally been limited to photo degradation processes [34, 36–39], as no radical formation is to be expected during hydrolysis, particularly in EVA [30, 31, 34, 108–113]. The comparison of the influence of UV and DH conditions based on IEC 61215 in section 3 has led to a fundamental understanding of the use of HALS in PV encapsulants [48] [50].

The UV aging of the mini modules led to the expected reactions in the EVA-embedded HALS. Especially at the edge of the modules, where both EVA layers were not separated by the solar cell, an increase up to the maximum of the nitroxide signal with subsequent decrease could be detected by EPR. The signal curve indicates the reactions to be expected with the formation of nitroxide radical intermediate accumulation with subsequent transformation in other molecule forms [239–241]. This can be understood by the fact that, in contrast to the center of the module, the UV radiation hits both EVA layers, and consequently, more radicals are produced by photo degradation. On the other hand, oxygen can diffuse through the edge and the backsheet without the solar cell being in the diffusion path. If the EPR analyses are compared with the results of mass spectrometry, the degradation of the HALS base molecule can be detected. During UV aging, the proportion of O_4N_2 groups (functional group of HALS) continues to decrease

and O_5N_2, O_6N_2 and higher order groups are formed as a result of the interaction with radicals during the Denisov cycle [34, 36–39].

During aging under DH conditions, the UV stabilizer behaves differently than under UV conditions. Using EPR, the formation of nitroxide groups can only be detected at the edge of the module. However, the nitroxide signal is significantly smaller than under UV aging and does not reach a maximum, so a much lower radical density can be assumed. This is not surprising, as no radicals should be formed during the pure hydrolysis process of EVA [110–112]. The fact that nitroxide groups are nevertheless formed at the edge of the modules could be due to the oxygen input by diffusion through the edge of the modules and through the backsheet [30, 31, 108, 109, 113]. Either the EVA degradation reactions generating radicals are thermally activated by the chamber temperature [30, 31, 108, 109, 113], or radicals formed during the lamination process and react with increased kinetics with the UV stabilizer molecules at elevated temperatures [69, 70]. The results of the mass spectrometry show a very interesting behavior of the UV stabilizer. The functional O_4N_2 group of the base molecule is degraded to the same extent as for UV aging. However, as expected from the nitroxide signal, hardly any O_5N_2 and O_6N_2 groups are formed. This means that the HALS base molecule degrades but does not react with radical bonding in the Denisov cycle [34, 36–39]. Although there are some studies showing increased HALS degradation under the influence of moisture, this is highly dependent on the chosen polymer matrix [240, 242–244]. Since the investigations carried out in this work were performed without the influence of UV radiation, it is also conceivable that the HALS base molecules were damaged directly by the penetrating moisture, but a hypothetical reaction is unclear at this point. For modules in the field, this means that under combined stress conditions, degradation of the UV stabilizer must be expected even without exposure to sunlight if sufficient moisture has diffused into the solar module.

UV stabilizer degradation in dependence of the encapsulant environment

In contrast to the UV absorber, the impact of the encapsulant environment on the degradation of the UV stabilizer is less influential. As shown in subsection 5.1, subsection 5.2 and subsection 6.2, an exponential degradation of the base molecule of approximately 80 % within 1500 h can be expected under moderate irradiation conditions. It did not matter whether the EVA was aged as a pure film (in combination with DH conditions), as a single layer between two glass layers, or as a full coupon sample. The comparison is justified by the fact that the same encapsulant was always used for all sample types except the diffusion experiments in subsection 5.2. This indicates that sufficient radicals were always available for all selected aging conditions, so that the rate of change in the number of HALS base molecules is significantly dependent on the number of particles (see subsection 6.2 [55]). As shown in subsection 6.2, this degradation behavior leads to the ability to predict the average HALS degradation from different locations within the EVA in a solar module with the degradation behavior of an EVA film aged under the same conditions. If UV stabilizer degradation is used as a marker for the degradation of solar modules, experiments with pure films could therefore be sufficient to obtain an

initial rough guide value for lifetime predictions.

UV stabilizer degradation in dependence of the UV spectrum and intensity

In this section, the degradation of the UV stabilizer is discussed as a function of the UV spectrum used and the UV intensity. As described above, the HALS molecules also degrade under the influence of moisture. However, this influence is neglected in this chapter, as most of the weathering series were carried out under similar humidity and temperature conditions, which ensures comparability of the different studies.

As it was observed in subsection 5.1, both the selection of the UV spectrum and the intensity within a spectrum have a significant influence on the degradation behavior of the HALS base molecule. Although after 2500 h UV-A fluorescent lamp weathering, approximately the same photon intensity was achieved as by 1250 h xenon lamp weathering with daylight filters (both types of weathering correspond to the conditions of IEC 62788-7-2-A3), only 40 % of the UV stabilizer was degraded under UV-A weathering, but 80 % under xenon weathering for the corresponding time points [49, 52]. This shows that the longer wavelength components of the UV spectrum probably play an important role in the degradation of the UV stabilizer. The results from subsection 6.2 also confirm this assumption. Although the irradiation intensity of the metal halide lamp between 280 nm to 380 nmis similar to that of the xenon lamp with daylight filters from subsection 5.1 and subsection 5.2, the spectral distribution is different. The metal halide lamps have a lower intensity in the range from 280 nm to 350 nm but a significantly higher intensity from 350 nm to 380 nm. Despite the lower intensity in the higher-energy UV range, the UV stabilizer is also degraded by approximately 80 % within 1250 h when using metal halide lamps. According to the previous chapter, however, it cannot be ruled out that the moisture used during this aging process has enhanced the degradation rate [240, 242–244].

In subsection 5.1 and subsection 6.2 it was also shown that the degradation of the UV stabilizer is strongly dependent on the UV intensity used. This can be explained by the mechanism of action of HALS as a radical scavenger [34, 36–39]. For polymers that are sensitive to photodegradation, it is to be expected that the radical density increases with increased radiation intensity, and consequently, more reaction partners are available to the UV stabilizer [30, 31, 108, 109, 113], which leads to a faster consumption of the latter. As described above, an exponential decrease with increasing weathering time was observed for the base molecule of the UV stabilizer in all experiments. In subsection 6.2, it was then assumed that the UV stabilizer always has a reservoir of radicals available for reaction, which were generated by the weathering stressors. As a result, the change in HALS particle density $\mathrm{d}N_T/\mathrm{d}t$ is dependent on the particle density itself, the UV Intensity I, and a constant chamber parameter B_T, which is dependent on temperature and humidity inside the chamber (pseudo first-order kinetics). It follows that

$$\frac{\mathrm{d}N_T(t)}{\mathrm{d}t} = -N_T I B_T(\varphi, T). \tag{53}$$

Since the chamber temperature and relative humidity were kept constant, the differential

equation could be solved using the normalized initial condition $N_T(0) = 1$.

$$N_T(t) = e^{-IB_T(\varphi,T)t}. \tag{54}$$

As shown in subsection 6.2, the chamber parameter can be determined analytically if two different UV intensities are used for aging.

As shown in subsection 6.2, Equation 54 can be used to predict the consumption of the UV stabilizer and correlate it with the degradation of the encapsulant and the electrical parameters of the solar modules. These relationships can be of great importance for lifetime predictions of solar modules and will be discussed in more detail later with reference to common degradation models.

7.1.3. Expected consequences for solar modules during operation

Based on the previous discussion, potential consequences can be derived for solar modules in the field:

i Benzophenone-based UV absorbers contained in the encapsulant are unlikely to degrade due to sole solar irradiation. However, due to interactions with the solar cell and the electrical connectors under the influence of UV irradiation, humidity and temperature, these molecules can be consumed in the solar module much faster than would be the case in pure polymer layers. As a result, the protective properties of UV absorbers can be lost much more quickly than assumed with pure films or coupon samples.

ii Additives can diffuse over long distances. UV additives are expected to migrate between the two encapsulant layers. It is also likely that additives from the backsheet will diffuse into the encapsulant and vice versa. This can lead to unexpected interactions in the long term. In particular, the optical properties and stabilization of the encapsulant are affected if additives migrate from the layers intended for them.

iii UV additives interact with radicals. UV stabilizers are consumed due to their mode of action. However, this can also occur through crosslinking peroxides that are not consumed during lamination and are activated by UV irradiation. When benzophenone-based UV absorbers react with radicals, chromophores can form and browning of the encapsulant occurs. In the long term, this is particularly problematic due to the pronounced diffusion properties of the UV absorber.

iv Contrary to assumptions, HALS in the encapsulant of solar modules is degraded by high humidity and temperature, even without the influence of UV irradiation. When designing the stabilization of encapsulants, it is therefore important to consider not only the expected irradiation dose but also humidity and temperature changes.

v The degradation of HALS can be modeled in good approximation using pseudo-first order kinetics. If the expected irradiation dose for solar modules is known, the required amount of HALS can be calculated to ensure sufficient protection of the encapsulant from photo degradation over a long period of time.

7.2. Encapsulant aging in dependence of different environmental stresses

In the course of this work, self-produced and commercial encapsulants were subjected to a variety of different forms of weathering. Pure film samples, coupons, but also mini solar modules were aged, the encapsulant was extracted and analyzed using various measurement methods. Although a commercial POE and TPO encapsulant were also aged by UV irradiation in subsection 5.1, the discussion focuses on the experiments with EVA encapsulants. The most important findings on the degradation of EVA as a function of the environmental parameters are presented below.

7.2.1. UV weathering

In section 3, subsection 5.1, and subsection 5.2 EVA encapsulants were aged under UV conditions based on IEC 61215 or IEC 62788-7-2 [48, 49]. The influence of the UV spectrum used, the UV intensity, and the additives used on the degradation behavior of EVA were investigated.

Influence of UV additives on the degradation of EVA

The analyses of the self-produced EVA films from subsection 5.2 have provided important insights into the stabilization of EVA. The glass-glass test specimens were aged under IEC 62788-7-2-A3 conditions [49], which was identified in subsection 5.1 as a realistic variant of artificial aging. As has been known since the Flat-Plate Array Project and by works of Klemchuck et al. and Jentsch et al., among others, the use of UV stabilizing additives is important to at least delay the degradation of EVA [29, 34, 35]. However, since most of the work in this area deals with commercial encapsulants with a predetermined additive structure, it has not yet been possible to specify the influence of these additives on EVA degradation.

The results in subsection 5.2 have shown that EVA stabilized with the benzophenone-based UV absorber Cyasorb UV 531 and the HALS Tinuvin 770 shows no signs of degradation within 1500 h UV weathering, which would be detectable with FTIR measurements. Although the glass layer on top of the EVA absorbs part of the UV radiation (see the absorption spectrum in subsection 5.1), the EVA is massively degraded in areas of the test specimens without protective UV additives after 750 h weathering. Various degradation reactions listed in subsubsection 2.1.3 can be observed:

i Formation of OH groups as a result of CH_2 group photo degradation. These hydroperoxides react further and create radicals or additional ketone groups in the main chain of the EVA [108, 109, 113]. This type of reaction is to be expected for all encapsulants that have polyethylene segments [113]. Consequently, it is also likely to occur for novel POEs and TPOs if they are not sufficiently stabilized.

ii VA units degrade through the back-biting degradation process of EVA and create γ-lactones [108, 109, 245].

iii Ketones are formed, either by reactions mentioned in i), or by Norrish type III reactions [84, 108, 109, 245, 246].

iv Additional C-O-C groups are formed. Either by aliphatic esters or as a result of chain scission [108, 109, 246].

v C=C double bonds are formed during the deacetylation process [108].

The local presence of the UV additives or the artificially created concentration gradient of these within the test specimens leads to further interactions. The diffusion of UV additives (see subsubsection 7.1.1) can actively prevent the degradation of the encapsulant at positions where no stabilizing additives were originally present. In the case of the test specimens, this was a lateral distance of approximately 1.3 cm next to the concentration gradient. Only slight ketone formation was observed in this area. On the other hand, UV absorber molecules diffused into the degraded EVA area and reacted with the radicals present there [34]. Through hydrogen abstraction, these molecules also became radicals and reacted further to form chromophores [34]. Browning of the encapsulants is therefore probably a direct consequence of poor stabilization of the encapsulants (too little or no HALS) in combination with the usage of benzophenone-based UV absorbers.

EVA degradation in dependence of the UV spectrum and intensity

In section 3 and subsection 5.1, EVA encapsulants embedded in solar modules or coupons were artificially aged using different types of lamps and intensities. Either by metal halide lamps based on IEC 61215 or by xenon lamps with daylight filters, on the one hand, based on IEC 62788-7-2-A3, on the other hand, the same spectrum was increased to 120 W/m^2 [48, 49]. Or by UV-A fluorescence lamps based on IEC 62788-7-2-B3 [49].

A comparison of the influence of the different spectra on EVA degradation shows that the oxidation index increases with all types of weathering. Consequently, ketones are formed by each spectrum [108, 109, 113]. These are formed either by Norrish type III reactions or by the decomposition of hydroperoxides [108, 109, 113]. In subsection 6.2 it was shown that for the metal halide lamp spectrum used, it is more likely that ketone formation follows from hydroperoxide decomposition. This could be explained by the fact that C=O groups were only formed at the lower edge of the mini modules. At this position, oxygen diffusion into the module is increased because the area of the electrical connectors was not completely sealed. Since the UV intensity used in subsection 5.1 for the **MAX** (120 W/m^2 xenon lamps with daylight filters) weathering is about the same as for the experiments in subsection 6.2 (see Figure 21) and significantly lower for the **A** (xenon lamps with daylight filters based on IEC 62788-7-2-A3) and **B** (UV-A fluorescence lamps based on IEC 62788-7-2-B3) weathering, it is likely that the ketone formation in EVA under IEC 623788-7-2 conditions is also caused by hydroperoxide decomposition. This would mean that C=O group formation by Norrish Type III reactions is not to be expected under normal solar irradiation since the solar spectrum has a significantly lower intensity than the IEC 62788-7-2-A3 spectrum with a similar spectral distribution. New C=O bonds are also formed under the metal halide lamp aging in subsection 5.1. However, the irradiation intensity in these experiments was significantly higher than in

the other weathering series. Thus it cannot be ruled out that these groups result from Norrish type III reactions instead of hydroperoxide breakdown [108, 109, 113].

With the exception of the UV-A fluorescence lamps under IEC 62788-7-2-B3 conditions [49], all spectra used led to the formation of C=C bonds. On the one hand these groups are formed by Norrish type II reactions with the formation of acetic acid, on the other hand they can be formed by further reactions after the hydroperoxide decomposition of the PE segments in EVA generating vinyl groups [108, 109, 113]. Since these C=C bonds were also observed in modules aged in the field [20, 247, 248], their possible formation is an important criterion for the choice of a spectrum for accelerated aging.

The comparison of the two xenon lamp intensities in subsection 5.1 has shown that no different degradation reactions are to be expected for the weathering duration of 2500 h. The consumption of the UV stabilizer is faster under higher intensity, and all degradation reactions can already be observed at a lower weathering duration. In particular, the formation of C=C bonds is much more pronounced for the higher intensity.

For solar modules in the field, these results mean that for encapsulants without stabilization, the in the previous chapter mentioned degradation reactions i) to v) are to be expected. For stabilized encapsulants, Norrish type II reactions and hydroperoxide decomposition are to be expected for the encapsulant as a result of sole UV aging [108, 109, 113]. The former leads to the formation of acetic acid, which in combination with additional moisture, can lead to corrosion of the electrical contacts [108, 109, 113, 200, 201]. Furthermore, the reaction is autocatalytic [114–117]. The latter leads to the formation of radicals [108, 109, 113], which consume the UV stabilizer, attack other polymer chains and lead to browning through reaction with the UV stabilizer [34, 36–39]. In addition, this reaction probably occurs for all polymers with PE segments in the polymer chain [113], i.e. also for newly developed POE and TPO encapsulants. This shows the importance of appropriate stabilization against photo degradation using HALS.

7.2.2. DH weathering

In addition to HALS consumption, pure DH weathering in section 3 generated interesting results regarding EVA degradation. As for UV aging, deacetylation was also observed as the main degradation reaction for DH weathering. However, the severity of the degradation is significantly greater than after UV aging. The relative abundance of polymer chains with cleaved vinyl acetate groups after 500 h DH weathering corresponds approximately to the amount that would occur after 2000 h UV aging. As described in subsubsection 2.1.3, this is most likely the result of hydrolysis of the EVA with the formation acetic acid [110–112]. In contrast to photo degradation, the encapsulant does not contain any stabilizing additives against hydrolysis reactions. This is also directly reflected in the performance of the solar modules. As the I-V curves and EL measurements show, significant degradation occurs after 2000 h DH weathering, which is most likely the result of corrosion of the electrical connectors [200, 201]. They react with the acetic acid formed by hydrolysis, as described in subsubsection 2.2.5 [200, 201].

These results are particularly problematic for solar modules in the field. With permeable backsheets, moisture penetrates the module over a longer period of time [202]. As

the hydrolysis reaction is autocatalytic [114–117], the hydrolysis of the EVA can damage the electrical connectors without the incidence of UV radiation even being necessary.

7.2.3. Combined stresses

In section 6, the effects of combined stress conditions at 60 % r.h.and 85 °C were investigated with irradiation using metal halide lamps of two different intensities (227.5 W/m^2 and 76.6 W/m^2 between 280 nm to 380 nm). In addition to the consumption of the UV additives already discussed, these experiments have shown that the encapsulant degrades differently depending on the microclimate present in the solar module.

The analyses at high radiation intensity in subsection 6.1 have shown that hydroperoxides are formed in the front EVA, as previously discussed for pure UV aging [108, 109, 113]. The encapsulant also turned brown, which is due to the formation of chromophores. Either these are caused by the degradation of the UV absorber, which was already completely consumed after 500 h, as previously described [32, 34, 61, 98, 205, 235, 236]. Or they are a consequence of alternating C=C bonds, which are formed by the further decomposition of the polymer chains and also absorb visible light [30, 32]. On the back side, the oxidation index has increased considerably, which is due to the formation of new C=O bonds. Interestingly, these groups should not be formed by the hydrolysis reaction of EVA [110–112]. They could therefore be the result of reactions with radicals that have been formed, for example, by the hydroperoxide decomposition in the front EVA and diffused into the back EVA [108, 109, 113]. This consideration is also supported by the fact that the degradation in front and back EVA is only observed in both cases when the base molecule of the UV stabilizer has been completely consumed. Prior to this, the radicals formed by hydroperoxide decomposition were bound by the HALS molecules [34, 36–39].

The moderate UV intensity of 76.6 W/m^2 in subsection 6.2 can be approximately compared with the conditions from IEC 62788-7-2-A3 despite the previously discussed different spectral distribution [49]. The combination with the humidity of 60 % at 85 °C probably leads to the most realistic accelerated aging conditions of this work. Several stressors expected from the field are used. The UV intensity corresponds to a value defined as usable for accelerated aging (see subsection 5.1 and the DH parameters are significantly milder than defined in IEC 61215 [48].

As for the more intensive irradiation conditions, different degradation reactions also occur in these experiments depending on the existing microclimate in the solar module. Two different degradation reactions could be determined for the front EVA. On the top side of the solar module, Norrish type II reactions with the formation of acetic acid occur significantly. This was detected by the formation of C=C bonds [31, 108, 109]. Norrish type II reactions also occur on the bottom side of the solar modules, in the area of the electrical connector. In addition, an increase in C=O groups was observed in this area, which can be attributed to the formation of ketones [31, 108, 109, 113]. As both positions were exposed to the same irradiation, the formation of these groups cannot have been caused by Norrish type III reactions [31, 108, 109], as otherwise, they would have to occur at both points. Consequently, it is more likely that the ketone formation

follows from hydroperoxide decomposition [108, 109, 113]. This is a result of oxygen diffusing in from the area of the electrical connectors, as these could not be completely sealed. Both types of photo degradation only begin to increase significantly when the majority of the HALS base molecule has been consumed.

Approximately independent of the HALS consumption, a shift of the C=O intensities can be observed for the back side EVA using FTIR. The total C=O peak (normalized integral ratio) remains almost constant. However, decomposition by means of difference spectra showed that the shift in intensities is probably due to the formation of acetic acid by EVA hydrolysis [110–112]. In comparison to weathering under stronger UV intensity, no ketone formation on the back side can be observed in these experiments.

These findings have a number of consequences for modules in the field. For modules with stabilized EVA encapsulant, Norrish type II reactions, hydroperoxide and ketone formation, as well as the hydrolysis of EVA are to be expected [30, 31, 108–113]. Two of these reactions form acetic acid [31, 108–112]. If one compares these results with the analyses from subsection 5.1, in which the same materials were used to produce the mini modules, but the stressors were used individually with higher intensity (significantly greater UV intensities, 80 % r.h. at 80 °C. This shows the extent of the combination of stressors. If the I-V and EL measurements are used as a measure of module degradation, this is significantly more pronounced for the combination of UV+DH, although the individual conditions were much milder than in subsection 5.1. This can be explained by the fact that acetic acid is formed in two ways. On the one hand, this is further intensified by the autocatalytic effect [114–117]. On the other hand, the acetic acid formed by Norrish type II reactions can also be dissolved by the additional moisture and distributed in the module, which can lead to corrosion at various points [200, 201]. This is also confirmed by the fact that the EL decrease takes place mainly on the edges. The acetic acid formed on the back side by hydrolysis can diffuse comparatively quickly around the cell at the corners and also damage the metallization on the front side.

Since several stressors always occur simultaneously in the field, it is important not to test the modules under individual stress factors. The synergy of different degradation reactions has a significant influence on module service life.

7.3. Degradation chain of PERC based solar modules

Based on the results of this work, the degradation under combined stress conditions (UV irradiation, relative humidity and increased temperature) of PERC-based solar modules with EVA encapsulant and permeable backsheet was divided into 4 steps and simplified summarized in Figure 36. It is important to mention that this summary is only valid for the material combination within this work and is not easily transferable to every PERC based solar module. As shown in the figure, the degradation chain depends on the encapsulant, its additivation, the barrier properties and interaction behavior of the backsheet and the passivation layer setup, and the electrical connectors of the solar cell. These relationships are discussed in more detail in the next chapter considering different material combinations.

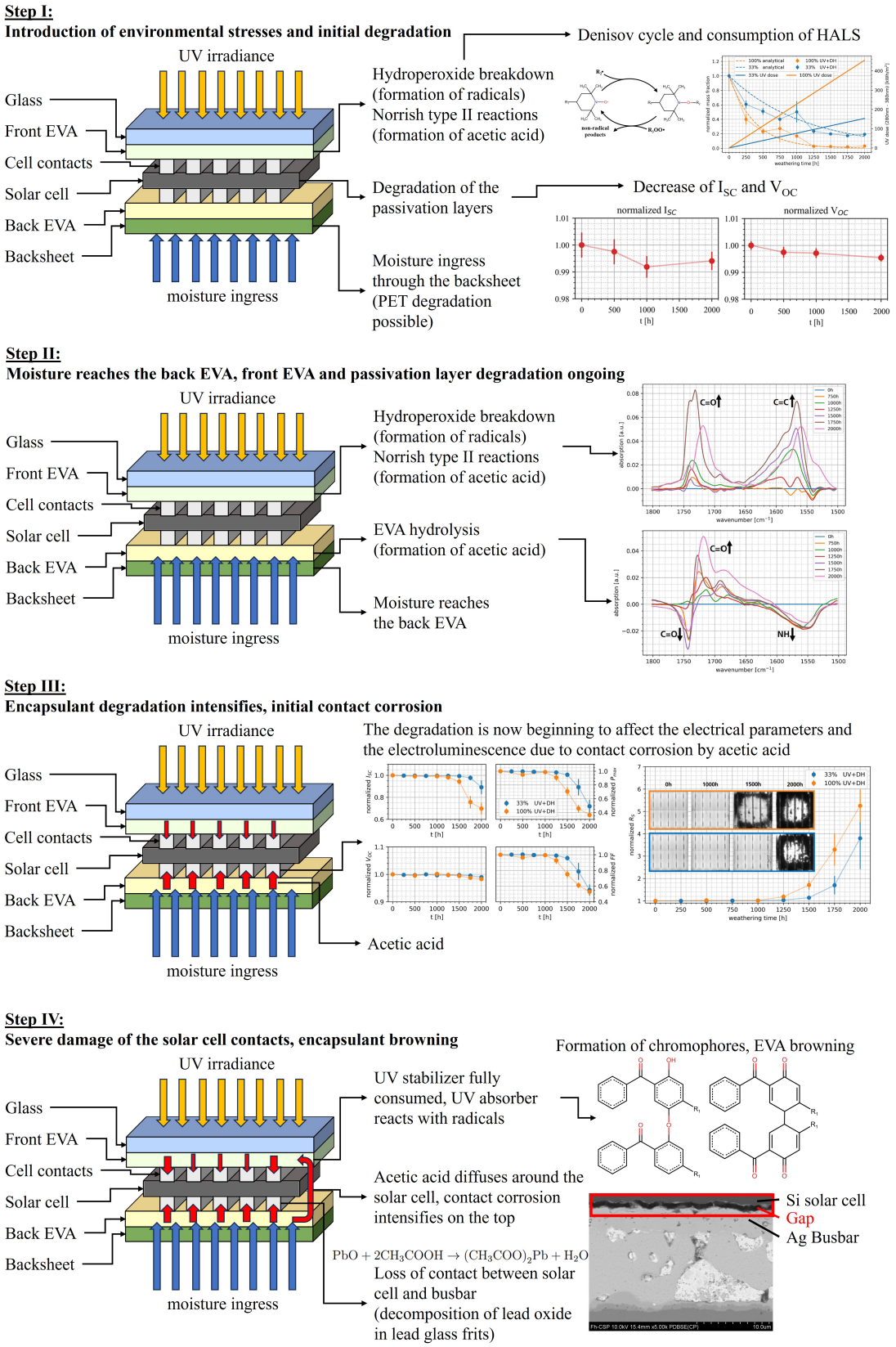

Figure 36: Simplified degradation chain of the PERC based modules with EVA encapsulant and diffusion open PET backsheet investigated within this work.

As shown in Figure 36, 4 degradation steps are proposed for the degradation of the PERC-based solar modules for combined stress conditions. As previously described, the UV intensity used for these results is of a similar order of magnitude to the IEC 62788-7-2-A3 conditions [49]. In addition, the DH conditions (60 % r.h. at 85 °C are milder than defined in IEC 61215 [48]. It can therefore be assumed that the phenomena listed also occur for solar modules after a few years in use and that the reaction chain shown represents a realistic scenario. However, the test specimens in this study were weathered without applied voltage so that PID effects were not provoked. These effects can also occur in the field, depending on the module composition. At the relevant points in the following text, reference is made to publications in which the degradation effects were observed in modules aged in the field.

Step I: Introduction of environmental stresses and initial degradation
In the first step, the UV radiation hits the solar modules on the glass side and the moisture on the back. These stressors remain present for the rest of the degradation chain. Some of the UV irradiation is immediately filtered out by the glass (see the spectrum in subsection 5.1). Nevertheless, a large proportion is transmitted. As described in subsubsection 2.2.5, photon energies of 3.5 eV ($\approx$ 354 nm) are sufficient to destroy the Si-H bonds of the passivation layer [194, 196]. This leads to an increase in the number of dangling bonds and to enhanced surface recombination at the emitter interface [194, 196]. In general, radiation-induced degradation is manifested by a reduction in I_{SC} and V_{OC} [194–197]. This was also observed in section 3 for single UV aging. However, since the performance losses due to degradation of the passivation layer are small compared to the degradation due to corrosion of the electrical connectors, they are probably superimposed in the later course.

The irradiation that reaches the front encapsulant is partially absorbed at this point (if present) by the UV absorber. If the irradiation nevertheless reaches the polymer matrix or if the UV absorber has already been consumed (see subsection 6.1 and subsection 6.2), this leads to Norrish type II reactions with the formation of acetic acid and to hydroperoxide decomposition with the formation of ketones, radicals and other groups [31, 108, 109, 113]. The latter reaction in particular has a decisive influence on the consumption of the HALS base molecule [34, 36–39]. As it was seen in subsection 5.1, subsection 5.2 and subsection 6.2, the degradation of the UV stabilizer begins very quickly, which indicates that the generation of radicals begins shortly after exposure to irradiation. However, since significant changes in the chemical structure of the encapsulant can only be observed after several hundred hours of artificial aging (see subsection 5.1, subsection 5.2 and subsection 6.2), it can be assumed that the UV stabilizer protects the encapsulant from degradation for a long time. The acetic acid produced by Norrish type II reactions is not as critical at this stage as it is later on. As shown in section 3, it does lead to a faster R_S increase at the beginning due to contact corrosion. However, it was also shown that the autocatalytic effect is limited by pure UV radiation (or at the beginning of weathering), as hardly any moisture is present in the top EVA [114–117].

Depending on the water permeation rate of the backsheet, the moisture needs a certain amount of time to penetrate it and reach the back encapsulant [202]. As described in subsubsection 2.1.5, the PET backsheet used (depending on the coating) can also be degraded by reflected UV irradiation or damaged by hydrolysis [146, 147, 150, 151]. As the UV irradiation is absorbed at the edges by the top encapsulant and in the middle of the module by the solar cell, no degradation effects are to be expected for the back encapsulant at this step of the degradation chain.

Step II: Moisture reaches the back EVA, front EVA, and passivation layer degradation is ongoing

In addition to the degradation effects in the first step, a more intensive degradation of the encapsulant begins in the second step. The moisture has now migrated through the diffusion-open backsheet (in the case of a diffusion-inhibiting backsheet, migration takes place via the edges of the solar module, but this takes considerably longer) [202]. This leads to hydrolysis of the EVA on the back [110–112]. As it can be seen in subsection 6.2 and Figure 36, this is already significantly pronounced after 750 h in the weathering chamber (shift of the C=O peak).

Depending on the microclimate, various degradation reactions occur in the EVA [30, 31, 108–113]. It was shown for the top EVA in subsection 6.1 and subsection 6.2 that the UV absorber is consumed relatively quickly in solar modules. the high-energy photons can therefore almost completely hit the encapsulant layers after about 1000 h in the weathering chamber. From this point onwards, the number of C=C bonds increases significantly, which are created by Norrish type II reactions with the formation of acetic acid [31, 108, 109]. In addition, the number of ketone groups increases in the edge area (or wherever oxygen can easily diffuse in). This is a consequence of hydroperoxide decomposition by photo oxidation of the CH_2 groups of EVA [31, 108, 109, 113]. The formation of these groups is also only significantly pronounced when the majority of the UV stabilizer has been consumed. Furthermore, both functional groups were also observed in solar modules aged in the field [20, 247, 248].

Step III: Encapsulant degradation intensifies, initial contact corrosion

At this point, most of the UV additives have been used up and polymer degradation is already well advanced. The acetic acid produced by Norrish Type II reactions on the front side and hydrolysis on the back side has now reacted with the electrical contacts of the solar cell for some time [30, 31, 108–113, 172, 200, 201]. As mentioned in subsubsection 2.2.5, the acetic acid leads to corrosion at these points [172, 200, 201]. The glass frits contained in the solder contain lead oxide, which reacts with the acetic acid and forms lead acetate and water [200]. This creates cavities between the Ag busbar and the cell and increases the series resistance [200, 201]. Tunneling of electrons through dissolved silver nanoparticles in the glass layer of the frits also reduces the fill factor [201].

The changed electrical parameters and the reduced electroluminescence due to the larger series resistances were also observed in subsection 6.1 and subsection 6.2. After

several years, similar electroluminescence patterns were observed in solar modules aged in the field [248–250]. The formation of cavities was also confirmed by SEM images for modules with similar configuration and cell structure within this work (see Figure 19 and Figure 36). As expected, there is a certain time lag between polymer degradation and corrosion of the electrical connectors. As shown in subsection 6.2, polymer degradation is distinct after approximately 1000 h (after consumption of the UV additives). After about 1500 h the series resistance starts to increase and the electroluminescence and fill factor decrease.

Step IV: Severe damage of the solar cell contacts, encapsulant browning
In the final stage, the corrosion of the contacts intensifies further and the solar modules become unusable. The corrosion is visible, among other things, through greatly reduced electroluminescence in the edge area. The increased degradation rate at these points is probably due to the fact that the acetic acid produced in the backsheet by hydrolysis diffuses around the cell and reaches the top encapsulant [110–112]. Here it leads to increased corrosion of the electrical contacts on the top of the solar cell in the edge area due to synergy with the acetic acid produced by Norrish type II reactions [30, 31, 108–113, 172, 200, 201]. As it can be seen in the electrical parameters at the end of the weathering time in subsection 6.2 (or in Figure 36), the short circuit current also drops after a significant increase in R_S and a decrease in FF. This is due to the fact that the electronic properties of the remaining silver columns change and capacitance are created [201].

If benzophenone-based UV absorbers are added to the back EVA, these could diffuse into the front EVA via the edges or the gaps between the solar cells (see subsection 5.2). As the UV stabilizer is heavily depleted at this point, the radicals that are produced in the front EVA by hydroperoxide decomposition, for example, cannot be bound [31, 108, 109, 113]. The UV absorber molecules now react with these radicals and chromophores are formed as observed in subsection 5.2 [34]. This reaction can also take place at an earlier stage of the degradation chain but is only visible to the naked eye when it is very pronounced.

7.4. Extension to emerging solar module compositions

The experiments presented in this work and the underlying publications focused mainly on PERC-based solar modules with EVA encapsulant and permeable backsheet. It was shown that many degradation mechanisms depend on the composition of the materials. In the course of this work, experiments were also carried out on other material combinations. The preliminary results shall be briefly presented here to illustrate that the degradation mechanisms of solar modules cannot be generalized. The following data are from modules that were also manufactured on a PERC-basis and aged under the same conditions as in subsection 6.2 (60 % r.h. at 85 °C and UV irradiation).

7.4.1. Influence of the backsheet permeability

As part of the new series of experiments, modules with built-in humidity sensors based on the setup from the University of Ljubljana were artificially aged alongside the regular mini modules. The setup is described in detail in [202] and measures the relative humidity and temperature at specific points. The sensor strips were equipped with 10 sensors each and placed diagonally in the mini modules. The sensor strips are located between the solar cell and the back encapsulant (with another layer of encapsulant placed before the cell). In the real module, the humidity values therefore correspond to the values that would be present in front of the solar cell. As the relative humidity is an unsuitable comparison parameter, the absolute humidity at various points in the modules was approximated using both measurement parameters. For this purpose, it was assumed that the area around the sensors is a closed system, and the vapor pressure was approximated with the saturation vapor pressure of water. It was therefore assumed that the absolute humidity is the relative proportion of the saturation humidity. By using the empirical Buck equation, a comparatively simple relationship between relative humidity ρ_{rel} and absolute humidity ρ_{abs} could be established with

$$\rho_{abs} = \rho_{rel} \frac{0.61121 e^{\left(\left(18.678 - \frac{T}{234.5}\right)\left(\frac{T}{257.14+T}\right)\right)}}{R_w T} \tag{55}$$

with the gas constant of water R_w and the temperature T [251–254]. The measurement results with a visualization of the sensor positions are shown in Figure 37.

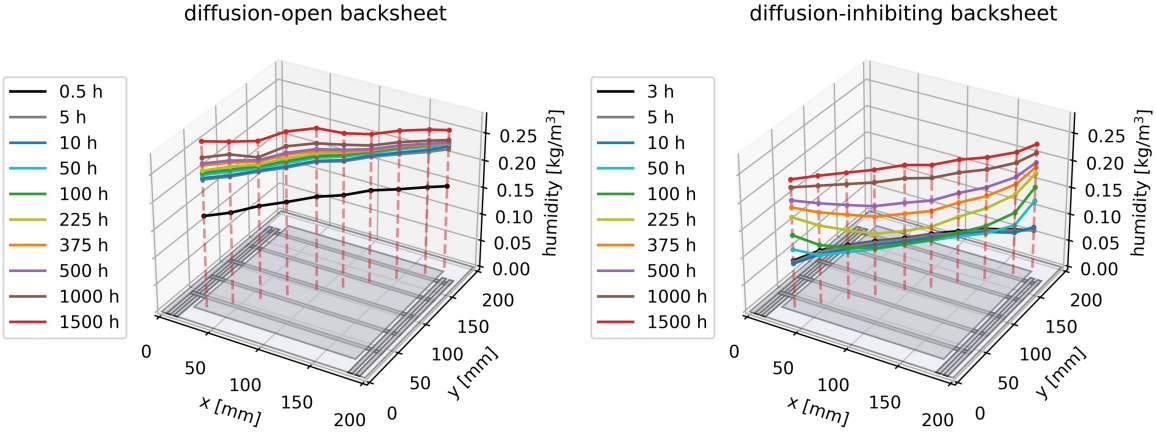

Figure 37: Moisture measurements of the 10 sensors within a solar module as a function of the weathering time, which was aged under the same conditions as in subsection 6.2. On the left a diffusion-open backsheet was used, on the right a diffusion-inhibiting one.

The graphs show clear differences in the permeation behavior of water depending on the choice of backsheet. For the diffusion-open backsheet, moisture values are already

achieved after 5 h that are close to the values after 1500 h. This occurs across all sensor positions, which confirms the work of Jankovec et al. as the moisture penetrates the entire backsheet [202]. Especially in comparison with the diffusion-inhibiting backsheet, it becomes apparent that the moisture values mentioned at 5 h are only reached after a weathering period of 1500 h. The reason for this can also be seen in the graph. The diffusion-inhibiting backsheet has an aluminum layer that blocks the migration of moisture. As can be seen in the figure, the moisture diffuses over the edges of the module so that the moisture values at these positions are significantly higher than in the middle of the module up to 500 h. Gradually, the concentration gradients from the edge compensate for the differences due to diffusion processes (see subsubsection 2.1.2). Nevertheless, the advance takes significantly longer, and a high level of moisture is only reached at the end of the weathering period.

If the solar cell or encapsulant is susceptible to moisture, the choice of backsheet can have far-reaching consequences. In particular, the hydrolysis of EVA is largely determined by the choice of backsheet as it is directly correlated with the present moisture [110–112]. However, it is also conceivable that, as shown in subsection 5.2, additives migrate from the backsheet into the encapsulant and lead to unforeseen interactions there.

7.4.2. Influence of the encapsulant choice

The different backsheets shown in the previous section were also combined with different encapsulants. As an example, the degradation behavior of a POE encapsulant combined with the diffusion-open backsheet from this series of experiments is briefly described below. In the data sheet, this is only listed as a crosslinking POE. It is probably (by FTIR measurements) polyethylene or an ethylene octene copolymer. As stated in section Z, the integral ratio of the 1700 cm^{-1} C=O peak integral was normalized to the 720 cm^{-1} CH_2 peak integral and evaluated in dependence of the weathering time and the sample position. The results are visualized in Figure 38.

As shown in subsection 2.1, there is no hydrolysis reaction for polyethylenes, and photo degradation starts with hydroperoxide formation through chromophoric defects [31, 113]. Except for the saturation reaction of the oxygen atom (reaction **a)** in Figure 11), all polymer chains resulting from subsequent reactions contain a C=O bond. The integral ratio from Figure 38 is therefore a good measure to study the degradation of the encapsulant.

The graphs clearly show that significant degradation is also to be expected for a POE encapsulant. The effects on the solar module are different from those with an EVA encapsulant, as no acetic acid is formed, for example. However, it cannot be ruled out that other effects, such as delamination, may occur as a result of this degradation. The graphs show that the photo oxidation of the POE occurs mainly at the edge. This can be understood by the fact that oxygen must be present for the initial reaction of the degradation chain. The oxygen apparently does not diffuse across the backsheet into the module like moisture but penetrates via the edges. This is also confirmed by the fact that these modules are test specimens with a transparent backsheet. The radiation can

therefore also be absorbed on the back of the cell (bifacial PERC modules). Nevertheless, the peak ratio on the rear side only increases at the edge.

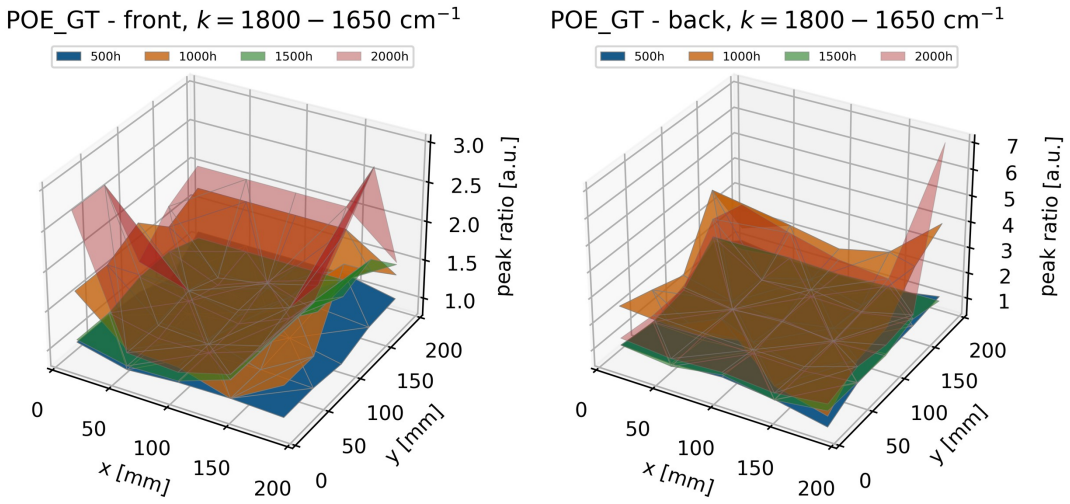

Figure 38: Development of the 1700 cm^{-1} C=O peak integral normalized to the 720 cm^{-1} CH_2 peak integral in dependence of the position and weathering time. The left image shows the integral ratios of the front encapsulant, while the right image shows the ratios of the back encapsulant

These results show that switching to a different encapsulant can lead to other degradation reactions. This is problematic because, as described in subsubsection 2.1.4, the terms POE and TPO are not clearly defined in the PV industry. For the TPO from subsection 5.1 (ethylene ethyl acrylate copolymer), acetic acid could also be formed as a degradation reaction and thus result in a similar degradation chain as described in the previous chapter for EVA [133, 134]. Furthermore, the benefit of using stabilizing additives to reduce encapsulant degradation was demonstrated in the course of this work. For example, second-order antioxidants (hydroperoxide scavengers - see Table 1) are of great importance for films that are mainly based on polyethylene (degradation always begins with hydroperoxide formation) [31, 59, 113]. However, the use of other additives is also of necessary and the composition must be coordinated, otherwise unexpected interactions could occur. As an example, it was seen in subsection 5.2 that unused crosslinking peroxide during lamination could otherwise react with the UV absorber molecules during aging, creating chromophores. The combination of encapsulant, backsheet, and the corresponding additives therefore plays a decisive role in determining which stress factors have an influence on the solar module longevity.

7.4.3. Influence of the solar cell and metallization type

The coming years will see many changes in solar module architecture. On the one hand, modules and cells will become larger and larger (2.5 m^2 to 3.0 m^2 or 182 mm to 210 mm), while on the other hand half cells will be mainly used [47]. However, these will become

about 30 % thinner by 2032 [47]. In conjunction with the trend towards thinner glass [47], new mechanical stress factors will arise that must somehow be compensated for by the encapsulant and the backsheet. In addition to resistance to degradation, mechanical properties will therefore also play a major role. The PERC cell used in this work will also be gradually replaced by silicon heterojunction solar cells (SHJ) and tunnel oxide passivated contact solar cells (TOPCon) over the next few years [47]. So far, however, their long-term stability is difficult to assess, as the number of studies is limited.

As already mentioned, the terms POE and TPO are not clearly defined in the PV industry. A new study, which has given rise to discussion, has shown that TOPcon modules perform significantly worse under DH conditions than conventional PERC modules [255]. Almost all module types were equipped with POE encapsulants and manufactured as backsheet variants [255]. The work has shown that the performance losses of the TOPCon modules are mainly due to an increase in series resistance [255]. This is due to electrochemical reactions between moisture, metallization, contamination, and solder [255]. However, the properties of the backsheets and encapsulants were not discussed in this paper [255]. It was assumed that the POE encapsulants do not contain any side groups that can form acetic acid [255]. Although similar failure modes as for PERC modules with EVA encapsulant can be observed, the exact cause is still unclear as the polymer layers were not investigated.

It has been observed that HJT modules are susceptible to radiation-induced degradation [256]. The reason for this is similar to that given in subsubsection 2.2.5 for PERC modules [256]. High energy photons destroy the SI-H passivation layer of the HJT cells [256]. Cells that were laminated with an encapsulant with UV absorbers showed significantly less degradation, as the short-wave UV components were filtered out [256]. However, the mini modules are already significantly degraded after 500 h DH tests (85 °C and 85 % r.h. based on IEC 61215 [48]) [256]. In this study, glass/glass modules with POE encapsulant were used [256]. Again, the encapsulant and the expected degradation reactions were not taken into account [256].

Further work has shown that TOPCon and HJT cells are very susceptible to metal contact corrosion [257]. The degradation of the metallization results on the one hand, in an increase in the series resistance [257]. On the other hand, recombination centers are created, which lead to a reduction in the open circuit voltage and the short circuit current [257].

Metallization also appears to have a major influence on the degradation behavior of TOPCon and HJT modules, as the increase in series resistance due to contact corrosion was observed in all studies (EL images in [256]) [255–257]. As interconnection technology will also change in the next few years [47], this may lead to further, previously unexpected problems. Figure 39 schematically shows various interconnection technologies. Traditionally, Cu ribbons were used as in **a)**, but these were already mainly replaced by Cu wires as in **b)** in 2022. Depending on the material composition of the solder, there is a risk of contact corrosion by acetic acid for these connections, as observed in this work [172, 200, 201]. This is because lead-containing solder will still be used to a large extent until 2032 [47]. New low-temperature solders allow the production of busbarless cells as displayed in **c)**. It is also possible to use a conductive adhesive (not shown).

The long-term properties of both technologies cannot yet be estimated. As shown in **c)**, the contact area between copper wire and cell is much smaller than when using busbars. Conductive adhesives are used for shingled modules [47]. Since it is a polymer, various forms of degradation and, above all, susceptibility to hydrolysis must be taken into account.

This work has shown that the degradation of solar modules is dependent on the material combinations used. the same applies to new solar cell and connector technologies. Every combination of backsheet, glass, solar cell, encapsulant, and the additives contained in the polymers should be extensively investigated in order to rule out undesirable interactions.

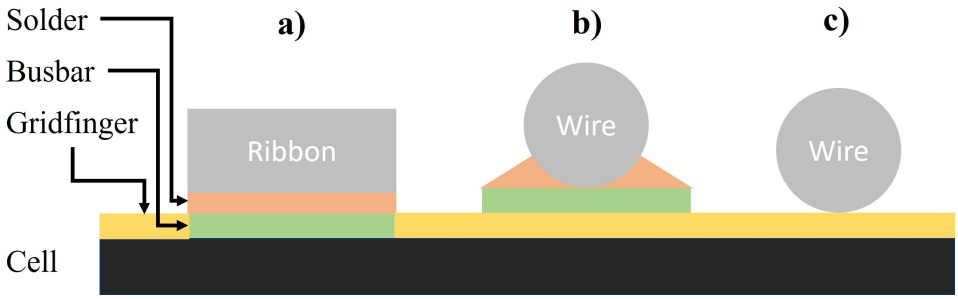

Figure 39: Different interconnection technologies based on conventional solders (**a)** and **b)** - typical lead containing) and low temperature solders (**c)** - typical lead free). Adapted from [47].

7.5. Degradation prediction in view of common models

The models currently used to predict the degradation of solar modules are mostly based on empirical approaches without taking into account the detailed underlying physical and chemical processes [15, 22–28]. On the one hand, this approach is obvious, as the exact material combination of the modules (e.g. the encapsulants used up to the additive level) is usually not known [15, 22–28]. On the other hand, it is very difficult to generalize the results in this way, as the model is often optimized for one type of module for a specific climate [15, 22, 24, 28]. A common approach to model the degradation of solar modules is to divide it into 3 different degradation modes - the degradation rate due to hydrolysis k_H, the degradation rate due to photodegradation k_P, and the degradation rate due to thermomechanical stresses k_{Tm}:

$$k_H = A_H \cdot rh_{eff}^n \cdot \exp\left(-\frac{E_H}{k_B \cdot T_m}\right) \tag{56}$$

$$k_P = A_P \cdot (UV_{\text{dose}})^X \cdot \left(1 + rh_{eff}^n\right) \cdot \exp\left(-\frac{E_P}{k_B \cdot T_m}\right) \tag{57}$$

$$k_{Tm} = A_{Tm} \cdot (T_U - T_L)^\theta \cdot C_N \cdot \exp\left(-\frac{E_{Tm}}{k_B \cdot T_U}\right) \tag{58}$$

with the scaling constants A_H, A_P, A_{Tm}, the effective relative humidity rh_{eff}, the activation energies E_H, E_P, E_{T_m}, the Boltzmann constant k_B, the UV dose, the average module temperature T_m, the upper module temperature T_U, the lower module temperature T_L and the cycling rate C_n [25, 27, 28]. The degradation rates are then combined to calculate the total module degradation rate k_T with the pre-factor A_N [27, 28]

$$k_T = A_N \prod_{i=1}^{n} (1 + k_i) - 1. \tag{59}$$

As Equation 56, Equation 57, Equation 58 and Equation 59 show, an Arrhenius approach is typically chosen for the degradation rates [25, 27, 28]. It is understandable that the degradation rates are temperature dependent, but the equations are too general to deal with different material combinations, leaving only the adjustment of the coefficients to bring the model into agreement with the data.

In this work it was shown that the degradation of solar modules is strongly dependent on the selected material combination. Even within the same material group, such as EVA encapsulants, these differ in their VA content and the additives used. In particular, section 3 and section 6 showed that the degradation of the modules strongly depends on the degradation of the encapsulation polymers, which in turn is strongly influenced by the additives used. There are studies that attempt to model the degradation of individual layers, such as the encapsulant as a function of the environmental parameters [258], or to simulate the water permeation of various backsheets [202, 259, 260]. However, these studies do not combine their findings into generalized concepts to predict the degradation of other layers or the overall module.

The results of this work have shown that the empirical degradation models could be extended with material-specific parameters. As already mentioned, the degradation model should be dependent on the selected material combination. In particular, hydrolysis-based and photodegradation could be adapted. The former depends on the barrier properties of the backsheet and the selected encapsulant. If the backsheet is open to diffusion, moisture can be expected to penetrate quickly, as described in subsection 7.4. If the encapsulant is EVA, hydrolysis reactions and the formation of acetic acid can be expected [110–112], which corrodes the contacts and increases the series resistance [200, 201]. In section 3 and section 6 it was shown that the base molecule of the UV stabilizer also degrades under the sole influence of moisture at the corresponding temperature. Consequently, the consumption is dependent on the chosen material combination, as this determines the water permeation rate. The UV stabilizer degradation rate could be used as a marker to determine the influence of this stressor on the modules and thus be able to correlate a loss of performance. In section 6, it was shown that the degradation of the UV stabilizer base molecule depends exponentially on the radiation intensity and the radicals generated by it. Significant polymer degradation was only observed when a large proportion of the HALS base molecule was consumed. The subsequent polymer degradation can, in turn, be correlated with the power loss of the modules, as Norrish type II reactions also produce acetic acid [30, 31, 108, 109], which corrodes the contacts

[200, 201]. Consequently, an extension of the models using UV stabilizer degradation as a marker for the degradation of the encapsulant and therefore of the entire module is also possible for photodegradation.

7.6. Things to consider for improved longevity of solar modules

Based on the results of this work, important considerations can be derived that could enable the PV industry to improve the longevity of solar modules on the one hand and to increase the predictive power of aging tests on the other:

i The terms TPO and POE are not well-defined in the PV sector. Both encapsulant types can contain side groups that lead to unforeseen reactions (see the potential acetic acid formation of ethylene ethyl acrylate in subsubsection 2.1.4).

ii Encapsulant 1 $\neq$ encapsulant 2. This applies in particular to POE and TPO. However, even when EVA is used, it can differ due to different VA contents and, above all, other additives.

iii Backsheet 1 $\neq$ backsheet 2 also applies. Typically, backsheets are structured in layers, which are also provided with additives. They can also have different permeation properties.

iv The degradation of the polymer layers, which directly influences the degradation of the overall module, is primarily determined by the additives used for stabilization. For EVA, the use of hydrolysis-stabilizing additives should be considered, as this could reduce acetic acid production. For POE and TPO encapsulants, which are mainly based on polyethylene, second-order antioxidants should be used to mitigate hydroperoxide formation as the first degradation step (see Table 1).

v Although additives generally serve to improve polymer properties, their interactions can also have adverse effects. As shown in this work, crosslinking peroxides can consume the UV stabilizer if they do not react during lamination. Furthermore, radicals can react with UV absorber molecules and form chromophores, leading to browning and reduced performance.

vi Additives can diffuse over comparatively large distances (see subsection 5.2) and interact positively (e.g. compensation of the UV stabilizer concentration and protection of the encapsulant), but also negatively (see chromophore formation of the UV absorber) at other points. This should be taken into account when different encapsulants are combined with each other, and there are large concentration gradients. Additives could also potentially diffuse from the backsheet into the encapsulant and vice versa. Especially the newly developed EVA-POE-EVA (EPE) films could cause unexpected diffusion effects.

vii The previous points clearly indicate that materials should only be tested individually to a limited extent. If different encapsulants, backsheets, and solar cell technologies

are combined, interactions that do not take place in the individual material can occur. To predict the long-term properties, it is therefore not sufficient to know the individual degradation of the materials. For example, as shown in subsection 6.2, the UV absorber does not degrade in plain foil samples but does degrade in the EVA inside the solar module.

viii Accelerated aging tests in accordance with the standards should be selected with care. subsection 5.1 has shown that the use of UV-A fluorescent lamps is unlikely to cause realistic encapsulant aging. section 6 has been demonstrated that combining several stressors leads to more significant degradation due to synergistic effects.

8. Conclusion

Within this work, various aspects of the degradation of solar modules were examined. The degradation chain could be traced from the penetration of moisture and the effects of UV irradiation to the consumption of stabilizing additives in the encapsulant to polymer degradation and the formation of corrosive acetic acid to the degradation of the electrical connectors and the associated loss of performance. This successive analysis was only possible thanks to a large number of previous investigations, each of which brought new insights into the aging of PV components. It was also shown that using UV-A fluorescence lamps within the current PV standard IEC 62788-7-2 does not necessarily lead to aging effects observed in the field. In contrast, the formation of C=C bonds (Norrish type II reactions of EVA with the formation of acetic acid) could be observed when using xenon lamps with daylight filters. For PV encapsulants, using the latter within the standard is therefore preferable to investigate the aging behavior under UV irradiation.

Fundamental degradation effects of EVA encapsulants in solar modules could be identified depending on individual stressors (UV irradiation or high relative humidity in combination with high temperature). It has been shown that deacetylation occurs for both types of weathering but can be significantly reduced by stabilizing the encapsulant against photodegradation with UV stabilizers (HALS). Thus, the effects on the solar module with pure UV weathering were limited to the degradation of the passivation layers of the PERC cell and a slight increase in the series resistance. The latter was caused by contact corrosion due to acetic acid produced by Norrish type II reactions. Further analyses of photodegradation during the course of the work showed a similar result. Only minor forms of degradation occur if the films are stabilized with UV absorbers and HALS. If these additives are missing, the film will likely fail after a short weathering period. In contrast, the encapsulant in the solar modules was not stabilized against hydrolysis reactions. This led to strong acetic acid formation due to EVA hydrolysis and, consequently, to increased degradation of the electrical connectors. Interestingly, the HALS molecules were also consumed under DH weathering, but no nitroxide groups were formed, indicating that the Denisov cycle is not working in this case. These experiments have shown that the stabilizing additives in encapsulants play an essential role. To predict the encapsulant's degradation and, thus, the degradation of the solar modules, it is necessary to measure and describe the consumption of stabilizing additives.

It was possible to determine the concentrations of common additives in PV encapsulants using self-developed measurement methods for quantification based on PY-GCMS and UV/VIS measurements, and it was possible to determine the concentrations of common additives in PV encapsulants. On the one hand, it is thus possible to investigate the degradation behavior of stabilizing additives and correlate it with polymer degradation. On the other hand, the non-destructive, optical method in particular enables the development of a device for inline quality control. The quantification also made it possible to investigate the migration behavior of stabilizing additives to describe basic diffusion effects within EVA films. The diffusion analyses have also shown that the

stabilizing additives can lead to undesirable side effects. If the radical density within the encapsulant is high due to photodegradation and the UV stabilizer is used up, the radicals can react with benzophenone-based UV absorber molecules. Through hydrogen abstraction, these also become radicals, react with other UV absorber molecules, and form chromophores. This leads to the browning of the encapsulant and consequently to reduced performance of the modules, as the transmittance is reduced.

Extensive analyses made it possible to derive a model for predicting UV stabilizer consumption as a function of the chamber parameters. Interestingly, the same model can be used for pure film, but also for EVA within solar modules. On the other hand, the UV absorber was stable under moderate (and standardized) UV conditions in pure EVA films and coupon samples. In solar modules, however, it is degraded in front EVA, indicating an interaction with the material of the solar cells or the electrical connectors. This reaffirms that materials should not be tested individually but in combination. It was also observed that the encapsulant in solar modules degrades differently at different locations depending on the microclimate present. This can lead to synergistic effects. For example, the acetic acid formed by hydrolysis in the back EVA can diffuse to the front EVA and, in combination with acetic acid formed by photodegradation (Norrish type II reactions), lead to increased corrosion of the electrical contacts.

The findings of this work have shown which measures could be taken to increase the service life of solar modules and which fundamental degradation effects are to be expected. In particular, with the switch to new solar cell technologies such as TOPCon and HJT and the use of TPO and POE-based encapsulants, various degradation modes can occur if the interactions listed in this work are ignored. New material combinations should be examined intensively and, above all, spatially resolved for degradation effects. The methodology presented in this paper provides a basis but can be extended as required to fully understand the degradation at all points of a solar module. This could make it possible to consider all local stressors and their synergies to reliably predict solar module degradation depending on the materials used and all environmental parameters. In this way, the previously rather empirical modeling of solar module degradation could also be extended by real, material-specific measured variables. On the one hand, the permeation behavior of moisture and oxygen into the modules can be used. On the other hand, the degradation of stabilizing additives can be correlated with polymer degradation and the corresponding subsequent reactions. Thus, macroscopic measured variables and pre-factors can be replaced by material-specific variables.

References

[1] James Rising et al. “The missing risks of climate change”. In: *Nature* 610.7933 (2022), pp. 643–651.

[2] Maximilian Kotz, Anders Levermann, and Leonie Wenz. “The economic commitment of climate change”. In: *Nature* 628.8008 (2024), pp. 551–557.

[3] Bas J Van Ruijven, Enrica De Cian, and Ian Sue Wing. “Amplification of future energy demand growth due to climate change”. In: *Nature communications* 10.1 (2019), p. 2762.

[4] Armin Razmjoo et al. “A Technical analysis investigating energy sustainability utilizing reliable renewable energy sources to reduce CO2 emissions in a high potential area”. In: *Renewable Energy* 164 (2021), pp. 46–57.

[5] Muhammad Badar Hayat et al. “Solar energy—A look into power generation, challenges, and a solar-powered future”. In: *International Journal of Energy Research* 43.3 (2019), pp. 1049–1067.

[6] Marta Victoria et al. “Solar photovoltaics is ready to power a sustainable future”. In: *Joule* 5.5 (2021), pp. 1041–1056.

[7] Femke JMM Nijsse et al. “The momentum of the solar energy transition”. In: *Nature Communications* 14.1 (2023), p. 6542.

[8] David EHJ Gernaat et al. “Climate change impacts on renewable energy supply”. In: *Nature Climate Change* 11.2 (2021), pp. 119–125.

[9] M Aghaei et al. “Review of degradation and failure phenomena in photovoltaic modules”. In: *Renewable and Sustainable Energy Reviews* 159 (2022), p. 112160.

[10] Dirk C Jordan, Nancy Haegel, and Teresa M Barnes. “Photovoltaics module reliability for the terawatt age”. In: *Progress in Energy* 4.2 (2022), p. 022002.

[11] L Koester et al. “Review of photovoltaic module degradation, field inspection techniques and techno-economic assessment”. In: *Renewable and Sustainable Energy Reviews* 165 (2022), p. 112616.

[12] Gernot Oreski et al. “Motivation, benefits, and challenges for new photovoltaic material & module developments”. In: *Progress in Energy* 4.3 (2022), p. 032003.

[13] Francisco Prieto-Castrillo, Neftalí Núñez, and Manuel Vázquez. “Warranty assessment of photovoltaic modules based on a degradation probabilistic model”. In: *Progress in Photovoltaics: Research and Applications* 28.12 (2020), pp. 1308–1321.

[14] Ismail Kaaya et al. “Assessment of uncertainties and variations in PV modules degradation rates and lifetime predictions using physical models”. In: *Solar Energy* 218 (2021), pp. 354–367.

[15] Arun Bala Subramaniyan et al. “Quantification of environmental effects on PV module degradation: A physics-based data-driven modeling method”. In: *IEEE Journal of Photovoltaics* 8.5 (2018), pp. 1289–1296.

[16] Ababacar Ndiaye et al. “Degradations of silicon photovoltaic modules: A literature review”. In: *Solar Energy* 96 (2013), pp. 140–151.

[17] Shuntaro Shimpo, Huynh Thi Cam Tu, and Keisuke Ohdaira. "Potential-induced degradation of encapsulant-less p-type crystalline Si photovoltaic modules". In: *Japanese Journal of Applied Physics* 62.SK (2023), SK1039.

[18] Cécile Molto et al. "Review of potential-induced degradation in bifacial photovoltaic modules". In: *Energy Technology* 11.4 (2023), p. 2200943.

[19] Martin Halwachs et al. "Statistical evaluation of PV system performance and failure data among different climate zones". In: *Renewable Energy* 139 (2019), pp. 1040–1060.

[20] Aesha Parimalbhai Patel, Archana Sinha, and Govindasamy Tamizhmani. "Field-aged glass/backsheet and glass/glass PV modules: encapsulant degradation comparison". In: *IEEE Journal of Photovoltaics* 10.2 (2019), pp. 607–615.

[21] Barbara Brune et al. "Quantifying the influence of encapsulant and backsheet composition on PV-power and electrical degradation". In: *Progress in Photovoltaics: Research and Applications* 31.7 (2023), pp. 716–728.

[22] Dirk C Jordan and Sarah R Kurtz. "Analytical improvements in PV degradation rate determination". In: *2010 35th IEEE Photovoltaic Specialists Conference*. IEEE. 2010, pp. 002688–002693.

[23] Dirk C Jordan et al. "Robust PV degradation methodology and application". In: *IEEE Journal of photovoltaics* 8.2 (2017), pp. 525–531.

[24] Hussain A Al Mahdi, Paul G Leahy, and Alan P Morrison. "Predicting early EVA degradation in photovoltaic modules from short circuit current measurements". In: *IEEE Journal of Photovoltaics* 11.5 (2021), pp. 1188–1196.

[25] Mohammed Adnan Hameed et al. "Analysis and Prediction of the Performance and Reliability of PV Modules installed in harsh climates: Case study Iraq". In: *Renewable Energy* 228 (2024), p. 120577.

[26] Mohammed Adnan Hameed et al. "Economic Consequences Based on Reversible and Irreversible Degradation of PV Park in the Harsh Climate Conditions of Iraq". In: *Energies* 17.11 (2024), p. 2652.

[27] Julián Ascencio-Vásquez et al. "Global climate data processing and mapping of degradation mechanisms and degradation rates of PV modules". In: *Energies* 12.24 (2019), p. 4749.

[28] Ismail Kaaya et al. "Modeling outdoor service lifetime prediction of PV modules: effects of combined climatic stressors on PV module power degradation". In: *IEEE Journal of Photovoltaics* 9.4 (2019), pp. 1105–1112.

[29] E Cuddihy et al. *Flat-plate solar array project. Volume 7: Module encapsulation*. Tech. rep. 1986.

[30] AW Czanderna and FJ Pern. "Encapsulation of PV modules using ethylene vinyl acetate copolymer as a pottant: A critical review". In: *Solar energy materials and solar cells* 43.2 (1996), pp. 101–181.

[31] Michele Cândida Carvalho de Oliveira et al. "The causes and effects of degradation of encapsulant ethylene vinyl acetate copolymer (EVA) in crystalline silicon photovoltaic modules: A review". In: *Renewable and Sustainable Energy Reviews* 81 (2018), pp. 2299–2317.

[32] FJ Pern. "Factors that affect the EVA encapsulant discoloration rate upon accelerated exposure". In: *Solar energy materials and solar cells* 41 (1996), pp. 587–615.

[33] FJ Pern, SH Glick, and AW Czanderna. "Review of the photothermal stability of EVA pottants: Effects of formulation on the discoloration rate and mitigation methods". In: *AIP Conference Proceedings*. Vol. 462. 1. American Institute of Physics. 1999, pp. 599–604.

[34] Peter Klemchuk et al. "Investigation of the degradation and stabilization of EVA-based encapsulant in field-aged solar energy modules". In: *Polymer degradation and stability* 55.3 (1997), pp. 347–365.

[35] A Jentsch, K-J Eichhorn, and B Voit. "Influence of typical stabilizers on the aging behavior of EVA foils for photovoltaic applications during artificial UV-weathering". In: *Polymer Testing* 44 (2015), pp. 242–247.

[36] Frank P Cortolano. "Antioxidants and UV stabilizers: A summary of their utilization in PVC". In: *Journal of Vinyl Technology* 15.2 (1993), pp. 69–75.

[37] ET Denisov. "The role and reactions of nitroxyl radicals in hindered piperidine light stabilisation". In: *Polymer degradation and stability* 34.1-3 (1991), pp. 325–332.

[38] Eugene N Step et al. "Model studies on the mechanism of HALS stabilization". In: *Die Angewandte Makromolekulare Chemie: Applied Macromolecular Chemistry and Physics* 232.1 (1995), pp. 65–83.

[39] Jennifer L Hodgson and Michelle L Coote. "Clarifying the mechanism of the Denisov cycle: how do hindered amine light stabilizers protect polymer coatings from photo-oxidative degradation?" In: *Macromolecules* 43.10 (2010), pp. 4573–4583.

[40] James E Pickett and James E Moore. "Photodegradation of UV absorbers: kinetics and structural effects". In: *Die Angewandte Makromolekulare Chemie: Applied Macromolecular Chemistry and Physics* 232.1 (1995), pp. 229–238.

[41] James E Pickett. "Review and kinetic analysis of the photodegradation of UV absorbers". In: *Macromolecular Symposia*. Vol. 115. 1. Wiley Online Library. 1997, pp. 127–141.

[42] Emil Bubev, Anton Georgiev, and Maria Machkova. "Kinetic study on UV-absorber photodegradation under different conditions". In: *Chemical Physics* 476 (2016), pp. 69–79.

[43] F Gugumus. "Current trends in mode of action of hindered amine light stabilizers". In: *Polymer Degradation and Stability* 40.2 (1993), pp. 167–215.

[44] HL Frisch and S Alexander Stern. "Diffusion of small molecules in polymers". In: *Critical Reviews in Solid State and Material Sciences* 11.2 (1983), pp. 123–187.

[45] J Sax and JM Ottino. "Modeling of transport of small molecules in polymer blends: Application of effective medium theory". In: *Polymer Engineering & Science* 23.3 (1983), pp. 165–176.

[46] Alain Reynier, Patrice Dole, and Alexandre Feigenbaum. "Additive diffusion coefficients in polyolefins. II. Effect of swelling and temperature on the D= f (M) correlation". In: *Journal of applied polymer science* 82.10 (2001), pp. 2434–2443.

[47] Jarett Zuboy et al. “Getting Ahead of the Curve: Assessment of New Photovoltaic Module Reliability Risks Associated With Projected Technological Changes”. In: *IEEE Journal of Photovoltaics* (2023).

[48] *IEC 61215-2:2021 - Terrestrial photovoltaic (PV) modules - Design qualification and type approval - Part 2: Test procedures*. Standard. International Electrotechnical Commission, 2021.

[49] *DIN IEC/TS 62788-7-2, Measurement procedures for materials used in photovoltaic modules - Part 7-2: Environmental exposures - Accelerated weathering tests of polymeric materials*. Standard. International Electrotechnical Commission, 2019.

[50] Robert Heidrich et al. “From Performance Measurements to Molecular Level Characterization: Exploring the Differences between Ultraviolet and Damp Heat Weathering of Photovoltaics Modules”. In: *Solar RRL* 8.10 (2024), p. 2400144.

[51] Robert Heidrich, Anton Mordvinkin, and Ralph Gottschalg. “Quantification of UV protecting additives in ethylene-vinyl acetate copolymer encapsulants for photovoltaic modules with pyrolysis-gas chromatography-mass spectrometry”. In: *Polymer Testing* 118 (2023), p. 107913.

[52] Robert Heidrich et al. “UV lamp spectral effects on the aging behavior of encapsulants for photovoltaic modules”. In: *Solar Energy Materials and Solar Cells* 266 (2024), p. 112674.

[53] Robert Heidrich et al. “Diffusion of UV Additives in Ethylene-Vinyl Acetate Copolymer Encapsulants and the Impact on Polymer Reliability”. In: *IEEE Journal of Photovoltaics* (2023).

[54] Robert Heidrich, Anton Mordvinkin, and Ralph Gottschalg. “Spatially resolved degradation analysis of solar modules after combined accelerated aging”. In: *2023 IEEE 50th Photovoltaic Specialists Conference (PVSC)*. IEEE. 2023, pp. 1–3.

[55] Robert Heidrich, Anton Mordvinkin, and Ralph Gottschalg. “Spatially Resolved Degradation of Solar Modules in Dependence of the Prevailing Microclimate”. In: *IEEE Journal of Photovoltaics* (2024).

[56] Gernot Oreski et al. “Properties and degradation behaviour of polyolefin encapsulants for photovoltaic modules”. In: *Progress in Photovoltaics: Research and Applications* 28.12 (2020), pp. 1277–1288.

[57] Michael Rubinsten. *Polymer physics*. United States of America, 2003.

[58] Gottfried Wilhelm Ehrenstein and Sonja Pongratz. *Resistance and stability of polymers*. Carl Hanser Verlag GmbH Co KG, 2013.

[59] Hans Zweifel. *Stabilization of polymeric materials*. springer science & business media, 2012.

[60] Hsinjin Edwin Yang, Roger French, and Laura Bruckman. *Durability and Reliability of Polymers and Other Materials in Photovoltaic Modules*. William Andrew, 2019.

[61] Cornelia Peike et al. “Towards the origin of photochemical EVA discoloration”. In: *2013 IEEE 39th Photovoltaic Specialists Conference (PVSC)*. IEEE. 2013, pp. 1579–1584.

[62] Angelika Beinert et al. "The influence of the additive composition on degradation induced changes in poly (ethylene-co-vinyl acetate) during photochemical aging". In: *29th European PV Solar Energy Conference and Exhibition, Amsterdam*. 2014.

[63] Ch Hirschl et al. "In-line determination of the degree of crosslinking of ethylene vinyl acetate in PV modules by Raman spectroscopy". In: *Solar Energy Materials and Solar Cells* 152 (2016), pp. 10–20.

[64] Gernot Oreski et al. "Crosslinking and post-crosslinking of ethylene vinyl acetate in photovoltaic modules". In: *Journal of Applied Polymer Science* 134.23 (2017).

[65] Ch Hirschl et al. "Determining the degree of crosslinking of ethylene vinyl acetate photovoltaic module encapsulants—A comparative study". In: *Solar Energy Materials and Solar Cells* 116 (2013), pp. 203–218.

[66] Sachiko Jonai et al. "Relationship between cross-linking conditions of ethylene vinyl acetate and potential induced degradation for crystalline silicon photovoltaic modules". In: *Japanese journal of applied physics* 54.8S1 (2015), 08KG01.

[67] Ramasatamy Anbarasan, Odile Babot, and Bernard Maillard. "Crosslinking of high-density polyethylene in the presence of organic peroxides". In: *Journal of applied polymer science* 93.1 (2004), pp. 75–81.

[68] Elisa Passaglia et al. "Modulated crosslinking of polyolefins through radical processes in the melt". In: *Macromolecular Materials and Engineering* 289.9 (2004), pp. 809–817.

[69] S Mishra, B Baweja, and R Chandra. "Studies on dynamic and static crosslinking of ethylene vinyl acetate and ethylene propylene diene tercopolymer blends". In: *Journal of applied polymer science* 74.11 (1999), pp. 2756–2763.

[70] HA Khonakdar et al. "An investigation of chemical crosslinking effect on properties of high-density polyethylene". In: *Polymer* 44.15 (2003), pp. 4301–4309.

[71] Wenzhen Lai et al. "Hydrogen-abstraction reactivity patterns from A to Y: The valence bond way". In: *Angewandte Chemie International Edition* 51.23 (2012), pp. 5556–5578.

[72] Shun Muroga et al. "New evaluation method for the curing degree of rubber and its nanocomposites using ATR-FTIR spectroscopy". In: *Polymer Testing* 93 (2021), p. 106993.

[73] Kimberly Miller McLoughlin et al. "Thermomechanical Properties of Cross-Linked EVA: A Holistic Approach". In: *ACS Applied Polymer Materials* 5.2 (2023), pp. 1430–1439.

[74] Hong Zhao et al. "Theoretical study on the reaction of triallyl isocyanurate in the UV radiation cross-linking of polyethylene". In: *RSC advances* 7.59 (2017), pp. 37095–37104.

[75] Yu-Wei Fu, Wei-Feng Sun, and Xuan Wang. "UV-initiated crosslinking reaction mechanism and electrical breakdown performance of crosslinked polyethylene". In: *Polymers* 12.2 (2020), p. 420.

[76] Gernot Oreski and GM Wallner. "Delamination behaviour of multi-layer films for PV encapsulation". In: *Solar energy materials and solar cells* 89.2-3 (2005), pp. 139–151.

[77] GJ Jorgensen et al. “Moisture transport, adhesion, and corrosion protection of PV module packaging materials”. In: *Solar Energy Materials and Solar Cells* 90.16 (2006), pp. 2739–2775.

[78] Roopmati Meena, Arti Pareek, and Rajesh Gupta. “A comprehensive Review on interfacial delamination in photovoltaic modules”. In: *Renewable and Sustainable Energy Reviews* 189 (2024), p. 113944.

[79] Barry Arkles. “Tailoring surfaces with silanes”. In: *Chemtech* 7 (1977), pp. 766–778.

[80] Evgenia Korzhikova-Vlakh, Mariia Antipchik, and Tatiana Tennikova. “Macroporous polymer monoliths in thin layer format”. In: *Polymers* 13.7 (2021), p. 1059.

[81] T Paunikallio, M Suvanto, and TT Pakkanen. “Grafting of 3-(trimethoxysilyl) propyl methacrylate onto polypropylene and use as a coupling agent in viscose fiber/poly propylene composites”. In: *Reactive and Functional Polymers* 68.3 (2008), pp. 797–808.

[82] Song-Hee Im and Sung-Seen Choi. “Analysis of polymeric UV absorber (Tinuvin 213) using LDI-TOFMS: Solvent effect in sample preparation”. In: *Bulletin of the Korean Chemical Society* 32.6 (2011), pp. 2093–2096.

[83] F Wetz et al. “A new long-chain UV absorber derived from 4-tert-butyl-4’-methoxydi 6 enzoylmethane: Absorbance stability under solar irradiation”. In: *Journal of cosmetic science* 56.2 (2005), pp. 135–148.

[84] Chiara Barretta et al. “Comparison of degradation behavior of newly developed encapsulation materials for photovoltaic applications under different artificial ageing tests”. In: *Polymers* 13.2 (2021), p. 271.

[85] Ibrahim M Maafa. “Inhibition of free radical polymerization: a review”. In: *Polymers* 15.3 (2023), p. 488.

[86] Jan Pospisil and Stanislav Nespurek. “Chain-breaking stabilizers in polymers: the current status”. In: *Polymer Degradation and Stability* 49.1 (1995), pp. 99–110.

[87] Kevin Fouyer, Olivier Lavastre, and David Rondeau. “Direct monitoring of the role played by a stabilizer in a solid sample of polymer using direct analysis in real time mass spectrometry: the case of Irgafos 168 in polyethylene”. In: *Analytical chemistry* 84.20 (2012), pp. 8642–8649.

[88] Rudinei Fiorio et al. “A statistical analysis on the effect of antioxidants on the thermal-oxidative stability of commercial mass-and emulsion-polymerized ABS”. In: *Polymers* 11.1 (2018), p. 25.

[89] Carlos Federico Jasso-Gastinel and José M Kenny. *Modification of polymer properties*. William Andrew, 2016.

[90] Enikõ Földes and Béla Turcsányi. “Transport of small molecules in polyolefins. I. Diffusion of irganox 1010 in polyethylene”. In: *Journal of applied polymer science* 46.3 (1992), pp. 507–515.

[91] Enikő Földes. “Transport of small molecules in polyolefins. II. Diffusion and solubility of irganox 1076 in ethylene polymers”. In: *Journal of applied polymer science* 48.11 (1993), pp. 1905–1913.

[92] Enikó Földes. “Transport of small molecules in polyolefins. III. Diffusion of topanol CA in ethylene polymers”. In: *Journal of applied polymer science* 51.9 (1994), pp. 1581–1589.

[93] Nancy Cliff et al. “Use of reactable light stabilizers to prevent migration and to improve durability of coatings on plastic substrates”. In: *JCT research* 2 (2005), pp. 371–387.

[94] John Crank. *The mathematics of diffusion*. Oxford university press, 1979.

[95] Adolf Fick. “Ueber diffusion”. In: *Annalen der Physik* 170.1 (1855), pp. 59–86.

[96] Albert Einstein. “Über die von der molekularkinetischen Theorie der Wärme geforderte Bewegung von in ruhenden Flüssigkeiten suspendierten Teilchen”. In: *Annalen der physik* 4 (1905).

[97] Albert Einstein. “Elementare theorie der brownschen) bewegung”. In: *Zeitschrift für Elektrochemie und angewandte physikalische Chemie* 14.17 (1908), pp. 235–239.

[98] Nicolas Pinochet, Romain Couderc, and Sandrine Therias. “Solar cell UV-induced degradation or module discolouration: Between the devil and the deep yellow sea”. In: *Progress in Photovoltaics: Research and Applications* 31.11 (2023), pp. 1091–1100.

[99] Eric J Schneller et al. “Manufacturing metrology for c-Si module reliability and durability Part III: Module manufacturing”. In: *Renewable and Sustainable Energy Reviews* 59 (2016), pp. 992–1016.

[100] Nadka Tz Dintcheva, Elisabetta Morici, and Claudio Colletti. “Encapsulant Materials and Their Adoption in Photovoltaic Modules: A Brief Review”. In: *Sustainability* 15.12 (2023), p. 9453.

[101] Zhengfeng Yang et al. “Novel EPE co-extruded encapsulating films with UV down-conversion power gain effect for highly efficient solar cells”. In: *Solar Energy Materials and Solar Cells* 257 (2023), p. 112373.

[102] Daniele C Bugada and Alfred Rudin. “Molecular structure and melting behaviour of ethylene-vinyl acetate copolymers”. In: *European polymer journal* 28.3 (1992), pp. 219–227.

[103] Alex M Henderson. “Ethylene-vinyl acetate (EVA) copolymers: a general review”. In: *IEEE Electrical Insulation Magazine* 9.1 (1993), pp. 30–38.

[104] A Badiee, IA Ashcroft, and Ricky D Wildman. “The thermo-mechanical degradation of ethylene vinyl acetate used as a solar panel adhesive and encapsulant”. In: *International Journal of Adhesion and Adhesives* 68 (2016), pp. 212–218.

[105] Bart Rimez et al. “The thermal degradation of poly (vinyl acetate) and poly (ethylene-co-vinyl acetate), Part I: Experimental study of the degradation mechanism”. In: *Polymer Degradation and Stability* 93.4 (2008), pp. 800–810.

[106] Bart Rimez et al. “The thermal degradation of poly (vinyl acetate) and poly (ethylene-co-vinyl acetate), Part II: Modelling the degradation kinetics”. In: *Polymer degradation and stability* 93.6 (2008), pp. 1222–1230.

[107] Kea Agroui, G Collins, and J Farenc. “Measurement of glass transition temperature of crosslinked EVA encapsulant by thermal analysis for photovoltaic application”. In: *Renewable Energy* 43 (2012), pp. 218–223.

[108] Norman S Allen et al. “Aspects of the thermal oxidation, yellowing and stabilisation of ethylene vinyl acetate copolymer”. In: *Polymer degradation and stability* 71.1 (2000), pp. 1–14.

[109] Jing Jin, Shuangjun Chen, and Jun Zhang. “UV aging behaviour of ethylene-vinyl acetate copolymers (EVA) with different vinyl acetate contents”. In: *Polymer degradation and stability* 95.5 (2010), pp. 725–732.

[110] Kohjiro Hara, Sachiko Jonai, and Atsushi Masuda. “Crystalline Si photovoltaic modules functionalized by a thin polyethylene film against potential and damp-heat-induced degradation”. In: *RSC advances* 5.20 (2015), pp. 15017–15023.

[111] Kohjiro Hara and Yasuo Chiba. “Spectroscopic investigation of long-term outdoor-exposed crystalline silicon photovoltaic modules”. In: *Journal of Photochemistry and Photobiology A: Chemistry* 404 (2021), p. 112891.

[112] Mogon Patel et al. “Thermal stability of poly (ethylene-co-vinyl acetate) based materials”. In: *Polymer testing* 32.4 (2013), pp. 785–793.

[113] Mélanie Gardette et al. “Photo-and thermal-oxidation of polyethylene: Comparison of mechanisms and influence of unsaturation content”. In: *Polymer Degradation and Stability* 98.11 (2013), pp. 2383–2390.

[114] Michael D Kempe et al. “Acetic acid production and glass transition concerns with ethylene-vinyl acetate used in photovoltaic devices”. In: *Solar energy materials and solar cells* 91.4 (2007), pp. 315–329.

[115] Bernt-Åke Sultan and Erling Sörvik. “Thermal degradation of EVA and EBA—A comparison. I. Volatile decomposition products”. In: *Journal of applied polymer science* 43.9 (1991), pp. 1737–1745.

[116] Bernt-Åke Sultan and Erling Sörvik. “Thermal degradation of EVA and EBA—A comparison. II. Changes in unsaturation and side group structure”. In: *Journal of applied polymer science* 43.9 (1991), pp. 1747–1759.

[117] Bernt-Åke Sultan and Erling Sörvik. “Thermal degradation of EVA and EBA—A comparison. III. Molecular weight changes”. In: *Journal of applied polymer science* 43.9 (1991), pp. 1761–1771.

[118] Archana Sinha, OS Sastry, and Rajesh Gupta. “Nondestructive characterization of encapsulant discoloration effects in crystalline-silicon PV modules”. In: *Solar Energy Materials and Solar Cells* 155 (2016), pp. 234–242.

[119] J.L. White and D. Choi. *Polyolefins: Processing, Structure Development and Properties*. Hanser Gardner Publications, 2005. ISBN: 9781569903698.

[120] Steven Wong et al. “Effect of processing parameters on the mechanical properties of injection molded thermoplastic polyolefin (TPO) cellular foams”. In: *Macromolecular Materials and Engineering* 293.7 (2008), pp. 605–613.

[121] Baloji Adothu, Francis Reny Costa, and Sudhanshu Mallick. “Damp heat resilient thermoplastic polyolefin encapsulant for photovoltaic module encapsulation”. In: *Solar Energy Materials and Solar Cells* 224 (2021), p. 111024.

[122] Baloji Adothu, Francis Reny Costa, and Sudhanshu Mallick. "UV resilient thermoplastic polyolefin encapsulant for photovoltaic module encapsulation". In: *Polymer Degradation and Stability* 201 (2022), p. 109972.

[123] Martin Tiefenthaler, Gernot M Wallner, and Robert Pugstaller. "Effect of global damp heat ageing on debonding of crosslinked EVA-and POE-glass laminates". In: *Solar Energy Materials and Solar Cells* 264 (2024), p. 112602.

[124] Soňa Uličná et al. "PV encapsulant formulations and stress test conditions influence dominant degradation mechanisms". In: *Solar Energy Materials and Solar Cells* 255 (2023), p. 112319.

[125] Jennifer L Jordan et al. "Mechanical properties of low density polyethylene". In: *Journal of dynamic behavior of materials* 2 (2016), pp. 411–420.

[126] Sundar L Aggarwal and Orville J Sweeting. "Polyethylene: preparation, structure, and properties". In: *Chemical Reviews* 57.4 (1957), pp. 665–742.

[127] L Lin and AS Argon. "Structure and plastic deformation of polyethylene". In: *Journal of Materials Science* 29 (1994), pp. 294–323.

[128] Hsien-Yi Hsu et al. "Oxidized low density polyethylene: A potential cost-effective, stable, and recyclable polymeric encapsulant for photovoltaic modules". In: *Solar energy materials and solar cells* 94.6 (2010), pp. 955–959.

[129] Ali Fazli and Denis Rodrigue. "Waste rubber recycling: A review on the evolution and properties of thermoplastic elastomers". In: *Materials* 13.3 (2020), p. 782.

[130] Richard J Spontak and Nikunj P Patel. "Thermoplastic elastomers: fundamentals and applications". In: *Current opinion in colloid & interface science* 5.5-6 (2000), pp. 333–340.

[131] Wenyue Ding and Megan L Robertson. "Sustainable thermoplastic elastomers with a transient network". In: *European Polymer Journal* 113 (2019), pp. 411–423.

[132] Zi-Long Li et al. "Ethylene–ethyl acrylate copolymers via ADMET polymerization: Effect of sequence distribution on thermal properties". In: *Journal of Polymer Science Part A: Polymer Chemistry* 51.13 (2013), pp. 2900–2909.

[133] Ian C McNeill and Musarrat H Mohammed. "A comparison of the thermal degradation behaviour of ethylene-ethyl acrylate copolymer, low density polyethylene and poly (ethyl acrylate)". In: *Polymer degradation and stability* 48.1 (1995), pp. 175–187.

[134] Jean-François Glikman et al. "Photolysis and photo-oxidation of ethylene-ethyl acrylate copolymers". In: *Polymer degradation and stability* 16.4 (1986), pp. 325–335.

[135] Andrew Fairbrother et al. "Differential degradation patterns of photovoltaic backsheets at the array level". In: *Solar Energy* 163 (2018), pp. 62–69.

[136] Claudia Buerhop-Lutz et al. "PV modules and their backsheets-A case study of a Multi-MW PV power station". In: *Solar Energy Materials and Solar Cells* 231 (2021), p. 111295.

[137] Jia-Wei Zhang et al. "Aging phenomena of backsheet materials of photovoltaic systems for future zero-carbon energy and the improvement pathway". In: *Journal of Materials Science & Technology* 153 (2023), pp. 106–119.

[138] Jai Prakash Singh et al. “Comparison of glass/glass and glass/backsheet PV modules using bifacial silicon solar cells”. In: *IEEE Journal of Photovoltaics* 5.3 (2015), pp. 783–791.

[139] Laura Spinella et al. “Chemical and mechanical interfacial degradation in bifacial glass / glass and glass / transparent backsheet photovoltaic modules”. In: *Progress in Photovoltaics: Research and Applications* 30.12 (2022), pp. 1423–1432.

[140] Namsu Kim et al. “Study on the degradation of different types of backsheets used in PV module under accelerated conditions”. In: *Solar energy materials and solar cells* 120 (2014), pp. 543–548.

[141] Chiao-Chi Lin et al. “Depth profiling of degradation of multilayer photovoltaic backsheets after accelerated laboratory weathering: Cross-sectional Raman imaging”. In: *Solar Energy Materials and Solar Cells* 144 (2016), pp. 289–299.

[142] Gernot Oreski et al. “Performance of PV modules using co-extruded backsheets based on polypropylene”. In: *Solar Energy Materials and Solar Cells* 223 (2021), p. 110976.

[143] Soňa Uličná et al. “A study of degradation mechanisms in PVDF-based photovoltaic backsheets”. In: *Scientific Reports* 12.1 (2022), p. 14399.

[144] Soshana Smith et al. “Transparent backsheets for bifacial photovoltaic (PV) modules: Material characterization and accelerated laboratory testing”. In: *Progress in Photovoltaics: Research and Applications* 30.8 (2022), pp. 959–969.

[145] Klaus J Geretschläger, Gernot M Wallner, and Jörg Fischer. “Structure and basic properties of photovoltaic module backsheet films”. In: *Solar Energy Materials and Solar Cells* 144 (2016), pp. 451–456.

[146] Jean-Luc Gardette et al. “Impact of photooxidative degradation on the oxygen permeability of poly (ethyleneterephthalate)”. In: *Polymer degradation and stability* 103 (2014), pp. 35–41.

[147] Florence Dubelley et al. “Predictive durability of polyethylene terephthalate toward hydrolysis over large temperature and relative humidity ranges”. In: *Polymer* 142 (2018), pp. 285–292.

[148] Roberto Nisticò. “Polyethylene terephthalate (PET) in the packaging industry”. In: *Polymer Testing* 90 (2020), p. 106707.

[149] William Gambogi et al. “A comparison of key PV backsheet and module performance from fielded module exposures and accelerated tests”. In: *IEEE Journal of Photovoltaics* 4.3 (2014), pp. 935–941.

[150] BJ Holland and JN Hay. “The thermal degradation of PET and analogous polyesters measured by thermal analysis–Fourier transform infrared spectroscopy”. In: *Polymer* 43.6 (2002), pp. 1835–1847.

[151] Firas Awaja and Dumitru Pavel. “Recycling of PET”. In: *European polymer journal* 41.7 (2005), pp. 1453–1477.

[152] Rudolf Gross and Achim Marx. *Festkörperphysik*. Oldenbourg Wissenschaftsverlag Verlag, 2012.

[153] Jürgen Smoliner. *Grundlagen der Halbleiterphysik*. Springer, 2018.

[154] Peter Würfel and Uli Würfel. *Physics of solar cells: from basic principles to advanced concepts*. John Wiley & Sons, 2016.

[155] Rolf Brendel. *Thin-film crystalline silicon solar cells: physics and technology*. John Wiley & Sons, 2011.

[156] Neil W Ashcroft and N David Mermin. *Solid state physics*. CENGAGE Learning, 1976.

[157] Andrew Blakers. "Development of the PERC solar cell". In: *IEEE Journal of Photovoltaics* 9.3 (2019), pp. 629–635.

[158] Chuanke Chen et al. "Investigating the viability of PERC solar cells fabricated on Ga-instead of B-doped monocrystalline silicon wafer". In: *Solar Energy Materials and Solar Cells* 227 (2021), p. 111134.

[159] Zhen Zhang and John T Yates Jr. "Band bending in semiconductors: chemical and physical consequences at surfaces and interfaces". In: *Chemical reviews* 112.10 (2012), pp. 5520–5551.

[160] Jonathan Warby et al. "Mismatch of Quasi–Fermi Level Splitting and Voc in Perovskite Solar Cells". In: *Advanced Energy Materials* 13.48 (2023), p. 2303135.

[161] William W Piper and FE Williams. "Electroluminescence". In: *Solid State Physics*. Vol. 6. Elsevier, 1958, pp. 95–173.

[162] M Ruff et al. "The spectral distribution of the intrinsic radiative recombination in silicon". In: *Journal of applied physics* 74.1 (1993), pp. 267–274.

[163] Yatendra Pal Varshni. "Temperature dependence of the energy gap in semiconductors". In: *physica* 34.1 (1967), pp. 149–154.

[164] Takashi Fuyuki et al. "Photographic surveying of minority carrier diffusion length in polycrystalline silicon solar cells by electroluminescence". In: *Applied Physics Letters* 86.26 (2005).

[165] Takashi Fuyuki et al. "Analytic findings in the electroluminescence characterization of crystalline silicon solar cells". In: *Journal of applied Physics* 101.2 (2007).

[166] Peter Würfel et al. "Diffusion lengths of silicon solar cells from luminescence images". In: *Journal of Applied Physics* 101.12 (2007).

[167] Matthew P Peloso, Bram Hoex, and Armin G Aberle. "Polarization analysis of luminescence for the characterization of silicon wafer solar cells". In: *Applied Physics Letters* 98.17 (2011).

[168] Matthew P Peloso et al. "Polarisation analysis of luminescence for the characterisation of defects in silicon wafer solar cells". In: *Progress in Photovoltaics: Research and Applications* 20.6 (2012), pp. 661–669.

[169] David Hinken et al. "Series resistance imaging of solar cells by voltage dependent electroluminescence". In: *Applied Physics Letters* 91.18 (2007).

[170] Jonas Haunschild et al. "Fast series resistance imaging for silicon solar cells using electroluminescence". In: *physica status solidi (RRL)–Rapid Research Letters* 3.7-8 (2009), pp. 227–229.

[171] O Breitenstein et al. "Quantitative evaluation of electroluminescence images of solar cells". In: *physica status solidi (RRL)–Rapid Research Letters* 4.1-2 (2010), pp. 7–9.

[172] C Peike et al. “Origin of damp-heat induced cell degradation”. In: *Solar Energy Materials and Solar Cells* 116 (2013), pp. 49–54.

[173] Du-Ming Tsai, Shih-Chieh Wu, and Wei-Chen Li. “Defect detection of solar cells in electroluminescence images using Fourier image reconstruction”. In: *Solar Energy Materials and Solar Cells* 99 (2012), pp. 250–262.

[174] Sergiu Deitsch et al. “Automatic classification of defective photovoltaic module cells in electroluminescence images”. In: *Solar Energy* 185 (2019), pp. 455–468.

[175] Taesoo D Lee and Abasifreke U Ebong. “A review of thin film solar cell technologies and challenges”. In: *Renewable and Sustainable Energy Reviews* 70 (2017), pp. 1286–1297.

[176] Tatsuo Saga. “Advances in crystalline silicon solar cell technology for industrial mass production”. In: *npg asia materials* 2.3 (2010), pp. 96–102.

[177] Thorsten Dullweber and Jan Schmidt. “Industrial silicon solar cells applying the passivated emitter and rear cell (PERC) concept—A review”. In: *IEEE journal of photovoltaics* 6.5 (2016), pp. 1366–1381.

[178] Stefan W Glunz and Frank Feldmann. “SiO2 surface passivation layers–a key technology for silicon solar cells”. In: *Solar Energy Materials and Solar Cells* 185 (2018), pp. 260–269.

[179] Sang Hee Lee et al. “Review of advanced hydrogen passivation for high efficient crystalline silicon solar cells”. In: *Materials Science in Semiconductor Processing* 79 (2018), pp. 66–73.

[180] S Ma et al. “Application of SiOxNy films in industrial bifacial PERC solar cells”. In: *Solar Energy Materials and Solar Cells* 230 (2021), p. 111199.

[181] Jerry G Fossum. “Physical operation of back-surface-field silicon solar cells”. In: *IEEE Transactions on Electron Devices* 24.4 (1977), pp. 322–325.

[182] Oldwig Von Roos. “A simple theory of back surface field (BSF) solar cells”. In: *Journal of Applied Physics* 49.6 (1978), pp. 3503–3511.

[183] JG Fossum, RD Nasby, and Shing Chong Pao. “Physics underlying the performance of back-surface-field solar cells”. In: *IEEE Transactions on Electron Devices* 27.4 (1980), pp. 785–791.

[184] Shreesh Narasimha, Ajeet Rohatgi, and AW Weeber. “An optimized rapid aluminum back surface field technique for silicon solar cells”. In: *IEEE Transactions on Electron Devices* 46.7 (1999), pp. 1363–1370.

[185] Farrukh ibne Mahmood and Govindasamy TamizhMani. “Impact of different backsheets and encapsulant types on potential induced degradation (PID) of silicon PV modules”. In: *Solar Energy* 252 (2023), pp. 20–28.

[186] Wei Luo et al. “Potential-induced degradation in photovoltaic modules: a critical review”. In: *Energy & environmental science* 10.1 (2017), pp. 43–68.

[187] Volker Naumann et al. “Explanation of potential-induced degradation of the shunting type by Na decoration of stacking faults in Si solar cells”. In: *Solar Energy Materials and Solar Cells* 120 (2014), pp. 383–389.

[188] Volker Naumann et al. “Microstructural analysis of crystal defects leading to potential-induced degradation (PID) of Si solar cells”. In: *Energy Procedia* 33 (2013), pp. 76–83.

[189] Quratulain Jamil et al. “Experimental investigation of potential induced degradation of poly-crystalline photovoltaic modules: Influence of superstrate and encapsulant types”. In: *Sustainable Energy Technologies and Assessments* 52 (2022), p. 102162.

[190] Djamel Eddine Mansour et al. “Effect of backsheet properties on PV encapsulant degradation during combined accelerated aging tests”. In: *Sustainability* 12.12 (2020), p. 5208.

[191] Kenta Nakayashiki et al. “Engineering solutions and root-cause analysis for light-induced degradation in p-type multicrystalline silicon PERC modules”. In: *IEEE Journal of Photovoltaics* 6.4 (2016), pp. 860–868.

[192] Axel Herguth, Christian Derricks, and David Sperber. “A detailed study on light-induced degradation of Cz-Si PERC-type solar cells: Evidence of rear surface-related degradation”. In: *IEEE Journal of Photovoltaics* 8.5 (2018), pp. 1190–1201.

[193] Ashley E Morishige et al. “Lifetime spectroscopy investigation of light-induced degradation in p-type multicrystalline silicon PERC”. In: *IEEE Journal of Photovoltaics* 6.6 (2016), pp. 1466–1472.

[194] Robert Witteck et al. “UV radiation hardness of photovoltaic modules featuring crystalline Si solar cells with AlOx/p+-type Si and SiNy/n+-type Si interfaces”. In: *physica status solidi (RRL)–Rapid Research Letters* 11.8 (2017), p. 1700178.

[195] Feng Ye et al. “UV-induced degradation in multicrystalline PERC cell and module”. In: *Solar Energy* 170 (2018), pp. 1009–1015.

[196] Robert Witteck et al. “UV-induced degradation of PERC solar modules with UV-transparent encapsulation materials”. In: *Progress in Photovoltaics: Research and Applications* 25.6 (2017), pp. 409–416.

[197] Archana Sinha et al. “UV-induced degradation of high-efficiency silicon PV modules with different cell architectures”. In: *Progress in Photovoltaics: Research and Applications* 31.1 (2023), pp. 36–51.

[198] Kai Sporleder et al. “Local corrosion of silicon as root cause for potential-induced degradation at the rear side of bifacial PERC solar cells”. In: *physica status solidi (RRL)–Rapid Research Letters* 13.9 (2019), p. 1900163.

[199] Kai Sporleder et al. “Root cause analysis on corrosive potential-induced degradation effects at the rear side of bifacial silicon PERC solar cells”. In: *Solar Energy Materials and Solar Cells* 201 (2019), p. 110062.

[200] Achim Kraft et al. “Investigation of acetic acid corrosion impact on printed solar cell contacts”. In: *IEEE Journal of Photovoltaics* 5.3 (2015), pp. 736–743.

[201] Marc Köntges et al. *Assessment of Photovoltaic Module Failures in the Field: International Energy Agency Photovoltaic Power Systems Programme: IEA PVPS Task 13, Subtask 3: Report IEA-PVPS T13-09: 2017*. International Energy Agency, 2017.

[202] Marko Jankovec et al. “In-situ monitoring of moisture ingress in PV modules using digital humidity sensors”. In: *IEEE journal of photovoltaics* 6.5 (2016), pp. 1152–1159.

[203] CR Osterwald and TJ McMahon. "History of accelerated and qualification testing of terrestrial photovoltaic modules: A literature review". In: *Progress in Photovoltaics: Research and Applications* 17.1 (2009), pp. 11–33.

[204] Karl-Anders Weiß, Elisabeth Klimm, and Ismail Kaaya. "Accelerated aging tests vs field performance of PV modules". In: *Progress in Energy* 4.4 (2022), p. 042009.

[205] David C Miller et al. "Degradation in photovoltaic encapsulant transmittance: Results of the first PVQAT TG5 artificial weathering study". In: *Progress in Photovoltaics: Research and Applications* 27.5 (2019), pp. 391–409.

[206] Joshua Morse et al. "Degradation in photovoltaic encapsulant transmittance: Results of the second PVQAT TG5 artificial weathering study". In: *Progress in Photovoltaics: Research and Applications* 30.7 (2022), pp. 763–783.

[207] Peter Hacke et al. "A status review of photovoltaic power conversion equipment reliability, safety, and quality assurance protocols". In: *Renewable and Sustainable Energy Reviews* 82 (2018), pp. 1097–1112.

[208] *ISO 4892-1:2016-05, Plastics - Methods of exposure to laboratory light sources - Part 1: General guidance*. Standard. International Organization for Standardization, 2016.

[209] *ISO 4892-2:2013 + A1:20215, Plastics - Methods of exposure to laboratory light sources - Part 2: Xenon-arc lamps*. Standard. International Organization for Standardization, 2021.

[210] *ISO 4892-3:2016 - Methods of exposure to laboratory light sources - Part 3: Fluorescent UV lamps*. Standard. International Organization for Standardization, 2016.

[211] Bengt Rånby. "Photodegradation and photo-oxidation of synthetic polymers". In: *Journal of Analytical and Applied Pyrolysis* 15 (1989), pp. 237–247.

[212] Stephen J Blanksby and G Barney Ellison. "Bond dissociation energies of organic molecules". In: *Accounts of chemical research* 36.4 (2003), pp. 255–263.

[213] Chiao-Chi Lin et al. "A novel test method for quantifying cracking propensity of photovoltaic backsheets after ultraviolet exposure". In: *Progress in Photovoltaics: Research and Applications* 27.1 (2019), pp. 44–54.

[214] Yoshiyuki Kobayashi et al. "Effect of barrier property of backsheet on degradation of crystalline silicon photovoltaic modules under combined acceleration test composed of UV irradiation and subsequent damp-heat stress". In: *Japanese Journal of Applied Physics* 57.12 (2018), p. 127101.

[215] Peter Hacke et al. "Combined and sequential accelerated stress testing for derisking photovoltaic modules". In: *Advanced micro-and nanomaterials for photovoltaics*. Elsevier, 2019, pp. 279–313.

[216] Michael Owen-Bellini et al. "Advancing reliability assessments of photovoltaic modules and materials using combined-accelerated stress testing". In: *Progress in Photovoltaics: Research and Applications* 29.1 (2021), pp. 64–82.

[217] Michael Wendt et al. "Crosslinking Behavior of Ethylene Vinyl Acetate Copolymer Encapsulants in Dependence of the Additive Composition". In: *Progress in Photovoltaics (accepted)* (2024).

[218] FJ Pern. "Ethylene-vinyl acetate (EVA) encapsulants for photovoltaic modules: Degradation and discoloration mechanisms and formulation modifications for improved photostability". In: *Die Angewandte Makromolekulare Chemie: Applied Macromolecular Chemistry and Physics* 252.1 (1997), pp. 195–216.

[219] Bhuwanesh K Sharma et al. "Effect of vinyl acetate content on the photovoltaic-encapsulation performance of ethylene vinyl acetate under accelerated ultra-violet aging". In: *Journal of Applied Polymer Science* 137.2 (2020), p. 48268.

[220] Wes McKinney. "Data Structures for Statistical Computing in Python". In: *Proceedings of the 9th Python in Science Conference*. Ed. by Stéfan van der Walt and Jarrod Millman. 2010, pp. 56–61.

[221] Charles R. Harris et al. "Array programming with NumPy". In: *Nature* 585.7825 (2020), pp. 357–362.

[222] J. D. Hunter. "Matplotlib: A 2D graphics environment". In: *Computing in Science & Engineering* 9.3 (2007), pp. 90–95.

[223] C Pilorget et al. "Wavelength dependence of scattering properties in the VIS–NIR and links with grain-scale physical and compositional properties". In: *Icarus* 267 (2016), pp. 296–314.

[224] Manuel Nieto-Vesperinas. "Fundamentals of Mie scattering". In: *Dielectric Metamaterials*. Elsevier, 2020, pp. 39–72.

[225] Thomas G Mayerhöfer, Susanne Pahlow, and Jürgen Popp. "The Bouguer-Beer-Lambert law: Shining light on the obscure". In: *ChemPhysChem* 21.18 (2020), pp. 2029–2046.

[226] Wolfgang Demtröder. *Experimentalphysik*. Vol. 2. Springer, 1998.

[227] Richard H Pletcher, John C Tannehill, and Dale Anderson. *Computational fluid mechanics and heat transfer*. CRC press, 1997.

[228] Parviz Moin. *Fundamentals of engineering numerical analysis*. Cambridge University Press, 2010.

[229] Gianluigi Maggioni, A Tessarollo, and SARA Carturan. "Study of the effects of incorporation of UV-absorbing compound in parylene C films". In: *Materials Chemistry and Physics* 149 (2015), pp. 530–538.

[230] Charles M Hansen. "Diffusion in polymers". In: *Polymer Engineering & Science* 20.4 (1980), pp. 252–258.

[231] Shlomo Havlin and Daniel Ben-Avraham. "Diffusion in disordered media". In: *Advances in physics* 36.6 (1987), pp. 695–798.

[232] Florian Müller-Plathe, Stephen C Rogers, and Wilfred F van Gunsteren. "Computational evidence for anomalous diffusion of small molecules in amorphous polymers". In: *Chemical physics letters* 199.3-4 (1992), pp. 237–243.

[233] Ralf Metzler and Joseph Klafter. "The random walk's guide to anomalous diffusion: a fractional dynamics approach". In: *Physics reports* 339.1 (2000), pp. 1–77.

[234] Matthias Jaunich et al. "Investigation of the curing state of ethylene/vinyl acetate copolymer (EVA) for photovoltaic applications by gel content determination, rheology, DSC and FTIR". In: *Polymer Testing* 52 (2016), pp. 133–140.

[235] John H Wohlgemuth, Michael D Kempe, and David C Miller. "Discoloration of PV encapsulants". In: *2013 IEEE 39th Photovoltaic Specialists Conference (PVSC)*. IEEE. 2013, pp. 3260–3265.

[236] Yadong Lyu et al. "Fluorescence imaging analysis of depth-dependent degradation in photovoltaic laminates: insights to the failure". In: *Progress in Photovoltaics: Research and Applications* 28.2 (2020), pp. 122–134.

[237] S Commereuc et al. "In situ detection of hindered amine stabilizer consumption in polymer through oxidation by indirect electron spin resonance". In: *Journal of applied polymer science* 69.6 (1998), pp. 1107–1114.

[238] S Commereuc et al. "A new ESR study of hindered amine stabilisers (HAS) and their oxidation products". In: *Polymer international* 52.4 (2003), pp. 576–580.

[239] J Durmis et al. "Photostabilization of polypropylene by a hindered amine". In: *Journal of Polymer Science: Polymer Letters Edition* 19.11 (1981), pp. 549–554.

[240] JL Gerlock, DR Bauer, and LM Briggs. "Photo-stabilisation and photo-degradation in organic coatings containing a hindered amine light stabiliser. Part I—ESR measurements of nitroxide concentration". In: *Polymer degradation and stability* 14.1 (1986), pp. 53–71.

[241] JL Gerlock, DF Mielewski, and DR Bauer. "Nitroxide decay assay measurements of free radical photo-initiation rates in polyester urethane coatings". In: *Polymer degradation and stability* 26.3 (1989), pp. 241–254.

[242] JL Gerlock, T Riley, and DR Bauer. "Photo-stabilisation and photo-degradation in organic coatings containing a hindered amine light stabiliser: Part II—Consumption of hindered amine". In: *Polymer degradation and stability* 14.1 (1986), pp. 73–84.

[243] DR Bauer and JL Gerlock. "Photo-stabilisation and photo-degradation of organic coatings containing a hindered amine light stabiliser: Part III—Kinetics of stabilisation during free radical oxidation". In: *Polymer degradation and stability* 14.2 (1986), pp. 97–112.

[244] DR Bauer and DF Mielewski. "The role of humidity in the photooxidation of acrylic melamine coatings". In: *Polymer degradation and stability* 40.3 (1993), pp. 349–355.

[245] Bettina Ottersböck, Gernot Oreski, and Gerald Pinter. "Comparison of different microclimate effects on the aging behavior of encapsulation materials used in photovoltaic modules". In: *Polymer Degradation and Stability* 138 (2017), pp. 182–191.

[246] Gernot Oreski, Gernot M Wallner, and RW Lang. "Ageing characterization of commercial ethylene copolymer greenhouse films by analytical and mechanical methods". In: *Biosystems Engineering* 103.4 (2009), pp. 489–496.

[247] Huili Han et al. "Analysis of the degradation of encapsulant materials used in photovoltaic modules exposed to different climates in China". In: *Solar Energy* 194 (2019), pp. 177–188.

[248] Archana Sinha et al. "Glass/glass photovoltaic module reliability and degradation: a review". In: *Journal of Physics D: Applied Physics* 54.41 (2021), p. 413002.

[249] Roger H French et al. *Reliability and Power Degradation Rates of PERC Modules Using Differentiated Packaging Strategies and Characterization Tools*. Tech. rep. Case Western Reserve Univ., Cleveland, OH (United States), 2021.

[250] Max Liggett et al. "Characterization of Field Exposed Photovoltaic Modules Featuring Signs of Contact Degradation". In: *2023 IEEE 50th Photovoltaic Specialists Conference (PVSC)*. IEEE. 2023, pp. 1–3.

[251] Martin Dehli. *Kompendium Technische Thermodynamik*. Springer, 2021.

[252] Arden L Buck. "New equations for computing vapor pressure and enhancement factor". In: *Journal of Applied Meteorology (1962-1982)* (1981), pp. 1527–1532.

[253] AL Buck. "Buck research cr-1a user's manual". In: *Buck Research Instruments: Boulder, CO, USA* (1996).

[254] AL Buck. "Buck research cr-1a user's manual (Appendix 1)". In: *Buck Research Instruments, Colorado* (1996).

[255] Chandany Sen et al. "Buyer aware: Three new failure modes in TOPCon modules absent from PERC technology". In: *Solar Energy Materials and Solar Cells* 272 (2024), p. 112877.

[256] Jiawen Ren et al. "Predicting the lifetime of HJT modules towards the outdoor real-world environment". In: *Solar Energy Materials and Solar Cells* 272 (2024), p. 112885.

[257] Chandany Sen et al. "Accelerated damp-heat testing at the cell-level of bifacial silicon HJT, PERC and TOPCon solar cells using sodium chloride". In: *Solar Energy Materials and Solar Cells* 262 (2023), p. 112554.

[258] Mariacristina Gagliardi and Marco Paggi. "Long-term EVA degradation simulation: Climatic zones comparison and possible revision of accelerated tests". In: *Solar Energy* 159 (2018), pp. 882–897.

[259] Akhilesh Dadaniya and Naresh Varma Datla. "Multilayer backsheet characterization using diffusion experiments and optimization method for water diffusion simulation inside the photovoltaic module". In: *IEEE Journal of Photovoltaics* 10.1 (2019), pp. 306–314.

[260] Shikha Marwaha and Kunal Ghosh. "Analytical modeling of diffusion of moisture in silicon photovoltaic module under damp heat testing condition". In: *Silicon* 14.9 (2022), pp. 4757–4766.

Publications, conference contributions, and supervised theses

Journal articles

[1] Robert Heidrich et al. "Impact of dynamic co-evaporation schemes on the growth of methylammonium lead iodide absorbers for inverted solar cells". In: *Scientific Reports* 12.1 (2022), p. 19167.

[2] Robert Heidrich, Anton Mordvinkin, and Ralph Gottschalg. "Quantification of UV protecting additives in ethylene-vinyl acetate copolymer encapsulants for photovoltaic modules with pyrolysis-gas chromatography-mass spectrometry". In: *Polymer Testing* 118 (2023), p. 107913.

[3] Anton Mordvinkin et al. "Effekte der Zusatzstoffe auf die Trübung und Alterung von Verbundsicherheitsgläsern". In: *Jahrbuch Glasbau 2023* (2023).

[4] Robert Heidrich et al. "Diffusion of UV Additives in Ethylene-Vinyl Acetate Copolymer Encapsulants and the Impact on Polymer Reliability". In: *IEEE Journal of Photovoltaics* (2023).

[5] Robert Heidrich, Anton Mordvinkin, and Ralph Gottschalg. "Spatially resolved degradation analysis of solar modules after combined accelerated aging". In: *2023 IEEE 50th Photovoltaic Specialists Conference (PVSC)*. IEEE. 2023, pp. 1–3.

[6] Robert Heidrich et al. "UV lamp spectral effects on the aging behavior of encapsulants for photovoltaic modules". In: *Solar Energy Materials and Solar Cells* 266 (2024), p. 112674.

[7] Robert Heidrich et al. "From Performance Measurements to Molecular Level Characterization: Exploring the Differences between Ultraviolet and Damp Heat Weathering of Photovoltaics Modules". In: *Solar RRL* 8.10 (2024), p. 2400144.

[8] Robert Heidrich, Anton Mordvinkin, and Ralph Gottschalg. "Spatially Resolved Degradation of Solar Modules in Dependence of the Prevailing Microclimate". In: *IEEE Journal of Photovoltaics* (2024).

[9] Michael Wendt et al. "Crosslinking Behavior of Ethylene Vinyl Acetate Copolymer Encapsulants in Dependence of the Additive Composition". In: *Progress in Photovoltaics (accepted)* (2024).

Conference contributions and invited talks

[1] Robert Heidrich, Anton Mordvinkin, and Ralph Gottschalg. "Quantitative Additivanalyse von PV-Verkapselungsmaterialien". PV Symposium (Poster). 2022.

[2] Robert Heidrich et al. "Dynamic Co-evaporation Schemes and their Impact on the Growth of Methylammonium Lead Iodide Absorbers for Inverted Solar Cells". 8th World Conference on Photovoltaic Energy Conversion (Talk). 2022.

[3] Robert Heidrich, Anton Mordvinkin, and Ralph Gottschalg. "Quantification of Additives within Polymer Films in Photovoltaic Modules". 8th World Conference on Photovoltaic Energy Conversion (Talk). 2022.

[4] Stephan Grosser et al. “Untersuchung der Korrosionsstruktur an massiv korrodierten Querverbindern”. PV Symposium (Poster). 2023.

[5] Robert Heidrich et al. “Untersuchungen zum Einfluss von Verkapselungsmaterialien auf die Moduldegradation”. PV Symposium (Talk). 2023.

[6] Marius Lüdemann et al. “Ortsaufgelöste Charakterisierung von Verkapselungsfolien für Solarzellen”. Thüringer Werkstofftag (Poster). 2023.

[7] Robert Heidrich, Anton Mordvinkin, and Gottschalg Ralph. “Untersuchungen zur Degradationskinetik von UV-Additiven in Verkapselungspolymeren für Solarmodule”. 23. Nachwuchswissenschaftler *innenkonferenz (Talk). 2023.

[8] Robert Heidrich, Anton Mordvinkin, and Gottschalg Ralph. “Spatially Resolved Degradation Analysis of Solar Modules After Combined Accelerated Aging”. 50th IEEE Photovoltaic Specialists Conference (PVSC) (Talk). 2023.

[9] Robert Heidrich et al. “Photovoltaic Encapsulant Aging in Dependence of Different Light Spectra”. 40th EU PVSEC 2023 (Talk). 2023.

[10] Robert Heidrich et al. “Diffusion of Additives in Photovoltaic Encapsulants and the Impact on Polymer Reliability”. NIST/UL Solutions Workshop on Photovoltaic Materials Durability (invited Talk). 2023.

[11] Robert Heidrich. “Polymer additives - curse and blessing for the reliability of photovoltaic modules”. IMWS Materials Insights (invited Talk). 2023.

[12] Robert Heidrich et al. “Polymer Additive - ein zweischneidiges Schwert für die Zuverlässigkeit von Photovoltaikmodulen”. PV Symposium (Poster). 2024.

Supervised theses

[1] Marius Lüdemann. “Ortsaufgelöste Charakterisierung von Verkapselungsfolien für Solarzellen”. MA thesis. Germany: Technische Universität Ilmenau, 2023.

[2] Geming Huang. “Influence of the material combination of backsheet and encapsulant on the degradation of solar modules”. MA thesis. Germany: Technische Universität Chemnitz, 2024.

[3] Lasse Baldauf. “Korrelation ortsaufgelöster Polymerdegradation mit Veränderungen der Leistungscharakteristik künstlich gealterter Solarmodule”. MA thesis. Germany: Otto-von-Guericke-Universität Magdeburg, 2024.

[4] Michael Wendt. “Vernetzungsverhalten von Ethylen - Vinylacetat - Copolymer (EVA) in Abhängigkeit der Additivzusammensetzung”. MA thesis. Germany: Hochschule Schmalkalden, 2024.

Awards

[1] Robert Heidrich, Anton Mordvinkin, and Ralph Gottschalg. “23. Nachwuchswissenschaftler *innenkonferenz”. Best presentation award - 3rd price. 2023.

[2] Robert Heidrich. “Fraunhofer IMWS and Schott AG - doctoral students seminar”. Best presentation award - 1st price. 2023.

[3] Robert Heidrich et al. “39. Symposium Photovoltaische Energie”. Best poster award - 2nd price. 2024.

Acknowledgments

I want to take this opportunity to thank the many supporters without whom this work could not have been completed. First and foremost, I would like to thank Prof. Dr. Ralph Gottschalg. I was accompanied from my unsolicited application to the Fraunhofer CSP to the completion of my dissertation. In addition to academic support, my personal development and future plans were always at the forefront. Furthermore, I thank the reviewers and the doctoral committee for their time and critical examination of my work.

I thank Dr. Sylke Meyer and Dr. Anton Mordvinkin for their trust in me and the good working atmosphere under their guidance. Although the project work is generally very goal-oriented, I was always given absolute freedom to find solutions and to choose various research topics. I would also like to thank all the members of the materials and processes working group - Michael, Basti, Mandy, Susi, Stefanie, Daniel, Patrick, and Jishnu, thank you for enriching my working days with your company.

Additionally, I would like to thank all the other Fraunhofer CSP employees. In particular, I would like to mention the members of my Mensa group: Paul, Matthias, Ulli (not a member of the Mensa Alliance, but fits in well here), Jens, Ringo, and Manuel. You have brought a lot of joy to my everyday work. I would also like to thank Uwe for preparing the countless mini-modules of my research work and Stephan for the microstructure investigations and the long discussions about the interpretation.

I owe thanks to my Master's students Marius, Geming, and Lasse for their trust, good cooperation, and contribution to this work's success.

This work would not have been possible in this form without the cooperation of other research institutes. I thank PD Dr. Gernot Oreski and Dr. Chiara Barretta from the PCCL for allowing me to learn much from them in two months as a visiting researcher. I would also like to thank my colleagues Camille Bainier, Dr. Simon Pondaven, Dr. Nikola Babic, and Dr. Oscar Lacroix Andrivet from TotalEnergies. On the one hand, for financing my work, for their trust, and for giving me the necessary scientific freedom. On the other hand, for joint analyses and stimulating discussions.

I want to thank my friends Johannes, Benji, Britta and Frances. We supported each other throughout our studies until the completion of this thesis so that acquaintances turned into long-term friendships. I also thank all the other friends and acquaintances who enriched my life during my doctoral studies. Even if there is not enough space to mention them all by name, everyone is welcome to feel addressed!

Lastly, I thank my family for their constant support and trust. I am particularly indebted to my wife, Wiebke. You have supported me unconditionally in every one of my goals. Without you, I would not be where I am today. I would also like to thank my daughter Emmi, who has shown me that even the most significant scientific problems can quickly become insignificant.

Statutory declaration / Eidesstattliche Erklärung

Hiermit versichere ich, die vorliegende Arbeit selbständig und ohne unzulässige fremde Hilfe angefertigt zu haben. Ich habe keine anderen als die angeführten Quellen und Hilfsmittel benutzt und sämtliche Textstellen, die wörtlich oder sinngemäß aus veröffentlichten oder unveröffentlichten Schriften entnommen wurden, als solche kenntlich gemacht. Ich erkläre, keine anderweitigen Promotionsversuche unternommen und die vorliegende Dissertation weder in der jetzigen noch in einer anderen Fassung einer anderen wissenschaftlichen Einrichtung vorgelegt zu haben.

Halle (Saale), 06.09.2024

Supporting information for

From performance measurements to molecular level characterization: Exploring the differences between UV and DH weathering of PV modules

Robert Heidrich[B,C,*,†], *Nikola Babić*[A,H,#,†], *Oscar Lacroix-Andrivet*[A,E,†], *Charles-Emmanuel Dutoit*[G,H], *Camille Bainier*[D], *Anton Mordvinkin*[B], *Ralph Gottschalg*[B,C], *Hervé Vezin*[G,H], *Carlos Afonso*[E,I], *Simon Pondaven*[A,H]

A: TotalEnergies OneTech, Centre de Recherche de Solaize (CRES), Chemin du canal, BP 22, 69360 Solaize, France

B: Fraunhofer CSP, Otto-Eissfeldt-Strasse 12, 06120 Halle (Saale), Germany

C: Anhalt University of Applied Sciences, Bernburger Strasse 55, 06336 Koethen (Anhalt), Germany

D: TotalEnergies OneTech, R&D Power, 7-9 Boulevard Thomas Gobert, 91120, Palaiseau, France

E: International Joint Laboratory—iC2MC: Complex Matrices Molecular Characterization, TRTG, BP 27, 76700 Harfleur, France

G: Université Lille Nord de France, CNRS UMR8516, Laboratoire Avancé de Spectroscopie pour les Interactions, la Réactivité et l'Environnement (LASIRE), 59655 Villeneuve d'Ascq, France

H: Joint Laboratory—CR2ME: Centre de Résonance Magnétique Électronique pour les Matériaux et l' Énergie, 59655 Villeneuve d'Ascq, France

I. Normandie Univ, COBRA, UMR6014 and FR3038, Université de Rouen, INSA de Rouen, CNRS, IRCOF, 1 rue Tesnière, 76821, Mont-Saint-Aignan Cedex, France

† These authors contributed equally to this work and share first authorship

E-mail: *robert.heidrich@csp.fraunhofer.de; #nikola.babic@totalenergies.com

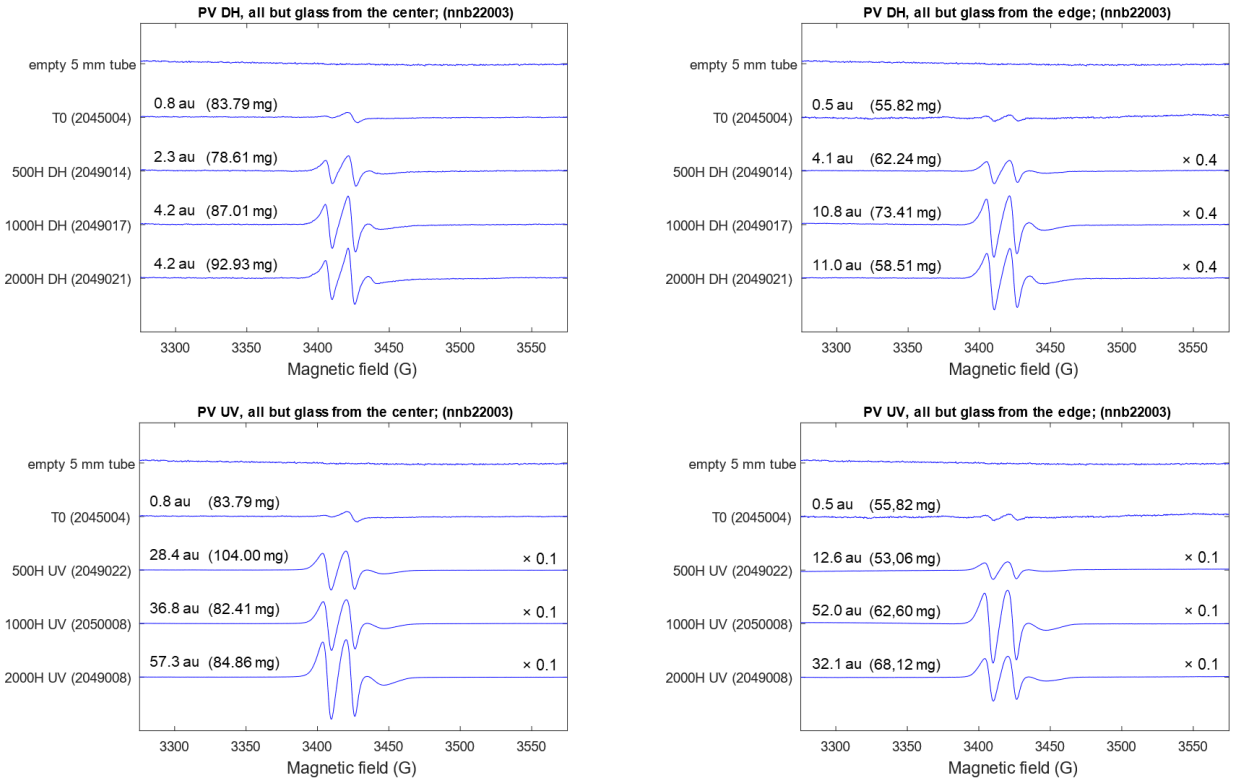

Figure S1. EPR spectra of all samples, as measured (not normalized by mass), with $NO^{\bullet}$ central line peak-to-peak height (A.U.) and mass of each sample.

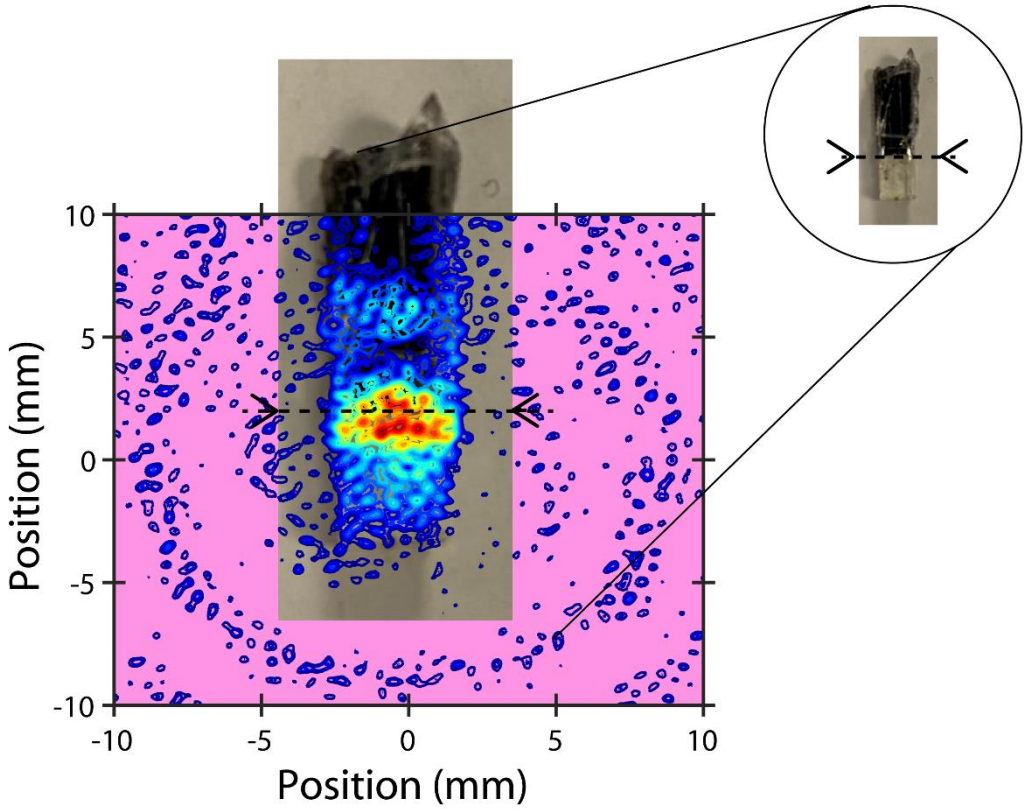

Figure S2. Second sample used for EPR imaging representing 2D map of spatial distribution of nitroxide radical within a cutout piece of the mini-module (5.0 × 17 mm). The relative abundance of nitroxide radical is presented as a color scale.

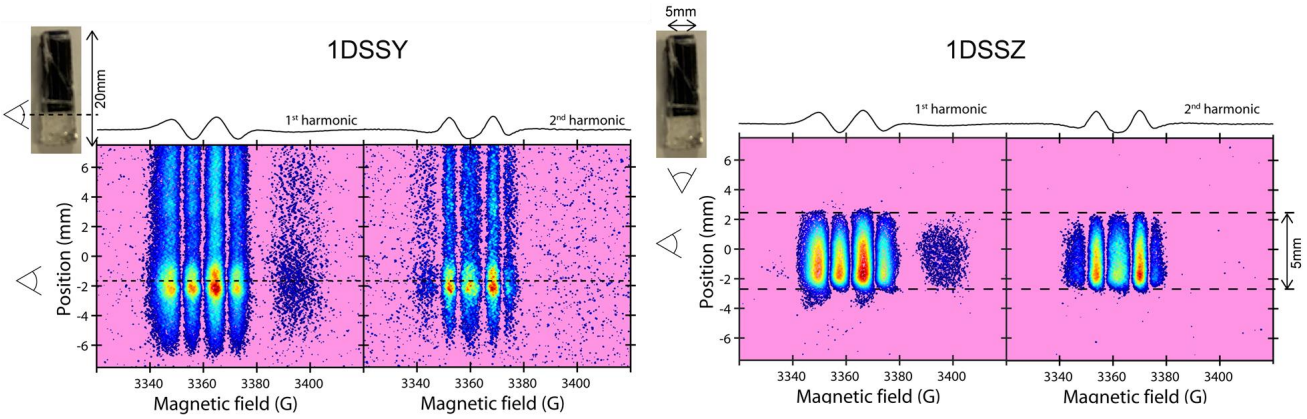

Figure S3.: 1D-spectral/spatial EPR image of Sample 1.

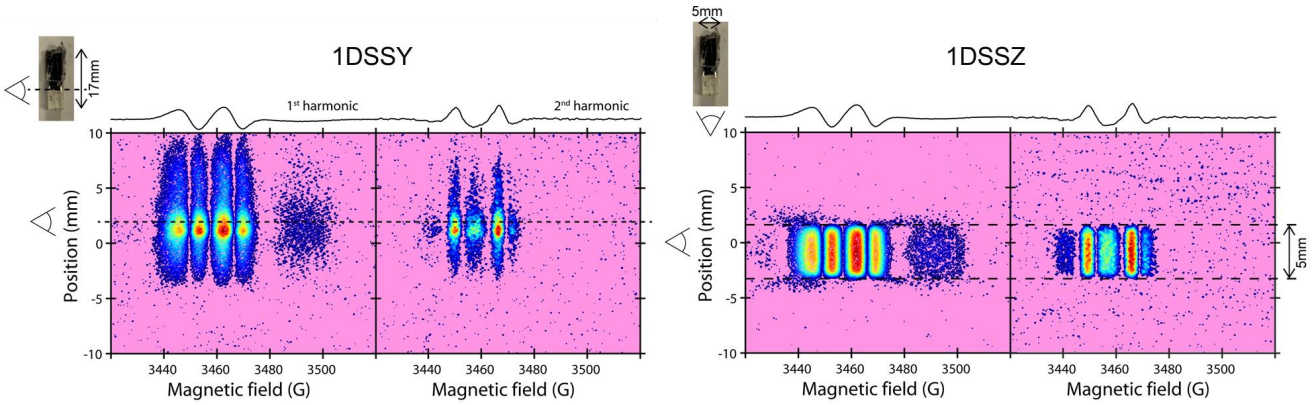

Figure S4.: 1D-spectral/spatial EPR image of Sample 2.

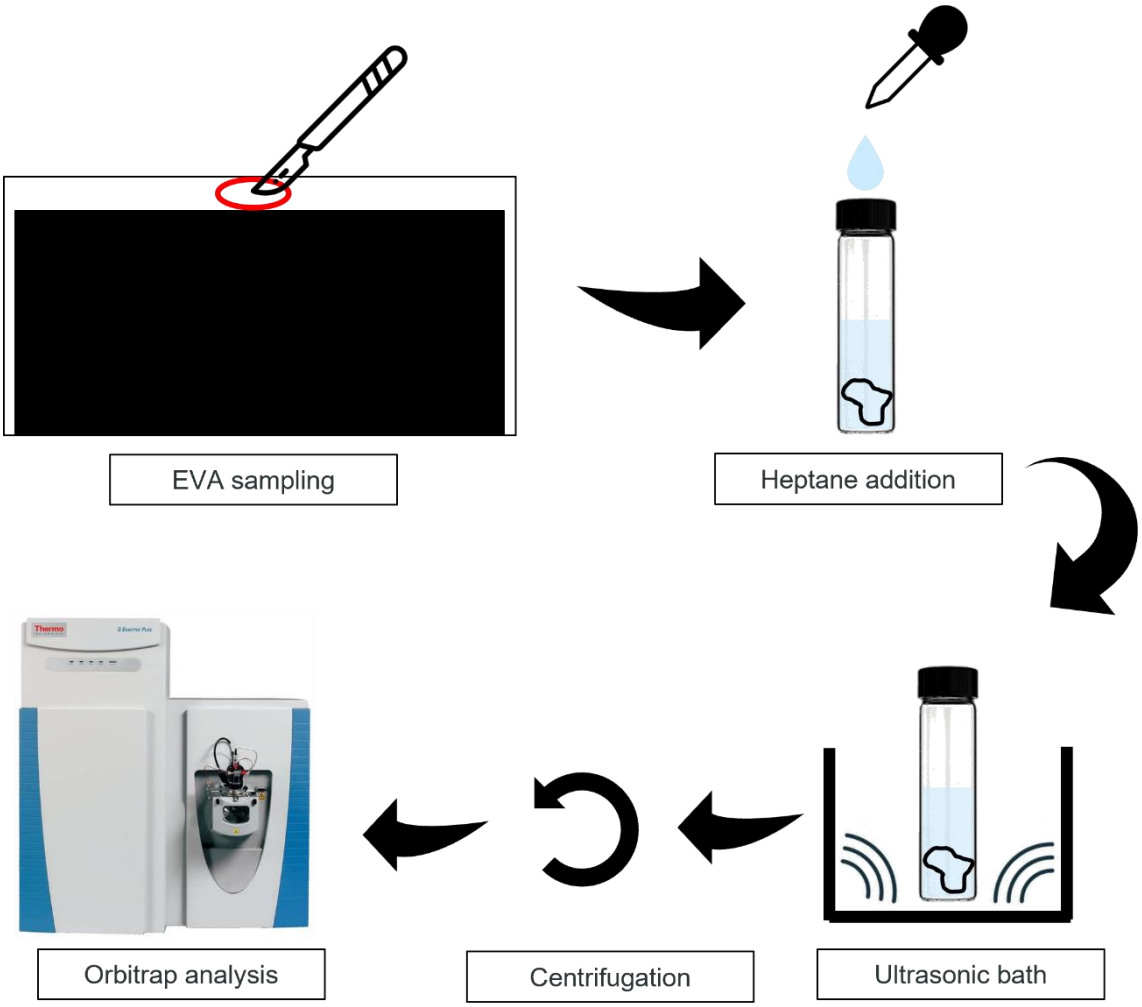

Figure S5. Scheme of sample preparation prior to Orbitrap mass spectrometry analysis

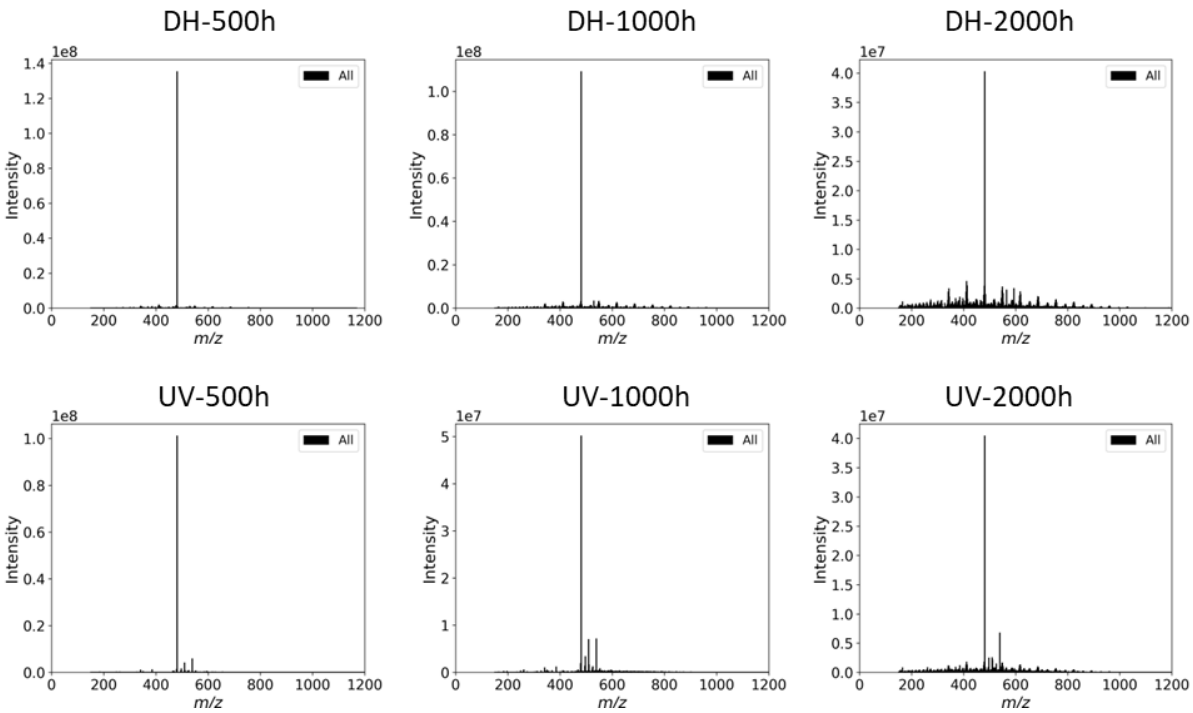

Figure S6. APCI(+)-Orbitrap mass spectra of DH and UV aged mini-modules.

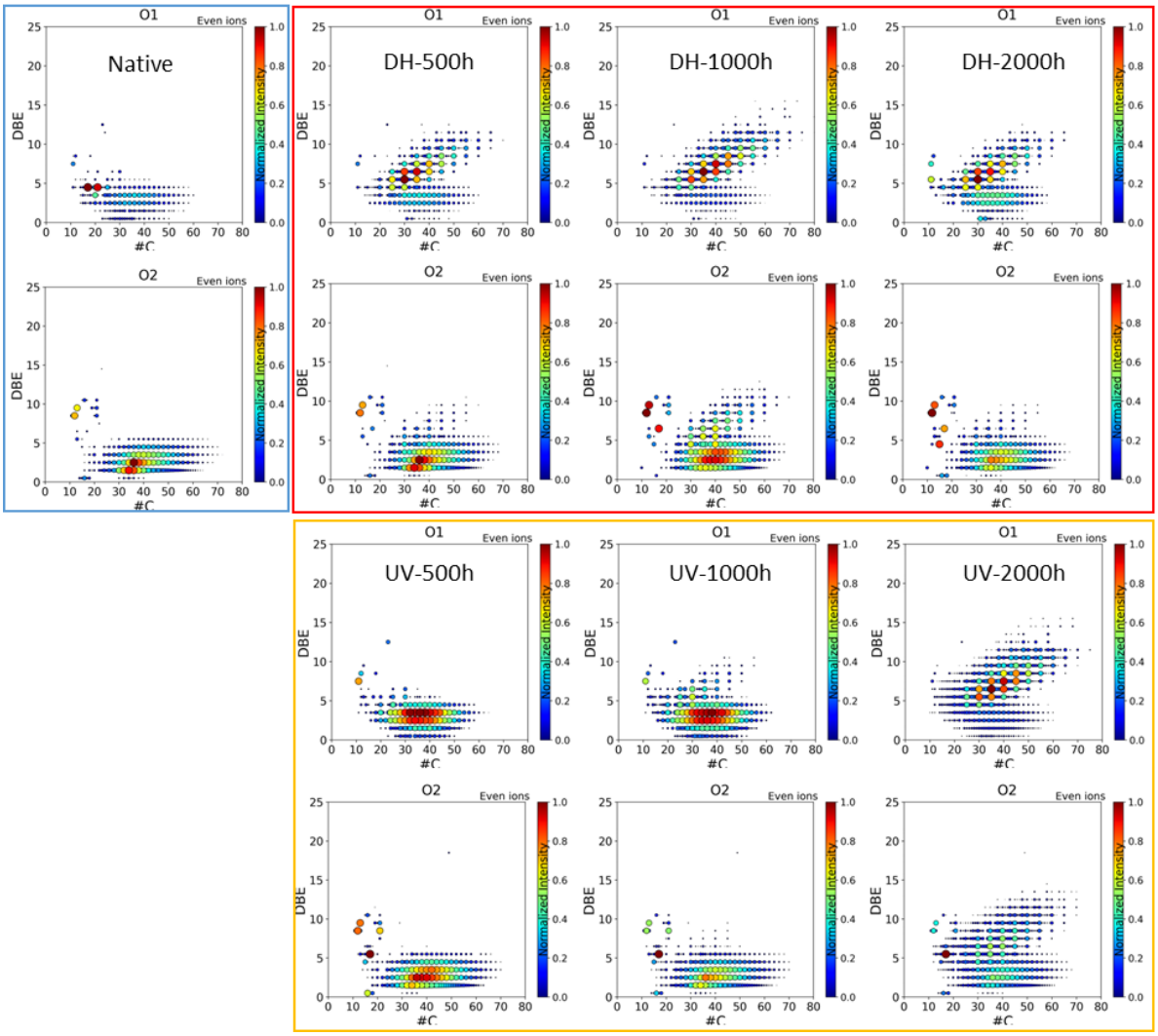

Figure S7. DBE vs C# maps for O_1 and O_2 compound classes obtained for all aging times

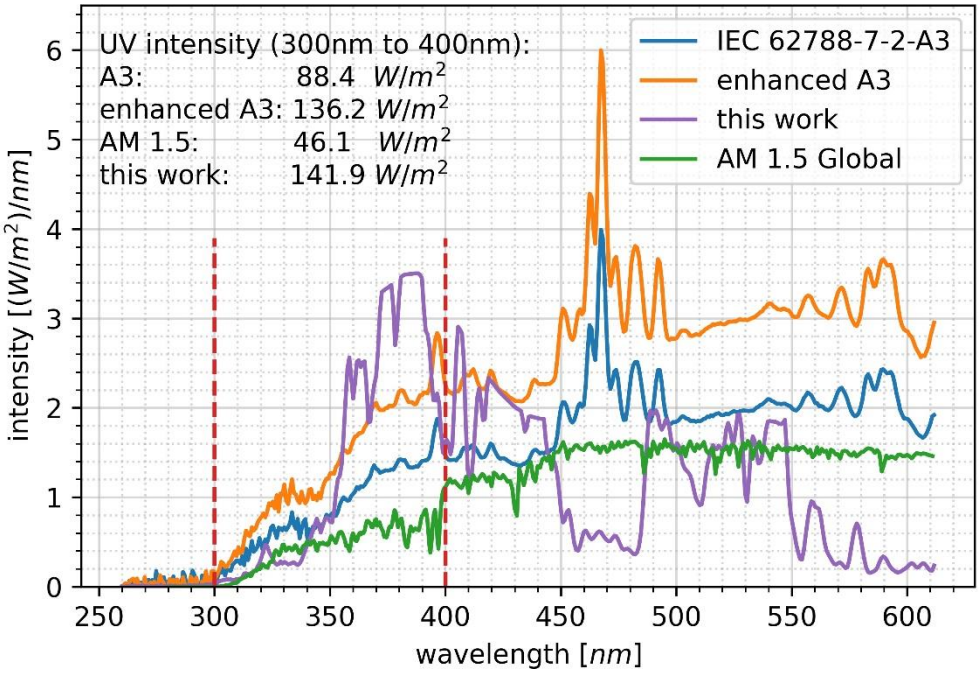

Figure S8. Example spectrum of the weathering chamber (purple) in comparison with the spectra used in our previous work (Heidrich, Robert, et al. "UV lamp spectral effects on the aging behavior of encapsulants for photovoltaic modules." Solar Energy Materials and Solar Cells 266 (2024): 112674.). The curve represents one of the lowest intensities in the chamber while the mean UV dose between 300nm and 400 nm is 175 W/m² ± 35 W/m².

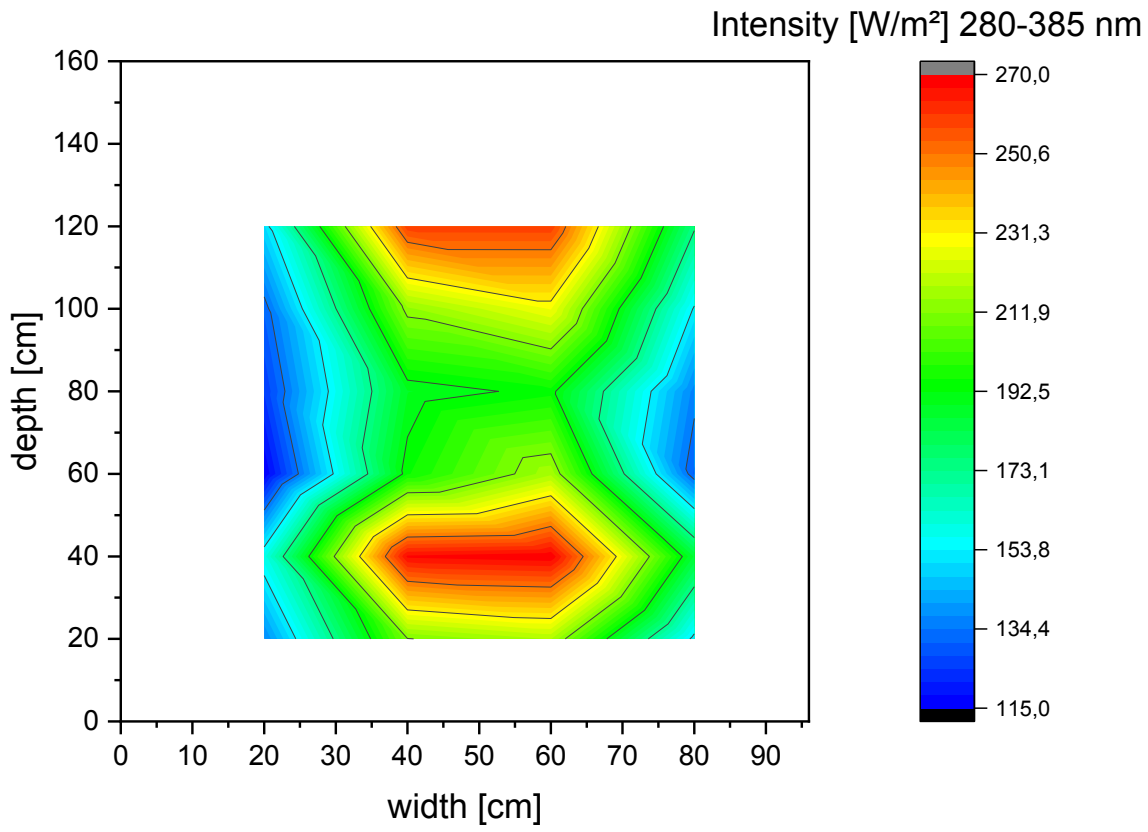

Figure S9. Intensity homogeneity inside the weathering chamber. The intensity values do not correspond to the intensities used for this weathering series. All samples have been placed inside the homogeneous green area between the two red areas.

Supporting Information

Quantification of UV protecting additives in ethylene-vinyl acetate copolymer encapsulants for photovoltaic modules with pyrolysis-gas chromatography-mass spectrometry

Robert Heidrich [a,b], Anton Mordvinkin [a], Ralph Gottschalg [a,b]

[a] *Fraunhofer CSP, Otto-Eißfeldt-Straße 12, Halle (Saale), 06120, Germany*
[b] *Anhalt University of Applied Sciences, Bernburger Str. 55, Koethen (Anhalt), 06366, Germany*

1. DSC measurements

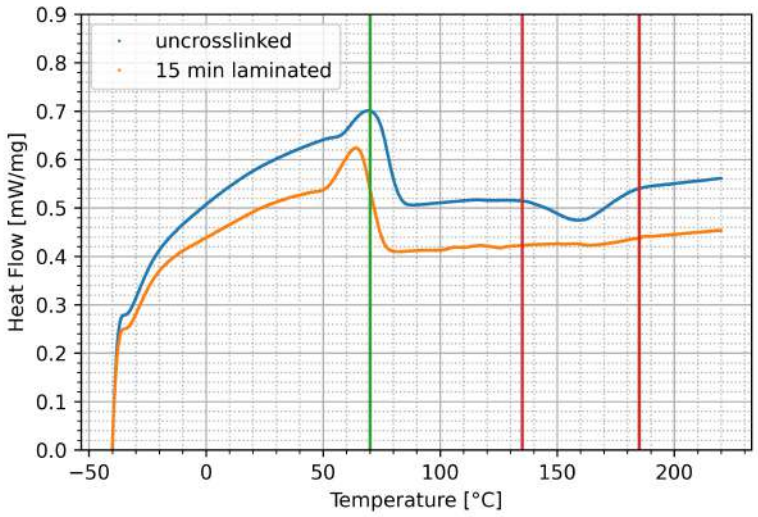

Figure 1: Comparison of the DSC measurements after 15 min lamination (orange line) and withouth lamination (uncrosslinked, blue line). The green line indicates the sample preparation temperature of the kneader and the hydraulic press, the area between the red lines shows the change in heat flow due to the crosslinking. The investigated sample is admixed with the same crosslinking additives as the quantification samples of own production.

As proposed in the article, DSC measurements have been carried out to determine the required thermal activation energy for the crosslinking additives. Figure 1 displays the DSC measurements for an uncrosslinked sample and after 15 min of lamination. The sample is using the same crosslinking additives as the reference samples of own production. The measurements show a

drop in heat flow from approximately 135 °C to 185 °C in the uncrosslinked case. Here, less thermal energy is absorbed due to crosslinking reactions. This reaction was already finished during lamination for the orange curve. Therefore there is no drop in heat flow. The combination of DSC and GCMS measurements shows that there is no crosslinking reaction occurring at the used temperatures in the kneader and the hydraulic press.

2. MS intensity for different measurement series

Figure 2 lists 5 different PY-GCMS measurement series of the Cyasorb UV 531 intensity of the same polymer film sample ($1c_0$ of the verification batch). Although the MS tuning was always carried out in the same way, the tune values differ in dependence of the ion source condition. Therefore, the measured intensities varied for every measurement. This property of the MS makes the use of calibration samples indispensable.

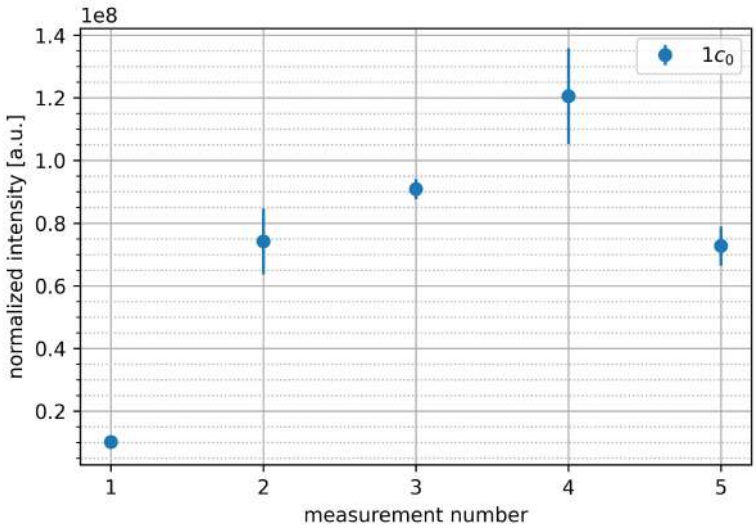

Figure 2: 5 PY-GCMS measurements of the Cyasorb UV 531 intensity (each in triple determination) of the same polymer film. The measured intensity is diverging between all measurements in dependence of the MS tune values and the condition of the ion source.

3. Calibration functions based on pure substances

The calibration functions were developed measuring pure substances in an n-hexane solution (SupraSolv MS-grade). The base solution was prepared by weighing 15 mg of the corresponding additive into a 25 ml measurement flask. Afterwards the flask was topped with n-hexane and slewed until the dissolving was complete. With a micro liter syringe volumes of 1 µl to 10 µl have been extracted into sample cups with 3 measurements per volume respectively. Previous experiments showed that the deposited masses in the sample cups generate intensities similar to values gained by 4 mg EVA films (average sample mass) with imbedded additives. The laboratory error was estimated with propagation of uncertainty and is displayed in detail in the next chapter.

In the subsequent quantification passages the laboratory uncertainty of the measurements was combined with the standard deviation respectively creating a total uncertainty.

Figure 3 is presenting the resulting calibration curves. As proposed in the article the linear proportionality of measured MS intensity and corresponding sample mass can be assumed. Displayed measurement points are mean values of 3 measurements respectively. Error bars show the combined uncertainty of laboratory uncertainty and standard deviation. For Cyasorb UV 531 only the characteristic m/z=213 peak was evaluated while for Tinuvin 770 the full spectrum was used.

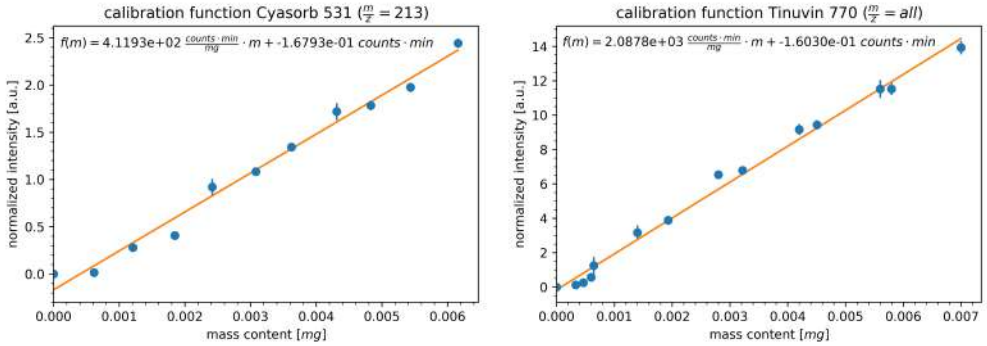

Figure 3: Calibration functions for Cyasorb UV 531 (left) and Tinuvin 770 (right) based on pure substances. For Cyasorb UV 531 the m/z=213 peak was evaluated while for Tinuvin 770 all m/z ratios have been used.

For fitting the calibration function the least squares method was used leading to a calibration function $f_{C_P}(m)$ for Cyasorb UV 531 and $f_{T_P}(m)$ for Tinuvin 770:

$$f_{C_P}(m) = 4.1193 \cdot 10^2 \left[\frac{1}{\text{mg}}\right] \cdot m - 1.6793 \cdot 10^{-1} \tag{1}$$

$$f_{T_P}(m) = 2.0878 \cdot 10^3 \left[\frac{1}{\text{mg}}\right] \cdot m - 1.6030 \cdot 10^{-1} \tag{2}$$

The derived pure-substance-based calibration functions were applied on the verification polymer film samples while the corresponding additive mass fraction is displayed in Figure 4. Here, the comparison between film-based and pure-substance-based calibration function suggests differences in the desorption behavior of polymer film samples and pure substances. These differences are probably caused by polymer matrix interactions which decrease the number of particles desorbing from polymer films at given temperatures while these interactions are missing for pure substances. Comparing the measured mass fraction and real mass fraction, the difference in slope impedes a simple offset correction. While an additive quantification with pure-substance-based calibration functions is comparatively fast and cheap, it cannot provide results with acceptable accuracy.

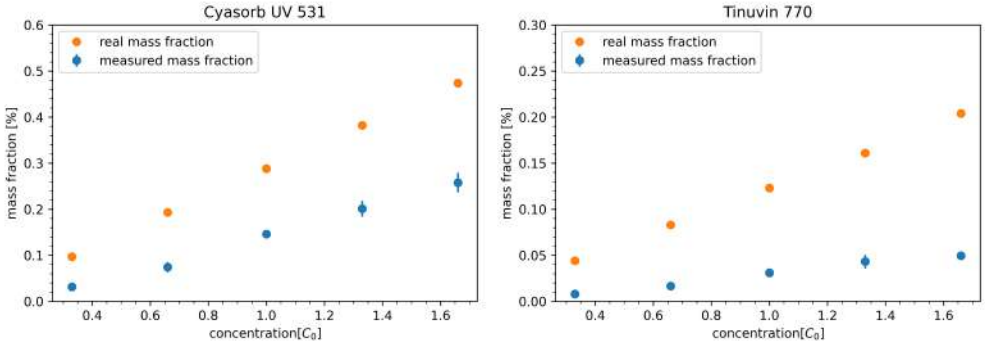

Figure 4: Measured and real UV-absorber and UV-stabilizer mass fractions on basis of the pure substance derived calibration functions.

4. Estimated laboratory error for pure substance GCMS measurements

The laboratory error was estimated with propagation of uncertainty due to the different preparation steps with $u_{m_w} = 0.2\,\text{mg}$ as weighing uncertainty, $u_{V_f} = 0.12\,\text{ml}$ as flask volume uncertainty and $u_{V_s} = 0.1\,\mu\text{l}$ as syringe uncertainty. As mentioned it was assumed that the measured intensity I is proportional to the sample mass m, therefore the uncertainty of the measured intensity ΔI is proportional to the uncertainty of the sample mass Δm. It follows

$$\Delta I \sim \Delta m = \Delta\left(\frac{m_w V_s}{V_f}\right) = \sqrt{\sum_{i=1}^{n}\left(\frac{\partial m}{\partial x_i}u_i\right)^2} \tag{3}$$

with x_i and as dependent variables of m and their uncertainties u_i and therefore

$$\Delta m = \sqrt{\left(\frac{V_s}{V_f}u_{m_w}\right)^2 + \left(\frac{m_w}{V_f}u_{V_f}\right)^2 + \left(-\frac{m_w V_s}{V_f^2}u_{V_f}\right)^2}. \tag{4}$$

It is obvious that Equation 4 is a function of the syringe volume V_s because the other quantities are constant.

Figure 5 is visualizing the relative sample mass uncertainty in dependence of the syringe volume. For small sample volumes the relative sample mass uncertainty ($\Delta m/m$) should be taken into account for quantification processes while it could be neglected for larger syringe volumes. In the carried out quantification processes for pure substances, the laboratory uncertainty of the measurements was combined with the standard deviation respectively creating a total uncertainty.

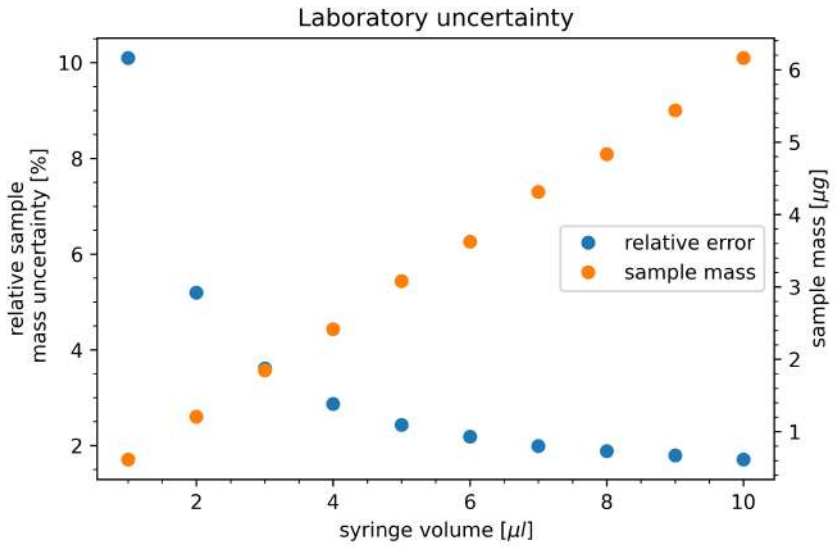

Figure 5: Relative sample mass uncertainty and sample mass in dependence of the used micro liter syringe volume. The relative sample mass uncertainty can be neglected for syringe volumes above 3 µl.

5. EVA film preparation

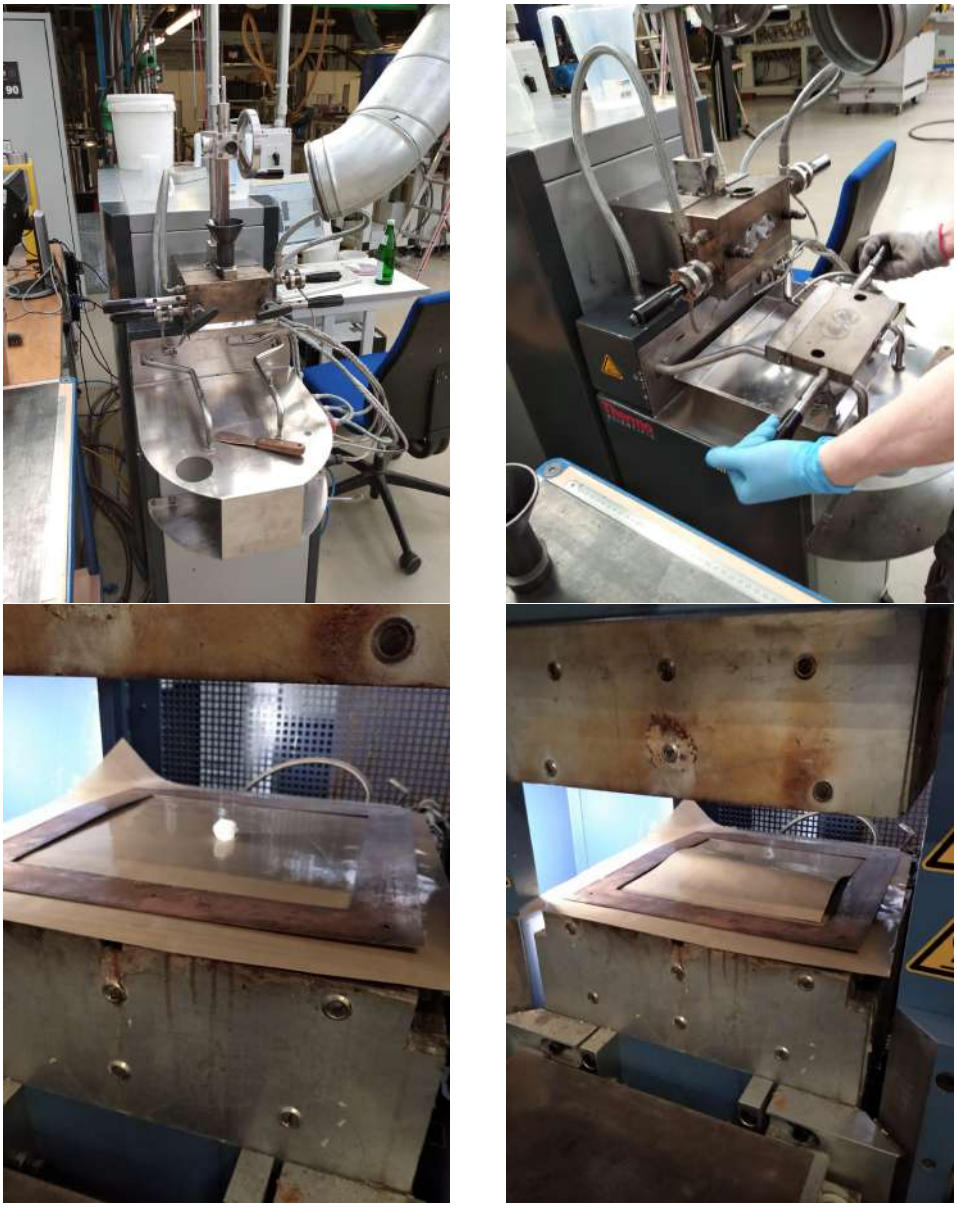

Figure 6: The top images show the kneader with the fabricated polymer melt after the kneading process. The pressing process is exemplary displayed in the bottom pictures.

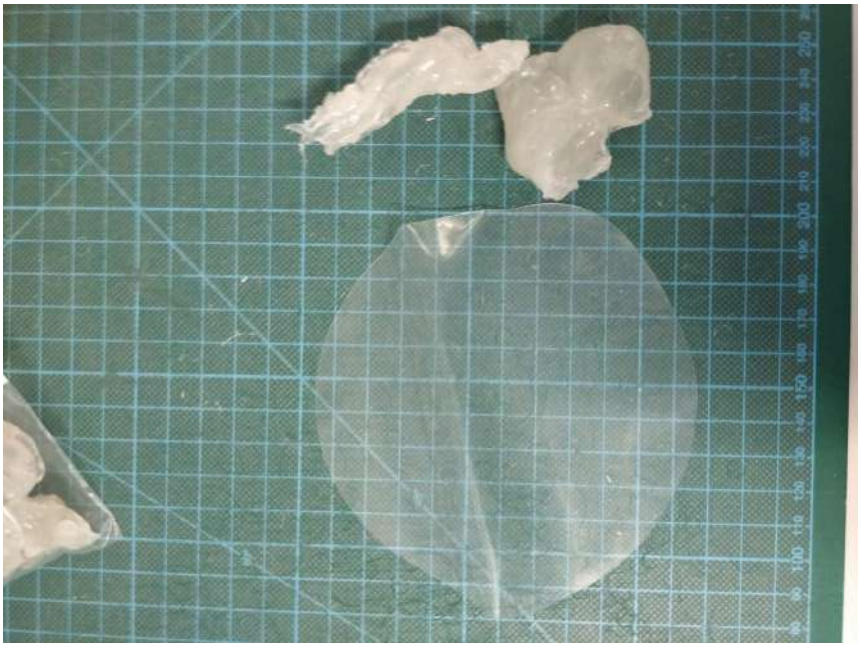

Figure 7: The resulting polymer chunks (top of the image) after the kneading process were pressed to polymer films (bottom of the image) for further investigation and quantification.

6. Used chemicals

chemical	supplier	CAS number
ELVAX 150W	Safic Alcan Germany (DOW)	
Cyasorb UV 531	Sigma Aldrich	1843-05-6
Tinuvin 770	Sigma Aldrich	52829-07-9
Luperox TBEC	Sigma Aldrich	34443-12-4
Perkalink 301	Sigma Aldrich	1025-15-6
Silan A 174	Sigma Aldrich	2530-85-0

7. Used polymer film compositions for calibration functions

$1/4c_0$	mass [g]	mass fraction [%]
ELVAX 150W	25,002+25,015	94,92693111
Cyasorb UV 531	0,038	0,072119947
Tinuvin 770	0,017	0,032264187
Luperox TBEC	0,749	1,42152211
Perkalink 301	1,267	2,40463086
Silan A 174	0,602	1,14253179
total	52,69	100

$1/2c_0$	mass [g]	mass fraction [%]
ELVAX 150W	25,003+25,001	94,84285796
Cyasorb UV 531	0,075	0,142252907
Tinuvin 770	0,032	0,060694574
Luperox TBEC	0,756	1,4339093
Perkalink 301	1,244	2,359501546
Silan A 174	0,612	1,160783719
total	52,723	100

$3/4c_0$	mass [g]	mass fraction [%]
ELVAX 150W	24,986+25,003	94,74252791
Cyasorb UV 531	0,114	0,216060497
Tinuvin 770	0,049	0,092868108
Luperox TBEC	0,758	1,436612778
Perkalink 301	1,249	2,367189129
Silan A 174	0,604	1,14474158
total	52,763	100

$1c_0$	mass [g]	mass fraction [%]
ELVAX 150W	24,988+24,999	94,65083693
Cyasorb UV 531	0,15	0,284026358
Tinuvin 770	0,066	0,124971597
Luperox TBEC	0,748	1,41634477
Perkalink 301	1,252	2,370673332
Silan A 174	0,609	1,153147012
total	52,812	100

$5/4c_0$	mass [g]	mass fraction [%]
ELVAX 150W	24,999+25,01	94,59040269
Cyasorb UV 531	0,187	0,353704439
Tinuvin 770	0,083	0,15699181
Luperox TBEC	0,748	1,414817757
Perkalink 301	1,24	2,345419811
Silan A 174	0,602	1,138663489
total	52,869	100

$3/2c_0$	mass [g]	mass fraction [%]
ELVAX 150W	25,008+25,003	94,48873942
Cyasorb UV 531	0,225	0,425105804
Tinuvin 770	0,097	0,183267836
Luperox TBEC	0,75	1,417019347
Perkalink 301	1,24	2,34280532
Silan A 174	0,605	1,143062273
total	52,928	100

$7/4c_0$	mass [g]	mass fraction [%]
ELVAX 150W	25,005+25,005	94,38342204
Cyasorb UV 531	0,261	0,492582946
Tinuvin 770	0,115	0,217038463
Luperox TBEC	0,753	1,42113011
Perkalink 301	1,245	2,349677273
Silan A 174	0,602	1,136149171
total	52,986	100

$2c_0$	mass [g]	mass fraction [%]
ELVAX 150W	25,014+25,005	94,26697574
Cyasorb UV 531	0,3	0,565387007
Tinuvin 770	0,132	0,248770283
Luperox TBEC	0,754	1,421006012
Perkalink 301	1,252	2,359548444
Silan A 174	0,604	1,138312508
total	53,061	100

$9/4c_0$	mass [g]	mass fraction [%]
ELVAX 150W	25,0+25,009	94,16826724
Cyasorb UV 531	0,337	0,634579897
Tinuvin 770	0,148	0,278687907
Luperox TBEC	0,75	1,4122698
Perkalink 301	1,255	2,363198132
Silan A 174	0,607	1,142997025
total	53,106	100

$5/2c_0$	mass [g]	mass fraction [%]
ELVAX 150W	25,003+25,01	94,07659606
Cyasorb UV 531	0,375	0,705391069
Tinuvin 770	0,162	0,304728942
Luperox TBEC	0,756	1,422068395
Perkalink 301	1,245	2,341898348
Silan A 174	0,611	1,149317181
total	53,162	100

8. Used polymer film compositions for validation

$1/3c_0$	mass [g]	mass fraction [%]
ELVAX 150W	24,994+25,0	94,87247609
Cyasorb UV 531	0,051	0,096781539
Tinuvin 770	0,023	0,043646577
Luperox TBEC	0,752	1,427053287
Perkalink 301	1,273	2,41574313
Silan A 174	0,603	1,144299378
total	52,696	100

$2/3c_0$	mass [g]	mass fraction [%]
ELVAX 150W	25,004+24,995	94,77585063
Cyasorb UV 531	0,102	0,193346602
Tinuvin 770	0,044	0,083404417
Luperox TBEC	0,75	1,421666193
Perkalink 301	1,243	2,35617477
Silan A 174	0,617	1,169557388
total	52,755	100

$1c_0$	mass [g]	mass fraction [%]
ELVAX 150W	24,994+25,018	94,65157652
Cyasorb UV 531	0,152	0,287671751
Tinuvin 770	0,065	0,123017525
Luperox TBEC	0,754	1,427003293
Perkalink 301	1,248	2,361936485
Silan A 174	0,607	1,148794428
total	52,838	100

$4/3c_0$	mass [g]	mass fraction [%]
ELVAX 150W	24,996+25,004	94,55191846
Cyasorb UV 531	0,202	0,381989751
Tinuvin 770	0,085	0,160738261
Luperox TBEC	0,748	1,4144967
Perkalink 301	1,247	2,358124846
Silan A 174	0,599	1,132731983
total	52,881	100

$5/3c_0$	mass [g]	mass fraction [%]
ELVAX 150W	25,005+25,016	94,41487354
Cyasorb UV 531	0,251	0,473763684
Tinuvin 770	0,108	0,20385051
Luperox TBEC	0,748	1,41185353
Perkalink 301	1,247	2,353718384
Silan A 174	0,605	1,141940355
total	52,98	100

C. Mass fractions for further additive quantifications

UV additive quantification by PY-GCMS in POE

chemical	supplier	CAS number
Engage PV 8669	DOW	
Cyasorb UV 531	Sigma Aldrich	1843-05-6
Tinuvin 770	Sigma Aldrich	52829-07-9
Luperox TBEC	Sigma Aldrich	34443-12-4
Perkalink 301	Sigma Aldrich	1025-15-6
Silane A 174	Sigma Aldrich	2530-85-0

$1/4c_0$	mass [g]	mass fraction [%]
Engage PV 8669	50.01	99.00421674
Cyasorb UV 531	0.04	0.079187536
Tinuvin 770	0.013	0.025735949
Luperox TBEC	0.148	0.292993883
Perkalink 301	0.15	0.29695326
Silane A 174	0.152	0.300912636
total	50.513	100

$1/2c_0$	mass [g]	mass fraction [%]
Engage PV 8669	50.013	98.8809585
Cyasorb UV 531	0.081	0.160145515
Tinuvin 770	0.026	0.051404733
Luperox TBEC	0.156	0.308428399
Perkalink 301	0.153	0.302497084
Silane A 174	0.15	0.296565768
total	50.579	100

$3/4c_0$	mass [g]	mass fraction [%]
Engage PV 8669	50.004	98.75772717
Cyasorb UV 531	0.12	0.236999585
Tinuvin 770	0.039	0.077024865
Luperox TBEC	0.159	0.31402445
Perkalink 301	0.148	0.292299488
Silane A 174	0.163	0.321924437
total	50.633	100

$1c_0$	mass [g]	mass fraction [%]
Engage PV 8669	49.999	98.71860686
Cyasorb UV 531	0.15	0.296161744
Tinuvin 770	0.052	0.102669405
Luperox TBEC	0.149	0.294187332
Perkalink 301	0.146	0.288264097
Silane A 174	0.152	0.300110567
total	50.648	100

$5/4c_0$	mass [g]	mass fraction [%]
Engage PV 8669	49.985	98.58779906
Cyasorb UV 531	0.189	0.372773713
Tinuvin 770	0.065	0.1282026
Luperox TBEC	0.15	0.295852153
Perkalink 301	0.154	0.303741544
Silane A 174	0.158	0.311630934
total	50.701	100

$3/2c_0$	mass [g]	mass fraction [%]
Engage PV 8669	50.019	98.48974127
Cyasorb UV 531	0.23	0.452880715
Tinuvin 770	0.077	0.151616587
Luperox TBEC	0.148	0.291418895
Perkalink 301	0.159	0.313078407
Silane A 174	0.153	0.301264128
total	50.786	100

Crosslinking additive quantification by PY-GCMS in EVA - Luperox TBEC

chemical	supplier	CAS number
ELVAX 150W	Safic Alcan Germany (DOW)	
Cyasorb UV 531	Sigma Aldrich	1843-05-6
Tinuvin 770	Sigma Aldrich	52829-07-9
Luperox TBEC	Sigma Aldrich	34443-12-4
Perkalink 301	Sigma Aldrich	1025-15-6
Silane A 174	Sigma Aldrich	2530-85-0

Calibration samples

$1/3c_0$	mass [g]	mass fraction [%]
ELVAX 150W	180.016	97.12115327
Cyasorb UV 531	0.541	0.291877077
Tinuvin 770	0.234	0.126246277
Luperox TBEC	0.906	0.488799689
Perkalink 301	1.498	0.808191981
Silane A 174	2.157	1.16373171
total	185.352	100

$1/2c_0$	mass [g]	mass fraction [%]
ELVAX 150W	180.032	96.50447862
Cyasorb UV 531	0.549	0.294286342
Tinuvin 770	0.234	0.125433523
Luperox TBEC	1.351	0.724190981
Perkalink 301	2.232	1.196442834
Silane A 174	2.155	1.1551677
total	186.553	100

$1c_0$	mass [g]	mass fraction [%]
ELVAX 150W	180.022	94.67815989
Cyasorb UV 531	0.538	0.282947918
Tinuvin 770	0.232	0.122014715
Luperox TBEC	2.699	1.419472917
Perkalink 301	4.495	2.364035111
Silane A 174	2.155	1.133369447
total	190.141	100

$2c_0$	mass [g]	mass fraction [%]
ELVAX 150W	179.993	91.2142097
Cyasorb UV 531	0.54	0.273653271
Tinuvin 770	0.234	0.118583084
Luperox TBEC	5.401	2.737039477
Perkalink 301	8.998	4.559874322
Silane A 174	2.164	1.096640146
total	197.33	100

$3c_0$	mass [g]	mass fraction [%]
ELVAX 150W	180.025	88.01155725
Cyasorb UV 531	0.541	0.264486891
Tinuvin 770	0.236	0.115376906
Luperox TBEC	8.092	3.956058999
Perkalink 301	13.499	6.599461249
Silane A 174	2.154	1.05305871
total	204.547	100

Quantification samples

#141	mass [g]	mass fraction [%]
ELVAX 150W	180.006	92.86701886
Cyasorb UV 531	0.54	0.27859177
Tinuvin 770	0.239	0.123302654
Luperox TBEC	2.697	1.391411119
Perkalink 301	8.19	4.225308515
Silane A 174	2.16	1.114367081
total	193.832	100

#142	mass [g]	mass fraction [%]
ELVAX 150W	180.021	95.56624357
Cyasorb UV 531	0.543	0.288257871
Tinuvin 770	0.236	0.125283347
Luperox TBEC	2.692	1.429079539
Perkalink 301	2.725	1.446597973
Silane A 174	2.156	1.144537699
total	188.373	100

#143	mass [g]	mass fraction [%]
ELVAX 150W	180.03	96.25934362
Cyasorb UV 531	0.54	0.288729909
Tinuvin 770	0.234	0.125116294
Luperox TBEC	2.699	1.443114861
Perkalink 301	1.358	0.726102253
Silane A 174	2.165	1.157593062
total	187.026	100

#144	mass [g]	mass fraction [%]
ELVAX 150W	180.021	96.96795044
Cyasorb UV 531	0.545	0.293563156
Tinuvin 770	0.233	0.125504982
Luperox TBEC	2.695	1.451656343
Perkalink 301	0	0
Silane A 174	2.156	1.161325074
total	185.65	100

Crosslinking additive quantification by PY-GCMS in EVA - Perkalink 301

chemical	supplier	CAS number
EVATANE 28-25	supplied by project partner	
Cyasorb UV 531	Sigma Aldrich	1843-05-6
Tinuvin 770	Sigma Aldrich	52829-07-9
Luperox TBEC	Sigma Aldrich	34443-12-4
Perkalink 301	Sigma Aldrich	1025-15-6
Silane A 174	Sigma Aldrich	2530-85-0

$1/4c_0$	mass [g]	mass fraction [%]
EVATANE 28-25	50.013	97.7007228
Cyasorb UV 531	0.149	0.291072475
Tinuvin 770	0.066	0.128931432
Luperox TBEC	0.301	0.58800547
Perkalink 301	0.06	0.117210393
Silane A 174	0.601	1.174057433
total	51.19	100

$1/2c_0$	mass [g]	mass fraction [%]
EVATANE 28-25	50.002	97.5858233
Cyasorb UV 531	0.151	0.294697398
Tinuvin 770	0.065	0.126856496
Luperox TBEC	0.3	0.58549152
Perkalink 301	0.121	0.236148246
Silane A 174	0.6	1.17098304
total	51.239	100

$3/4c_0$	mass [g]	mass fraction [%]
EVATANE 28-25	49.997	97.48094133
Cyasorb UV 531	0.15	0.292460372
Tinuvin 770	0.065	0.126732828
Luperox TBEC	0.3	0.584920743
Perkalink 301	0.178	0.347052974
Silane A 174	0.599	1.167891751
total	51.289	100

$1c_0$	mass [g]	mass fraction [%]
EVATANE 28-25	50.012	97.36591064
Cyasorb UV 531	0.15	0.292027645
Tinuvin 770	0.065	0.126545313
Luperox TBEC	0.301	0.586002142
Perkalink 301	0.238	0.463350531
Silane A 174	0.599	1.16616373
total	51.365	100

$5/4c_0$	mass [g]	mass fraction [%]
EVATANE 28-25	50	97.2422109
Cyasorb UV 531	0.152	0.295616321
Tinuvin 770	0.065	0.126414874
Luperox TBEC	0.3	0.583453265
Perkalink 301	0.3	0.583453265
Silane A 174	0.601	1.168851375
total	51.418	100

$3/2c_0$	mass [g]	mass fraction [%]
EVATANE 28-25	50.02	97.13941701
Cyasorb UV 531	0.15	0.29130173
Tinuvin 770	0.065	0.12623075
Luperox TBEC	0.3	0.582603461
Perkalink 301	0.358	0.69524013
Silane A 174	0.6	1.165206921
total	51.493	100

UV additive quantification by UV/VIS in EVA - Tinuvin 329

chemical	supplier	CAS number
ELVAX 150W	Safic Alcan Germany (DOW)	
Tinuvin 329	Sigma Aldrich	3147-75-9
Tinuvin 770	Sigma Aldrich	52829-07-9
Luperox TBEC	Sigma Aldrich	34443-12-4
Perkalink 301	Sigma Aldrich	1025-15-6
Silane A 174	Sigma Aldrich	2530-85-0

$1/4c_0$	mass [g]	mass fraction [%]
ELVAX 150W	49.995	98.99019899
Tinuvin 329	0.042	0.083160083
Tinuvin 770	0.015	0.02970003
Luperox TBEC	0.153	0.302940303
Perkalink 301	0.152	0.300960301
Silane A 174	0.148	0.293040293
total	50.505	100

$2/4c_0$	mass [g]	mass fraction [%]
ELVAX 150W	49.999	98.91194682
Tinuvin 329	0.08	0.15826228
Tinuvin 770	0.026	0.051435241
Luperox TBEC	0.148	0.292785218
Perkalink 301	0.148	0.292785218
Silane A 174	0.148	0.292785218
total	50.549	100

$3/4c_0$	mass [g]	mass fraction [%]
ELVAX 150W	50.014	98.79308642
Tinuvin 329	0.118	0.23308642
Tinuvin 770	0.039	0.077037037
Luperox TBEC	0.152	0.300246914
Perkalink 301	0.152	0.300246914
Silane A 174	0.15	0.296296296
total	50.625	100

$4/4c_0$	mass [g]	mass fraction [%]
ELVAX 150W	50.009	98.71106549
Tinuvin 329	0.149	0.294106036
Tinuvin 770	0.05	0.098693301
Luperox TBEC	0.154	0.303975366
Perkalink 301	0.15	0.296079902
Silane A 174	0.15	0.296079902
total	50.662	100

$5/4c_0$	mass [g]	mass fraction [%]
ELVAX 150W	49.993	98.59579923
Tinuvin 329	0.192	0.378660882
Tinuvin 770	0.068	0.134109062
Luperox TBEC	0.15	0.295828814
Perkalink 301	0.154	0.303717582
Silane A 174	0.148	0.29188443
total	50.705	100

$6/4c_0$	mass [g]	mass fraction [%]
ELVAX 150W	50.011	98.50308247
Tinuvin 329	0.229	0.451044888
Tinuvin 770	0.08	0.157570266
Luperox TBEC	0.149	0.293474621
Perkalink 301	0.153	0.301353135
Silane A 174	0.149	0.293474621
total	50.771	100

Supporting Information

UV lamp spectral effects on the aging behavior of encapsulants for photovoltaic modules

Robert Heidrich [1,2,*], Chiara Barretta [3], Anton Mordvinkin [1], Gerald Pinter [4], Gernot Oreski [3], and Ralph Gottschalg [1,2]

[1]Fraunhofer CSP, Otto-Eissfeldt-Strasse 12, Halle (Saale), 06120, Germany
[2]Anhalt University of Applied Sciences, Bernburger Strasse 55, Koethen (Anhalt), 06366, Germany
[3]Polymer Competence Center Leoben, Roseggerstrasse 12, Leoben, 8700, Austria
[4]Montanuniversitaet Leoben, Otto Gloeckel-Strasse 2, Leoben, 8700, Austria
[*]robert.heidrich@csp.fraunhofer.de

Error propagation for normalized values

The time development of data points is displayed with mean values while the standard deviation expresses the error bars. After normalizing the data y_i to the initial value y_0, the error needs to be transformed. In general, the standard deviation σ was used as uncertainty. The standard deviations and resulting errors were expected to be independent from each other. Gaussian error propagation was used as follows:

$$y_{n_i} = \frac{y_i}{y_0}, \quad \sigma_{n_i} = \sqrt{\sum_{i=1}^{n} \left(\frac{\partial y_{n_i}}{\partial x_i} \sigma_i \right)^2} = \sqrt{\frac{\sigma_i^2}{{y_0}^2} + \frac{{y_i}^2 {\sigma_0}^2}{{y_0}^4}}, \quad \text{for} \quad y_i = y_0 \quad \text{it follows that} \quad \sigma_{n_0} = \sqrt{2}\frac{\sigma_0}{y_0} \tag{1}$$

Pictures of sample preparation

Figure 1. Sample preparation (from left to right) of the weathered coupons.

Figure 1 visualizes the different steps of the sample preparation of the weathered coupons. After extraction from the weathering chamber, the busbar was removed carefully with a cutter knife. In the second step, a rectangular area around the busbar was cut with a cutter knife and peeled with a chisel. When the encapsulant was loose on one side, the layer was peeled by hand or with pliers.

GCMS measurements

Figure 2, Figure 3 and Table 1 are listing the results of the GCMS analysis of the raw encapsulant samples. All assignments in the chromatograms are in accordance with Table 1.

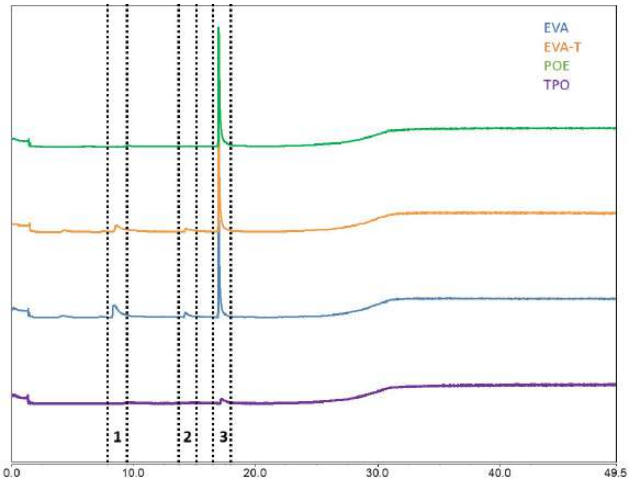

Figure 2. Chromatogram of the 100 °C thermo desorption.

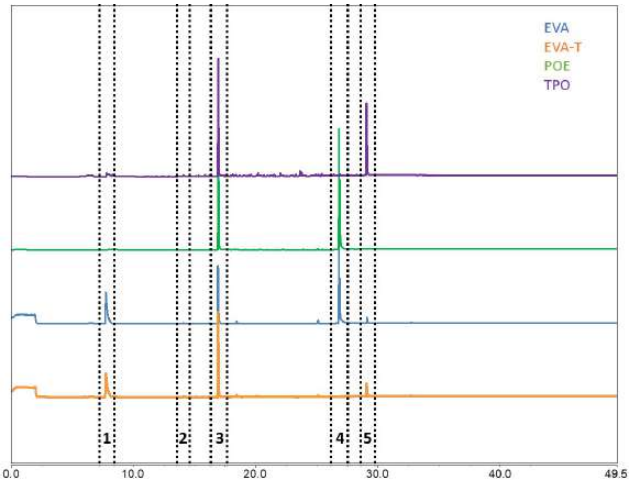

Figure 3. Chromatogram of the 300 °C thermo desorption.

#	Name	Function	EVA	EVA-T	POE	TPO
1	Luperox TBEC	crosslinking agent	++	++	+	+
2	silan A174	adhesion promoter	++	++	-	++
3	Perkalink 301	crosslinking accel.	++	++	++	++
4	Cyasorb UV 531	UV absorber	++	-	++	+
5	Tinuvin 770	UV stabilizer	++	++	-	++

Table 1. Additive mixture of the investigated encapsulants. Additives with ++ are certainly detected in significant amounts, while for + only traces were found. Encapsulants with - do not contain the corresponding additive.

Spectrometer measurements of the A and MAX weathering chamber

Figure 4 visualizes the spectrometer measurements of the weathering chambers for A and MAX weathering using daylight filters. It must be noted that the spectrometer was not calibrated to the used chamber geometry. Therefore, the measured (and integrated) intensity is slightly higher as stated in the program parameters and should be understood qualitatively.

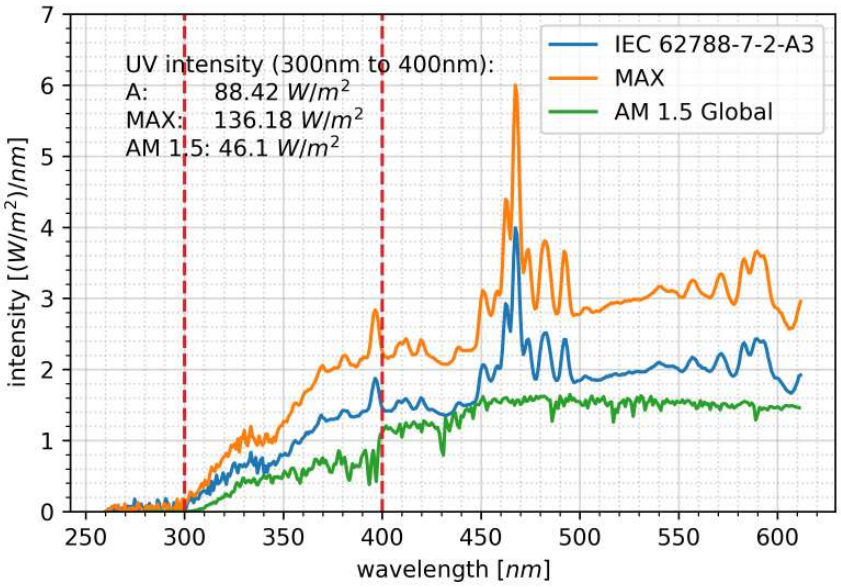

Figure 4. Intensity measurements of the A and MAX weathering chamber.

FTIR difference spectra

Differential spectra of the analyses were plotted to improve the significance of the FTIR measurements and to expand the possibilities for interpretation. For this purpose, the respective initial measurement was subtracted from all other measurements after normalization using the 2850 cm^{-1} CH_2 peak. The resulting peak changes are discussed in the original document with reference to the supporting information.

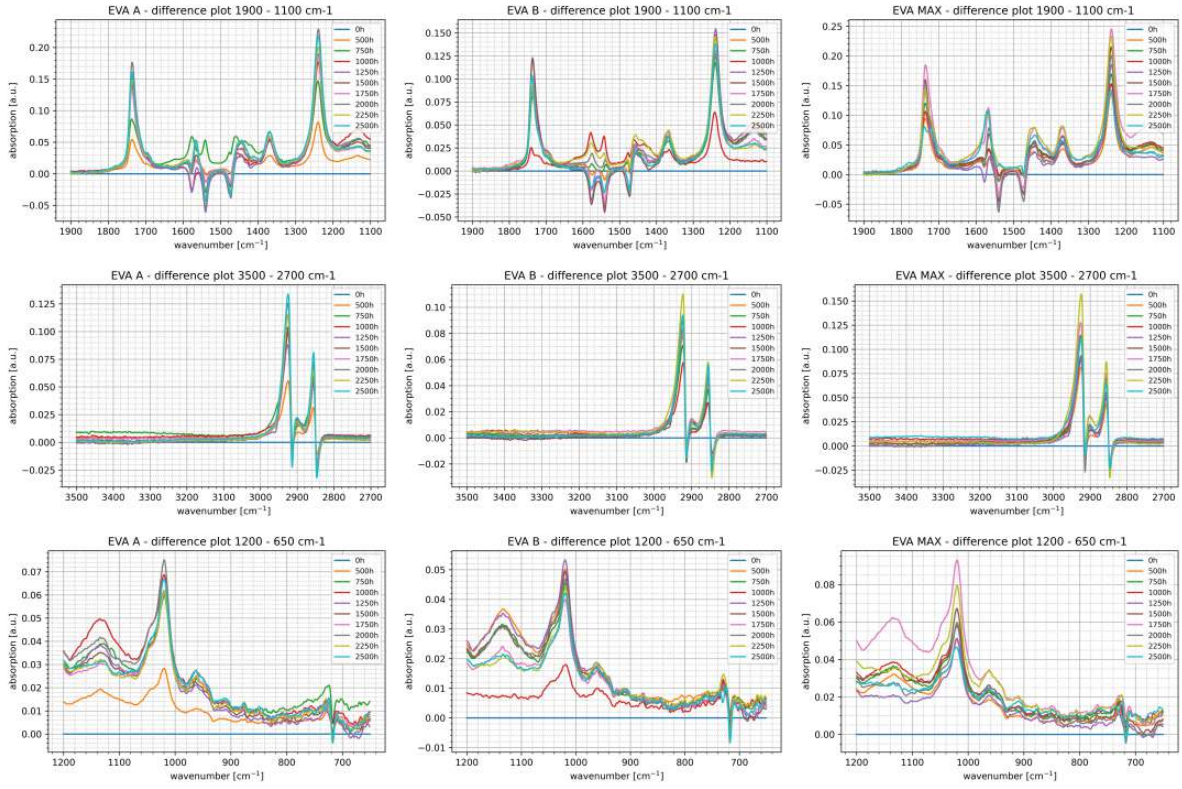

Figure 5. FTIR difference spectra of the EVA samples in the 3500 cm^{-1} to 2700 cm^{-1} interval, the 1900 cm^{-1} to 1100 cm^{-1} interval and the 1200 cm^{-1} to 650 cm^{-1} interval. The initial spectrum (0 h) was subtracted after normalization using the 2850 cm^{-1} CH_2 peak.

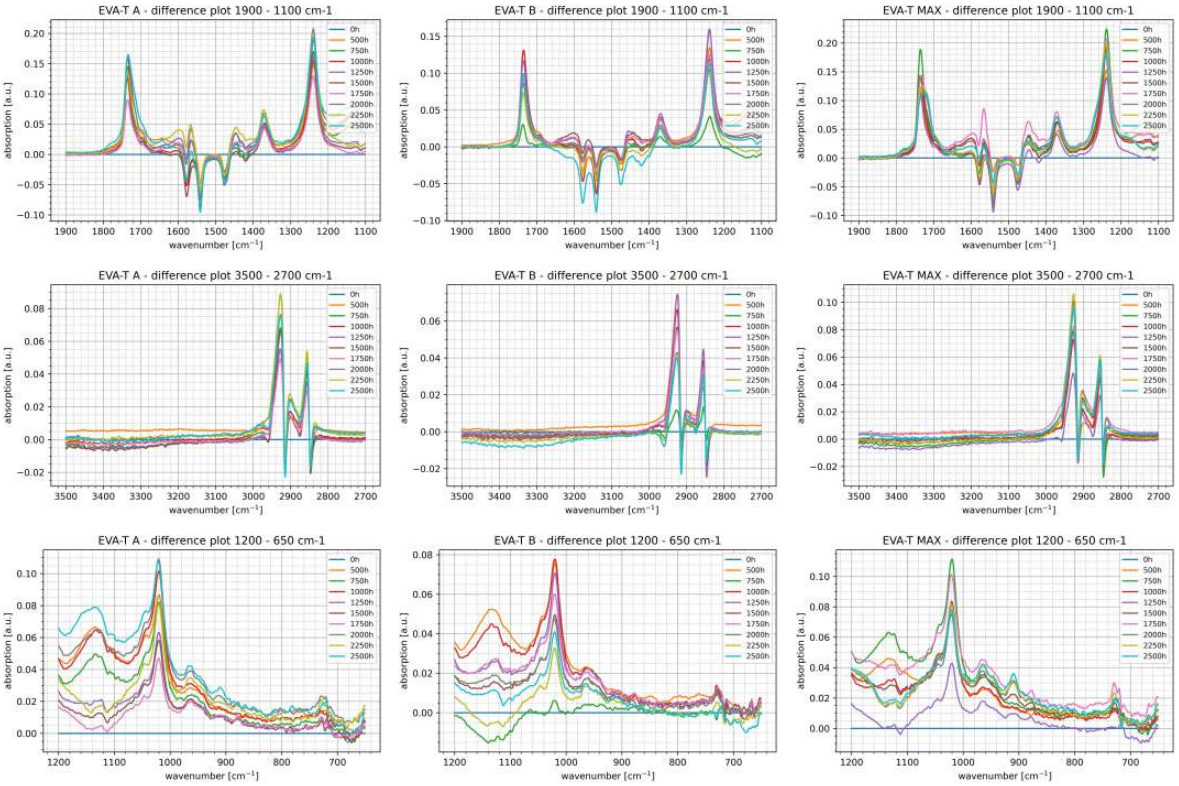

Figure 6. FTIR difference spectra of the EVA-T samples in the 3500 cm^{-1} to 2700 cm^{-1} interval, the 1900 cm^{-1} to 1100 cm^{-1} interval and the 1200 cm^{-1} to 650 cm^{-1} interval. The initial spectrum (0 h) was subtracted after normalization using the 2850 cm^{-1} CH_2 peak.

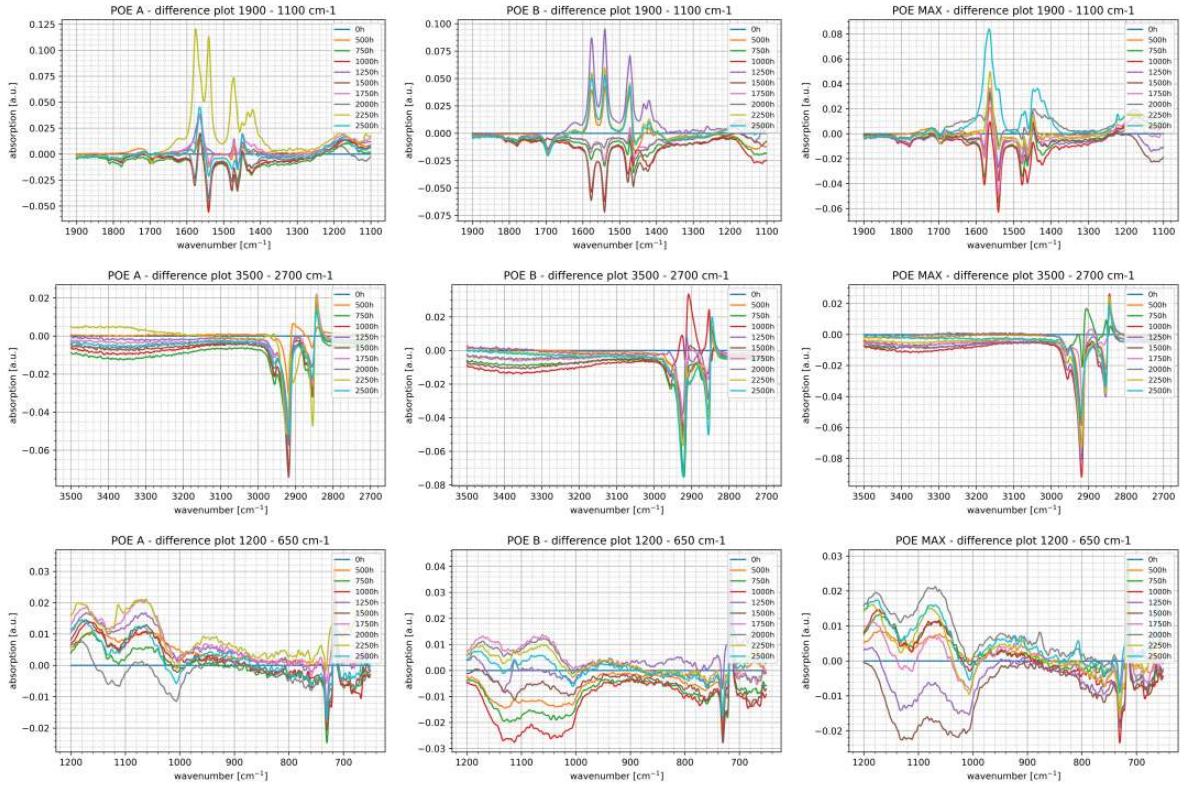

Figure 7. FTIR difference spectra of the POE samples in the 3500 cm^{-1} to 2700 cm^{-1} interval, the 1900 cm^{-1} to 1100 cm^{-1} interval and the 1200 cm^{-1} to 650 cm^{-1} interval. The initial spectrum (0 h) was subtracted after normalization using the 2850 cm^{-1} CH_2 peak.

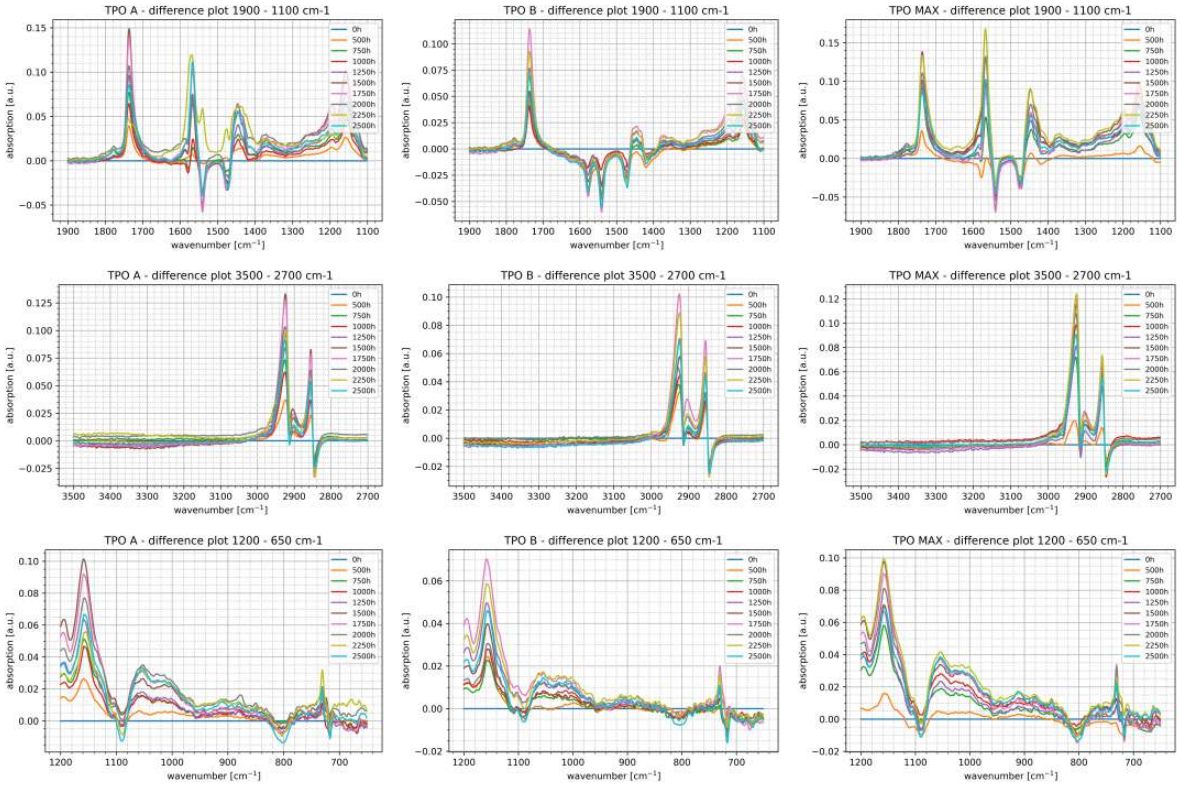

Figure 8. FTIR difference spectra of the TPO samples in the 3500 cm^{-1} to 2700 cm^{-1} interval, the 1900 cm^{-1} to 1100 cm^{-1} interval and the 1200 cm^{-1} to 650 cm^{-1} interval. The initial spectrum (0 h) was subtracted after normalization using the 2850 cm^{-1} CH_2 peak.

PCA weights

EVA

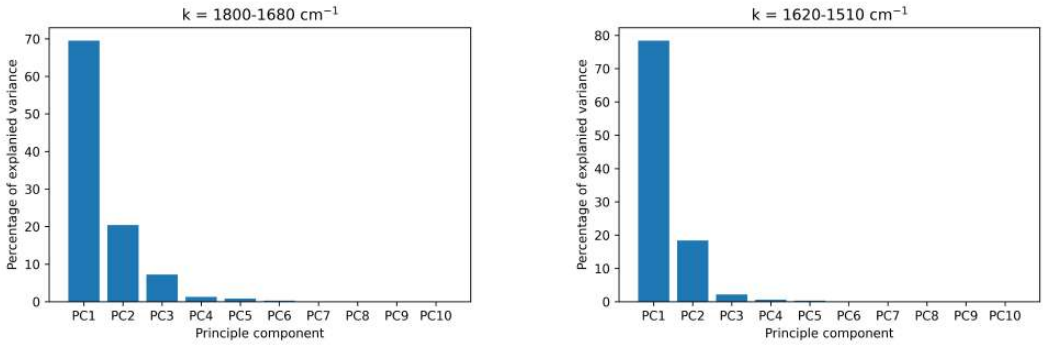

Figure 9. PCA weight distribution of the 1800 cm^{-1} to 1680 cm^{-1} peak (left) and the 1620 cm^{-1} to 1510 cm^{-1} peaks (right).

EVA-T

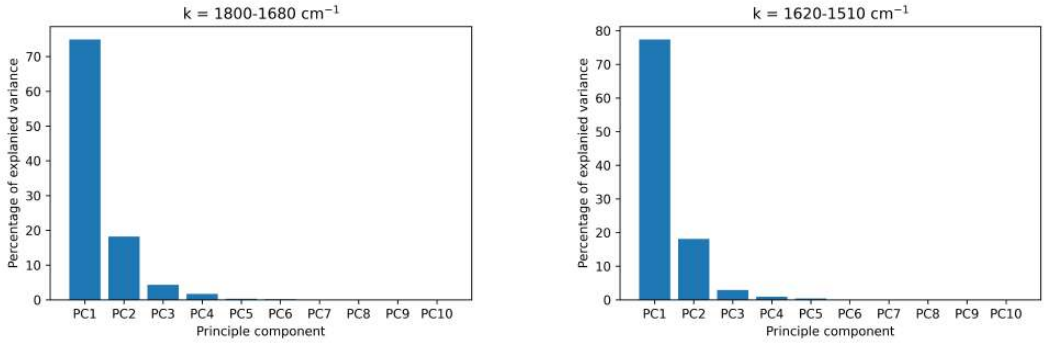

Figure 10. PCA weight distribution of the 1800 cm^{-1} to 1680 cm^{-1} peak (left) and the 1620 cm^{-1} to 1510 cm^{-1} peaks (right).

POE

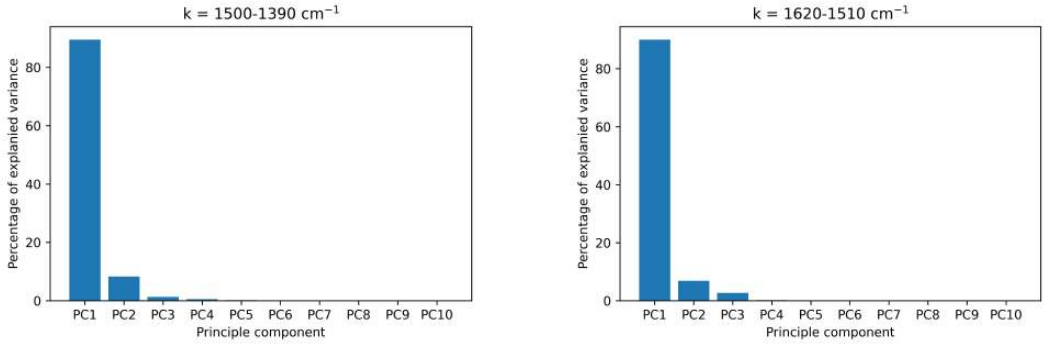

Figure 11. PCA weight distribution of the 1500 cm^{-1} to 1390 cm^{-1} peak (left) and the 1620 cm^{-1} to 1510 cm^{-1} peaks (right).

TPO

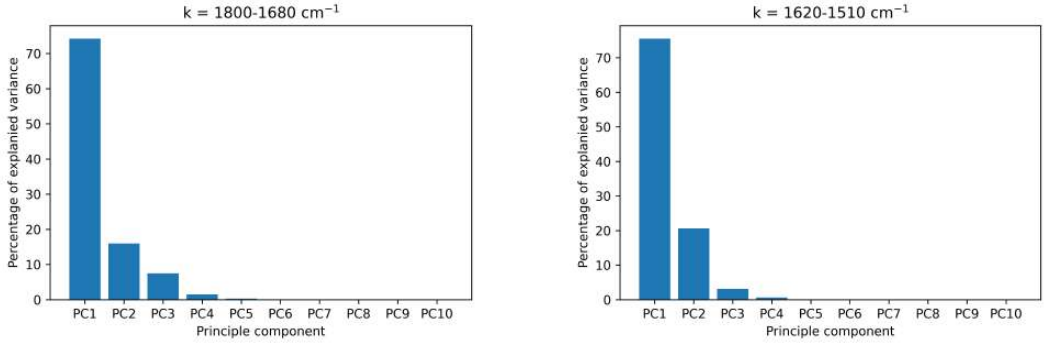

Figure 12. PCA weight distribution of the 1800 cm^{-1} to 1620 cm^{-1} peak (left) and the 1620 cm^{-1} to 1510 cm^{-1} peaks (right).

POE delamination

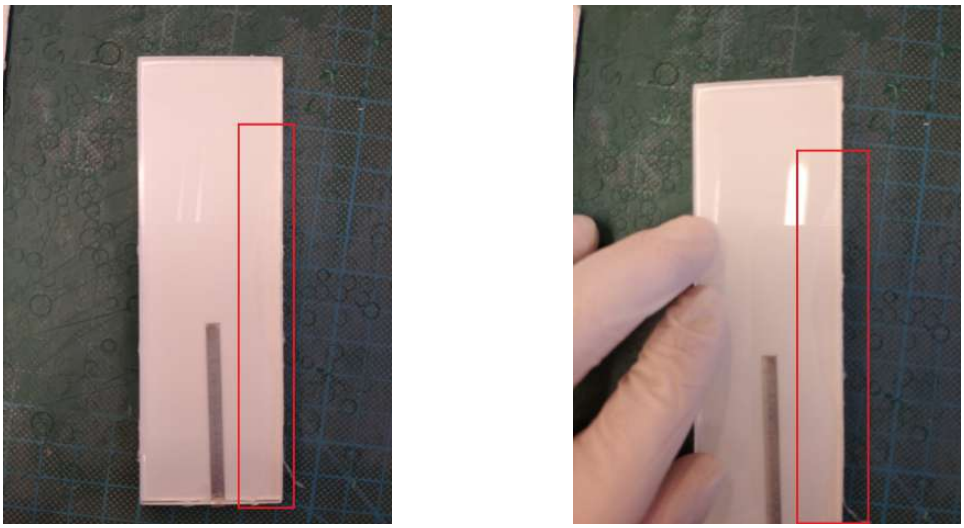

Figure 13. Delamination of a POE sample after 2000 h of weathering under MAX parameters.

EGA-FTIR

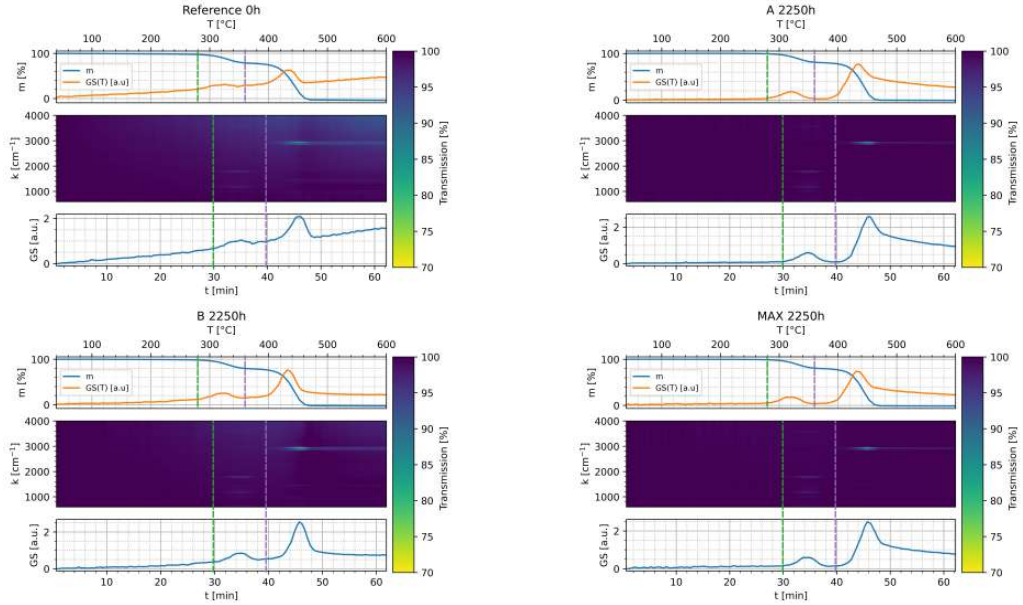

Figure 14. EGA FTIR measurements of the EVA reference (0h, top left), 2250h A weathering (top right), 2250h B weathering (bottom left) and 2250h MAX weathering (bottom right).

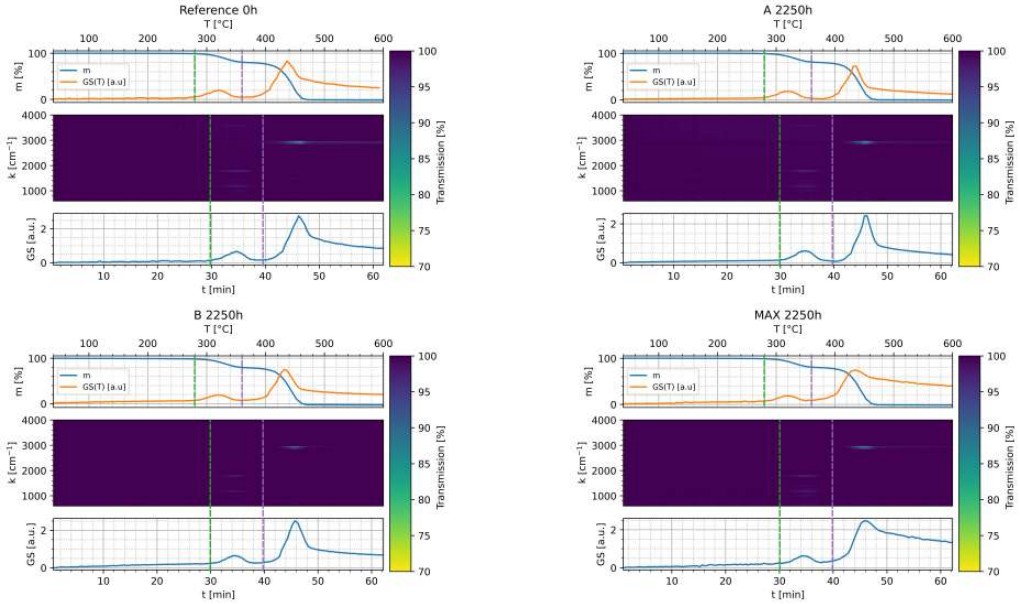

Figure 15. EGA FTIR measurements of the EVA-T reference (0h, top left), 2250h A weathering (top right), 2250h B weathering (bottom left) and 2250h MAX weathering (bottom right).

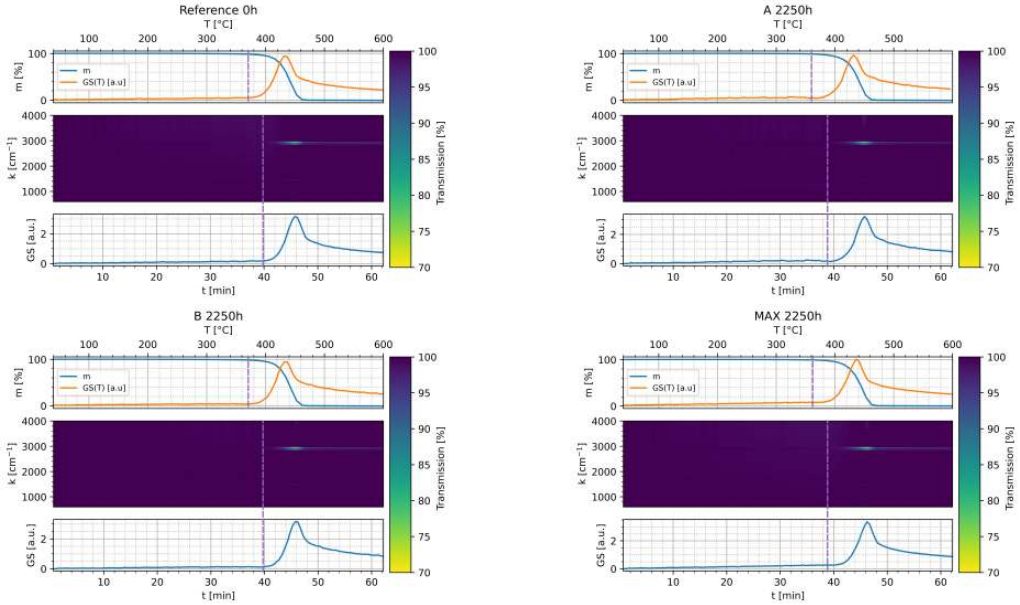

Figure 16. EGA FTIR measurements of the POE reference (0h, top left), 2250h A weathering (top right), 2250h B weathering (bottom left) and 2250h MAX weathering (bottom right).

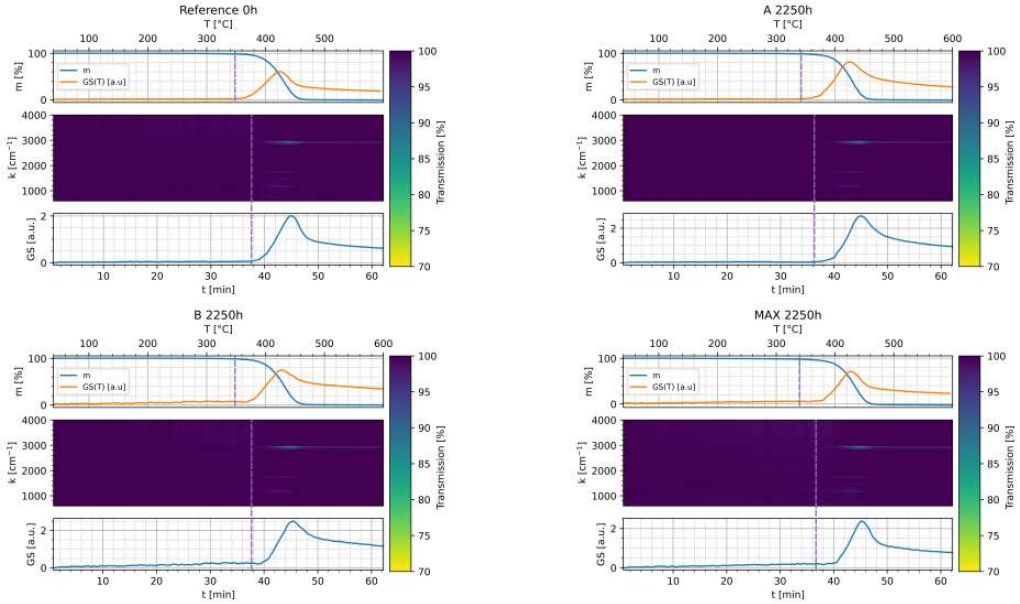

Figure 17. EGA FTIR measurements of the TPO reference (0h, top left), 2250h A weathering (top right), 2250h B weathering (bottom left) and 2250h MAX weathering (bottom right).

UV/VIS reflection measurements

UV/VIS reflection measurements were carried out with a Perkin Elmer Lambda 950 spectrometer. The wavelength interval was set from 300 nm to 800 nm with $\Delta\lambda = 1$ nm. All samples of the same encapsulant type were measured within one measurement cycle.

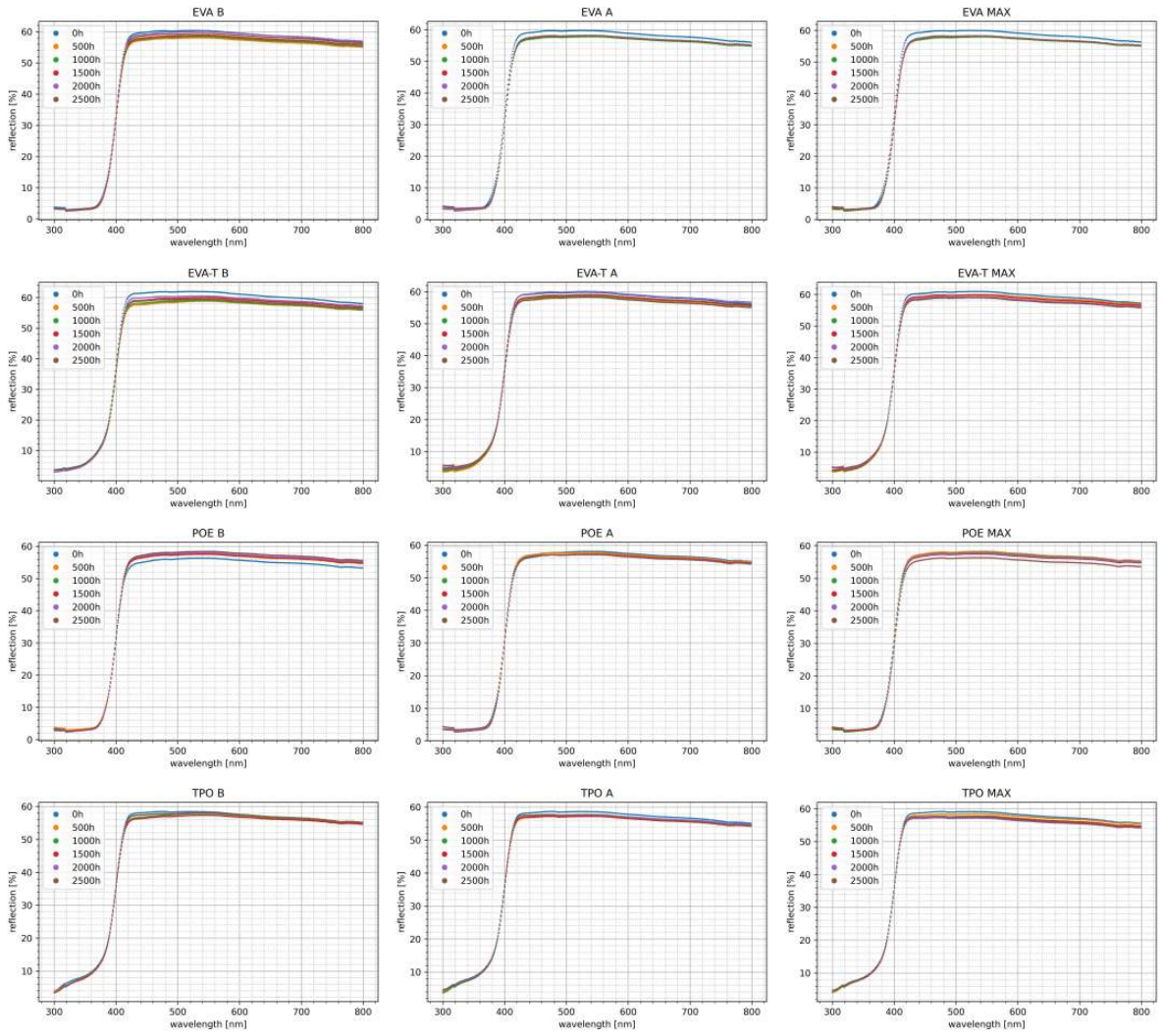

Figure 18. Summary of UV/VIS reflection measurements after B weathering (left), A weathering (middle) and MAX weathering (right).